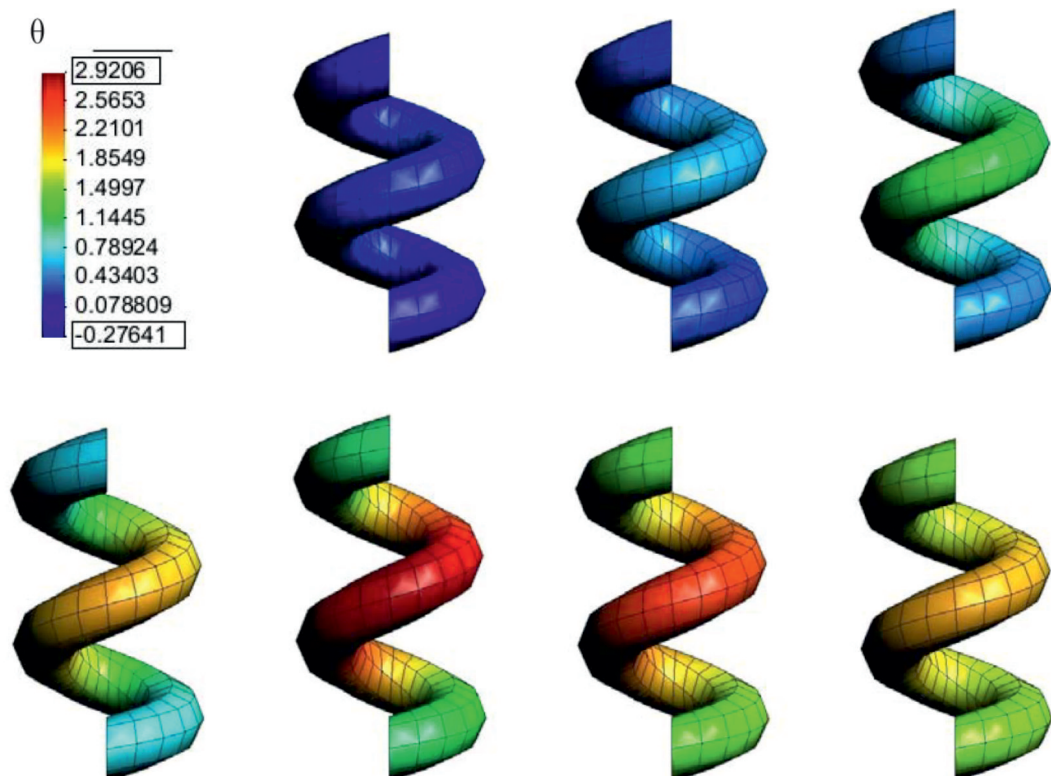


# Simulation of shape memory alloys: material modeling using the principle of maximum dissipation

Philipp Junker



**Simulation of Shape Memory Alloys**  
—  
**Material Modeling using the  
Principle of Maximum Dissipation**

Dissertation  
zur  
Erlangung des Grades  
Doktor-Ingenieur  
  
der  
Fakultät für Maschinenbau  
der Ruhr-Universität Bochum

von

Philipp Junker  
aus Bochum

Bochum 2011

Dissertation eingereicht am: 17.10.2011  
Tag der mündlichen Prüfung: 06.12.2011

1. Gutachter: Prof. rer. nat. Klaus Hackl  
2. Gutachter: Prof. rer. nat. Alexander Hartmaier  
Vorsitzender: Prof. Dr.-Ing. Franz Peters





Herausgeber:

Institut für Mechanik

— Schriftenreihe —

Ruhr-Universität Bochum

D-44780 Bochum

## Summary

This thesis deals with the concept of maximum dissipation in order to derive material models for shape memory alloys. This principle of material modeling allows to fulfill the first and second law of thermodynamics, to include constraints like mass conservation very easily and to end up with thermo-mechanically coupled governing equations. To demonstrate these advantages, in the first part of this work different principles of material modeling are recalled and compared. Based on the example of perfect plasticity the interrelation between material modeling by means of yield functions and the principle of the minimum of the dissipation potential is shown. The inclusion of constraints for modeling inelastic materials is much simplified by this second principle. Afterwards, the principle of maximum dissipation is presented and its embedding in the thermodynamical context is explained.

Based on the theoretical foundations for material modeling discussed in the first part, the second part of this work is dedicated to the application of the principle of maximum dissipation to the modeling and simulation of shape memory alloys. The physical behavior of this fascinating class of materials is explained both for the macro- and microscopic scale. Additionally, its description in an energetic framework is presented. Finally, three different models are derived in a row, each serving as basis for the subsequent one. All models are evaluated in a finite element scheme and compared to experimental data. Wires of Nickel Titanium at different temperatures are simulated such as stripes of different length. Furthermore, numerical results for springs round the entire analysis of each model. The last model is able to display almost all important aspects of shape memory alloys such as localized transformation fronts, temperature dependence and pseudo-elastic as well as pseudo-plastic material behavior. The material softening which associates with the localized phase transformation in pseudo-elasticity and which would cause mesh dependence is solved by a regularization approach. Due to the energetic formulation the model's deductive universality is empirically shown.

Concluding, a new interpretation of a factor that measures the amount of produced entropy is presented. This parameter would be quite hard to determine experimentally. In this work a new scheme of calculating the parameter was found since it could be shown that the parameter is directly linked to chemical energies which are well known. Various numerical examples prove the applicability of this interpretation.

## Kurzfassung

In der vorliegenden Arbeit wird das Konzept der maximalen Dissipation angewendet, um Materialmodelle für Formgedächtnislegierungen zu entwickeln. Dieses Prinzip der Materialmodellierung ermöglicht das identische und simultane Erfüllen des ersten sowie des zweiten Hauptsatzes der Thermodynamik. Weiterhin wird das Einfügen von Nebenbedingungen, wie bspw. Massenerhaltung, sowie das Herleiten von thermo-mechanisch gekoppelten Gleichungen, die das Materialverhalten vorhersagen, wesentlich vereinfacht. Um diese Vorteile zu demonstrieren, werden im ersten Teil der Arbeit verschiedene Prinzipien zur Materialmodellierung miteinander verglichen. Ideale Plastizität dient dabei als Referenz, um den Zusammenhang zwischen der Methode von Fließfunktionen und dem Prinzip des Minimums des Dissipationspotentials aufzuzeigen. Das Einfügen von Nebenbedingungen wird durch das zweite Prinzip wesentlich vereinfacht. Im Anschluss wird das Prinzip der maximalen Dissipation erläutert und seine Einbettung in den thermodynamischen Kontext erklärt.

Basierend auf den theoretischen Grundlagen der Materialmodellierung aus dem ersten Teil der Arbeit greift der zweite Teil das Prinzip der maximalen Dissipation auf, um Formgedächtnislegierungen zu modellieren und zu simulieren. Das physikalische Verhalten dieser besonderen Klasse von Werkstoffen wird sowohl auf makro- als auch auf mikroskopischer Ebene erklärt. Zusätzlich wird eine Beschreibung des Materials von einem energetischen Standpunkt dargelegt. Schließlich werden drei verschiedene Materialmodelle hergeleitet, die aufeinander aufbauen und eine kontinuierliche Verbesserung in ihrer jeweiligen Realitätsnähe aufweisen. Alle Modelle werden im Rahmen der Finite-Elemente Methode ausgewertet und mit experimentellen Daten verglichen. Drähte aus Nickel-Titan bei verschiedenen Temperaturen werden simuliert genauso wie Flachproben unterschiedlicher Länge. Weiterhin runden numerische Ergebnisse für Federn die Analyse der einzelnen Materialmodelle ab.

Das letzte Model ist schließlich in der Lage fast alle wichtigen Eigenschaften von Formgedächtnislegierungen wiederzugeben wie lokalisierte Phasenumwandlungen und die Temperaturabhängigkeit des Materialverhaltens. Dabei liefert das Modell realistische Ergebnisse sowohl für pseudo-elastische als auch für pseudo-plastische Formgedächtnislegierungen, einzig abhängig von der entsprechenden Legierung und Umgebungstemperatur. Der Materialentfestigung, die im pseudo-elastischen Fall mit der lokalisierten Phasenumwandlung einhergeht und Netzabhängigkeiten der numerischen Lösung hervorrufen würde, wird durch einen Regularisierungsansatz begegnet. Aufgrund der energetischen Formulierung des Modells ist es in einem sehr hohen Maße universell anwendbar: Es liefert realistische Ergebnisse für beliebige Lastfälle und Geometrien. Dies wird empirisch an unterschiedlichen Beispielen demonstriert.

Abschließend wird eine neue Interpretation eines Modellparameters präsentiert, der ein Maß für die produzierte Entropie ist. Dieser Parameter ist experimentell nur sehr schwer zu bestimmen. In dieser Arbeit konnte jedoch ein neues Berechnungsverfahren für diesen Parameter gefunden werden. Es wurde gezeigt, dass er direkt in Verbindung zu chemischen Energien steht, die wohlbekannt sind. Verschiedene numerische Beispiele belegen die Anwendbarkeit der neuen Interpretation und schließen die Arbeit ab.

## Acknowledgments

This thesis is the outcome of my work in the years 2008 to 2011 at the Ruhr-University of Bochum. It was funded by Deutsche Forschungsgemeinschaft (DFG) within the scope of SFB 459 Formgedächtnistechnik and supported by Ruhr-University Research School. I am grateful for this financial support.

First of all, I would like to thank Prof. K. Hackl for giving me the opportunity to work at the chair Mechanics of Materials in the Ruhr-University of Bochum. Under his supervision I could broaden my mind considerably: I learned a dealing with material modeling that was completely new to me. During my entire time at his chair he was always a reliable person to go to whenever I needed help or discussion. On the other hand, it was him giving me as much freedom as necessary to pursue my own ideas. This combination created a working setting which was perfect for me.

Additionally, I thank Prof. A. Hartmaier for being the second referee of this work. He was always very polite, not only in this regard but also in his role as my second supervisor in the Ruhr-University Research School. During the entire time he attended interestedly the development of my results.

Furthermore, I thank Prof. F. Peters, the chairman of the examining board. He was one of the first professors who draw my enthusiasm to engineering science.

My further thanks go to all of my colleagues which have become friends in many cases. In the beginning, Th. Bartel and Prof. D. Kochmann were enormous helps and great motivators. S. Krieger, N. Wessels, Ch. Moos and M. Goodarzi gave me much emotional support when I went through tough personal times. In the same setting I want to mention J. Nagel and B. Susteck who proved to be real friends.

It was J. Makowski who had always time and advises for me when I had scientific questions. S. Krieger was in many cases my last resort when I had - once again - problems with my software, hardware and network. Thank you very much!

Finally I want to express my thanks and love to my sister Eva, my mother Andrea and to Nilofar for their motivation and patience.



# Contents

<b>1</b>	<b>Introduction</b>	<b>1</b>
<b>2</b>	<b>Fundamentals</b>	<b>5</b>
2.1	Introduction to Continuum Mechanics . . . . .	5
2.1.1	Mathematical Basis: Scalars, Vectors, Tensors . . . . .	5
2.1.2	abs-function: Subdifferentials and differential inclusions . . . . .	9
2.1.3	Kinematics: Displacement, Deformation and Strain . . . . .	10
2.1.4	Interaction between bodies: Force and Stress . . . . .	11
2.1.5	Balancing: Conservation of Mass . . . . .	14
2.1.6	Kinetic equilibrium conditions: Linear and Angular Momentum . .	14
2.1.7	(Im-)Balances: Energy and Entropy . . . . .	16
2.1.8	Dependences on free energy: Constitutive equations . . . . .	19
2.1.9	Elastic Materials: Free Energy and HOOKE's Law . . . . .	20
2.1.10	Elastic Materials: Elasticity, Hyperelasticity and Hypo-Elasticity . .	21
2.1.11	Potential: Energy Minimization and Equilibrium Conditions . . . .	22
2.2	Inelastic Materials . . . . .	23
2.2.1	Physical Properties of Inelastic Materials . . . . .	23
2.2.2	Mechanical Modeling of Inelastic Materials . . . . .	25
<b>3</b>	<b>Principles for Evolution Equations</b>	<b>29</b>
3.1	Plasticity and Dissipation Potential . . . . .	29
3.1.1	Simplest Approach for Plasticity . . . . .	29
3.1.2	Plasticity with Constraints . . . . .	32
3.2	Principle of the Minimum of the Dissipation Potential . . . . .	34
3.3	Principle of Maximum Dissipation . . . . .	38
<b>4</b>	<b>Smart Materials – Simulation of Shape Memory Alloys</b>	<b>41</b>
4.1	Physical Properties of Shape Memory Alloys . . . . .	41
4.1.1	Macroscopic Behavior of Shape Memory Alloys . . . . .	41
4.1.2	Microscopic Behavior of Shape Memory Alloys . . . . .	43
4.2	Micromechanical Modeling of Shape Memory Alloys . . . . .	47
4.2.1	Energy Convexification . . . . .	47
4.2.2	A basic Model . . . . .	51
4.2.3	An extended Model . . . . .	57
4.2.4	A thermo-mechanically coupled Model . . . . .	60
4.3	Phenomenological Modeling of Shape Memory Alloys . . . . .	64

<b>5</b>	<b>The Finite Element Method</b>	<b>67</b>
5.1	Fundamentals of the Finite Element Method . . . . .	67
5.2	The Finite Element Method for non-linear Materials . . . . .	73
5.2.1	Implementation of the basic Model . . . . .	75
5.2.2	Implementation of the extended Model . . . . .	76
5.2.3	Implementation of the thermo-mechanically coupled Model . . . . .	78
<b>6</b>	<b>Numerical Results</b>	<b>81</b>
6.1	Numerical Results for the basic Model . . . . .	83
6.2	Numerical Results for the extended Model . . . . .	95
6.3	Numerical Results for the thermo-mechanically coupled Model . . . . .	105
6.3.1	Evaluation on the GAUSS point level . . . . .	105
6.3.2	Estimation of the dissipation coefficient $r$ from experiments . . . . .	106
6.3.3	Finite Element Results for the thermo-mechanically coupled Model . . . . .	110
6.3.4	Comparison between the basic model and the phenomenological model of Auricchio and Taylor . . . . .	126
<b>7</b>	<b>Conclusions and Outlook</b>	<b>129</b>
7.1	Conclusions . . . . .	129
7.2	Outlook . . . . .	131
<b>A</b>	<b>Material Data</b>	<b>133</b>
A.1	Nickel Titanium . . . . .	133

## Nomenclature

### Latin notations

$a$	scalar
$A$	area
$dA_1, dA_2, dA_3$	increment in area $A_1, A_2, A_3$
$a_i, b_i$	energetic constants for austenite ( $i = 0$ ) and martensite ( $i \neq 0$ )
$\mathbf{b}_{in}$	inertial forces
$\tilde{\mathbf{B}}$	operator matrix for finite element scheme
$\mathbf{B}$	left CAUCHY-GREEN tensor,
$= \tilde{\mathbf{B}} \cdot \mathbf{N}_u$	operator matrix for finite element scheme applied on the shape functions
$c_i$	chemical energy for austenite ( $i = 0$ ) and martensite ( $i \neq 0$ )
$c_\theta$	heat capacity
$\mathbf{C}$	right CAUCHY-GREEN tensor
$\mathbf{e}_i$	$i$ th unit vector
$\mathbf{E}$	GREEN-ST. VERNANT tensor
$\mathbf{f}$	force
$\mathbf{f}_f$	nodal forces due to internal forces
$\mathbf{f}_t$	nodal forces due to external forces
$\mathbf{F}$	matrix,
	deformation gradient
$g$	arbitrary function
$h$	specific internal heat source
$i \in \{0, \dots, n\}$	crystallographic variant, $i = 0$ is austenite, $i > 0$ martensite variant $i$
$\mathbf{I}$	unit matrix, $(\mathbf{I})_{ij} = \delta_{ij} \mathbf{e}_i \mathbf{e}_j$
$j$	grain with orientation $j$
$J^I, J^{II}, J^{III}$	invariant $I, II, III$
$\mathbf{J}$	JACOBIan
$\mathbf{K}$	stiffness matrix
$m$	mass
$\mathbf{m}_{in}$	inertial moments
$n$	number of crystallographic variants, material dependent
$N$	number of grain orientations
$\mathbf{n}^j$	unit vector normal to area $j$
$\mathbf{N}_u$	shape functions for the displacements
$\mathbf{N}_\varphi$	shape functions for the field function
$\mathbf{N}_\theta$	shape functions for the temperature
$\mathbf{P}$	conjugated thermodynamical driving forces
$\mathbf{q}$	vector of heat flux
$\mathbf{Q}$	rotation matrix



$r$	yield limit, dissipation parameter
$r_{A_s}$	dissipation parameter for starting austenite
$r_{A_f}$	dissipation parameter for finishing austenite
$r_{M_s}$	dissipation parameter for starting martensite
$r_{M_f}$	dissipation parameter for finishing martensite
$\mathbf{R}_u$	nodal residual for the displacements
$\mathbf{R}_\varphi$	nodal residual for the field function
$\mathbf{R}_\theta$	nodal residual for the temperature
$s$	specific entropy
$t$	time
$\mathbf{t}$	traction vector
$\mathbf{t}^*$	prescribed tractions
$\mathbf{T}$	arbitrary tensor of second order
tol	numerical tolerance
$\mathbf{u}$	displacement
$dV = dx_1 dx_2 dx_3$	increment of volume
$w_i$	weighting factor
$\mathbf{w} = \dot{\mathbf{x}}$	velocity
$dx_1, dx_2, dx_3$	increment in coordinate $x_1, x_2, x_3$
$\mathbf{x}$	vector, space coordinate in the undeformed configuration
$\ddot{\mathbf{x}} = \frac{d^2 \mathbf{x}}{dt^2}$	acceleration
$\tilde{\mathbf{x}}$	space coordinate in the deformed configuration

### Greek notations & symbols

$\alpha_\theta$	dissipation parameter for heat flux $\equiv$ inverse of heat conductivity
$\beta$	LAGRANGE parameter
$\beta_\varphi$	coupling parameter
$\chi$	mapping between original and deformed configuration
$c_\varphi$	average surface energy, penalization parameter
$\delta$	variation (operator)
$\delta_{ij}$	KRONECKER delta
$\Delta$	dissipation functional
$\boldsymbol{\varepsilon}$	(total) strain
$\boldsymbol{\varepsilon}_i^j$	strain of crystallographic variant $i$ in grains with orientation $j$
$\boldsymbol{\varepsilon}^{\text{el}}$	elastic strains
$\boldsymbol{\varepsilon}^{\text{pl}}$	plastic strains
$\varphi$	scalar function, field function
$\Phi$	yield function
$\gamma_i^j$	KUHN-TUCKER parameter

$\eta_i^j$	transformation strains for martensite variant $i > 0$ rotated in grain orientation $j$
$\kappa$	LAGRANGE parameter
$\lambda$	tensor of internal variables, volume fractions
$ \lambda_0 $	average amount of austenite
$\Pi$	total potential
$\Pi_{\text{in}}$	internal potential
$\Pi_{\text{ex}}$	external potential
$\theta$	(absolute) temperature
$\theta$	mass moment of inertia
$\rho$	density, consistency parameter
$\sigma$	stress
$\Sigma$	indicator function for plastic material behavior
$\dot{\omega}$	angular acceleration
$\Omega$	body's volume
$\partial\Omega$	body's surface
$\partial\Omega_u$	boundary with prescribed displacements
$\partial\Omega_t$	boundary with prescribed tractions
$\xi^j$	volume fraction of grains with orientation $j$
$\Xi$	value for a subdifferential for $\dot{\lambda} = 0$
$\Psi$	HELMHOLTZ free energy
$\Psi^{\text{con}}$	condensed energy
$\Psi^{\text{rel}}$	relaxed energy
$\Psi^{\text{tot}}$	total free energy
$\mathbb{C}$	elastic constants
$\mathbb{C}_i^j$	elastic constants for crystallographic phase $i$ rotated in direction $j$
$(\mathbb{C})^{-1}$	inverse of tensor $\mathbb{C}$
$\mathbb{S}$	tensor of fourth order
$\mathcal{A}$	active set
$\mathcal{B}$	passive set
$\mathcal{D}$	dissipation
$\mathcal{E}$	internal energy
$\mathcal{J}$	entropy flux and supply, LEGENDRE transformation
$\mathcal{K}$	kinetic energy
$\mathcal{L}$	LAGRANGEan
$\mathcal{L}^*$	LEGENDRE transformed LAGRANGEan
$\mathcal{O}$	order
$\mathcal{Q}$	rate of heat supply
$\dot{\mathcal{S}}$	rate of total entropy
$\mathcal{W}$	mechanical power

dev	deviator
$\text{dev}_{\mathcal{A}^j} P_i^j$	active deviator
$(\mathbf{F})^T$	transpose of matrix $\mathbf{F}$
$\det \mathbf{F}$	determinant of matrix $\mathbf{F}$
$\text{tr} \mathbf{F} := \sum_i F_{ii}$	trace of matrix $\mathbf{F}$
$\partial$	partial derivative
$\nabla := \left( \frac{\partial}{\partial x_1}, \frac{\partial}{\partial x_2}, \frac{\partial}{\partial x_3} \right)$	nabla operator, construction operator for gradient and divergence
$\partial g$	subdifferential of function $g$
arg	argument
inf	infimum
sign	signum function
$(\cdot)^n$	former time step
$(\cdot)^{n+1}$	current time step
$(\cdot) = \frac{d}{dt}$	derivative with respect to time

### Notations & symbols in the material model of Auricchio and Taylor

$R_s^{\text{AS}}$	starting yield limit, transformation austenite to martensite
$R_f^{\text{AS}}$	final yield limit, transformation austenite to martensite
$R_s^{\text{SA}}$	starting yield limit, transformation martensite to austenite
$R_f^{\text{SA}}$	final yield limit, transformation martensite to austenite
$\tilde{q}$	driving forces
$\varepsilon_L$	maximum transformation strain in tension test
$\tilde{\Phi}$	yield function
$\gamma_A$	volume fraction of austenite
$\gamma_M$	volume fraction of martensite
$\vartheta$	tension-compression asymmetry parameter
$\sigma_c^{\text{AS}}$	plateau stress during compression, transformation from austenite to martensite
$\sigma_t^{\text{AS}}$	plateau stress during tension, transformation from austenite to martensite
$\sigma_c^{\text{SA}}$	plateau stress during compression, transformation from martensite to austenite
$\sigma_t^{\text{SA}}$	plateau stress during tension, transformation from martensite to austenite
$\mathbb{C}$	averaged elastic constants

# Chapter 1

## Introduction

Material modeling in continuum mechanics is the science of finding equations which are able to display a reaction of a certain material which was observed in experimental testing. The entire set of equations which describe the material behavior is termed *material model*. In general there exist several different principles to establish a model for a specific material. One way are phenomenological models whose aim is to display the observed material reaction as best as possible by means of different parameters which have to be fit. Another possibility of material modeling is to understand the underlying processes which evolve in materials during loads and include these processes directly into the material model. Such models are called *micromechanical* models. After deriving this, the micromechanical model's quality and the correctness as well as the completeness of the implemented assumptions are tested by comparison between numerical simulation results and experiments. Due to the incorporation of the specific reasons for a certain material behavior via the micromechanical considerations, in general a more universal application of micromechanical models can be expected. An universal material model which is capable of reproducing experimental observations can be used to predict the material reaction of more complex structures and geometries. This may reduce the expenses for experiments if that they are possible which is of great interest in industrial applications.

Although micromechanical models are designed in a way the knowledge about the physical properties of a specific material is implemented, they still may depend on parameters which are only valid for some loading states. A micromechanical model which uses only *global* parameters which are independent of certain local quantities such as stress or strain is called in this work *energetic* model. If only parameters are used which are independent of loading, geometry and others that energetic model is universal and even the parameter identification from experiments is relatively easy since every arbitrary test could be used.

As there exist a whole variety of different methods to execute material modeling, this work focuses on a class of methods which are based on potential principles. This may be understood as deriving the governing equations which are needed to describe the material behavior coming from an energetic point of view. This has the great importance - for example compared to the phenomenological approach mentioned before, for instance in [32], [26], [30], [7], [49] - that energy principles are the most basic physical consideration and independent of any load state or geometry of specimens. Effects which may cause a certain material response do not have to be taken into account while dealing with phenomenological modeling which is in contrast to micromechanical modeling. Here, the internal processes have to be implemented in a more detailed way and thus special artifacts are not smeared out which can be the case if models are basically just relied on rather simple load states. Unfortunately the numerical treatment of micromechanical material models is more com-

plex than that of phenomenological ones which means that the numerical effort measured in computation time is higher. Examples for micromechanical modeling can be found in [16], [53] or in [52].

The aim of this work is to contribute to the field of material theory by application of the principle of maximum dissipation to the case of *shape memory alloys*. Shape memory alloys belong to the class of *smart materials* which are self-adapting. They own the fascinating features of *pseudo-elasticity* and *pseudo-plasticity* which are both of great interest in the field of science as well as in the field of industrial engineering. The property of pseudo-elasticity allows to deform an *alloy* - hence a metallic material - up to 8% *elastically* which is an enormous number. Steel, for instance, can be deformed only up to approx. 0.2 % until plastic deformation takes place, [13]. So, pseudo-elasticity combines parts of the high elasticity of polymers with the high strength of metals. An application of pseudo-elastic shape memory alloys are medical stents, for instance, which open a closed blood vessel. This obviates a by-pass surgery.

Pseudo-plasticity gives this class of alloys its name and reminds to perfect plasticity in a stress-strain diagram at first glance (constant or 'plateau' stress in the stress-strain diagram after exceeding a certain threshold although strain is increased further). In a macroscopic observation, after application and removing of an external mechanical load to a specimen reacting pseudo-plastically, an apparent durable deformation remains in the specimen. Surprisingly, heating the specimen up the 'plastic' deformation will be reversed and the original, undeformed configuration is restored. For this effect only a certain threshold temperature has to be overcome. An application example is a valve which is supposed to open or to close at specific fluid temperatures.

The triggering variable for pseudo-elasticity and pseudo-plasticity is temperature: above a certain temperature pseudo-elastic material behavior is observed, below a certain temperature pseudo-plasticity takes place, [46], [45].

Other material models for shape memory alloys can be found in [2], [4], [15], [16], [40], [41] or [62].

Taking the example of perfect plasticity where its modeling via yield functions is well known as methodical reference, this work will light on different energy based principles of material modeling. The principles discussed here are the usage of yield functions, see [33], [51] and [47] for instance, the principle of the minimum of the dissipation potential, used for example in [35], [23] [36], [4], [20], [25], and the principle of maximum dissipation which was introduced in [43] and [44], rediscovered in [55] and used in [54] and [56]. Particularly the two last mentioned principles make use of the advantage of potentials. Having a potential, there are two main benefits: first, one can be sure that the resulting material model is of a quite constant quality in its ability to deliver realistic simulation results. If the model is able to predict a material answer which coincides well with experiments, the application of the model to any other load state and any other specimen's geometry will create results of similar correctness. Secondly, the inclusion of constraints is much more simplified when dealing with potentials compared to the introduction of yield functions, for instance. In conclusion, energy based methods synthesize a much broader reliability and a very simple and elegant way to take constraints into account.

Processes in shape memory alloys are strongly connected and dependent on temperature. This is why the principle of maximum dissipation is applied in this work to derive a material model for shape memory alloys. Phase transformations in shape memory alloys evolve in a very localized way. Since the basic material model is not able to display this phenomenon,

it is extended in order to display the mentioned localized phase transformations which are observed in experiments. To take the influence of temperature into account, finally a fully thermo-mechanically coupled material model is derived. All models are solved in a finite element scheme which allows to simulate entire specimens made of shape memory alloys. Various numerical examples are presented and compared to experiments from [59] and [48]. Making use of the principle of the minimum of the dissipation potential as well as of the principle of maximum dissipation, a so-called dissipation parameter has to be defined which is quite difficult to be measured directly. Interestingly, a new interpretation of this dissipation parameter or dissipation coefficient could be found in this work which allows to calculate it straight forwardly from well known experimental quantities as enthalpy and entropy differences. This interpretation and this ability of calculation may be valid for all materials undergoing smooth phase transformations (shape memory alloys and water for instance).

In order to clarify the notation as well as to give a very short introduction into the field of continuum mechanics which is supposed to be sufficient to understand the rest of the work, Sec. 2.1 deals with mathematical and physical fundamentals. In Sec. 2.2 the physics of inelastic materials are described as well as their mechanical treatment. As basic example plasticity is discussed in Sec. 2.2.2.

Section 3 deals with different principles of material modeling. Thus, in Sec 3.1 the interrelation between the method yield function and the principle of the minimum of the dissipation potential is pointed out using the example of perfect plasticity, first without any constraints, later including the constraints of volume preservation. Section 3.2 gives a general outline how the principle of the minimum of the dissipation potential is used until in Sec. 3.3 the principle of maximum dissipation is presented. This principle is even more convincing from a thermodynamical point of view and allows for the inclusion of thermal effects.

Section 4 is dedicated to the topic of shape memory alloys. So, in Sec. 4.1 physical properties of shape memory alloys are discussed, both on macroscopic and microscopic scale. The following Sec. 4.2 deals with the micromechanical modeling of shape memory alloys for which in Sec. 4.2.1 a rather short excursion to energy convexification is performed. In Secs. 4.2.2, 4.2.3 and 4.2.4 three different models for shape memory alloys are presented, starting from a basic version which is extended in a first step and to which finally thermal dependence is added.

In order to evaluate the material models on a macroscopic scale - thus for entire specimens - in Sec. 5 a short introduction to the finite element method is given, first for elastic materials and later for inelastic materials, Sec. 5.2. The treatment of the different models in a finite element scheme is presented in Secs. 5.2.1, 5.2.2 and 5.2.3.

In Sec. 6 numerical results for all models are presented for different geometries as well as parameter studies. In Sec. 6.3.1 the new interpretation of the dissipation parameter is pointed out and its calculation can be found in Sec. 6.3.2.

Finally, a conclusion and an outlook is given in Sec. 7.



# Chapter 2

## Fundamentals

### 2.1 Introduction to Continuum Mechanics

Continuum Mechanics is most generally spoken the science of modeling materials with *continuously* distributed mass. The issue of continuum mechanics is the transportation of an observed material's physical behavior under certain loads to a mathematical level. In this way, a prediction of the material's reaction is possible which is of great interest in the field of engineering. Since this work contributes to continuum mechanics, a basic introduction to the theme is given in this section. More general and detailed information may be found in [27], [33], [50] or [22], for example.

#### 2.1.1 Mathematical Basis: Scalars, Vectors, Tensors

The purpose of this section is to lay down a mathematical basis and to clarify the used notation. Although this foundation is sufficient to understand this work, it is certainly not enough to serve as a general basis for continuum mechanics.

Mathematical fields of different order are important in this work. Thus, a short introduction in tensor calculus and analysis is given.

##### Notation

A number can be interpreted as a tensor of zero order - the dimension of this single valued array is zero. These quantities are denoted as *scalars* and will be indicated by a small letter, *a* for instance. A combination of scalars in a one dimensional array are *vectors*. Vectors are equivalently tensors of order one if there exist certain transformation rules, [29]. For vectors small but **bold** letters are used, for example

$$\boldsymbol{x} = \begin{pmatrix} x_1 \\ x_2 \\ x_3 \end{pmatrix} . \quad (2.1)$$

A combination of vectors to a two dimensional array gives a *matrix*. They are tensors of second order only if the aforementioned transformation rules are fulfilled. Such quantities are indicated by capital and **bold** symbols. Thus,

$$\boldsymbol{F} = \begin{pmatrix} F_{11} & F_{12} & F_{13} \\ F_{21} & F_{22} & F_{23} \\ F_{31} & F_{32} & F_{33} \end{pmatrix} . \quad (2.2)$$



This scheme can be extended to tensors of arbitrary order. A tensor of fourth order, for instance, can be represented as a matrix having matrices themselves as components. One famous tensor of fourth order is the elasticity tensor. These class of tensors (tensors of fourth order) is indicated by double stroke symbols, for example  $\mathbb{C}$ .

## Products

A normal multiplication with a scalar is denoted by a small gap between the individual terms which are supposed to be multiplied,  $a = b\,c$  (two scalars) or  $\mathbf{x} = b\,\mathbf{y}$  (a scalar with a vector) for example. Multiplication of a scalar with a tensor of higher order than zero is carried out by multiplying every single component of the tensor with the scalar, hence

$$a\,\mathbf{B} = \begin{pmatrix} a\,B_{11} & a\,B_{12} & a\,B_{13} \\ a\,B_{21} & a\,B_{22} & a\,B_{23} \\ a\,B_{31} & a\,B_{32} & a\,B_{33} \end{pmatrix}. \quad (2.3)$$

Of course, as well as there exists the operation to associate scalars with scalars and scalars with tensors, operations can be introduced which associate tensors with tensors. The first one introduced here is the so-called *dyadic* or *tensor* product. It is indicated by a  $\otimes$  symbol, hence  $\mathbf{x} \otimes \mathbf{F}$  or simply  $\mathbf{x}\,\mathbf{F}$ . This operation multiplies each entry of one tensor with each entry of the other tensor while each scalar valued product is 'saved' in a component of the resulting tensor. In order to provide enough components, the resulting tensor has always an order equivalent to the sum of the single orders the multiplied tensors have. Thus,

$$\mathbf{x} \otimes \mathbf{y} = \mathbf{x}\,\mathbf{y} = \begin{pmatrix} x_1 \\ x_2 \\ x_3 \end{pmatrix} \otimes \begin{pmatrix} y_1 \\ y_2 \\ y_3 \end{pmatrix} = \begin{pmatrix} x_1 y_1 & x_1 y_2 & x_1 y_3 \\ x_2 y_1 & x_2 y_2 & x_2 y_3 \\ x_3 y_1 & x_3 y_2 & x_3 y_3 \end{pmatrix}. \quad (2.4)$$

This product is a very useful and important point in tensor calculus to represent tensors in a so-called *index notation*.

To illustrate this tool, imagine the unit vectors in two dimensions. They are indicated by  $\mathbf{e}_1$  and  $\mathbf{e}_2$  and read

$$\mathbf{e}_1 = \begin{pmatrix} 1 \\ 0 \end{pmatrix}, \quad \mathbf{e}_2 = \begin{pmatrix} 0 \\ 1 \end{pmatrix}. \quad (2.5)$$

Application of the tensor product associating two of the unit vectors gives

$$\mathbf{e}_1\mathbf{e}_1 = \begin{pmatrix} 1 & 0 \\ 0 & 0 \end{pmatrix}, \quad \mathbf{e}_1\mathbf{e}_2 = \begin{pmatrix} 0 & 1 \\ 0 & 0 \end{pmatrix}, \quad \mathbf{e}_2\mathbf{e}_1 = \begin{pmatrix} 0 & 0 \\ 1 & 0 \end{pmatrix}, \quad \mathbf{e}_2\mathbf{e}_2 = \begin{pmatrix} 0 & 0 \\ 0 & 1 \end{pmatrix}. \quad (2.6)$$

Then, obviously every second order tensor  $\mathbf{A}$  can be represented by

$$\mathbf{A} = \begin{pmatrix} A_{11} & A_{12} \\ A_{21} & A_{22} \end{pmatrix} = A_{11} \begin{pmatrix} 1 & 0 \\ 0 & 0 \end{pmatrix} + A_{12} \begin{pmatrix} 0 & 1 \\ 0 & 0 \end{pmatrix} + A_{21} \begin{pmatrix} 0 & 0 \\ 1 & 0 \end{pmatrix} + A_{22} \begin{pmatrix} 0 & 0 \\ 0 & 1 \end{pmatrix}. \quad (2.7)$$

Thus, it is possible to write

$$\mathbf{A} = \sum_{i,j} A_{ij} \mathbf{e}_i \mathbf{e}_j \quad (2.8)$$

or just

$$\mathbf{A} = A_{ij} \mathbf{e}_i \mathbf{e}_j. \quad (2.9)$$

The summation convention after EINSTEIN has been used in Eq. (2.9). That means, every time two *same* indices occur, a summation over this index has to be carried out for which the

summation sign can be dropped. This convention is used in this work if nothing different is said. Of course, same derivations can be carried out for tensors of arbitrary order. Then, the elasticity tensor as example for tensors of fourth order can be written as

$$\mathbb{C} = \mathbb{C}_{ijkl} \mathbf{e}_i \mathbf{e}_j \mathbf{e}_k \mathbf{e}_l . \quad (2.10)$$

The first inner product recalled here is the so-called *dot-product*. This is indicated by  $\mathbf{x} \cdot \mathbf{y}$  and defined to be calculated as

$$\mathbf{x} \cdot \mathbf{y} := \sum_i x_i y_i . \quad (2.11)$$

The advantage of tensor calculus is evident when the index notation is considered. Then, the dot-product only acts on the basis vectors spanning the tensor and gives

$$\delta_{ij} := \mathbf{e}_i \cdot \mathbf{e}_j = \begin{cases} 1, & i = j \\ 0, & i \neq j \end{cases} \quad (2.12)$$

for which the KRONECKER delta  $\delta_{ij}$  can be defined. The result of a dot-product is always a tensor whose dimension is the sum of single dimensions of the product's components minus two.

An important property of the dot-product is that it is equivalent to

$$\mathbf{x} \cdot \mathbf{y} = |\mathbf{x}| |\mathbf{y}| \cos \angle(\mathbf{x}, \mathbf{y}) \quad (2.13)$$

where  $|\cdot|$  indicates the EUCLIDIAN norm calculated by

$$|\mathbf{x}| := \sqrt{\sum (x_i)^2} . \quad (2.14)$$

In an analogous way this norm is applied to tensors of higher order as well.

Another inner product is the so-called *double dot-product* or *double contraction* which is denoted by  $(\cdot) : (\cdot)$ . This operation associates two pairs of basis vectors instead of one pair in the dot-product. Therefore, the double dot-product reduces the resulting dimension by four. It is defined as

$$\begin{aligned} \mathbb{C} : \mathbb{S} &= \mathbb{C}_{ijkl} \mathbf{e}_i \mathbf{e}_j \mathbf{e}_k \mathbf{e}_l : \mathbb{S}_{opqr} \mathbf{e}_o \mathbf{e}_p \mathbf{e}_q \mathbf{e}_r \\ &= \mathbb{C}_{ijkl} \mathbb{S}_{opqr} \mathbf{e}_i \mathbf{e}_j \underbrace{\mathbf{e}_k \cdot \mathbf{e}_o}_{=\delta_{ko}} \underbrace{\mathbf{e}_l \cdot \mathbf{e}_p}_{=\delta_{lp}} \mathbf{e}_q \mathbf{e}_r \\ &= \mathbb{C}_{ijkl} \mathbb{S}_{klqr} \mathbf{e}_i \mathbf{e}_j \mathbf{e}_q \mathbf{e}_r . \end{aligned} \quad (2.15)$$

A different definition for a double contraction is given by  $(\cdot) \cdot (\cdot)$  which associates different basic vectors, namely

$$\begin{aligned} \mathbb{C} \cdot \mathbb{S} &= \mathbb{C}_{ijkl} \mathbf{e}_i \mathbf{e}_j \mathbf{e}_k \mathbf{e}_l \cdot \mathbb{S}_{opqr} \mathbf{e}_o \mathbf{e}_p \mathbf{e}_q \mathbf{e}_r \\ &= \mathbb{C}_{ijkl} \mathbb{S}_{opqr} \mathbf{e}_i \mathbf{e}_j \underbrace{\mathbf{e}_k \cdot \mathbf{e}_p}_{=\delta_{kp}} \underbrace{\mathbf{e}_l \cdot \mathbf{e}_o}_{=\delta_{lo}} \mathbf{e}_q \mathbf{e}_r \\ &= \mathbb{C}_{ijkl} \mathbb{S}_{lkqr} \mathbf{e}_i \mathbf{e}_j \mathbf{e}_q \mathbf{e}_r . \end{aligned} \quad (2.16)$$

If there exists an appropriate symmetry of the associated tensors, both double contractions yield same results, for example in the HOOKE's law, Sec. 2.1.9.

### Tensor analysis

To model and simulate materials the analysis of tensor valued functions is necessary. Therefore, a small introduction in tensor analysis is given in this section. A function is called *field function* if its variable is the spatial vector, given by  $\mathbf{x}$ , no matter whether the resulting function value is a scalar or a tensor of higher order. Thus,

$$\varphi = \varphi(\mathbf{x}) , \quad \mathbf{u} = \mathbf{u}(\mathbf{x}) \quad (2.17)$$

for example. Now, the gradient of the functions, denoted by a nabla symbol  $\nabla$ , can be interesting which is calculated for  $\varphi$  by the partial derivatives of the scalar function  $\varphi$  with respect to each spatial coordinate, thus

$$\nabla \varphi := \begin{pmatrix} \frac{\partial \varphi}{\partial x_1} \\ \frac{\partial \varphi}{\partial x_2} \\ \frac{\partial \varphi}{\partial x_3} \end{pmatrix} . \quad (2.18)$$

If the function itself is a vector, as it is the case for  $\mathbf{u}$ , then the gradient is the conclusion of all partial derivatives of every component of  $\mathbf{u}$  with respect to every component of  $\mathbf{x}$ , so

$$\nabla \mathbf{u} = \nabla \begin{pmatrix} u_1 \\ u_2 \\ u_3 \end{pmatrix} := \begin{pmatrix} \frac{\partial u_1}{\partial x_1} & \frac{\partial u_1}{\partial x_2} & \frac{\partial u_1}{\partial x_3} \\ \frac{\partial u_2}{\partial x_1} & \frac{\partial u_2}{\partial x_2} & \frac{\partial u_2}{\partial x_3} \\ \frac{\partial u_3}{\partial x_1} & \frac{\partial u_3}{\partial x_2} & \frac{\partial u_3}{\partial x_3} \end{pmatrix} . \quad (2.19)$$

In order to simplify this, the general notation under consideration of the different products can be used. Hence, the nabla operator is introduced in index notation as

$$\nabla := \frac{\partial}{\partial x_i} \mathbf{e}_i . \quad (2.20)$$

This simplifies the formulation of Eq. (2.18) to

$$\nabla \varphi = \frac{\partial \varphi}{\partial x_i} \mathbf{e}_i . \quad (2.21)$$

For the second case application of this notation yields

$$\nabla \mathbf{u} = \frac{\partial u_i}{\partial x_j} \mathbf{e}_i \mathbf{e}_j , \quad (2.22)$$

where the dyadic product has been used. It is emphasized that the basis vector of the nabla operator, although incorporating the first position in the operation, always takes the *last* position in the dyadic product. This special treatment of the nabla operator is very common. From these examples and in particular from the introduction of the nabla operator as vectorial quantity, it is obvious that the result of nabla acting on a certain quantity will have a dimension increased by one compared to the previous one. Another way to define this is the gradient operator, thus  $\text{grad } \varphi \hat{=} \nabla \varphi$ . The divergence of a vector, introduced as sum of all

partial derivatives, is by usage of the nabla operator equivalent to  $\text{div } \mathbf{u} \triangleq \nabla \cdot \mathbf{u}$ .

If the chain rule has to be applied to a function with a tensorial argument caution has to be exercised which scalar product has to be used. Let the arbitrary function  $\Psi$  be a function of the tensorial quantity  $\boldsymbol{\lambda} = (\lambda_{ij})$  which is a function of a scalar variable  $t$  itself, thus  $\Psi = \Psi(\boldsymbol{\lambda}(t))$ , then the derivative of  $\Psi$  with respect to  $t$  is

$$\frac{d\Psi}{dt} = \dot{\Psi} = \sum_{i,j} \frac{\partial \Psi}{\partial \lambda_{ij}} \dot{\lambda}_{ij} = \frac{\partial \Psi}{\partial \boldsymbol{\lambda}} : \dot{\boldsymbol{\lambda}}. \quad (2.23)$$

This scheme holds in general.

### 2.1.2 abs-function: Subdifferentials and differential inclusions

In this work several times subdifferentials and differential inclusions occur. To illustrate a subdifferential, the curve of the function  $r|x|$  is printed in Fig. 2.1. Since there is no unique

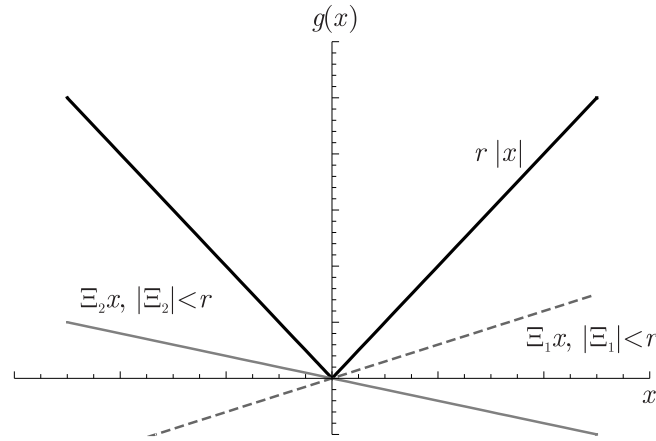


Figure 2.1: Different subdifferentials for the function  $r|x|$  at  $x = 0$ .

derivative at the point  $x = 0$ , there are all tangents possible whose slope is between  $-r$  and  $r$ , for example  $\Xi_1 x$  or  $\Xi_2 x$ . The set of all tangents with slope between these bounds is called subdifferential of  $r|x|$  and indicated by  $\partial(r|x|)$ .

$$\partial(r|x|) = \begin{cases} r \frac{x}{|x|} & x \neq 0 \\ \Xi, |\Xi| < r & x = 0 \end{cases} \quad (2.24)$$

If a subdifferential occurs in an equation, there is no unique way to find the solution since the value of the subdifferential is not unique. Hence, as there exists a set of valid functions, there exists a unique solution for each of these functions. The specific solution has to be taken out of the set of all admissible solutions. This set is called differential inclusion and as it is a mathematical set, the  $\in$  symbol is used.

For the function above, one example could be

$$g'(x) - \partial(r|x|) \ni 0. \quad (2.25)$$

In this case, the solution is just

$$g'(x) = \begin{cases} r & x > 0 \\ \Xi, |\Xi| < r & x = 0 \\ -r & x < 0 \end{cases} \quad (2.26)$$

which is nothing else but  $g'(x) = r \text{ sign } x$ .

### 2.1.3 Kinematics: Displacement, Deformation and Strain

In this work, a mechanical body will be treated as an ensemble of *points*. That means that under deformation the material points forming the body may move and show exactly *as ensemble* a rotation – each single material point does not have any rotation due to its treatment in this work as mathematical point with infinitely small extension. Hence, here only the CAUCHY theory is used instead of the theory of COSSERAT .

In order to describe each point in the material, a vector may be used, denoted by  $\mathbf{x}$ . It contains components in each direction of a Cartesian coordinate system and gives therefore the position of each material point *with reference to the origin of ordinates*, see Fig. 2.2. This vector  $\mathbf{x}$  gives the position of the *undeformed* configuration, while the material points

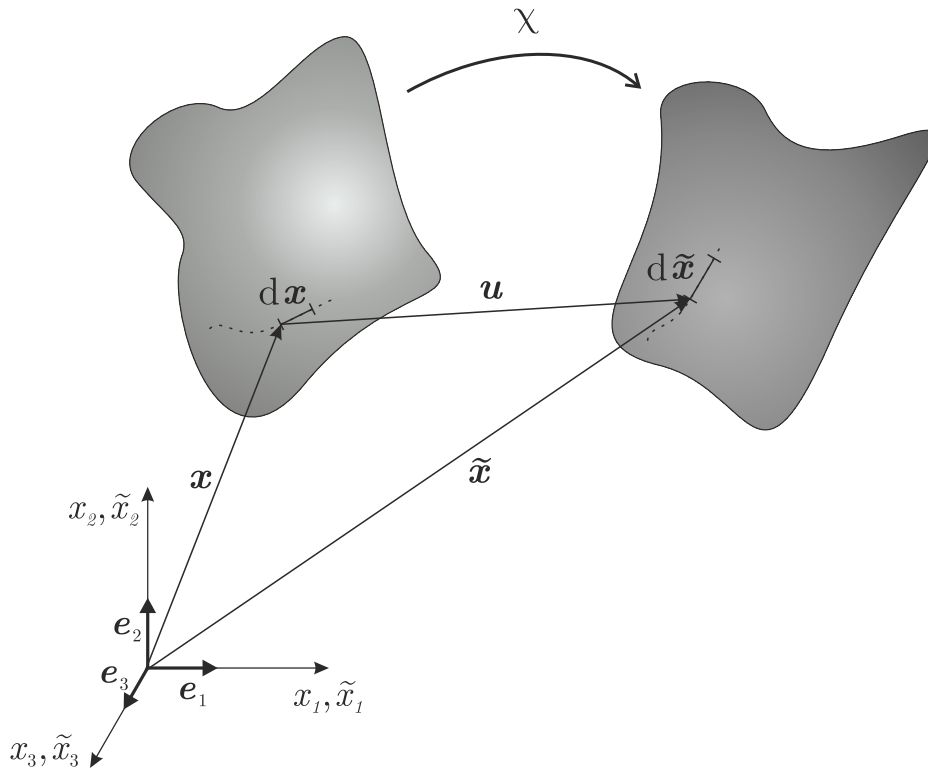


Figure 2.2: Mechanical body at various time steps.

of the body in its *deformed* configuration are indicated by  $\tilde{\mathbf{x}}$ . Then, the displacements, so the difference between the deformed and the original configuration, can be estimated by

$$\mathbf{u} := \tilde{\mathbf{x}} - \mathbf{x} . \quad (2.27)$$

Of course, there will exist a relation between the position vectors in the deformed configuration and those in the original configuration, so  $\tilde{\mathbf{x}}$  can be expressed by means of  $\mathbf{x}$  through a mapping  $\chi$ , namely

$$\tilde{\mathbf{x}} = \chi(\mathbf{x}) , \quad (2.28)$$

where  $\chi$  is called deformation. Hence, the displacements read

$$\mathbf{u} = \chi(\mathbf{x}) - \mathbf{x} = \mathbf{u}(\mathbf{x}) . \quad (2.29)$$

Two neighboring points have in the original configuration a distance which tends to zero. This allows to write  $d\mathbf{x}$  for exactly this difference. Since this analysis is restricted to continuous materials, it is always possible to find points which have in the original as well as in the

deformed configuration a distance tending to zero. Therefore, the two points having  $d\mathbf{x}$  as distance in the original configuration have a distance of  $d\tilde{\mathbf{x}}$  in the deformed configuration. These two lines are linked via

$$d\tilde{\mathbf{x}} = \frac{\partial \tilde{\mathbf{x}}}{\partial \mathbf{x}} \cdot d\mathbf{x} \quad (2.30)$$

which follows from the chain rule. Now, the transition from the original line increment  $d\mathbf{x}$  to the deformed one  $d\tilde{\mathbf{x}}$  can obviously be carried out by means of the derivative of the material points in the deformed configuration with respect to the position vector in the original configuration. This gradient is denoted by *deformation gradient* and termed  $\mathbf{F}$ . It can be calculated according to

$$\mathbf{F} := \frac{\partial \tilde{\mathbf{x}}}{\partial \mathbf{x}} \stackrel{(2.28)}{=} \frac{\partial \chi(\mathbf{x})}{\partial \mathbf{x}} \stackrel{(2.29)}{=} \frac{\partial \mathbf{u}(\mathbf{x})}{\partial \mathbf{x}} + \mathbf{I} \quad (2.31)$$

where  $\mathbf{I}$  is the identity matrix, or in components

$$F_{ij} = \chi_{i,j} = u_{i,j} + \delta_{ij} . \quad (2.32)$$

From now on,  $(\cdot)_{,i}$  means the derivative with respect to component  $i$ .

As usual, as measure for the change in distance of two neighboring points the EUCLIDIAN norm is chosen which is

$$|d\tilde{\mathbf{x}}|^2 = d\tilde{\mathbf{x}} \cdot d\tilde{\mathbf{x}} = (\mathbf{F} \cdot d\mathbf{x}) \cdot (\mathbf{F} \cdot d\mathbf{x}) = d\mathbf{x} \cdot \mathbf{F}^T \cdot \mathbf{F} \cdot d\mathbf{x} . \quad (2.33)$$

From Eq. (2.33) it becomes obvious that the term  $\mathbf{F}^T \cdot \mathbf{F}$  serves as measure how a line element with previously known length  $d\mathbf{x}$  changes its length to the one of  $d\tilde{\mathbf{x}}$ . This term is named as *right CAUCHY-GREEN* tensor and denoted by  $\mathbf{C}$  whereas the *left CAUCHY-GREEN* tensor is indicated by  $\mathbf{B}$ , depending on the position of  $\mathbf{F}$ , so

$$\mathbf{C} := \mathbf{F}^T \cdot \mathbf{F} , \quad \mathbf{B} := \mathbf{F} \cdot \mathbf{F}^T . \quad (2.34)$$

Thus,  $\mathbf{C}$  and  $\mathbf{B}$  serve as measure for the change of distances between neighboring points. However, GREEN-ST.VERNANT proposed a more meaningful measure which is

$$\mathbf{E} := \frac{1}{2} (\mathbf{C} - \mathbf{I}) = \frac{1}{2} (\nabla \mathbf{u} + \mathbf{u} \nabla + (\nabla \mathbf{u}) \cdot (\mathbf{u} \nabla)) . \quad (2.35)$$

Imaging  $\mathbf{F}$  describing a pure rotation, then it follows due to the resulting orthogonality of  $\mathbf{F}$  that  $\mathbf{C} = \mathbf{I}$ . For this example no changes in the distances occur for which a measure yielding zero is more meaningful. This property is exactly fulfilled by  $\mathbf{E}$ . If small derivations between original and deformed configuration are assumed, which is done in this work, a simplified version of Eq. (2.35) can be used as measure. This measure is called *linear strain tensor* and denoted as

$$\boldsymbol{\varepsilon} := \frac{1}{2} (\nabla \mathbf{u} + \mathbf{u} \nabla) = \frac{1}{2} \left( \nabla \mathbf{u} + (\nabla \mathbf{u})^T \right) . \quad (2.36)$$

It can be seen from Eq. (2.36) that  $\boldsymbol{\varepsilon}$  is symmetric.

### 2.1.4 Interaction between bodies: Force and Stress

In contrast to other physical quantities, such as mass or temperature, the purpose of forces and stress is of rather auxiliary character. Derived from the observation that some quantities cause bodies under load to deform, forces are introduced which may react inside a

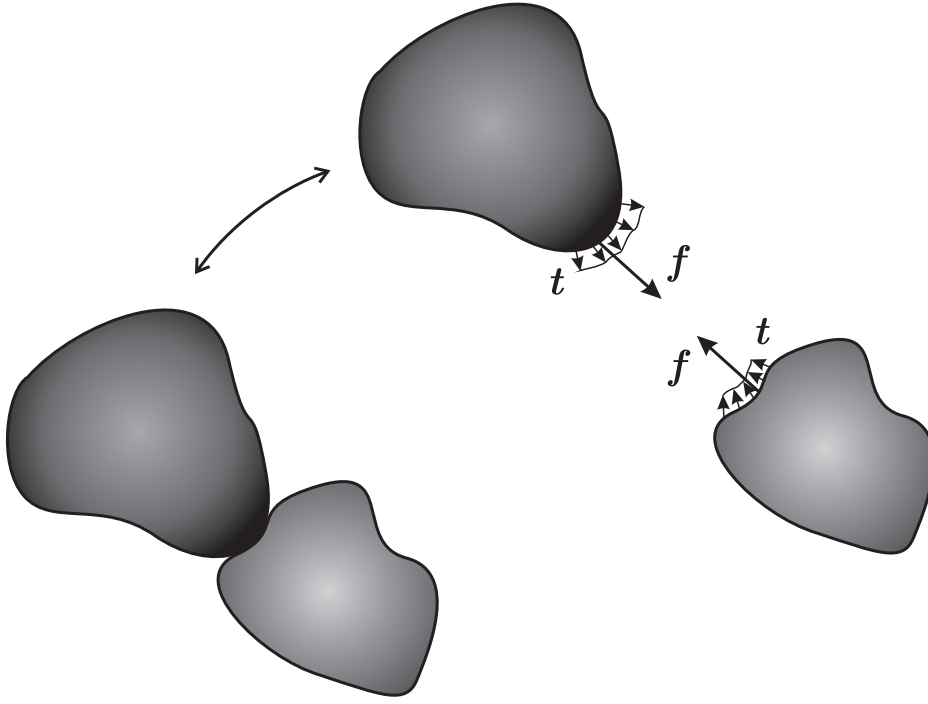


Figure 2.3: Interaction between bodies: forces.

body (volume forces) and on its outside (surface forces). Since a general force may cause deformations in every direction of the current space (mostly a three-dimensional space), it is mathematically a vector with components in each of the individual basic directions. The vector of a surface force is termed *traction vector* and denoted by  $\mathbf{t}$ . Traction vectors can be synthesized by integration to the resulting force  $\mathbf{f}$  according to

$$\mathbf{f} := \int_{\partial\Omega} \mathbf{t} \, dA \quad (2.37)$$

with  $\partial\Omega$  as the body's surface. Forces are then used to take the interactions of different bodies into account which form the entire physical system. This allows to treat single bodies individually.

On the other hand, sometimes the definition of traction vectors by means of forces is carried out as

$$\mathbf{t} := \lim_{\Delta A \rightarrow 0} \frac{\Delta \mathbf{f}}{\Delta A} = \frac{d\mathbf{f}}{dA}, \quad (2.38)$$

see [22], for instance.

To determine the load state of an infinitesimal small volume element uniquely in a Cartesian coordinate system, three traction vectors have to be estimated: One traction vector for each of the three planes perpendicular to one basic direction,  $\mathbf{t}^1$ ,  $\mathbf{t}^2$  and  $\mathbf{t}^3$ , Fig. 2.4. The information carried by the three traction vectors can be synthesized in a new quantity  $\boldsymbol{\sigma}$  in the way that

$$\boldsymbol{\sigma} \cdot \mathbf{n}^j = \mathbf{t}^j \quad (2.39)$$

for  $\mathbf{n}^j$  as unit vector normal to a plane  $j$ , ( $j = 1, 2, 3$ ), stretched by two basic vectors  $\mathbf{e}_i$  and  $\mathbf{e}_k$  with  $i \neq k \neq j$ . With the valid notation

$$\mathbf{t}^j = t_i^j \mathbf{e}_i, \quad (2.40)$$

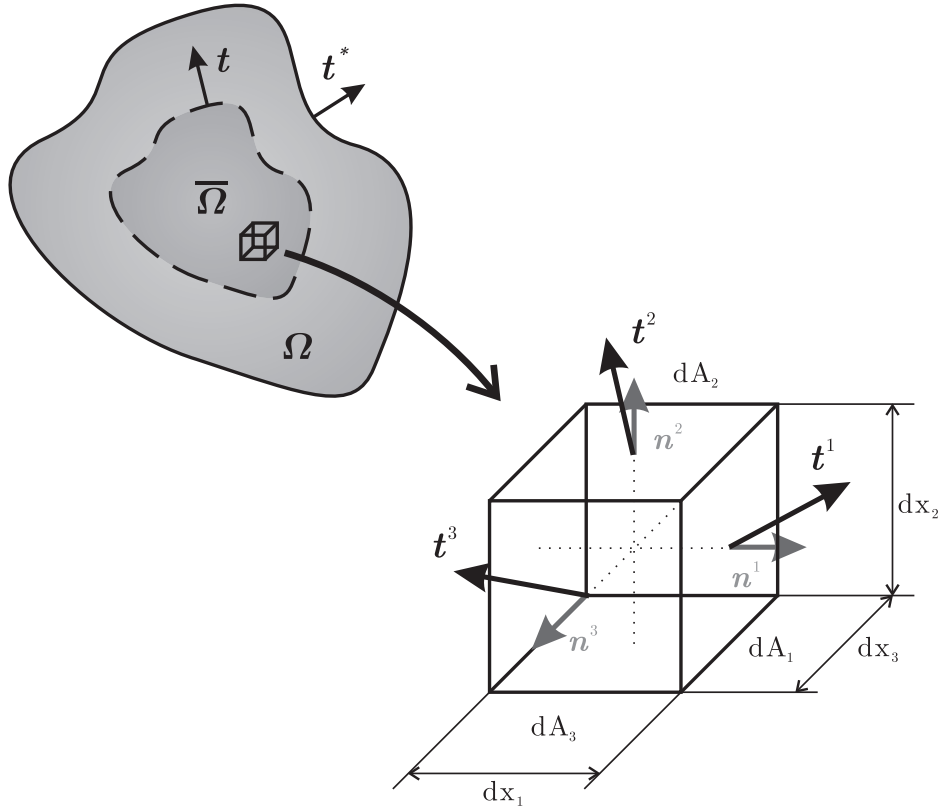


Figure 2.4: Traction vectors.

$e_i$  unit vectors in each direction  $i$ , for the components of  $\sigma$  has to hold

$$\sigma_{i1} = t_i^1, \quad \sigma_{i2} = t_i^2, \quad \sigma_{i3} = t_i^3. \quad (2.41)$$

This yields

$$(\sigma)_{ij} = \begin{pmatrix} \sigma_{11} & \sigma_{12} & \sigma_{13} \\ \sigma_{21} & \sigma_{22} & \sigma_{23} \\ \sigma_{31} & \sigma_{32} & \sigma_{33} \end{pmatrix} = \begin{pmatrix} t_1^1 & t_1^2 & t_1^3 \\ t_2^1 & t_2^2 & t_2^3 \\ t_3^1 & t_3^2 & t_3^3 \end{pmatrix}. \quad (2.42)$$

The quantity  $\sigma$  is called *stress* and provides as space dependent function information about the load state of each point. Of course, if the body deforms under load and the material points change their position, it is necessary to indicate in which coordinate system the stress is given: for the deformed body in the deformed configuration, for the deformed body in the undeformed configuration or for the undeformed body in the undeformed configuration. Since in this work small deformations are assumed, this topic is not discussed here but can be found in [27], [33] or [50], for instance. As a small remark, it is mentioned that again the deformation gradient can be used to transform the information between the different states.

For a given stress tensor, it is possible to find the traction vectors acting on arbitrary surfaces with normal direction  $\mathbf{n}$  according to Eq. (2.39). This relation is called the CAUCHY hypothesis.

In general, forces are grouped into *internal* and *external* forces. The internal forces are equivalently stresses. External forces are body forces such as gravitation and electromagnetic forces, surface forces denoted by  $\mathbf{t}^*$ , and inertial forces due to acceleration. The boundary of the entire body where external loads are given is indicated by  $\partial\Omega_t$ . Here

$$\sigma \cdot \mathbf{n} \stackrel{!}{=} \mathbf{t}^* \quad \text{on } \partial\Omega_t \quad (2.43)$$



has to hold. The total surface of the body is

$$\partial\Omega = \partial\Omega_t \cup \partial\Omega_u \quad (2.44)$$

where the displacements are prescribed on  $\partial\Omega_u$ .

It can be shown that the stress tensor carries information which remains unchanged under rotation. That is, if for one given stress state the point of view is changed by changing the orientation of the coordinate system. This effect of information independent from the coordinate system is quite reasonable since the physics which is mapped by  $\boldsymbol{\sigma}$  must not depend on the choice of view. Then, the traction vectors for an infinitesimal small cube with reference areas perpendicular to the respective basis vectors of the coordinate system can be calculated. The so-called invariants, thus constant properties under rotations, are

$$J^I = \text{tr}\boldsymbol{\sigma} = \sigma_{ii} , \quad (2.45)$$

$$J^{II} = \frac{1}{2}(\sigma_{ij}\sigma_{ji} - \sigma_{ii}\sigma_{jj}) , \quad (2.46)$$

$$J^{III} = \det \boldsymbol{\sigma} = \frac{1}{3} \sigma_{ij}\sigma_{jk}\sigma_{ki} . \quad (2.47)$$

Therefore, if the stress state is once known in one specific coordinate system the state can be given in any other rotated coordinate system as well.

### 2.1.5 Balancing: Conservation of Mass

No processes including nuclear fission or atomic fusion are treated here. Hence, the total amount of mass in a system, denoted by  $m$ , must not change. This is

$$m = \int_{\Omega} \rho dV = \text{const} \quad \Leftrightarrow \quad \dot{m} = 0 . \quad (2.48)$$

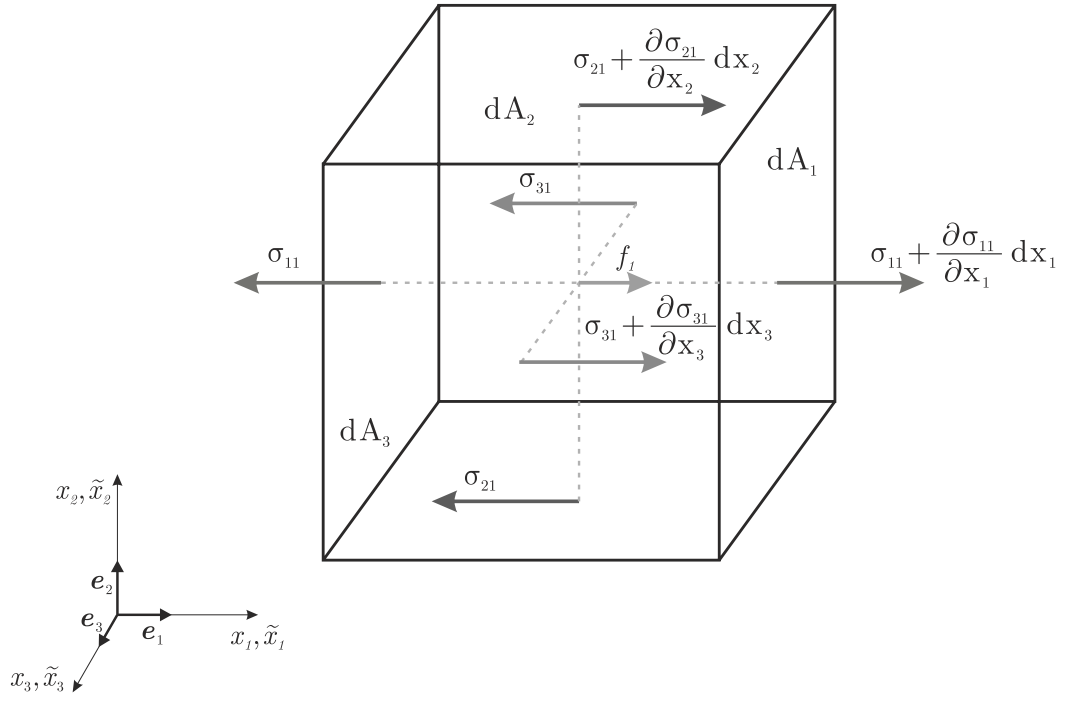
### 2.1.6 Kinetic equilibrium conditions: Linear and Angular Momentum

#### Linear Momentum

The equilibrium condition in classical mechanics in terms of forces, often called NEWTONean laws, are

$$\sum_i \mathbf{f}_i = -\mathbf{b}_{\text{in}} = m \ddot{\mathbf{x}} \quad (2.49)$$

with  $\mathbf{b}_{\text{in}}$  as inertial force. This means that the sum of all forces  $\mathbf{f}_i$  acting on a body yields a change in impulse which is given by mass  $m$  times the acceleration  $\ddot{\mathbf{x}}$ . Regard the cubic volume element already used in Sec. 2.1.4 to introduce stress. This element is cut off the body for which on all sides traction vectors have to be considered. The traction vectors form the components of the stress matrix, Eq. (2.42). Now, in general the values of tractions may change over space. Thus, if the extensions of the cube tend to an infinitesimal length the stresses acting on the cube can be formulated as shown in Fig. 2.5 (only components which contribute to the equilibrium condition in  $x_1$ -direction are plotted). Furthermore, there may occur body forces denoted by  $\mathbf{f}$ . Now, the NEWTONean law can be executed by multiplying

Figure 2.5: Stresses acting in  $x_1$ -direction

the stresses with their respective area and summing these resulting forces up. This results in

$$\begin{aligned}
 \sum_i \mathbf{f}_i &= \left( -\sigma_{11} + \sigma_{11} + \frac{\partial \sigma_{11}}{\partial x_1} dx_1 \right) dx_2 dx_3 \\
 &+ \left( -\sigma_{21} + \sigma_{21} + \frac{\partial \sigma_{21}}{\partial x_2} dx_2 \right) dx_1 dx_3 \\
 &+ \left( -\sigma_{31} + \sigma_{31} + \frac{\partial \sigma_{31}}{\partial x_3} dx_3 \right) dx_1 dx_2 + f_1 dV = \ddot{x}_1 dm = \rho \ddot{x}_1 dV \Big|_{\frac{1}{dV}} \\
 \Leftrightarrow &\quad \frac{\partial \sigma_{11}}{\partial x_1} + \frac{\partial \sigma_{21}}{\partial x_2} + \frac{\partial \sigma_{31}}{\partial x_3} + f_1 = \rho \ddot{x}_1 . \quad (2.50)
 \end{aligned}$$

Similar derivations for the  $x_2$ - and  $x_3$ -direction yield the complete set of *equilibrium conditions for continuous materials* as

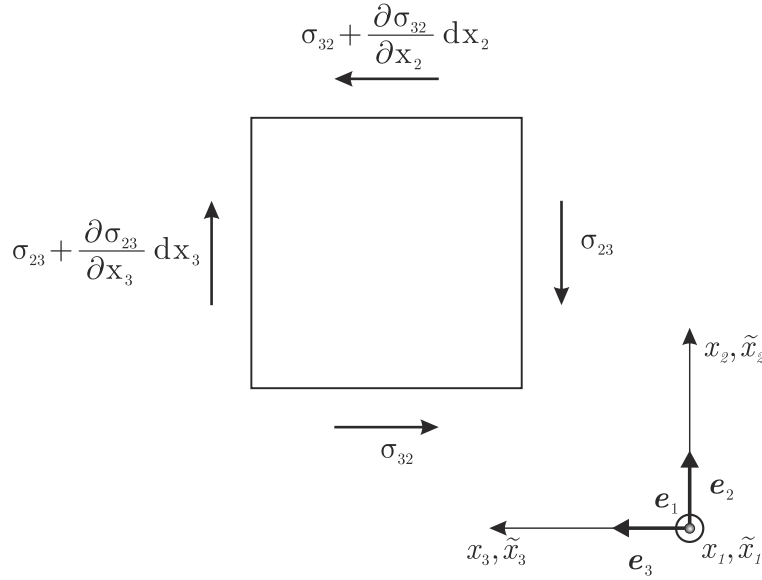
$$\nabla \cdot \boldsymbol{\sigma} + \mathbf{f} = \rho \ddot{\mathbf{x}} . \quad (2.51)$$

### Angular Momentum

The linear momentum refers to a change in impulse, thus a change in a translational movement. For an arbitrary body with finite expansion a translational movement is not the only degree of freedom but rotations about the three axes are possible, too. Thus, a change in angular impulse can be used to state the second equilibrium condition in terms of moments. This is

$$\sum_i \mathbf{m}_i = -\mathbf{m}_{\text{in}} = \boldsymbol{\Theta} \cdot \dot{\boldsymbol{\omega}} \quad (2.52)$$

with the vector of angular accelerations around each of the axes  $\dot{\boldsymbol{\omega}}$  and the mass and geometry dependent factor  $\boldsymbol{\Theta}$ . The moments are defined as force times the orthogonal distance to a reference point. This point may be chosen arbitrarily. Application of the equilibrium

Figure 2.6: Stresses causing an angular momentum around the  $x_1$ -axis

condition for angular moments to the cubic volume element of Sec. 2.1.4 yields for angular moments around the  $x_1$ -axes with the center of the element as reference point

$$\begin{aligned}
 \sum_i \mathbf{m}_i &= \left( \sigma_{32} + \frac{\partial \sigma_{32}}{\partial x_2} dx_2 + \sigma_{32} \right) dx_1 dx_3 \frac{dx_2}{2} \\
 &\quad - \left( \sigma_{23} + \frac{\partial \sigma_{23}}{\partial x_3} dx_3 + \sigma_{23} \right) dx_1 dx_2 \frac{dx_3}{2} = -m_{\text{in},x_1} = 0 \quad \Big| \frac{1}{dV} \\
 \Leftrightarrow \quad \sigma_{32} - \sigma_{23} &= 0, \tag{2.53}
 \end{aligned}$$

see Fig. 2.6.

The cubic volume element tends to a point with infinitesimal small edge lengths. Therefore, the inertial moment in Eq. (2.53) is identically zero since the CAUCHY theory is used. Additionally, the changes of the shear stress are of smaller order for which they do not have to be considered. Similar derivations for the  $x_2$ - and  $x_3$ -axes lead to a symmetric stress tensor,

$$\boldsymbol{\sigma} = \boldsymbol{\sigma}^T. \tag{2.54}$$

## 2.1.7 (Im-)Balances: Energy and Entropy

### Energy

In this section the two laws of thermodynamics are recalled. The first law deals with the conservation of energy since in a closed system, which is the case in this work. The energy cannot be lost but only transferred between different states. Regarding an arbitrary volume element of an arbitrary body, Fig. 2.7, the postulation is made that a change or the rate of the body's entire energy, split into the internal part and the kinetic part, is caused by external mechanical power (due to external forces, for instance) on the one hand and by the heat flow or rate of heat supply (due to heat fluxes) on the other hand. Introducing  $\mathcal{E}$  for the *internal energy*,  $\mathcal{K}$  for the *kinetic energy*,  $\mathcal{W}$  for the *mechanical power* and  $\mathcal{Q}$  for the *rate of heat supply*, the postulate can be brought into the formula

$$\dot{\mathcal{E}} + \dot{\mathcal{K}} = \mathcal{W} + \mathcal{Q}. \tag{2.55}$$

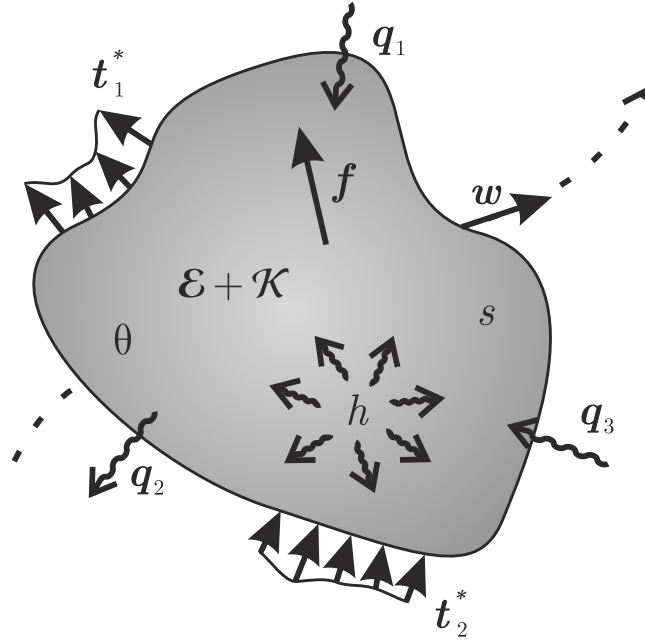


Figure 2.7: Arbitrary body with internal and kinetic energy under the influence of tractions and heat fluxes.

Since the so called (specific) HELMHOLTZ free energy, or just free energy,  $\Psi$  is defined as

$$\int_{\Omega} \Psi \, dV = \mathcal{E} - \int_{\Omega} s \theta \, dV, \quad (2.56)$$

measuring the 'usable' amount of energy which is not 'tied' due to the material's temperature, it is possible to exchange the internal energy in Eq. (2.55) by the free energy. In Eq. (2.56)  $s$  denotes the specific entropy and  $\theta$  the absolute temperature. The integral is taken over the entire material's volume denoted by  $\Omega$ . Furthermore, the mechanical power is given by

$$\mathcal{W} = \int_{\Omega} \mathbf{f} \cdot \mathbf{w} \, dV + \int_{\partial\Omega_t} \mathbf{t}^* \cdot \mathbf{w} \, dA \quad (2.57)$$

with  $\mathbf{f}$  being internal forces (gravitation, for instance) and  $\mathbf{w}$  the velocity vector. Applying the CAUCHY -hypothesis, Eq. (2.39), and considering the balance of linear momentum, Eq. (2.51), the mechanical power can be brought into the form

$$\mathcal{W} = \int_{\Omega} \left( \frac{d}{dt} \frac{1}{2} \rho |\mathbf{w}|^2 + \boldsymbol{\sigma} : \dot{\boldsymbol{\varepsilon}} \right) dV \quad (2.58)$$

Internal heat sources,  $h$ , as well as the heat flux,  $\mathbf{q}$ , entering the body contribute to the rate of heat supply, hence

$$\mathcal{Q} = \int_{\Omega} h \, dV - \int_{\partial\Omega} \mathbf{q} \cdot \mathbf{n} \, dA, \quad (2.59)$$

$\mathbf{n}$  is a normal vector pointing to the *outside* of the body. Using GAUSS theorem, Eq. (2.59) can be transformed to

$$\mathcal{Q} = \int_{\Omega} (h - \nabla \cdot \mathbf{q}) \, dV. \quad (2.60)$$

Introducing

$$\mathcal{K} = \int_{\Omega} \frac{1}{2} \rho |\mathbf{w}|^2 \, dV \quad (2.61)$$

as kinetic energy, the balance of energy, Eq. (2.55), finally reads

$$\begin{aligned} \int_{\Omega} \left( \dot{\Psi} + (s\theta) + \frac{d}{dt} \frac{1}{2} \rho |\mathbf{w}|^2 \right) dV &= \int_{\Omega} \left( \frac{d}{dt} \frac{1}{2} \rho |\mathbf{w}|^2 + \boldsymbol{\sigma} : \dot{\boldsymbol{\varepsilon}} + h - \nabla \cdot \mathbf{q} \right) dV \\ \Leftrightarrow \quad \dot{\Psi} + (s\theta) &= \boldsymbol{\sigma} : \dot{\boldsymbol{\varepsilon}} + h - \nabla \cdot \mathbf{q} \end{aligned} \quad (2.62)$$

since the volume over which the integral is taken may be chosen arbitrarily.

## Entropy

The second law of thermodynamics deals with the direction processes evolve in time. This is caught by the internal variable  $s$ , called *entropy*, and its evolution. More details for internal variables and the entropy are given in Sec. 2.2.2. In contrast to energy which has to be maintained, entropy may only increase in closed systems. Therefore the entropy production,  $\mathcal{D}$ , for the entire body has to be non negative. On the other hand the entropy can be changed, similar to energy, due to entropy fluxes and entropy supplies. Entropy flux and entropy supply are collected in  $\mathcal{J}$ . This yields

$$\begin{aligned} \dot{\mathcal{S}} &= \mathcal{J} + \int_{\Omega} \mathcal{D} dV \\ \Leftrightarrow \quad \int_{\Omega} \mathcal{D} dV &= \dot{\mathcal{S}} - \int_{\Omega} \frac{h}{\theta} dV + \int_{\partial\Omega} \frac{\mathbf{q}}{\theta} \cdot \mathbf{n} dA \stackrel{!}{\geq} 0 \end{aligned} \quad (2.63)$$

with

$$\dot{\mathcal{S}} = \int_{\Omega} \dot{s} dV \quad (2.64)$$

and the usual assumption for the relation of  $\mathcal{J}$  to other thermodynamic quantities. The part  $\mathbf{q}/\theta$  is the amount of entropy leaving the volume due to conduction while  $h/\theta$  indicates the change of entropy by effects such as radiation and chemical or radioactive processes. Applying GAUSS theorem the imbalance of Eq. (2.63) can be transferred to the balance

$$\begin{aligned} \int_{\Omega} \left( \dot{s} - \frac{h}{\theta} + \nabla \cdot \left( \frac{\mathbf{q}}{\theta} \right) \right) dV &= \int_{\Omega} \mathcal{D} dV \\ \Leftrightarrow \quad \dot{s} - \frac{h}{\theta} + \nabla \cdot \left( \frac{\mathbf{q}}{\theta} \right) &= \mathcal{D}. \end{aligned} \quad (2.65)$$

This theorem is obviously true if and only if

$$\mathcal{D} \stackrel{!}{\geq} 0 \quad (2.66)$$

holds. Of course, an expression for the entropy production  $\mathcal{D}$  cannot be found from thermodynamical principles whereas Eq. (2.63), known as the CLAUSIUS-DUHEM inequality, is sometimes more often used. However, if there can be made a reasonable ansatz for the entropy production, Eq. (2.65) offers a very elegant way of mechanical modeling as it is shown in Sec. 3.3. More details on that can be found in [58] or [57].

## Entropy production and energy conservation

Having now two equations at hand which describe the first and second law of thermodynamics, Eqs. (2.62) and (2.65) can be combined. This yields under elimination of  $h$

$$\mathcal{D} = \frac{1}{\theta} \left( \boldsymbol{\sigma} : \dot{\boldsymbol{\varepsilon}} - \dot{\Psi} - s\dot{\theta} \right) + \mathbf{q} \cdot \nabla \frac{1}{\theta}. \quad (2.67)$$

### 2.1.8 Dependences on free energy: Constitutive equations

In this section the relation between the free energy  $\Psi$  and other variables is investigated. When it comes to modeling by means of the principle of maximum dissipation (further details will be given in Sec. 3.3), an approach has to be made for both, energy and entropy production  $\mathcal{D}$ . Although in this section no explicit formulation for the energy is made, a more general property of  $\Psi$  is used to show how stress and entropy depend on the free energy due to the second law of thermodynamics. A more detailed focus on the energy for elastic materials is given in Sec. 2.1.9 and for the class of materials being topic of this work in Sec. 4.2.1.

Energy serves as measure for stored abilities. If a certain material possesses some energy due to its current state (loads, temperature e.g.) there exists the possibility that the material may change this state when the outside conditions are changed, such as an elastic material will restore the original configuration if former external loads are removed. In general the free energy may be a function of displacement, strain, temperature and the gradient of temperature, hence  $\Psi = \Psi(\mathbf{u}, \boldsymbol{\varepsilon}, \theta, \nabla\theta)$  in the thermo-elastic case. Then, the rate of energy can be calculated as

$$\dot{\Psi} = \frac{\partial \Psi}{\partial \mathbf{u}} \cdot \dot{\mathbf{u}} + \frac{\partial \Psi}{\partial \boldsymbol{\varepsilon}} : \dot{\boldsymbol{\varepsilon}} + \frac{\partial \Psi}{\partial \theta} \dot{\theta} + \frac{\partial \Psi}{\partial (\nabla\theta)} \cdot (\nabla\theta) \dot{\phantom{x}}. \quad (2.68)$$

Now, this expression can be plugged into Eq. (2.67) which results in

$$\theta \mathcal{D} = -\frac{\partial \Psi}{\partial \mathbf{u}} \cdot \dot{\mathbf{u}} + \left( \boldsymbol{\sigma} - \frac{\partial \Psi}{\partial \boldsymbol{\varepsilon}} \right) : \dot{\boldsymbol{\varepsilon}} - \left( \frac{\partial \Psi}{\partial \theta} + s \right) \dot{\theta} - \frac{\partial \Psi}{\partial (\nabla\theta)} \cdot (\nabla\theta) \dot{\phantom{x}} + \theta \mathbf{q} \cdot \nabla \frac{1}{\theta} \stackrel{(2.66)}{\geq} 0 \quad (2.69)$$

since for the absolute temperature  $\theta \geq 0$  holds. The velocity  $\dot{\mathbf{u}}$  as well as the rates of strain  $\dot{\boldsymbol{\varepsilon}}$ , temperature  $\dot{\theta}$ , and gradient of temperature,  $(\nabla\theta) \dot{\phantom{x}}$ , may take arbitrary values. Furthermore, all terms of the sum are independent of each other at first glance. Thus, in general the in-equality condition in Eq. (2.69) can only be fulfilled if

$$\begin{aligned} \boldsymbol{\sigma} - \frac{\partial \Psi}{\partial \boldsymbol{\varepsilon}} &= 0 \\ \Leftrightarrow \quad \boldsymbol{\sigma} &= \frac{\partial \Psi}{\partial \boldsymbol{\varepsilon}}, \end{aligned} \quad (2.70)$$

$$\begin{aligned} \frac{\partial \Psi}{\partial \theta} + s &= 0 \\ \Leftrightarrow \quad s &= -\frac{\partial \Psi}{\partial \theta}, \end{aligned} \quad (2.71)$$

and

$$\mathbf{q} \cdot \nabla \frac{1}{\theta} \geq 0 \quad (2.72)$$

hold since. Additionally, the free energy cannot be a function of displacement nor gradient of temperature,  $\Psi = \Psi(\boldsymbol{\varepsilon}, \theta)$ . Hence, the energy fulfills the purpose of a potential field from the mathematical point of view. Stress and entropy can be recast from this potential through the so-called *constitutive equations* Eqs. (2.70) and (2.71).

If the energy depends on more variables than just strain and temperature, for example on another *state* variable (see Sec. 2.2.2) which is termed  $\lambda$ , then the rate of the energy gives

$$\dot{\Psi} = \frac{\partial \Psi}{\partial \boldsymbol{\varepsilon}} : \dot{\boldsymbol{\varepsilon}} + \frac{\partial \Psi}{\partial \theta} \dot{\theta} + \frac{\partial \Psi}{\partial \lambda} \dot{\lambda}. \quad (2.73)$$

Putting this energy into Eq. (2.67), the additional condition

$$-\frac{\partial \Psi}{\partial \lambda} : \dot{\lambda} \geq 0 \quad (2.74)$$

has to be fulfilled which is valid for any additional state variable. This property will be important in Sec. 3.2.

### 2.1.9 Elastic Materials: Free Energy and HOOKE's Law

As this work is restricted to small deformations, the free energy  $\Psi$  for elastic materials can be derived in terms of  $\varepsilon$ . A TAYLOR expansion of the (isothermal) energy  $\Psi(\varepsilon)$  around  $\varepsilon = \mathbf{0}$  yields

$$\Psi(\varepsilon) = \Psi(\mathbf{0}) + \left. \frac{\partial \Psi}{\partial \varepsilon} \right|_{\varepsilon=\mathbf{0}} : \varepsilon + \frac{1}{2} \varepsilon : \left. \frac{\partial^2 \Psi}{\partial \varepsilon^2} \right|_{\varepsilon=\mathbf{0}} : \varepsilon + \mathcal{O}(|\varepsilon|^2). \quad (2.75)$$

Since the energy is a potential field, the reference value, namely  $\Psi(\mathbf{0})$ , can be chosen arbitrarily and is set without any restrictions to zero. Even if the energy may have a value different from zero at zero strain due to chemical parts which are temperature dependent, this constant in the sense of strains would not contribute to any derivative with respect to strain.

Furthermore, it can be postulated that in a so called *natural* configuration the free energy has a local minimum at  $\varepsilon = \mathbf{0}$ . As necessary consequence the first derivative of  $\Psi$  with respect to strain is a zero tensor, namely

$$\left. \frac{\partial \Psi}{\partial \varepsilon} \right|_{\varepsilon=\mathbf{0}} = \mathbf{0} = \sigma|_{\varepsilon=\mathbf{0}} \quad (2.76)$$

from which follows, according to Eq. (2.70), that in the natural configuration an elastic material is *stress-free*. In plasticity, inelastic parts of strain would cause stresses even if the total strain is zero.

The sufficient condition for the minimum is that the second derivative of  $\Psi$  is positive-semidefinite. That means

$$\mathbf{T} : \left. \frac{\partial^2 \Psi}{\partial \varepsilon^2} \right|_{\varepsilon=\mathbf{0}} : \mathbf{T} \geq 0 \quad (2.77)$$

for any given tensor  $\mathbf{T}$ . In Eq. (2.75) the evaluation of the second derivative of the free energy at  $\varepsilon = \mathbf{0}$  is obviously a constant which is called *elasticity tensor* and denoted as

$$\mathbb{C} := \left. \frac{\partial^2 \Psi}{\partial \varepsilon^2} \right|_{\varepsilon=\mathbf{0}}. \quad (2.78)$$

The entries of this tensor of fourth order depend on the specific material and can be estimated experimentally. In result, the free energy for an elastic material is given by

$$\Psi(\varepsilon) = \frac{1}{2} \varepsilon : \mathbb{C} : \varepsilon. \quad (2.79)$$

From Eq. (2.79) the constitutive equation between stress and strain can be derived using Eq. (2.70) as

$$\sigma = \frac{\partial \Psi(\varepsilon)}{\partial \varepsilon} = \mathbb{C} : \varepsilon. \quad (2.80)$$

This linear relation between stress and strain is the famous HOOKE's law and displays exactly the well known experimental observations for linear elastic materials such as steel

under small loads.

Since stress  $\sigma$  and strain  $\varepsilon$  are both symmetric from Eqs. (2.36) and (2.54), respectively, there has to be a symmetry relation in the elastic constant  $\mathbb{C}$  as

$$\mathbb{C}_{ijkl} = \mathbb{C}_{ijlk} \quad \text{and} \quad \mathbb{C}_{ijkl} = \mathbb{C}_{jikl} . \quad (2.81)$$

Equation (2.78) gives in components

$$\mathbb{C}_{ijkl} = \frac{\partial^2 \Psi}{\partial \varepsilon_{ij} \partial \varepsilon_{kl}} = \frac{\partial^2 \Psi}{\partial \varepsilon_{kl} \partial \varepsilon_{ij}} = \mathbb{C}_{klij} \quad (2.82)$$

from which follows that  $\mathbb{C}$  has another symmetry, namely

$$\mathbb{C}_{ijkl} = \mathbb{C}_{klij} . \quad (2.83)$$

### 2.1.10 Elastic Materials: Elasticity, Hyperelasticity and Hypo-Elasticity

In the Secs. 2.1.8 and 2.1.9 the term 'elasticity' has been used quite naturally. However, elasticity can be defined in a finer way. A purely *elastic material* follows the HOOKE's law, Eq. (2.80), in a way that

$$\sigma = \mathbb{C} : \varepsilon \quad (2.84)$$

holds, see Sec. 2.1.9. Hence, the stress only depends linearly on the strains. This very simple relation is not fulfilled by many materials. Therefore, a material is called *hyperelastic* if a free energy can be found such that

$$\sigma|_{t^*} = \left. \frac{\partial \Psi}{\partial \varepsilon} \right|_{t^*} . \quad (2.85)$$

In other words, a material is hyperelastic if for every single point in time  $t^*$  the free energy may be defined right ahead. In this case, if  $\Psi = \Psi(\varepsilon(t))$  is known the stress can be calculated without any additional equations or relations. Of course, coming from this mathematical and physical potential, a non-linearity in the material reaction can be taken into account which has a broader applicability than Eq. (2.84). The problem in this case is that the closed formulation of the free energy for every point in time can be hardly found even for simpler materials.

To circumvent the problem of a closed formulation for  $\Psi$ , it may be defined in dependence of additional variables which change in time, too. So, if the free energy is not only a function of strain but also of some problem specific internal variables called  $\lambda$ , additional equations are necessary, namely *evolution equations* for  $\lambda$ . Then, the set of equations

$$\begin{cases} \sigma &= \frac{\partial \Psi(\varepsilon, \lambda, \theta, \dots)}{\partial \varepsilon} \\ \dot{\lambda} &= g_1(\varepsilon, \lambda, \theta, \dots) \\ \vdots & \end{cases} \quad (2.86)$$

has to be solved for the entire solution of the material's behavior. Although now more equations have to be found, the formulation of the additional equations is easier to execute than finding the 'correct' potential according to Eq. (2.85). Still, there are different ways of finding these equations. This topic is discussed in Sec. 3.



To close the classification of materials, it is mentioned that materials whose governing equations are stated in *rate*-form are termed *hypo-elastic*,

$$\dot{\boldsymbol{\sigma}} = \mathbf{g}_2(\dot{\boldsymbol{\varepsilon}}, \dots) . \quad (2.87)$$

In contrast to hyperelasticity, Eq. (2.85), now the free energy is not used. Instead, by integration of Eq. (2.87) the material reaction can be prescribed.

More detailed discussion on that may be found in [58].

### 2.1.11 Potential: Energy Minimization and Equilibrium Conditions

The free energy can be used to introduce the so-called *internal potential*. That is just

$$\Pi_{\text{in}} := \int_{\Omega} \Psi(\boldsymbol{\varepsilon}) \, dV . \quad (2.88)$$

Then the internal potential measures the energy stored inside the material. Furthermore, a so-called *external potential* can be defined. All internal and external forces which contribute to the total energy of the material are collected in here. Thus, it follows

$$\Pi_{\text{ex}} := - \int_{\Omega} \mathbf{f} \cdot \mathbf{u} \, dV - \int_{\partial\Omega} \mathbf{t}^* \cdot \mathbf{u} \, dA \quad (2.89)$$

with the (prescribed) traction vectors  $\mathbf{t}^*$  acting on the body's surface. Since the total potential as combination of the internal and the external potential is supposed to indicate only the potential stored in the material, the external potential contributes with a negative sign, similar to the definition of the free energy in Eq. (2.56). Consequently,

$$\Pi := \Pi_{\text{in}} + \Pi_{\text{ex}} = \int_{\Omega} \Psi(\boldsymbol{\varepsilon}) \, dV - \int_{\Omega} \mathbf{f} \cdot \mathbf{u} \, dV - \int_{\partial\Omega} \mathbf{t}^* \cdot \mathbf{u} \, dA . \quad (2.90)$$

This potential can be used to find the displacement field  $\mathbf{u}$  for a body under certain internal,  $\mathbf{f}$ , and external,  $\mathbf{t}^*$ , loads by minimizing it with respect to the displacements. This procedure is based on the physical axiom that a system will always tend to a configuration which minimizes its energy. Since the variable of  $\Pi$  (which are the displacements  $\mathbf{u}$ ) is a function itself, the necessary condition for the minimization of  $\Pi$  is that its variation vanishes, so

$$\delta\Pi = \int_{\Omega} \frac{\partial\Psi}{\partial\boldsymbol{\varepsilon}} : \delta\boldsymbol{\varepsilon} \, dV - \int_{\Omega} \mathbf{f} \cdot \delta\mathbf{u} \, dV - \int_{\partial\Omega} \mathbf{t}^* \cdot \delta\mathbf{u} \, dA \stackrel{!}{=} 0 . \quad (2.91)$$

The first part in Eq. (2.91) can be reformulated since the order of the derivative of  $\mathbf{u}$  (which gives the strain) and the derivation can be changed. Furthermore, the identity of Eq. (2.70) allows to write in sum for the first integral

$$\int_{\Omega} \frac{\partial\Psi}{\partial\boldsymbol{\varepsilon}} : \delta\boldsymbol{\varepsilon} \, dV = \int_{\Omega} \boldsymbol{\sigma} : \nabla(\delta\mathbf{u}) \, dV . \quad (2.92)$$

Partial integration of Eq. (2.92) gives

$$\int_{\Omega} \boldsymbol{\sigma} : \nabla(\delta\mathbf{u}) \, dV = \int_{\partial\Omega} \boldsymbol{\sigma} \cdot \mathbf{n} \cdot \delta\mathbf{u} \, dA - \int_{\Omega} \nabla \cdot \boldsymbol{\sigma} \cdot \delta\mathbf{u} \, dV . \quad (2.93)$$

Inserting this result in Eq. (2.91) yields

$$- \int_{\Omega} (\nabla \cdot \boldsymbol{\sigma} + \mathbf{f}) \cdot \delta\mathbf{u} \, dV + \int_{\partial\Omega} (\boldsymbol{\sigma} \cdot \mathbf{n} - \mathbf{t}^*) \cdot \delta\mathbf{u} \, dA = 0 . \quad (2.94)$$

Since the integrals are independent at first glance and furthermore the variation of the displacement  $\delta \mathbf{u}$  may take arbitrary values, it must hold

$$\nabla \cdot \boldsymbol{\sigma} + \mathbf{f} = 0, \mathbf{x} \in \Omega \quad (2.95)$$

$$\boldsymbol{\sigma} \cdot \mathbf{n} - \mathbf{t}^* = 0, \mathbf{x} \in \partial\Omega_t. \quad (2.96)$$

The approach of minimizing the potential consequently results in the equilibrium condition for continua, Eq. (2.95), and gives furthermore the CAUCHY hypothesis, Eqs. (2.39) and (2.96). On the other hand, the (unknown) displacements can be found through minimizing  $\Pi$  under the constraints of prescribed displacements  $\mathbf{u}^*$  on the boundary  $\partial\Omega_u$ . Thus,

$$\mathbf{u} = \arg \min \{ \Pi(\mathbf{u}) \mid \mathbf{u} = \mathbf{u}^* \text{ on } \partial\Omega_u \}. \quad (2.97)$$

If the boundary conditions change in time, for each point in time, or better to say time step, the minimization has to be executed.

This method will be applied to evaluate the material models derived in Sec. 4.2 for entire bodies, see Sec. 5.

## 2.2 Inelastic Materials

The specific constitutive relation between stress and strain is obviously of great importance for the engineering point of view. As the most simple possible relation, the HOOKE's law has been presented in Sec. 2.1.9. However, this linear relation does not hold for many materials, not only due to large deformation so that the introduced measure 'strain' is not valid anymore. In fact, in many materials changes in the physical properties occur during loading (mechanical, thermal, electric, ...) which influence the macroscopic material behavior. Some examples for these changes are described in the following Sec. 2.2.1. This work focuses on alloys so this section is restricted to metals. Since the aim is to model and simulate shape memory alloys which belong to the class of materials with changing physical properties, a general overview of mechanical modeling of inelastic materials is given in Sec. 2.2.2 using the example of perfect plasticity. Although a different approach will be used later on, perfect plasticity will be used as methodical reference.

### 2.2.1 Physical Properties of Inelastic Materials

Metals are composed of atoms forming, at least locally, periodic and structured patterns. An example is presented in Fig. 2.8, [42]. This pattern is always a lattice for whose description different geometrical objects (cube, hexahedron, ...) are used. For further details see Sec. 4.1.2. In reality this lattice is never perfect but inhibits certain forms of defects. These can be inclusions, vacancies, grain boundaries where lattices of different orientations meet, micro-cracks and others, see Fig. 2.9. All of them have significant influence on the material behavior: at least when the number of defects increases it is easy to imagine that the material reacts different than in the original configuration. Cyclic loading or stress greater than a certain threshold stimulates the growth of defects until the specimen fails. Thus, the current microstructure is of substantial importance from the engineering point of view. This becomes evident in Fig. 2.10 where one famous material behavior is caught in a stress-strain diagram: the plastic behavior of steel with hardening (non-linear part with positive slope) and softening region (non-linear part with negative slope). After linear parts non-linear regions follow which may be of quite different character. Whereas the stress-strain diagrams reflect a rather global effect, the underlying reason are the processes which take place on the

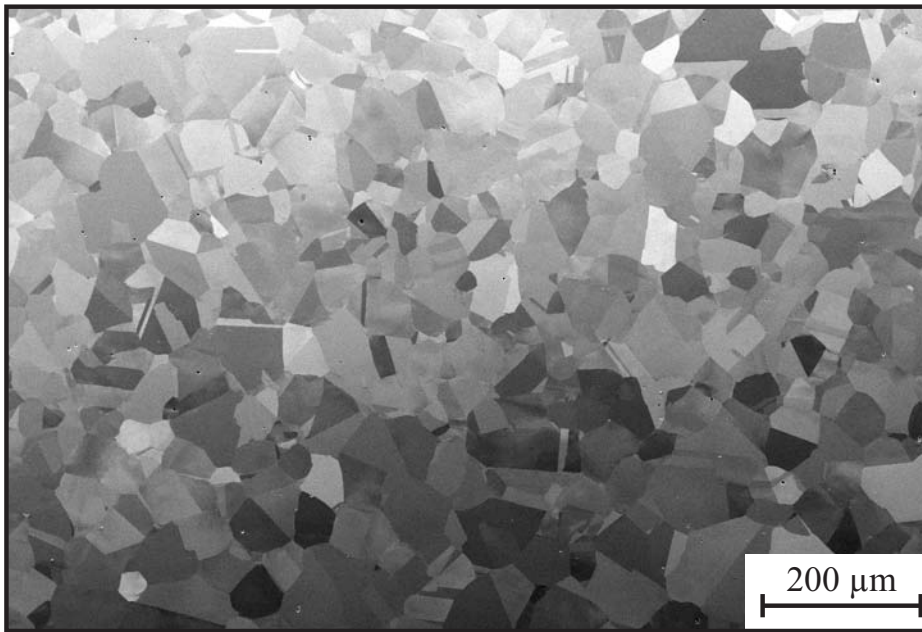


Figure 2.8: Experimentally observed microstructure in steel, courtesy of [42]. Regions of same orientation appear as continuous areas. These areas are single crystals and called in this work grains.

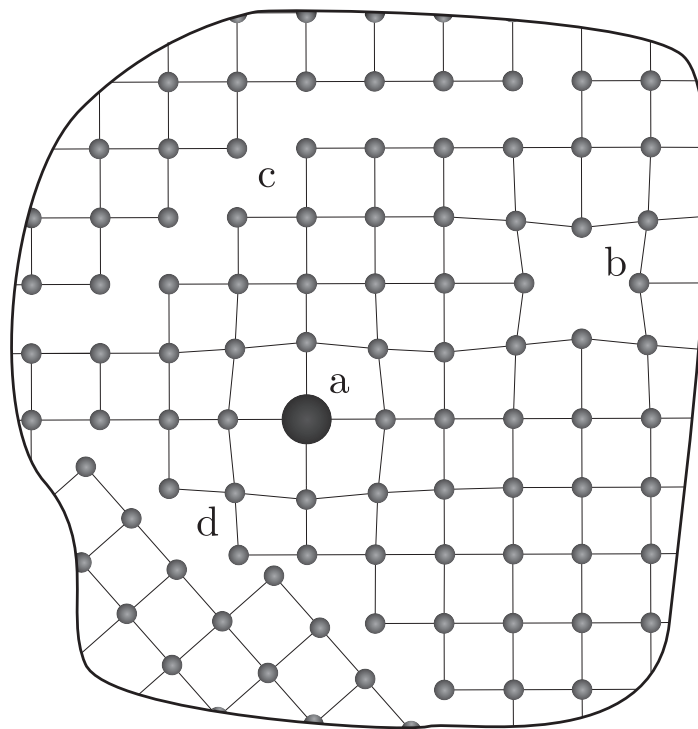


Figure 2.9: Schematic plot of a microstructure. **a**: inclusion, **b**: vacancy, **c**: micro-crack, **d**: grain boundary.

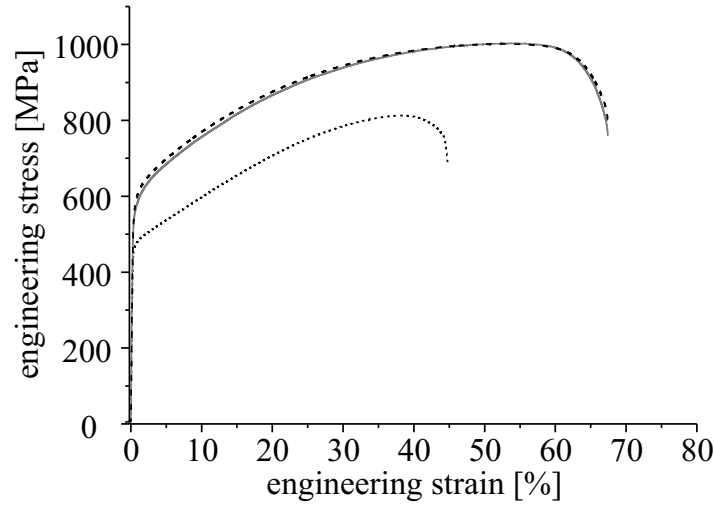


Figure 2.10: Experimentally observed material behavior of a steel, courtesy of [42]

micro-mechanical level.

Similar to the aforementioned changes in microstructure which are permanent, some materials provide the possibility of reversible, elastic changes which offer completely different application than 'regular' materials as steel, for instance. One class of these 'smart' materials are shape memory alloys which are of main interest in this work. A detailed discussion on the processes evolving in shape memory alloys will be given in Sec. 4.1.

### 2.2.2 Mechanical Modeling of Inelastic Materials

In Sec. 2.1.3 the displacement field denoted by  $\mathbf{u}$  was introduced. This field is sufficient to describe the 'macroscopic' and isothermal state of a body and could be used for the linear constitutive relation between stress and strain in the HOOKE's law. As it was pointed out in Sec. 2.2.1, there exists a huge variety of materials which do not follow this law. Therefore, the displacement field as only variable cannot be enough to model inelastic and particularly hypo-elastic materials, see Sec. 2.1.10. From the physical point of view, changes of the micromechanical properties effect the macroscopic material behavior significantly. In order to take this phenomenon into account during modeling, additional information is needed which describes exactly these physical changes. Hence, problem dependent additional variables have to be used which describe the *internal* state of the material which are therefore called *internal variables*. The most general and universal internal variable is the well known entropy  $s$  which purpose is to provide information about the direction of time. For example, the entropy can be used to describe the cooling process of a piece of heated metal in a cool surrounding. Since the direction of heat flow (from the hot metal to the cool surrounding) is not reversible in time, the entropy may be used to take exactly this phenomenon into account. In contrast to the elastic specimen under mechanical load where a release of the specimen will be accompanied by a return to the original zero displacement field, the heat will not flow back to its source when the heating process is stopped. Thus, this *irreversible* process of heating has a well defined and unique direction in time which is expressed by

$$\dot{s} \geq 0 \quad (2.98)$$

for closed systems. This equation is known as second law of thermodynamics, Sec. 2.1.7. Similar to the internal variable 'entropy' additional internal variables can be introduced in a

way that they are able to provide the desired information.

The modeling of plasticity for instance can be carried out by defining an internal variable which collects all effects causing a plastic deformation. These effects may be inclusions, vacancies, micro-cracks and others which are synthesized in one additional variable, called plastic strain and denoted by  $\epsilon^{\text{pl}}$ . Since this work is restricted to small deformations, the total strain is just the addition of its elastic and plastic part, thus

$$\begin{aligned}\epsilon &= \epsilon^{\text{el}} + \epsilon^{\text{pl}} \\ \Leftrightarrow \epsilon^{\text{el}} &= \epsilon - \epsilon^{\text{pl}}.\end{aligned}\quad (2.99)$$

Obviously, the elastic free energy is only a function of the elastic part of the strain. Application to the energy used in Sec. 2.1.9 gives

$$\Psi(\epsilon) = \frac{1}{2}(\epsilon - \epsilon^{\text{pl}}) : \mathbb{C} : (\epsilon - \epsilon^{\text{pl}}) \quad (2.100)$$

and using the constitutive equation for stress yields

$$\sigma = \frac{\partial \Psi}{\partial \epsilon} = \mathbb{C} : (\epsilon - \epsilon^{\text{pl}}). \quad (2.101)$$

Hence, for a given strain  $\epsilon$  the energy as well as the stress can be calculated if the plastic part of the strain,  $\epsilon^{\text{pl}}$ , is known. Until now, only the equations derived in Sec. 2.1.11 are given which can be solved for the displacements  $\mathbf{u}$ . From the displacements both strain and stress can be estimated. As shown in that section, the equilibrium equation may be obtained from the physical principle of energy minimization. Here, the additional variable  $\epsilon^{\text{pl}}$  is introduced which has to be determined and consequently equations are needed describing its evolution.

As shown in Fig. 2.10, a steel under load first reacts linearly in the stress strain diagram. If the total load is too small to leave that region (a value of app. 580 MPa in Fig. 2.10), removing of the load causes the specimen to return to its original undeformed state. On the other hand, if a certain threshold value (here 580 MPa) has been overcome the material behaves non-linearly. From the modeling point of view, in the linear part the simple HOOKE's law is completely sufficient to display the material reaction. Reaching the non-linear plastic part the HOOKE's law has to be extended according to the presented idea of introducing the addition internal variable  $\epsilon^{\text{pl}}$ . Thus, the introduction of a measure which distinguishes between these two parts seems to be convenient. The most popular measure is a so-called *yield function* denoted by  $\Phi$ . This yield function is defined in a way that if  $\Phi$  is smaller than zero a modeling with the use of the linear HOOKE's law is chosen, plastic behavior takes place for  $\Phi = 0$ . Positive values are not allowed and thus  $\Phi$  equals zero indicates that a plastic deformation takes place. In this case, a switch to the non-linear modeling is necessary and an evolution of the plastic strains has to be regarded. In a numerical treatment testing values for the plastic strain will cause positive values for  $\Phi$ . Then, an update of the plastic strains is executed until the yield function is zero again. Hence, for each state, irrelevant if elastic or plastic deformation is taking place, the yield function has to be less or equal to zero. Assuming that the yield function is a function of some variable  $\mathbf{P}$  it may be defined as

$$\Phi(\mathbf{P}) := f(\mathbf{P}) - r^2 \stackrel{!}{\leq} 0 \quad (2.102)$$

with an appropriate function  $f(\mathbf{P})$ . The value of  $r$  has to be chosen such that the previously mentioned threshold value for plastic behavior is mapped correctly. From the mathematical

point of view the yield function defines a (hyper-)plane in the space of the variable  $\mathbf{P}$  for which the plastic strains have to be updated until the yield *surface* is reached again. For the yield surface  $\Phi = 0$  holds true. Consequently, the derivative of  $\Phi$  with respect to some parameter  $a$  defined on the surface ( $\Rightarrow \mathbf{P} = \mathbf{P}(a)$ ) is

$$\Phi' = \frac{\partial f}{\partial \mathbf{P}} : \frac{\partial \mathbf{P}}{\partial a} \stackrel{!}{=} 0. \quad (2.103)$$

The derivative of  $\mathbf{P}$  with respect to  $a$  is the tangent to the surface whereas  $\partial f / \partial \mathbf{P} = \partial \Phi / \partial \mathbf{P}$  is its normal. Thus, for a given  $\Phi(\mathbf{P})$  the normal vector  $\mathbf{n}$  to the function is obtained by its gradient in the corresponding space

$$\mathbf{n} = \nabla_{\mathbf{P}} \Phi = \frac{\partial \Phi(\mathbf{P})}{\partial \mathbf{P}} \stackrel{(2.102)}{=} \frac{\partial f(\mathbf{P})}{\partial \mathbf{P}}. \quad (2.104)$$

Back to the modeling of plasticity once an update of the load yields  $\Phi > 0$  with the internal state (expressed by  $\epsilon^{\text{pl}}$ ) of the previous load state, the plastic state in the material will accommodate to a state most closely to the initial state. This assumption is convenient since a complete jump to a state without any connection to the previous one would cost infinite energy in the limit case. In the mathematical discretization during the numerical treatment the shortest path between the point outside and onside the yield surface has to be chosen, Fig. 2.11. This shortest path is naturally given through a straight line going through the point

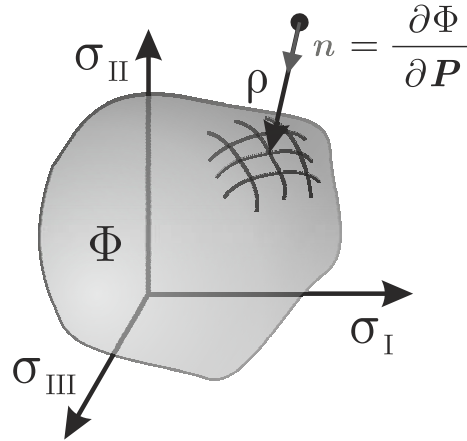


Figure 2.11: Schematic plot of a yield surface in the principle stress space. During numerical discretization the plastic strains are updated with direction  $\partial \Phi / \partial \mathbf{P}$  and norm  $\rho$  until the yield surface is reached again.

outside the surface and having a direction which coincides with the normal to the yield surface. Thus, the change of the plastic strains which is called *rate* or *evolution* is related to a given yield function through

$$\dot{\epsilon}^{\text{pl}} = \rho \frac{\partial \Phi(\mathbf{P})}{\partial \mathbf{P}}, \quad (2.105)$$

where  $\rho$  is a scalar parameter which has to be estimated such that  $\Phi(\mathbf{P}) = 0$  holds again. In Eq. (2.105) the derivative is equivalent to the normal in direction to the yield surface as pointed out previously. Therefore, the *direction* in which the plastic strains may evolve is completely determined by this normal for which the quantity  $\rho$  must not have any influence on the direction. This can only be fulfilled if  $\rho$  is positive. Then and only then  $\rho$  measures the rate of  $\epsilon^{\text{pl}}$  *consistently* for which  $\rho$  is called *consistency parameter*. Obviously,  $\rho$  may only have a value differently from zero if plastic processes evolve in the material and it has

then to be chosen so that the indicator function  $\Phi$  is zero again. These relations can be caught by

$$\rho \geq 0, \quad \Phi \leq 0, \quad \rho \Phi = 0. \quad (2.106)$$

The relations in Eq. (2.106) are called KUHN-TUCKER conditions after the KUHN-TUCKER theorem known from the field of convex optimization. This theorem generalizes the usage of LAGRANGE parameters when inequalities occur as side constraints.

# Chapter 3

## Principles for Evolution Equations

In Secs. 2.1.10 and 2.2.2 it has been pointed out that so-called evolution equations for the additional internal variables which describe the inner state of the material are needed. As an example the modeling of plasticity has been presented. There, a yield function has been introduced in order to serve as indicator whether plastic deformation is taking place or not. The internal variable *plastic strain* has then to be updated until the yield function again turns to zero for each time step. The yield function consists of two parts: primarily, the threshold value  $r$  which has to be overcome before plastic behavior can be assumed and secondly, the function  $f(\mathbf{P})$  which has to be chosen 'appropriately'. At that point mechanical modeling has to be carried out by assuming  $f(\mathbf{P})$  in a way that the experimental observations are caught best.

In this section a different approach of modeling is presented where not the yield function directly has to be assumed but a so-called dissipation potential. This different way, which yields however same results, is based on potentials as the name indicates. The difference between these two ways, yield function on the one hand, dissipation potential on the other hand, is basically only the point of view, similar to finding equilibrium equations which can be carried out through NEWTONian principles or through potentials, see Secs. 2.1.6 and 2.1.11. To prove that both ways give identical results for the governing equations, the dissipation potential is introduced in the upcoming Sec. 3.1 using the example of plasticity without, Sec. 3.1.1, and with constraints, Sec. 3.1.2. In Sec. 3.2 this concept is put on a general basis and discussed from the thermodynamic point of view before in Sec. 3.3 a comparable but thermodynamically even more convincing approach is presented.

### 3.1 Plasticity and Dissipation Potential

#### 3.1.1 Simplest Approach for Plasticity

As presented in Sec. 2.2.2, the yield function  $\Phi$  depends on some variable  $\mathbf{P}$ . Through Eq. (2.105),

$$\dot{\epsilon}^{\text{pl}} = \rho \frac{\partial \Phi(\mathbf{P})}{\partial \mathbf{P}}, \quad (3.1)$$

a relation between the yield function and the plastic strain rate  $\dot{\epsilon}^{\text{pl}}$  is given. From various other examples it is known that the use of a mathematical potential may provide different positive aspects. One example for this tool has already been presented in Sec. 2.1.11. Analogously, a potential  $\mathcal{L}$  is now introduced in a way that its minimization condition  $\partial \mathcal{L} / \partial \dot{\epsilon}^{\text{pl}} = 0$  yields exactly the evolution equation presented in Eq. (3.1). One can easily imagine that the plastic strain rate and the variable  $\mathbf{P}$  are not independent from each



other. Thus, a re-formulation of the yield function  $\Phi(\mathbf{P})$  is necessary.

Differently to the application of certain yield functions  $\Phi(\mathbf{P})$  a so-called *characteristic function*, denoted by  $\Sigma(\mathbf{P})$ , may be used to serve as indicator whether elastic or plastic material behavior takes place. This function is defined by

$$\Sigma(\mathbf{P}) := \begin{cases} 0 & , \Phi(\mathbf{P}) < 0 \\ \infty & , \Phi(\mathbf{P}) \geq 0 \end{cases} \quad (3.2)$$

and exhibits the 'pure' information about the material reaction. That means  $\Sigma(\mathbf{P})$  is in-

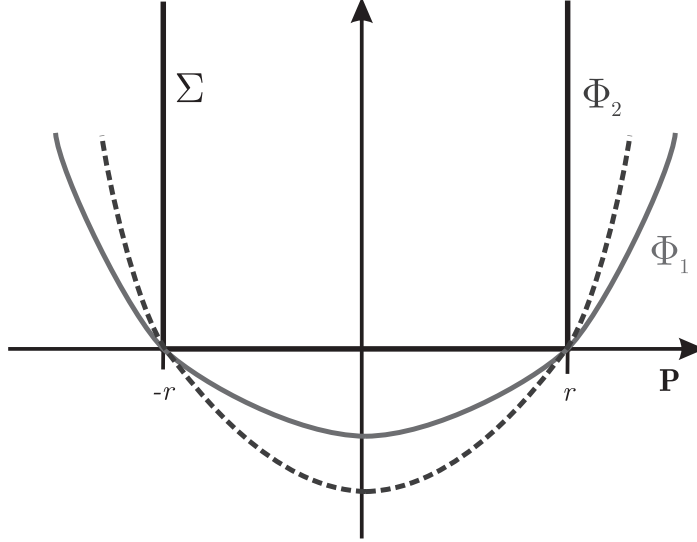


Figure 3.1: Different approaches for yield functions  $\Phi_1$ ,  $\Phi_2$ , and the characteristic function  $\Sigma$ .

dependent from the exact choice of  $\Phi(\mathbf{P})$ , see Fig. 3.1. A frequently used approach is  $f(\mathbf{P}) = |\mathbf{P}|^a$ . For instance, the exponent may be chosen to  $a = 2$  or can be chosen to any other even number. Since this exponent does not have an influence on the resulting governing equations and furthermore the values of  $\Phi(\mathbf{P})$  outside its valid region ( $\Phi(\mathbf{P}) > 0$ ) are not supposed to be taken into account,  $\Sigma(\mathbf{P})$  is taken to change the mathematical space: from a function depending on  $\mathbf{P}$  now a function depending on the plastic strain rate is searched for. In order to change the mathematical basis for description, a LEGENDRE transformation of  $\Sigma(\mathbf{P})$  is carried out by means of

$$\begin{aligned} \mathcal{J}(\dot{\epsilon}^{\text{pl}}) &= \sup_{\mathbf{P}} \{ \dot{\epsilon}^{\text{pl}} : \mathbf{P} - \Sigma(\mathbf{P}) \} \\ &\stackrel{(3.2)}{=} \sup_{\mathbf{P}} \{ \dot{\epsilon}^{\text{pl}} : \mathbf{P} \mid \Phi(\mathbf{P}) < 0 \} . \end{aligned} \quad (3.3)$$

The supremum in Eq. (3.3) has to be found under the constraint  $\Phi(\mathbf{P}) < 0$ . Similar to Eq. (2.106) this constraint can be reformulated to  $-\rho \Phi(\mathbf{P}) = 0$  where  $\rho$  is a KUHN-TUCKER parameter for the inequality in Eq. (2.102). Hence, a LAGRANGEan  $\mathcal{L}^*$  is introduced which serves as formulation for the entire optimization problem according to Eq. (3.3). This is

$$\mathcal{L}^* = \dot{\epsilon}^{\text{pl}} : \mathbf{P} - \rho \Phi(\mathbf{P}) \rightarrow \max_{\mathbf{P}} . \quad (3.4)$$

The maximization condition of Eq. (3.4) gives

$$\frac{\partial \mathcal{L}^*}{\partial \mathbf{P}} = \dot{\epsilon}^{\text{pl}} - \rho \frac{\partial \Phi(\mathbf{P})}{\partial \mathbf{P}} = \mathbf{0} \quad (3.5)$$

from which follows according to the example above

$$\dot{\epsilon}^{\text{pl}} = 2\rho \mathbf{P} . \quad (3.6)$$

Now, this result is plugged into the approach for  $\Phi(\mathbf{P})$  which gives

$$\Phi(\mathbf{P}) = |\mathbf{P}|^2 - r^2 \stackrel{(3.6)}{=} \frac{1}{(2\rho)^2} |\dot{\epsilon}^{\text{pl}}|^2 - r^2 \stackrel{!}{<} 0 . \quad (3.7)$$

Then, this yields

$$\frac{1}{2\rho} < \frac{r}{|\dot{\epsilon}^{\text{pl}}|} \rightarrow \left( \frac{1}{2\rho} \right)_{\text{max}} = \frac{r}{|\dot{\epsilon}^{\text{pl}}|} \quad (3.8)$$

from which the final formula for the LEGENDRE transformation results as

$$\mathcal{J}(\dot{\epsilon}^{\text{pl}}) = \frac{1}{2\rho} |\dot{\epsilon}^{\text{pl}}|^2 = r |\dot{\epsilon}^{\text{pl}}| . \quad (3.9)$$

Now, it is necessary to focus on the variable  $\mathbf{P}$  which has been introduced in Sec. 2.2.2 quite arbitrarily. Obviously this variable has to be related to the internal variable since the value  $\mathbf{P}$  determines whether a plastic deformation occurs or not. Therefore,  $\mathbf{P}$  can be identified as thermodynamic force acting on the thermodynamic flux  $\dot{\epsilon}^{\text{pl}}$ . Thus,

$$\mathbf{P} = - \frac{\partial \Psi}{\partial \dot{\epsilon}^{\text{pl}}} . \quad (3.10)$$

Introducing the above mentioned potential  $\mathcal{L}$  as

$$\mathcal{L} := -\mathbf{P} : \dot{\epsilon}^{\text{pl}} + r |\dot{\epsilon}^{\text{pl}}| = \dot{\Psi} + \Delta \rightarrow \text{stat}_{\dot{\epsilon}^{\text{pl}}} \quad (3.11)$$

with  $\Delta := r |\dot{\epsilon}^{\text{pl}}|$  which is called *dissipation functional*, the minimization condition of Eq. (3.11) exactly yields the evolution equation as in Eq. (3.1). Since the minimization of Eq. (3.11) is carried out with respect to the internal variable's rate, it is valid to use the rate of the free energy  $\dot{\Psi}$ . The entire LAGRANGEan  $\mathcal{L}$  is termed as *dissipation potential* or sometimes as *total power* of the material which is in contrast to the thermodynamical definition of power. However,  $\mathcal{L}$  is rather a mechanical / mathematical tool for finding evolution equations for internal variables in an elegant way.

The great advantage of this approach is now that the evolution equation can be derived from a potential which has several benefits: due to its minimization character it can be evaluated without any order like it would be the case for a saddle point problem (first minimization, then maximization or the other way round) - this point will be discussed more detailed later. Another positive outcome is that constraints can be taken into account much more easily as it is going to be presented.

Therefore, it has been shown that minimization of the dissipation potential is equivalent to the introduction of a yield function in plasticity. The two approaches differ in the way a modeling of a material can be carried out: The yield function requires an appropriate assumption for yielding which can be quite difficult for some materials (if there are constraints) as it can be seen in Sec. 4.2.2. On the other hand, the dissipation potential demands an ansatz for the entropy production,  $\Delta$ , which is in many cases easier to formulate. As usual, coming from a potential, roughly speaking from an energetic point of view, any possible coupling between variables is much more intuitive since it is a straight side effect of the model's derivation. For the entropy production, such coupling has not to be considered which makes this strategy much more favorable than the 'direct' way of formulating a yield function. A general framework for material modeling based on the so-called principle of the minimum of the

dissipation potential is given in Sec. 3.2.

If the way is taken from the opposite side, thus by minimizing  $\dot{\Psi} + \Delta$  with respect to  $\dot{\epsilon}^{\text{pl}}$

$$\min_{\dot{\epsilon}^{\text{pl}}} \left\{ \dot{\Psi} + \Delta \right\} = \min_{\dot{\epsilon}^{\text{pl}}} \left\{ \frac{\partial \Psi}{\partial \epsilon^{\text{pl}}} : \dot{\epsilon}^{\text{pl}} + r |\dot{\epsilon}^{\text{pl}}| \right\} , \quad (3.12)$$

the result is

$$\frac{\partial \Psi}{\partial \epsilon^{\text{pl}}} + \partial \Delta \ni \mathbf{0} . \quad (3.13)$$

In Eq. (3.13) the derivative of  $\Delta = r |\dot{\epsilon}^{\text{pl}}|$  is not uniquely defined for  $\dot{\epsilon}^{\text{pl}} = \mathbf{0}$ . Therefore in the differential inclusion the sub-differential for  $\Delta$  has to be found according to

$$\partial \Delta = \begin{cases} r \frac{\dot{\epsilon}^{\text{pl}}}{|\dot{\epsilon}^{\text{pl}}|} & , \dot{\epsilon}^{\text{pl}} \neq \mathbf{0} \\ \dot{\epsilon} \mid |\dot{\epsilon}| \leq r & , \dot{\epsilon}^{\text{pl}} = \mathbf{0} \end{cases} . \quad (3.14)$$

With the usage  $\partial \Psi / \partial \dot{\epsilon}^{\text{pl}} = -\mathbf{P}$  Eq. (3.13) can be reformulated to

$$\dot{\epsilon}^{\text{pl}} = \begin{cases} \underbrace{\frac{|\dot{\epsilon}^{\text{pl}}|}{r}}_{=\rho} \mathbf{P} & , \dot{\epsilon}^{\text{pl}} \neq \mathbf{0} \\ \dot{\epsilon} \mid |\dot{\epsilon}| \leq r & , \dot{\epsilon}^{\text{pl}} = \mathbf{0} \end{cases} . \quad (3.15)$$

Regarding Eq. (3.1) in combination with Eq. (3.7)

$$\dot{\epsilon}^{\text{pl}} = \rho \frac{\partial \Phi(\mathbf{P})}{\partial \mathbf{P}} = 2\rho \mathbf{P} , \quad (3.16)$$

it turns out that the evolution equations for the plastic strains, obtained on the one hand by the minimum of the dissipation potential, Eq. (3.15), and on the other hand through the normal of the yield function, Eq. (3.16), 'differ' by a factor of 2. This artifact comes from the choice of the yield function and is of no influence on the evolution equation's function: in both cases, the driving forces  $\mathbf{P}$  determine the direction in which the plastic strains are supposed to evolve. The pre-factor  $\rho$  and  $2\rho$ , respectively, have to be determined in both ways so that the yield function gives zero again. Hence, choosing the way of the minimum of the dissipation potential, valid evolution equations result – for an easier execution it is convenient to find the corresponding yield function via an associated LEGENDRE transformation in order to have an exit criteria at hand when the update of the plastic strains has completed,  $\Phi(\mathbf{P}) \leq 0$ .

Similar derivations can be found in [18] and [31].

### 3.1.2 Plasticity with Constraints

In the previous Sec. 3.1.1, very basic plasticity has been introduced, indeed a model for plasticity which probably is not used at all. This comes from the fact that this model does not account for any constraints, particularly the constraint that plasticity is a volume preserving process. Normally, this fact is taken into play through defining the yield function not in terms of stress (stress is indeed the thermodynamical driving force for plastic strains according to the constitutive relation Eq. (2.70),  $\mathbf{P} = -\partial \Psi / \partial \epsilon^{\text{pl}} = \boldsymbol{\sigma}$ ), but in terms of the so-called stress deviator. That this method identically fulfills the constraint of volume

preservation and additionally the principle of the minimum of the dissipation potential allows to take this constraint into account very intuitively is shown in this section.

The constraint of volume preservation of the plastic strains can be brought into formulas simply by

$$\dot{\varepsilon}_{11}^{\text{pl}} + \dot{\varepsilon}_{22}^{\text{pl}} + \dot{\varepsilon}_{33}^{\text{pl}} = \dot{\varepsilon}_{ii}^{\text{pl}} = 0, \quad (3.17)$$

since only the parts of  $\dot{\varepsilon}^{\text{pl}}$  with two *same* indices contribute to a change of the element's volume. Now, the previously introduced dissipation potential

$$\mathcal{L} = \dot{\Psi} + \Delta \quad (3.18)$$

has to be extended by the constraint according to Eq. (3.17) via usage of a LAGRANGE parameter, denoted by  $\kappa$ . Thus, the LAGRANGEan of the problem reads

$$\mathcal{L} = \dot{\Psi} + \Delta + \kappa \dot{\varepsilon}_{ii}^{\text{pl}} = \frac{\partial \Psi}{\partial \varepsilon^{\text{pl}}} : \dot{\varepsilon}^{\text{pl}} + \Delta + \kappa \dot{\varepsilon}_{ii}^{\text{pl}} \rightarrow \min_{\dot{\varepsilon}^{\text{pl}}}. \quad (3.19)$$

Since a quasi-static behavior is expected – in contrast to a visco-plastic one – for the dissipation the form

$$\Delta = r |\dot{\varepsilon}^{\text{pl}}| \quad (3.20)$$

is chosen. The minimizing condition of Eq. (3.19) gives for every component  $\dot{\varepsilon}_{ij}^{\text{pl}}$

$$\frac{\partial \mathcal{L}}{\partial \dot{\varepsilon}_{ij}^{\text{pl}}} = \frac{\partial \Psi}{\partial \varepsilon_{ij}^{\text{pl}}} + \partial \Delta_{ij} + \kappa \delta_{ij} \ni 0. \quad (3.21)$$

Summing this result up over all three components with pairs of same indices the sub-differential vanishes (see constraint) and it remains

$$\begin{aligned} \frac{\partial \Psi}{\partial \varepsilon_{kk}^{\text{pl}}} + 3\kappa &= 0 \\ \Leftrightarrow \quad \kappa &= -\frac{1}{3} \frac{\partial \Psi}{\partial \varepsilon_{kk}^{\text{pl}}} = \frac{1}{3} P_{kk}. \end{aligned} \quad (3.22)$$

With the use of the sub-differential already applied in Sec. 3.1.1 and the expression for the LAGRANGE parameter  $\kappa$ , Eq. (3.21) can be evaluated as

$$\dot{\varepsilon}_{ij}^{\text{pl}} = \begin{cases} \underbrace{\frac{|\dot{\varepsilon}^{\text{pl}}|}{r}}_{=\rho} \left( P_{ij} - \delta_{ij} \frac{1}{3} P_{kk} \right) & , \dot{\varepsilon}^{\text{pl}} \neq 0 \\ \dot{\varepsilon}^{\text{pl}} \mid |\dot{\varepsilon}^{\text{pl}}| \leq r & , \dot{\varepsilon}^{\text{pl}} = 0 \end{cases}. \quad (3.23)$$

The first line of Eq. (3.23) can be reformulated using the property  $\mathbf{P} = -\partial \Psi / \partial \varepsilon^{\text{pl}} = \boldsymbol{\sigma}$  to

$$\dot{\varepsilon}_{ij}^{\text{pl}} = \rho \left( \sigma_{ij} - \delta_{ij} \frac{1}{3} \sigma_{kk} \right). \quad (3.24)$$

This expression is well known: the second part in Eq. (3.24) (in matrix notation)  $\frac{1}{3} \text{tr } \boldsymbol{\sigma} \mathbf{I}$  is termed *deviatoric* part of the stresses which forces a material element to change its volume. In plasticity, the most commonly used yield function is

$$\Phi = |\text{dev } \boldsymbol{\sigma}|^2 - r^2 \quad (3.25)$$

with the *deviator*

$$\text{dev} \boldsymbol{\sigma} := \boldsymbol{\sigma} - \frac{1}{3} \mathbf{I} \text{tr} \boldsymbol{\sigma} \quad (\mathbf{I} : \text{identity matrix}). \quad (3.26)$$

Exactly this yield function results from a LEGENDRE transformation of Eq. (3.19). The only 'difference' between both ways lies, again, in a factor of 2 in the evolution equations,

$$\dot{\epsilon}^{\text{pl}} = 2\rho \text{dev} \boldsymbol{\sigma}, \quad (3.27)$$

which, as pointed out, has no influence at all. Concluding, the principle of the minimum of the dissipation potential has the great advantage that constraints, like in this case the volume preservation due to normal plastic strains, can be included in a very elegant way.

## 3.2 Principle of the Minimum of the Dissipation Potential

As it was exemplarily shown in Sec. 3.1, the formulation of a so-called dissipation potential and its minimization yield same results for the governing equations for material modeling. This is quite clear since in the previous example the characteristic function of plasticity and the dissipation functional could be interchanged through a LEGENDRE transformation which is a bijective mapping. However, to lay down a more general basis for material modeling using this principle, the general framework is discussed in this section.

The starting point for each modeling based on the minimum of the dissipation principle is the so-called LAGRANGEan, denoted by  $\mathcal{L}$ . It consists of two parts, first the time derivative of the free HELMHOLTZ energy  $\dot{\Psi}$  and second the dissipation or entropy production  $\Delta$ . The unit of this LAGRANGEan is obviously the same as a mechanical power. However, it is *not equivalent* to the power. In contrast, from the thermodynamical point of view two problems occur: first, the time derivative of the free energy is already defined to be the mechanical power. Thus, the summation of  $\dot{\Psi}$  and  $\Delta$  can not be the power of the system. Second, and this is maybe of even greater importance, according to the second law of thermodynamics the dissipation  $\mathcal{D}$  is already included in the power  $\dot{\Psi}$ , or vice versa. Concluding, an interpretation of the principle of the minimum of the dissipation potential is not very straight forward from a thermodynamical point of view. However, as illustrated via the example of plasticity, this principle can be interpreted *generally* as the LEGENDRE transformation of an associated characteristic function. Therefore, this principle has an equivalent justification as the principle of yield functions for hyper-elastically or plastically behaving materials. It is rather a tool to formulate material models in continuum mechanics. And this tool provides everything required to find a closed model: the evolution equations for internal variables and yield functions indicating whether elastic or hyper-elastic processes evolve. As already mentioned, the usage of this tool allows to include constraints very easily.

The general framework of the principle of the minimum of the dissipation potential is then as follows:

1. introduction of the problem's LAGRANGEan  $\Leftrightarrow$  stating approaches for  $\Psi$  and  $\Delta$
2. adding constraints
3. evaluation of the minimum condition
4. search for the constraints and the evolution equations

## 5. introduction of the associated LEGENDRE transformation to find the yield function

The LAGRANGEan of the problem always consists of the free energy's rate and the dissipation. Obviously, both the free energy as well as the dissipation are material and problem dependent. Thus, 'modeling' has directly to perform when expressions for energy and dissipation have to be found. An important question is then which of the variables the energy depends on are dissipative and have therefore to be regarded in the formulation for the dissipation functional.

$$\mathcal{L} := \dot{\Psi}(\boldsymbol{\varepsilon}, \boldsymbol{\lambda}) + \Delta(\dot{\boldsymbol{\lambda}}) + \text{cons} \rightarrow \min_{\dot{\boldsymbol{\lambda}}} \quad (3.28)$$

In a general context, the problem specific and dissipative variables are denoted by  $\boldsymbol{\lambda}$ . Then, the LAGRANGEan would look like in Eq. (3.28), cons indicates constraints which are added via LAGRANGE or KUHN-TUCKER parameters, depending on whether the constraints are equations or inequations. The explicit formulation of the energy depends, again, on the current problem. For the dissipation itself two main formulations can be chosen - depending on the expected material reaction. One possibility is the choice as done before: the norm of the internal variable's rate. For these cases it turns out that the resulting evolution equations as well as the yield functions are of the expected type for quasi-static processes, thus for processes which will accommodate from a given initial state to new boundary values in an infinitesimal small amount of time. In terms of the dissipative variable  $\boldsymbol{\lambda}$  it would be

$$\Delta(\dot{\boldsymbol{\lambda}}) := r_1 |\dot{\boldsymbol{\lambda}}| \quad (3.29)$$

Another possibility to choose the general approach for the dissipation is an additive combination of the norm of the internal variables and the norm to a specific power differently to one, for instance

$$\Delta(\dot{\boldsymbol{\lambda}}) := r_1 |\dot{\boldsymbol{\lambda}}| + r_2 |\dot{\boldsymbol{\lambda}}|^2 . \quad (3.30)$$

This time, the resulting governing equations reflect viscous processes.

The time derivative of the free energy in Eq. (3.28) is always the product of the conjugated thermodynamical forces ( $\partial\Psi/\partial\boldsymbol{\lambda} =: -\boldsymbol{P}$ ) and the associated thermodynamic fluxes ( $\dot{\boldsymbol{\lambda}}$ ) - the derivative of  $\Psi$  with respect to strains can be neglected since  $\mathcal{L}$  is minimized with respect to the rate of the internal variables. In general the internal variables  $\boldsymbol{\lambda}$  may be tensorial quantities. Thus, attention has to be payed which product is the appropriate one. For the example of  $\boldsymbol{\lambda}$  being a tensor of second order, the LAGRANGEan of Eq. (3.28) reads

$$\mathcal{L} = -\boldsymbol{P} : \dot{\boldsymbol{\lambda}} + \Delta(\dot{\boldsymbol{\lambda}}) + g \rightarrow \min_{\dot{\boldsymbol{\lambda}}} , \quad (3.31)$$

where  $g$  are all side constraints of the problem, see previous examples. For the first case of quasi-statically behaving materials the minimization conditions for  $\mathcal{L}$  yields evolution equations of the form

$$-\boldsymbol{P} + \partial\Delta(\dot{\boldsymbol{\lambda}}) + \boldsymbol{g}' \ni \mathbf{0} \quad (3.32)$$

with  $\partial\Delta$  as subdifferential and  $\boldsymbol{g}'$  as appropriate derivative of  $g$  with respect to  $\dot{\boldsymbol{\lambda}}$ . This equation can be reformulated to

$$\dot{\boldsymbol{\lambda}} = \rho(\boldsymbol{P} + \boldsymbol{g}') \quad (3.33)$$

with  $\rho = |\dot{\boldsymbol{\lambda}}|/r_1$  for  $\dot{\boldsymbol{\lambda}} \neq \mathbf{0}$ . The corresponding yield functions are like

$$\Phi = (\boldsymbol{P} + \boldsymbol{g}')^2 - r_1^2 \stackrel{!}{\leq} 0 . \quad (3.34)$$

Then, the internal variable may be updated from the previous time step  $(\cdot)^n$  to the current one  $(\cdot)^{n+1}$  according to

$$\begin{aligned} \dot{\lambda} &= \frac{\lambda^{n+1} - \lambda^n}{\Delta t} = \frac{|\lambda^{n+1} - \lambda^n|}{r_1 \Delta t} (\mathbf{P} + \mathbf{g}') \\ \Leftrightarrow \quad \lambda^{n+1} &= \lambda^n + \underbrace{\frac{|\lambda^{n+1} - \lambda^n|}{r_1}}_{=: \tilde{\rho}} (\mathbf{P} + \mathbf{g}') \end{aligned} \quad (3.35)$$

where the parameter  $\tilde{\rho} = \rho \Delta t$  ( $\Delta t$  is an arbitrary (positive) time increment) has to be estimated such that  $\Phi \leq 0$  from Eq. (3.34) holds again. This is synthesized in the KUHN-TUCKER conditions

$$\rho \geq 0, \quad \Phi \leq 0, \quad \rho \Phi = 0. \quad (3.36)$$

Choosing the driving forces from the current time step which is  $\mathbf{P}^{n+1}$  or from the previous one,  $\mathbf{P}^n$ , determines whether an EULER backward ( $n+1$ ) or forward ( $n$ ) scheme is used to solve the evolution equation numerically.

For the second case where the dissipation consists of two parts, Eq. (3.30), the minimization condition for  $\mathcal{L}$  is

$$\frac{\partial \mathcal{L}}{\partial \dot{\lambda}} = -\mathbf{P} + r_1 \frac{\dot{\lambda}}{|\dot{\lambda}|} + 2r_2 \dot{\lambda} + \mathbf{g}' \stackrel{!}{=} \mathbf{0}. \quad (3.37)$$

From Eq. (3.37) the evolution equation for  $\lambda$  can be calculated to

$$\dot{\lambda} = \frac{1}{2r_2} \left( \mathbf{P} - r_1 \operatorname{sign} \dot{\lambda} + \mathbf{g}' \right). \quad (3.38)$$

The signs of the flux  $\dot{\lambda}$  and the force  $\mathbf{P}$  have to be identical according to the second law of thermodynamics, Eq. (2.74). Thus, it is possible to write

$$\dot{\lambda} = \frac{1}{2r_2} (\operatorname{abs} \mathbf{P} - r_1 \mathbf{1} + \mathbf{g}') \quad (3.39)$$

with

$$\operatorname{abs} \mathbf{P} := \begin{pmatrix} |P_{11}| & \cdots & |P_{1l}| \\ \vdots & \ddots & \vdots \\ |P_{k1}| & \cdots & |P_{kl}| \end{pmatrix}. \quad (3.40)$$

In this case a yield function is not introduced: a viscous process will always evolve *immediately* for which an indicator function like a yield function is not needed as in the previous case (however, sometimes a yield function is defined anyways, [51]). Then, the process has to be discretized directly in time by assuming a specific value for the time increment  $\Delta t$  which allows to update the internal variables with

$$\lambda^{n+1} = \lambda^n + \Delta t \dot{\lambda}. \quad (3.41)$$

Although this principle of the minimum of the dissipation potential can be used as tool for mechanical modeling of classes of materials, in the upcoming section the principle of maximum dissipation will be discussed which allows material modeling in a more consistent way from the thermodynamical point of view and additionally the derivation of heat conduction equations.

Subsequently, a short excursion is presented from which method the principle of minimum of the dissipation potential was derived. So, the great advantage of  $\mathcal{L}$  being just a pure minimization problem is pointed out in detail.

The principle of the minimum of the dissipation potential is a continuation of a different approach, presented in [38] or [39] for instance. The method used here is based on the minimization of the total potential introduced in Sec. 2.1.11. If the description and thus the modeling of a certain material requires more variables than just the displacements, the free energy  $\Psi$  in the potential  $\Pi$  is exchanged by

$$\Psi \rightarrow \int_{t^n}^{t^{n+1}} (\dot{\Psi} + \Delta) dt. \quad (3.42)$$

Here,  $t^{n+1}$  is, again, the current time step and  $t^n$  the previous one. Through this exchange the path dependence of the material's reaction can be taken into account:  $\Psi$  is a function of strains and internal variables whose change contributes to the potential via the introduction of  $\Delta = \Delta(\dot{\lambda})$ . Of course, the displacements may depend on time as well. Hence, the potential reads

$$\begin{aligned} \Pi &= \int_{\Omega} \int_{t^n}^{t^{n+1}} (\dot{\Psi} + \Delta) dt dV - \int_{\Omega} \int_{t^n}^{t^{n+1}} \mathbf{f} \cdot \dot{\mathbf{u}} dt dV - \int_{\partial\Omega} \int_{t^n}^{t^{n+1}} \mathbf{t}^* \cdot \dot{\mathbf{u}} dt dA \\ &= \int_{\Omega} \int_{t^n}^{t^{n+1}} (\dot{\Psi} + \Delta) dt dV - L(\mathbf{u}, t). \end{aligned} \quad (3.43)$$

In Eq. (3.43) the parts depending linearly on  $\mathbf{u}$  are collected in  $L(\mathbf{u}, t)$ . Naturally, by introduction of  $t^{n+1}$  and  $t^n$  as specific points in time, a discretization in time is executed implicitly which stands in contrast to the principle of the minimum of the dissipation potential. The integration over time gives (for small time increments  $\Delta t = t^{n+1} - t^n$ )

$$\begin{aligned} \Pi &= \int_{\Omega} (\Psi(\boldsymbol{\varepsilon}^{n+1}, \boldsymbol{\lambda}^{n+1}) - \Psi(\boldsymbol{\varepsilon}^n, \boldsymbol{\lambda}^n) + \Delta(\boldsymbol{\lambda}^{n+1} - \boldsymbol{\lambda}^n)) dV \\ &\quad - \int_{\Omega} \mathbf{f} \cdot (\mathbf{u}^{n+1} - \mathbf{u}^n) dV - \int_{\partial\Omega} \mathbf{t}^* \cdot (\mathbf{u}^{n+1} - \mathbf{u}^n) dA \\ &\rightarrow \inf_{\mathbf{u}^{n+1}, \boldsymbol{\lambda}^{n+1}} \end{aligned} \quad (3.44)$$

Seeking for the infimum of  $\Pi$  with respect to the current displacements and the current variables yields the entire set of variables necessary to describe the material, quite similar to the case without internal variables Eq. (2.97). For the infimum, the parts in Eq. (3.44) which depend only on the previous time step are of no interest. Thus,

$$\{\mathbf{u}^{n+1}, \boldsymbol{\lambda}^{n+1}\} = \arg \inf \left\{ \int_{\Omega} (\Psi(\boldsymbol{\varepsilon}^{n+1}, \boldsymbol{\lambda}^{n+1}) + \Delta(\boldsymbol{\lambda}^{n+1} - \boldsymbol{\lambda}^n)) dV - L(\mathbf{u}^{n+1}, t^{n+1}) \right\}. \quad (3.45)$$

Obviously,  $L(\mathbf{u}, t)$  does not depend on the internal variables for which a minimization of the first part in Eq. (3.45) can be carried out *first* with respect to the current internal variables. Inserting the result into the minimization problem *subsequently* gives then the current displacement field. This way allows to define the so-called *condensed energy*

$$\Psi^{\text{con}}(\boldsymbol{\varepsilon}^{n+1}, \boldsymbol{\lambda}^n) := \inf_{\boldsymbol{\lambda}^{n+1}} \{ \Psi(\boldsymbol{\varepsilon}^{n+1}, \boldsymbol{\lambda}^{n+1}) + \Delta(\boldsymbol{\lambda}^{n+1} - \boldsymbol{\lambda}^n) \}. \quad (3.46)$$

from which the current internal variables can be found as

$$\boldsymbol{\lambda}^{n+1} = \arg \inf \{ \Psi^{\text{con}}(\boldsymbol{\varepsilon}^{n+1}, \boldsymbol{\lambda}^n) \}. \quad (3.47)$$



Analogously, the *condensed potential* is

$$\Pi^{\text{con}}(\mathbf{u}^{n+1}, \boldsymbol{\lambda}^n) := \int_{\Omega} \Psi^{\text{con}}(\boldsymbol{\varepsilon}^{n+1}, \boldsymbol{\lambda}^n) \, dV - L(\mathbf{u}^{n+1}, t^{n+1}) \quad (3.48)$$

and the current displacements  $\mathbf{u}^{n+1}$  are found from

$$\mathbf{u}^{n+1} = \arg \inf \{ \Pi^{\text{con}}(\mathbf{u}^{n+1}, \boldsymbol{\lambda}^n) \mid \mathbf{u} = \mathbf{u}^*(t^{n+1}) \text{ on } \Gamma_u \} . \quad (3.49)$$

From Eq (3.47) the current internal variables can be calculated as

$$\underbrace{\frac{\partial \Psi(\boldsymbol{\varepsilon}^{n+1}, \boldsymbol{\lambda}^{n+1})}{\partial \boldsymbol{\lambda}^{n+1}}}_{= -\mathbf{P}^{n+1}} + \frac{\partial \Delta(\boldsymbol{\lambda}^{n+1} - \boldsymbol{\lambda}^n)}{\partial \boldsymbol{\lambda}^{n+1}} \ni \mathbf{0} \quad (3.50)$$

For the case  $\Delta(\dot{\boldsymbol{\lambda}}) = r|\dot{\boldsymbol{\lambda}}|$ , Eq. (3.50) reads

$$\begin{aligned} \mathbf{P}^{n+1} &\in r \operatorname{sign}(\boldsymbol{\lambda}^{n+1} - \boldsymbol{\lambda}^n) \\ \Rightarrow \quad |\mathbf{P}^{n+1}| &:= \mathbf{P}^{n+1} : \mathbf{P}^{n+1} \leq r \end{aligned} \quad (3.51)$$

Eq. (3.51) can be evaluated as

$$\begin{cases} |\mathbf{P}^{n+1}| < r & \rightarrow \quad \boldsymbol{\lambda}^{n+1} = \boldsymbol{\lambda}^n \\ |\mathbf{P}^{n+1}| = r & \rightarrow \quad \boldsymbol{\lambda}^{n+1} - \boldsymbol{\lambda}^n = \hat{\rho} \mathbf{P}^{n+1} \end{cases} \quad (3.52)$$

which is equivalent to Eq. (3.35), thus a discretized version of Eq. (3.33). In combination with the fact that the maximum value for the norm of  $\mathbf{P}^{n+1}$  can only be  $r$ , Eq. (3.51) serves as a kind of yield function ( $\mathbf{P}^{n+1} = \mathbf{P}^{n+1}(\boldsymbol{\lambda}^{n+1})$ ). Here, constraints have not been considered yet. Of course, this result has to be plugged back into the condensed energy and minimized with respect to the displacements afterwards. Due to the dependence of Eq. (3.51) on the current displacements and due to the closed formulation over the entire body, the missing (global) minimization of  $\Pi^{\text{con}}$  in order to finally arrive at  $\mathbf{u}^{n+1}$  and  $\boldsymbol{\lambda}^{n+1}$  is a challenging task.

In contrast to this approach, the principle of the minimum of the dissipation potential gives evolution equations as well as yield functions for which a global minimization over the internal variables is not necessary any more since the evolution equations can be evaluated *locally* on the material point level. The costs for the resulting significantly reduced numerical effort is that an assumption for the occurring microstructure has to be made. This assumption influences the shape of the energy  $\Psi$ , see Sec. 4.2.1.

### 3.3 Principle of Maximum Dissipation

As it was shown in the previous Secs. 3.1 and 3.2 the so-called principle of the minimum of the dissipation potential was mainly a LEGENDRE transformation of a characteristic function. Due to its bijectivity it is only a 'personal choice' which way is taken. Though, from a thermodynamical point of view the term 'dissipation' is not unique since dissipation in thermodynamics is already well defined as

$$\mathcal{D} = -\frac{\partial \Psi}{\partial \boldsymbol{\lambda}} : \dot{\boldsymbol{\lambda}} = \mathbf{P} : \dot{\boldsymbol{\lambda}}, \quad (3.53)$$

Eq. (2.67) in the isothermal case. Then, it becomes obvious that the previously presented principle of the minimum of the dissipation potential is not very straightforward from the

thermodynamical point of view. Therefore, a different scheme is presented here, named *principle of maximum dissipation*. This principle is based on works and ideas of ONSAGER which can be found for example in [43]. In contrast to the principle of the minimum of the dissipation potential, the principle of maximum dissipation is derived directly from thermodynamics. In order to do so, the observation is used that systems always tend from one state to another by losing the maximum amount of energy. This can be performed by consideration of the thermodynamical identity, Eq. (2.67)

$$\mathcal{D} = \frac{1}{\theta} \left( \boldsymbol{\sigma} : \dot{\boldsymbol{\varepsilon}} - \dot{\Psi} - s \dot{\theta} \right) + \mathbf{q} \cdot \nabla \frac{1}{\theta} . \quad (3.54)$$

This identity was derived from the most general first and second laws of thermodynamics which are valid for every material without any restrictions. Now, the key idea of a maximum of the dissipation  $\mathcal{D}$  is followed by the introduction of a LAGRANGEan as

$$\mathcal{L} = \mathcal{D} + \beta \left\{ \mathcal{D} - \frac{1}{\theta} \left( \boldsymbol{\sigma} : \dot{\boldsymbol{\varepsilon}} - \dot{\Psi} - s \dot{\theta} \right) - \mathbf{q} \cdot \nabla \frac{1}{\theta} \right\} + \text{cons} \rightarrow \max . \quad (3.55)$$

Here, the LAGRANGEan consists of the dissipation which is going to be maximized under several constraints: on the one hand the identity of Eq. (3.54) which comes into play through a LAGRANGE parameter  $\beta$  and on the other hand additional problem dependent constraints  $\text{cons}$ . Beside the formulation of the material specific free energy  $\Psi$  and the dissipation  $\mathcal{D}$ , the free variables have to be determined which maximize the dissipation. Without question, some variables are always free and do always occur. These are the rate of strain,  $\dot{\boldsymbol{\varepsilon}}$ , the rate of temperature,  $\dot{\theta}$ , and the heat flux,  $\mathbf{q}$ . Additionally, the rate of the problem dependent internal variables are quantities the dissipation may have to be maximized with respect to, for example  $\dot{\boldsymbol{\lambda}}$ . Then, the maximization reads

$$\mathcal{L} \rightarrow \max_{\dot{\boldsymbol{\varepsilon}}, \dot{\theta}, \mathbf{q}, \dot{\boldsymbol{\lambda}}} . \quad (3.56)$$

Of course, there exists no 'thermodynamic rule' or even 'law' which demands the dissipation to be maximized. However, when it comes to modeling, assumptions always have to be made for instance that the amount of lost energy is always at its maximum. This is consistent with thermodynamical observations. Furthermore going this way the first and the second law of thermodynamics are fulfilled identically and no confusion between the tool dissipation potential and the thermodynamical quantity dissipation occurs. On the other hand, it has been shown in [18] that for some cases  $\Delta$  of the dissipation functional and  $\mathcal{D}$  as dissipation are identical if and only if the relation

$$\frac{\partial \mathcal{D}}{\partial v_i} \frac{\partial^2 \mathcal{D}}{\partial v_j \partial v_k} v_k \equiv \frac{\partial \mathcal{D}}{\partial v_j} \frac{\partial^2 \mathcal{D}}{\partial v_i \partial v_k} v_k \quad (3.57)$$

holds, where  $\mathbf{v}$  denotes the vector of the dissipative internal rates, [18]. This relation holds true for instance when the dissipation is chosen to be the norm of all internal rates.

The driving forces, which can be calculated either from Eq. (3.33) (principle of the minimum of the dissipation potential) or from

$$\frac{\partial \mathcal{L}}{\partial \dot{\boldsymbol{\lambda}}} = \mathbf{0} \quad (3.58)$$

(principle of maximum dissipation), are identical if and only if

$$\left( \frac{\partial \Delta}{\partial \dot{\boldsymbol{\lambda}}} : \dot{\boldsymbol{\lambda}} \right) \left( \frac{\partial^2 \Delta}{\partial \dot{\boldsymbol{\lambda}}^2} : \dot{\boldsymbol{\lambda}} \right) \equiv \left( \dot{\boldsymbol{\lambda}} : \frac{\partial^2 \Delta}{\partial \dot{\boldsymbol{\lambda}}^2} : \dot{\boldsymbol{\lambda}} \right) \frac{\partial \Delta}{\partial \dot{\boldsymbol{\lambda}}} \quad (3.59)$$

This can also be found in [18].

The advantage of the principle of maximum dissipation is now that additionally to the simplified consideration of constraints it is more straight forward from the thermodynamical point of view. Due to the identical fulfillment of both energy conservation and the second law of thermodynamics (requiring that  $\mathcal{D} : \mathbb{R}^{n \times \dots \times w} \mapsto \mathbb{R}_{\geq 0}$ ), it is possible to take temperature dependencies into account for which the maximization condition with respect to the heat flux  $\mathbf{q}$  serves.

In this work different models for shape memory alloys are derived by using the principle of maximum dissipation. This method serves in conclusion best to fulfill the goals of this work. First, the hard task of introducing 'correct' or appropriate yield functions from which the driving forces can be calculated is circumvented. Secondly, entire specimens made of shape-memory alloys are going to be simulated. In this context the approach which serves as historical basis for the minimum of the dissipation potential would cost too much computational power. Additionally, thermodynamically more convincing approaches than the minimum of the dissipation potential are supposed to be used. The principle of maximum dissipation will serve deductively as methodical basis for all material models derived in this work. Furthermore, the influence of thermo-mechanical coupling comes out immediately as well. This is of great importance since the processes evolving in shape-memory alloys are highly dependent on temperature.

# Chapter 4

## Smart Materials – Simulation of Shape Memory Alloys

From the engineering point of view the evolution of new materials is strongly connected to the industrial progress and provides a huge variety of applications. One class of new materials are *functional materials*. This group is characterized by its ability to adapt to specific load states. A sub-group of functional materials are the so-called *shape memory alloys*. These metals provide a huge variety of fascinating properties. This is why shape memory alloys can be found in many industrial applications. Although not all processes evolving in shape memory alloys are already completely understood, shape memory alloys can be found for instance in medical devices, actuators and automotive engineering even today and are expected to keep on capturing markets.

This work is intended to contribute to the understanding as well as the applicability of shape memory alloys by developing new approaches for their numerical simulations. Thus, in this section first an introduction to the physical properties of shape memory alloys is given, both on a macro- and microscopic scale. The main focus of this section is laid on the derivation of different material models for shape memory alloys based on the principle of maximum dissipation. Because of the necessity to provide an approach for the free energy, a short excursion to energy convexification introduces the section of micromechanical modeling of shape memory alloys.

### 4.1 Physical Properties of Shape Memory Alloys

#### 4.1.1 Macroscopic Behavior of Shape Memory Alloys

Shape memory alloys have been discovered in 1951, [45]. The first alloy exhibiting the fascinating properties which define shape memory alloys was Au<sub>47.5</sub>Cd. Later, in 1963 Nickel Titanium (NiTi) was reported. Until today, NiTi is the most widely used shape memory alloy. Therefore, although the models derived in this work are valid for all kind of shape memory alloys, numerical results will be given for NiTi and a GAUSS point analysis for CuAlNi, Secs. 6.3.1 and 6.3.2.

Fig. 4.1 shows a plot of a stress-strain diagram received from experimental observations, [59]. In the experiment a wire of NiTi has been clamped at both sides into a testing machine which sets the wire under tension. The prescribed displacements as well as the resulting force yield the mentioned stress-strain diagram. From Fig. 4.1 it can be seen that the material reacts in a quite unexpected way: After reaching a certain threshold the force

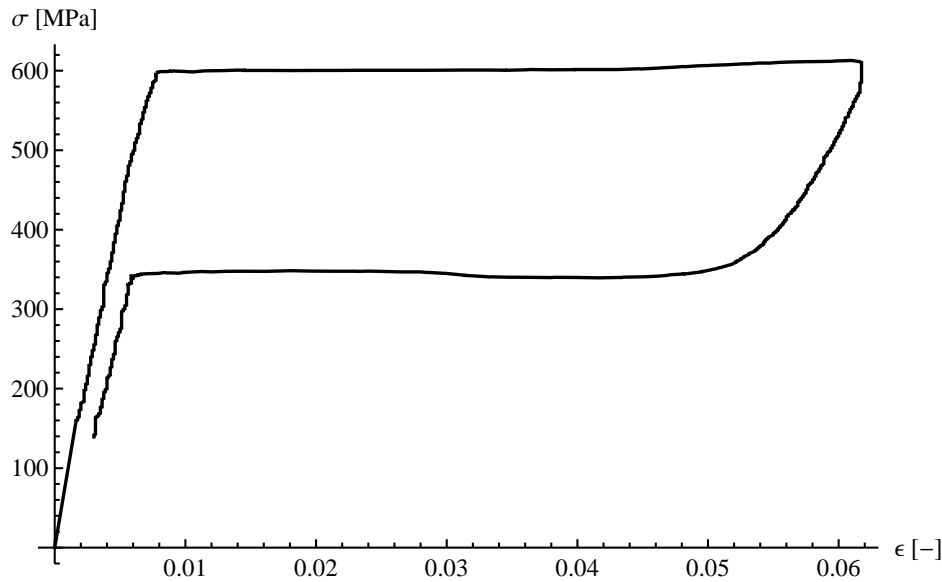


Figure 4.1: NiTi-wire under tension at 60° C, courtesy of [59].

remains constant which strongly reminds of plasticity, see Fig. 2.10. In contrast, increasing the load, in this case the displacements, the force starts to grow again linearly but with a different slope compared to the first part. During unloading, even more surprising, the force decreases first linearly but then its curve turns again into that plateau-like branch as during loading. The level of the plateau while unloading is less than during loading. After reaching the linear branch of the elastic region again, the material behaves purely elastic once more. During the entire process remarkable high strains occur. However, the material goes back into its original state. Since no permanent deformations remain but the behavior still is not purely elastic, this phenomenon is called *pseudo-elasticity*.

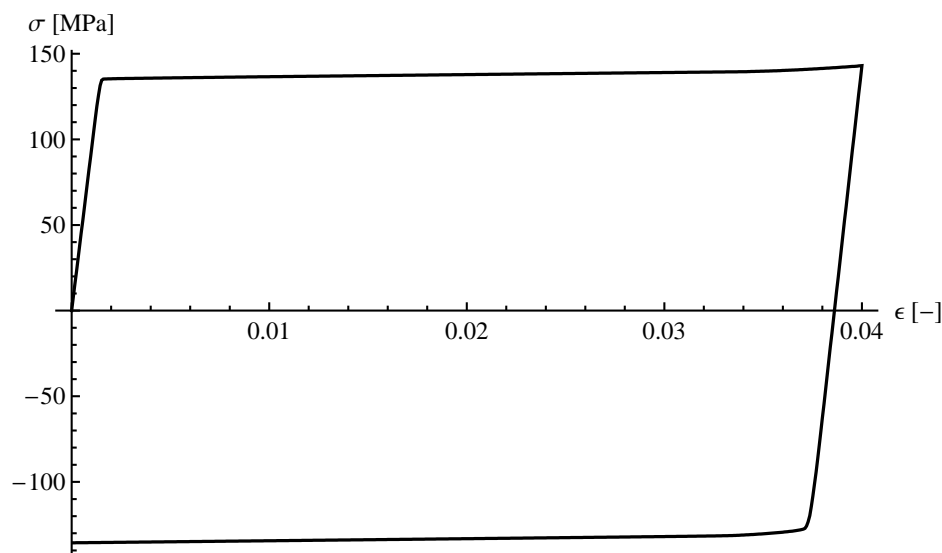


Figure 4.2: NiTi-wire under tension at -40° C, simulation.

A completely different material response is given via the next Fig. 4.2. Here, the material response is similar to the case of pseudo-elasticity in the beginning: first a linear reaction, then a plateau and finally again a linear response. However, when the prescribed deformation is being decreased the resulting force reduces linearly but without turning into

that plateau branch like in the previous case. Instead, the resulting force decreases further and further and even at zero force a remaining deformation is observed which reminds even more of plasticity as the first experiment. Interestingly, a further reduction of the load yields again a plateau but with negative resulting force. Despite the linear branch at the very beginning, the entire material reaction is point symmetric to the origin of ordinates which induces that the material does not return to its original, undeformed configuration.

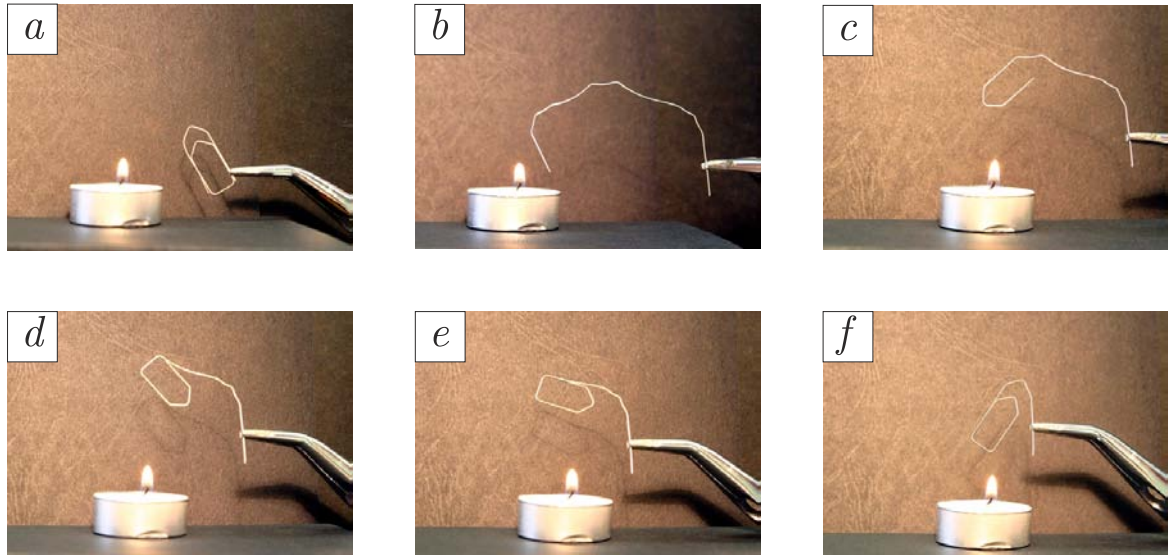


Figure 4.3: Paper clip made of NiTi in its original configuration (a), after mechanical loading and unloading with remaining deformations (b). Heating forces the material to restore its original configuration (c - f).

Fig. 4.3 shows a deformation of a wire made of exactly the same material as discussed for Fig. 4.1 but with a different chemical composition. Here, an apparently durable deformation is observed after removing the load (b). Fascinatingly, providing heat to the wire yields the material to spontaneously returning to the undeformed configuration (c - f). Due to this remarkable effect in combination with the observations in the force-displacement diagram, Fig. 4.2, the material response is called *pseudo-plastic*.

Which effect arises is a matter of the specific alloy's composition and temperature. At relatively high temperatures the material behaves pseudo-elastically, at relatively low temperatures pseudo-plasticity is observed. Hence, materials of this class can show, although not at the same point in time, both features. Therefore, pseudo-plasticity is taken to call this class of materials *shape memory alloys* which comes from the impression that these materials can remember their original shape.

In both cases a hysteresis occurs in the stress-strain diagrams. Thus, both pseudo-elasticity and pseudo-plasticity are dissipative.

#### 4.1.2 Microscopic Behavior of Shape Memory Alloys

The remarkable effects of shape memory alloys have their origin in the specific atomistic arrangement of this class of materials. Such as all alloys, shape memory alloys are composed of metallic elements which are ordered in so-called *crystallographic lattices*. That means that - at least locally - the atoms are grouped in a periodic way. So-called *lattice vectors* are introduced to describe the atomistic structure. Due to its periodicity a lattice can be represented via *elementary cells* which are the smallest pattern to describe the atomistic

arrangement. From those elementary cells the entire lattice can be reconstructed. Figure 4.4 shows the atomic arrangement in NiTi at high (left) and low (right) temperatures. The high temperature phase is characterized by a high symmetry and called *austenite* whereas the low temperature phase splits in several variants which are all termed *martensite*. The different martensitic variants can be converted into each other by means of rotation and mirroring matrices, see A.3.

What happens to a two dimensional austenitic lattice under tension is drawn in Fig. 4.5

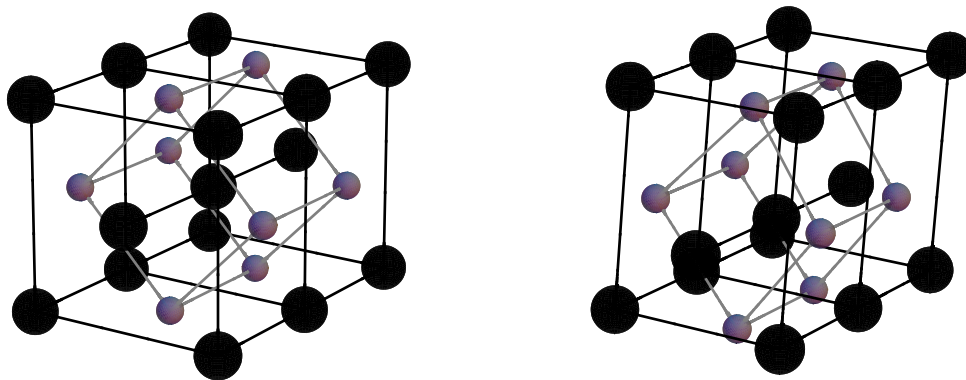
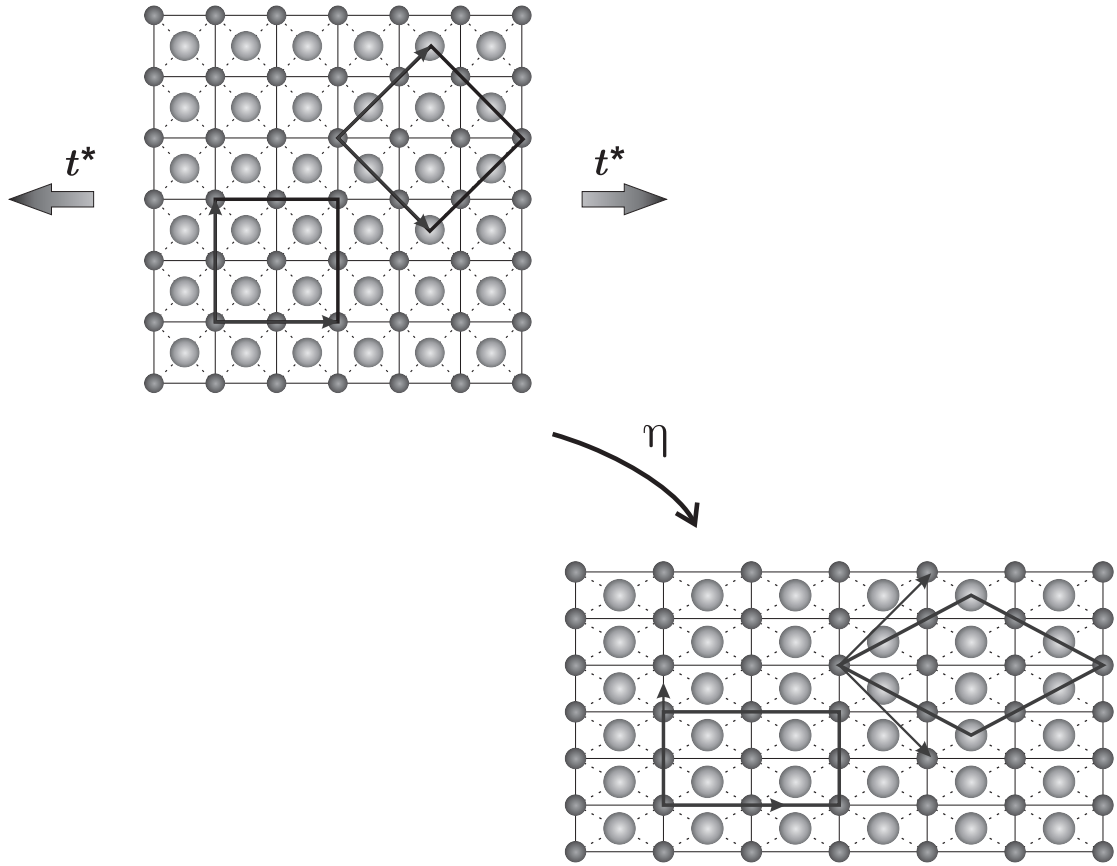


Figure 4.4: Atomic structure in NiTi. Austenite (left) and one variant of martensite (right). Black atoms are Nickel, gray atoms are Titanium.

where a view on the  $x_1$ - $x_2$ -plane is presented. Due to mass conservation the atoms do not only move in  $x_1$  direction but also in (negative)  $x_2$  direction. The elementary cell is deforming during this process from a cube to a rectangle. On the right hand side of the lattice a cube which is rotated about  $45^\circ$  serves as representative pattern for the lattice structure. This cube is changing its shape much more drastically during deformation, namely to a sheared and shuffled parallelogram. Hence, it follows that there exist different possibilities to describe the same lattice, namely the different martensitic variants.

The occurring martensite results from a diffusion-less *solid to solid phase transformation*, in this presentation the transformation comes just from a mechanical load without any chemical gradient. Of course, according to this introduction it would follow that an austenitic lattice under load entirely would transform to martensite. Indeed, that is true only for perfect single crystals which cannot be found in reality. In contrast, due to imperfections in the entire structure, e.g. dislocations or precipitates which cause a specific stress field, at some point the nucleation of martensite is preferred. Starting from nucleation zones the phase transition spreads through the specimen. During this evolution other effects due to the underlying microstructure, such as grain boundaries, may influence the further expansion of the transformation, but they do not inhibit phase transition as it is the case in most other materials. The entire process is accompanied by a relaxation of strain.

Such a transformation of the lattice can not only be evolved due to mechanical loads as presented here, but also - and even more generally - due to temperature. The high temperature phase is the austenite while martensite can be found at low temperatures with a *transformation temperature* between which a smooth transformation between austenite and martensite takes place. Then, a mapping from the phase found at high temperature to the phase found

Figure 4.5:  $x_1$ - $x_2$ -plane of a crystal lattice.

at low temperature can be derived from the experimental measurements of the atomic (average) position. Outgoing from this mapping, which is actually a deformation, a strain is derived which describes the transformation from austenite to martensite. Consistently, this strain is called *transformation strain* and denoted by  $\eta$ .

From Fig. 4.5 it is obvious that a load in  $x_2$  direction would force the material to generate martensite which is rotated about  $90^\circ$  around the  $x_3$  direction. Thus, the mapping  $\eta$  is not unique but - depending on the specific material - there exists a certain number of martensitic *variants* as already mentioned.

In material science it is more usual to identify the martensitic elementary cell according to [46] or [60] which is obviously only a rotation of the reference coordinate system.

Forming martensite from an originally austenitic state due to *mechanical loading* is the reason why shape memory alloys exhibit the property of pseudo-elasticity: the transformation from austenite to martensite is a diffusion-less and furthermore elastic process. Therefore, shape memory alloys can sustain high strains elastically.

The scheme of forming martensite from austenite was very general, thus it is valid for all metals. However, ordinary metals do not show the characteristics of shape memory alloys because of the properties of  $\eta$ . In contrast to all other alloys the transformation strain for shape memory alloys is (nearly) *volume preserving*. Thus, dislocations, grain boundaries and others do not prevent the process of mechanically induced, reversible phase transformations which is normally the case. In regular metals a transformation between austenite and martensite only occurs reversibly only due to change of temperatures, not because of mechanical loads (TRIP-steels may transform from austenite to martensite, too, but this is an *irreversible* and *inelastic* process).



The property to undergo phase transformations from martensite to austenite due to temperature as well, gives rise for the effect of pseudo-plasticity. Starting from a random crystal all possible martensitic variants occur (this is called disordered martensite). Due to external mechanical loading the different variants reorientate, see Fig. 4.6 upper part, and ordered martensite arises. If the load is removed no orientation back to the disordered martensite

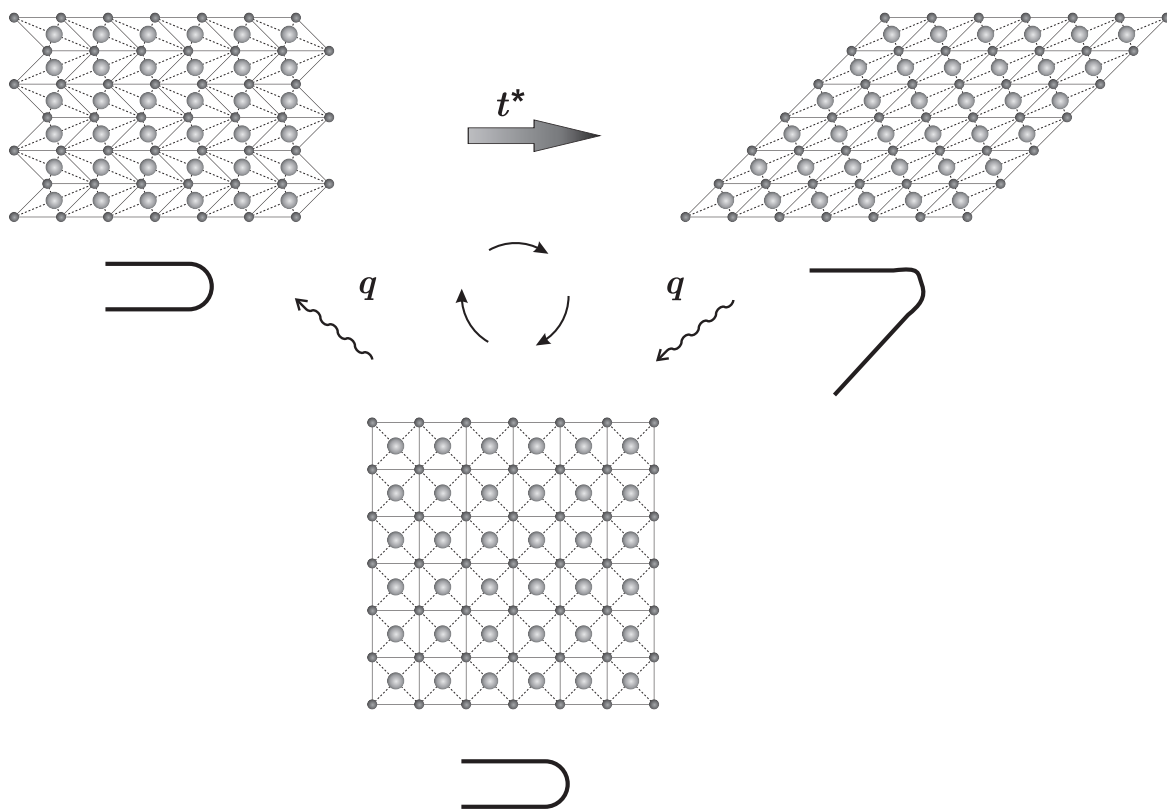


Figure 4.6: Schematic illustration of the one-way-effect which is called *pseudo-plasticity*.

occurs. This is since all martensitic variants exhibit the same chemical (thus temperature dependent part of the free) energy. Hence, the body deforms elastically until the load vanishes but some deformations maintain. Application of heat to the system allows the material to transform from ordered martensite to austenite, the high temperature phase, which is accompanied by a deformation back to the initial state (a body in the initial state as well as in the austenitic state has the same shape because of the transformation strains being volume preserving). If the body is cooled down afterwards to the original temperature there is not reason for the material to favor a specific martensitic configuration of variant. Thus, a (nearly) uniform composition of all martensitic variants evolves which is exactly the initial state of disordered martensite. Concluding, due to a martensite  $\leftrightarrow$  martensite and a subsequent martensite  $\rightarrow$  austenite transformation the effect of pseudo-plasticity is accomplished by a final austenite  $\rightarrow$  martensite transition. The entire process is illustrated in Fig. 4.6.

Naturally, in most cases the schemes presented here are too simplified. In reality the most common case is that the material comes along with combinations of single crystals. For the description of single crystals only one lattice orientation is sufficient. Compositions of single crystals are called poly-crystals where every single crystal (which is termed as grain in this context) has its own lattice coordinate system for identification. More detailed discussion about shape memory alloys both from a material scientist's and a mechanical point of view can be found for instance in [45], [34], [46] and [6].

## 4.2 Micromechanical Modeling of Shape Memory Alloys

### 4.2.1 Energy Convexification

In order to model materials it is necessary to make assumptions for both the free energy and  $\Delta$  from the minimum of the dissipation potential or the dissipation  $\mathcal{D}$  respectively, depending on the principle which is chosen. In this section a rather short introduction to convexification is given since this is necessary to find an appropriate approach for the free energy.

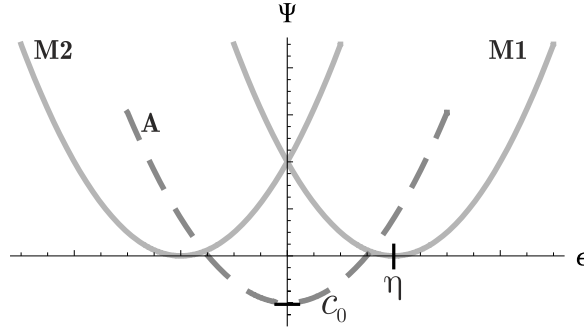


Figure 4.7: Energies for austenite **A** (dashed) and two martensitic variants **M1** and **M2**, respectively. The transformation strain  $\eta$  as well as the chemical energy for austenite  $c_0$  are indicated.

From the physical point of view, shape memory alloys are compositions of different crystallographic phases whose volume fractions may change during mechanical and / or thermal loading. For each phase an energy can be assumed according to

$$\Psi_i^j(\epsilon_i^j) = \frac{1}{2} (\epsilon_i^j - \eta_i^j) : \mathbb{C}_i^j : (\epsilon_i^j - \eta_i^j) + c_i(\theta), \quad (4.1)$$

since in the linear case an additional decomposition of the total strain into the elastic part and the transformation part is possible. Here, a distinction between the different phases  $i$  has been made. The index  $i$  runs from 0, which refers to the austenitic phase, to  $n$  which is the material dependent maximum number of different martensitic phases. Additionally, the index  $j$  runs from 1 to  $N$  and indicates  $N$  orientations of grains a poly-crystal may consist of.  $c_i(\theta)$  is the phase and temperature dependent chemical part of the energy. Each energy has a minimum if the strain in the corresponding grains and phases coincides with same experimentally determined *transformation strain* denoted by  $\eta_i^j$ . For the one dimensional cases it is possible to draw the energies which is executed in Fig. 4.7.

In the landscape of energies the example of pseudo-elasticity is discussed and presented in Fig. 4.8. Then, at zero strain only the austenite phase exists because this yields the minimum energy. Increasing the load (that means the strain) the austenitic energy is the lowest one for which this path has to be followed (dashed branch). At a certain point ( $\downarrow$ ) both energies (for austenite and martensite) yield the same value whereas for a further increased strain the path of the martensitic energy would yield minimum energy. Thus, after reaching this point ( $\downarrow$ ) spontaneously a phase transformation from the completely austenitic case to a purely martensitic case evolves, according to Fig. 4.8. So, the black branch indicates the combination of energies chosen during loading. Actually, this behavior is not observed in reality. Indeed, a smooth transition from austenite to martensite takes place in experiments. Hence, the path described in Fig. 4.8 cannot be the 'correct' one. Therefore, in Fig.

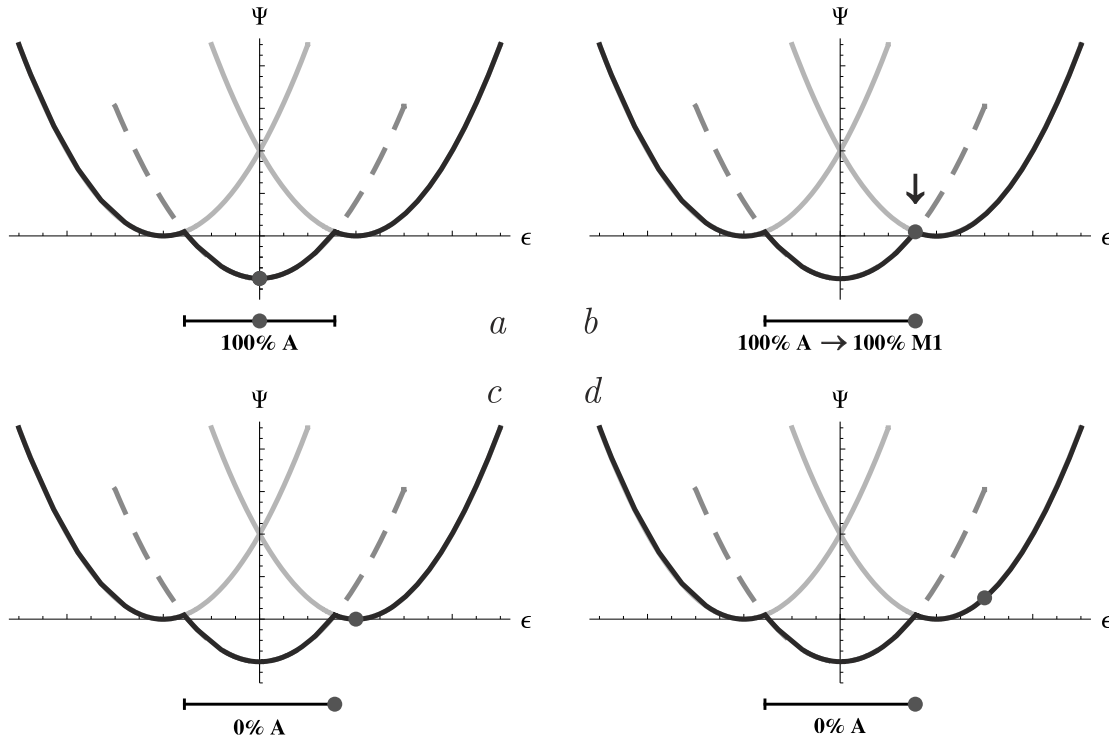


Figure 4.8: Multi-well potential. Dashed line refers to the austenite energy, gray lines refer to martensite one and two, respectively. **A**: austenite, **M1**: martensite variant 1. Reversible way:  $a \leftrightarrow b \leftrightarrow c \leftrightarrow d$ . The black line is the lowest energy path which coincides with a spontaneous and complete phase transition at point  $\downarrow$ .

4.9 a different path is drawn while neglecting dissipation. The energies for austenite and martensite remain the same. However, if now a mixture of the two pure phases is allowed an obviously different path results (black curve again): it is smooth (differentiable at every point) and consequently the transition which is described by that path is smooth as well. This phenomenon reflects the experimental observations remarkably better. Furthermore, from the mathematical point of view the black curve is a so-called *convex hull*. The individual energies are convex, the combination of both according to Fig. 4.8 is obviously not. Since for a modeling the entire energy for a material point has to be used this non-convex hull would have been taken. This hull would have been used to find a microstructure which minimizes exactly this hull. Then, there are several points where the criteria of minimum energy hull does not yield unique solutions, see Fig. 4.8. Therefore, this idea could not be applied here.

In contrast, the hull in Fig. 4.9 is indeed convex which is equivalent to a one-to-one relation between strain and energy. This makes it possible to use the convex hull for a prediction of microstructure.

The case of pseudo-plasticity is illustrated in Fig. 4.10, again without dissipation. Pseudo-plasticity is observed when room temperature is too low for the high temperature phase austenite at zero strains. Then, the energy for austenite (dashed curve, part *a*) lies above the energy for martensite. Since all martensitic variants incorporate the same chemical energy at zero load, in the beginning there exists a uniform distribution of martensite (in this case: **M1** = 50%, **M2** = 50%). By increasing the load the material undergoes a phase transformation to martensite one at the expense of martensite two. This process takes place when the material behavior is described by the horizontal part of the convex energy (black

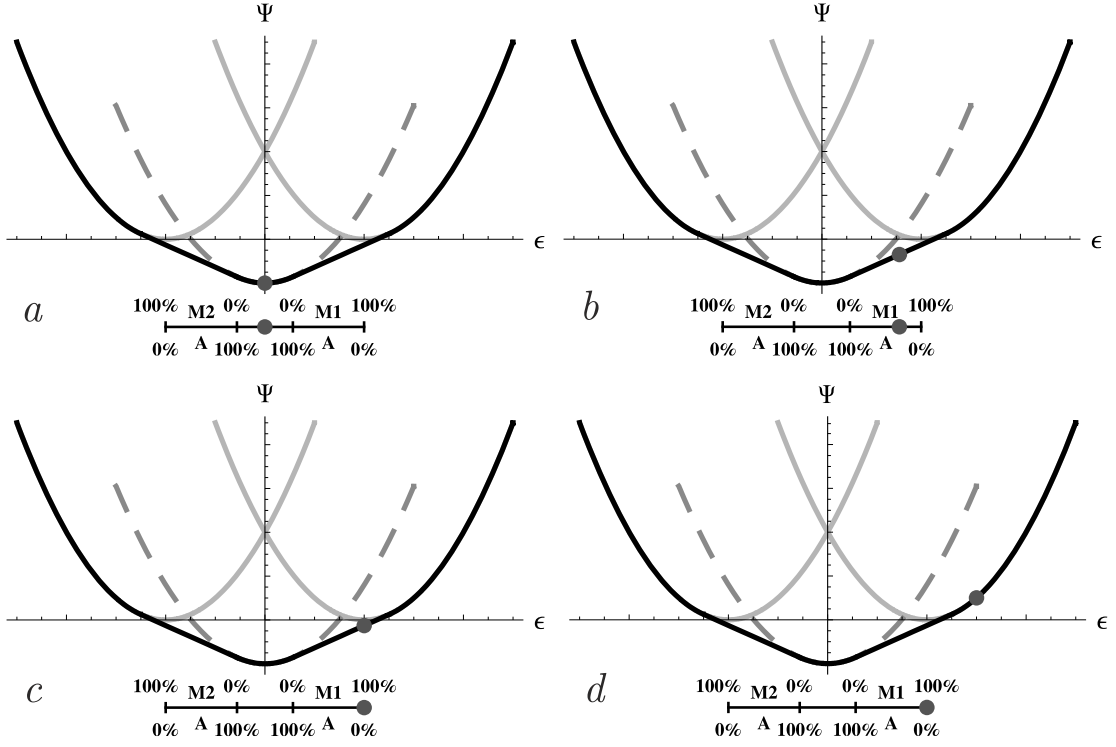


Figure 4.9: Relaxed energy for pseudo-elastic shape-memory alloys (black curve). **A**: austenite, **M1**: martensite variant 1, **M2**: martensite variant 2. Reversible way:  $a \leftrightarrow b \leftrightarrow c \leftrightarrow d$ .

branch, *a*). When this part of the energy turns into the quadratic function, phase transformation is accomplished (*b*) and the material reacts in the following (*c*). During unloading, that means removing the force, an apparently durable strain remains (*d*), equivalent to the transformation strain. If now the temperature is changed, so heat is supplied to the system, the energy of austenite becomes more and more favorable, in other words it is moved downwards (*d*). When the temperature has overcome a certain threshold value, the energy of austenite has a lower value than the energy of martensite. Hence, a transformation from the martensite one variant, **M1**, which was due to the direction of load, to the pure austenite phase takes place (*e*). During subsequent cooling, the energy of austenite moves back upwards and the martensite becomes more favorable again. Thus, the material transforms back into martensite and since there is no energetic reason, the evolving microstructure is again the uniformly distributed martensite (*f*).

In the multi-dimensional case (strain as full tensor) the convex hull cannot be drawn. Additionally, it is not possible to postulate a single definition for convexity. However, the derivation of one convex hull for the material point's free energy is recalled here due to the need of having approaches for energy and dissipation to apply the principle of maximum dissipation introduced in Sec. 3.3.

Going back to the energy  $\Psi_i^j$  in Eq. (4.1), the rotation of the tensors can be executed simply by using orthogonal matrices  $Q^j$  for each randomly chosen direction  $j$ . Then, the rotated transformation strains can be calculated according to

$$\eta_i^j = (Q^j)^T \cdot \eta_i \cdot Q^j \quad (4.2)$$

and the entries of the rotated elastic constants with

$$\mathbb{C}_{i,opqr}^j = Q_{so}^j Q_{tp}^j Q_{uq}^j Q_{vr}^j \mathbb{C}_{i,stu} \quad (4.3)$$

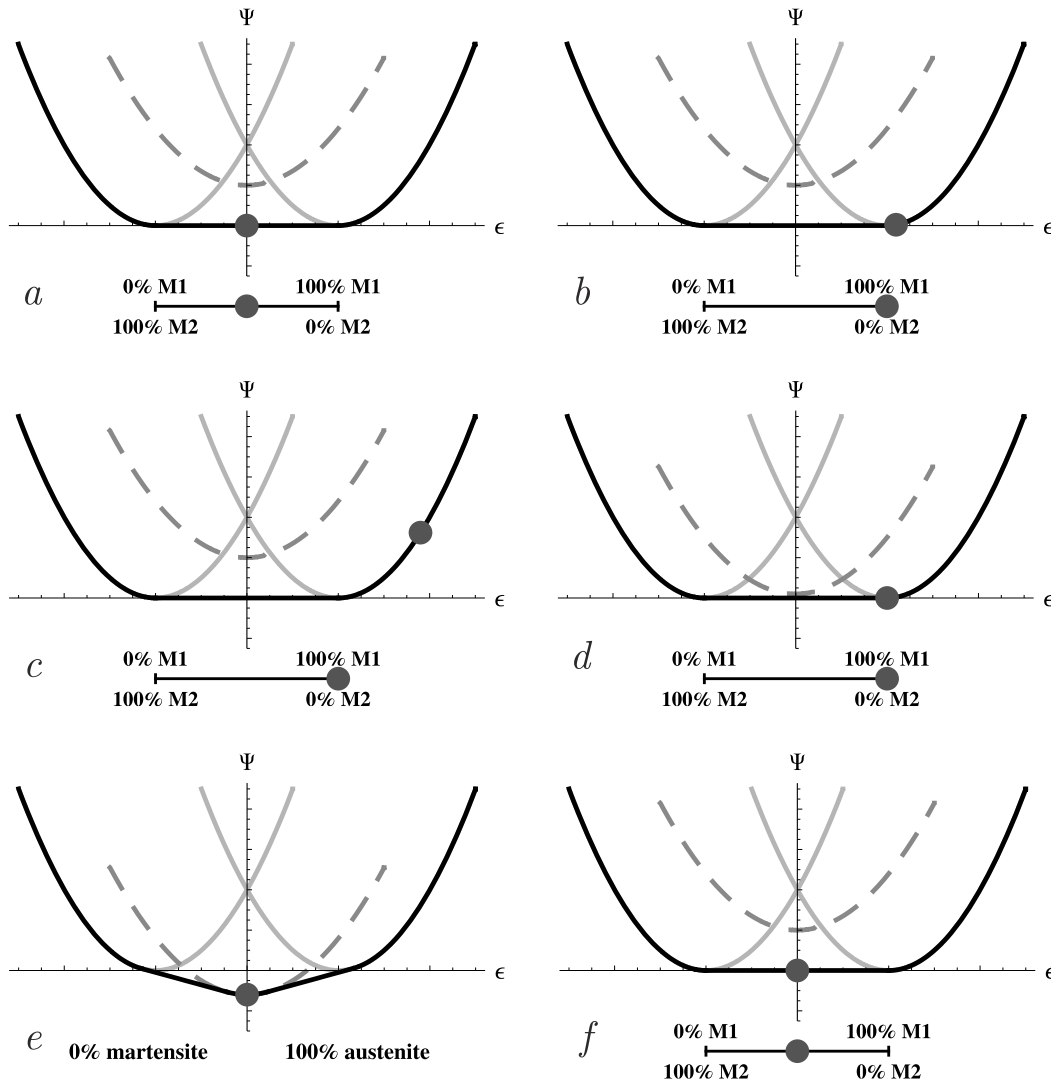


Figure 4.10: Schematic energy plot for the case of pseudo-plasticity without dissipation. **M1**: martensite variant one, **M2**: martensite variant two. Way:  $a \rightarrow b \rightarrow c \rightarrow d \rightarrow e \rightarrow f \rightarrow a$ .

As pointed out, a material point in a poly-crystal consists of a certain amount of grains in which different crystallographic phases may be found, namely austenite and / or variants of martensite. Therefore, it is convenient to introduce quantities which measure the amount of a single phase in comparison to the mass of a single grain. This quantity is defined through

$$\lambda_i^j := \frac{m_i^j}{m^j} = \frac{\int_{\Omega_i^j} \rho_d dV}{\int_{\Omega^j} \rho_d dV} = \frac{\int_{\Omega_i^j} dV}{\int_{\Omega^j} dV} \quad (4.4)$$

with the material's density  $\rho_d$  (although there are different phases the density remains the same and constant) and  $m_i^j$  and  $\Omega_i^j$  being the mass and the volume, respectively, of a phase  $i$  in a grain  $j$ . From the definition of  $\lambda_i^j$  it is straight forward to call it *volume fraction* and collect all single  $\lambda_i^j$  in a quantity  $\lambda$ . According to the definition of  $\lambda_i^j$  it is necessary to introduce a measure for the volume fraction of grains in comparison to the entire material point. This quantity is denoted by

$$\xi^j := \frac{m^j}{m} = \frac{\int_{\Omega^j} \rho_d dV}{\int_{\Omega} \rho_d dV} = \frac{\int_{\Omega^j} dV}{\int_{\Omega} dV} \quad (4.5)$$

and all single entries are synthesized in  $\xi$ . With the volume fractions and the free energies  $\Psi_i^j$  at hands, it is possible to postulate that the free energy of the entire material point is the sum of the single free energies, weighted with their respective volume fractions. Then, for fixed volume fractions the convex hull of the energy can be calculated by minimizing the weighted sum of individual energies with respect to the strains in each phase and each direction,  $\epsilon_i^j$ . Obviously, this minimization is not constraint free. At least, the result for the convex hull is supposed to yield a value for the energy when an *average value for the individual strains* is given. This average value is the strain  $\epsilon$  which is known from a more smeared scale for which the constraint can be put into the minimization problem

$$\Psi^{\text{rel}} = \inf_{\epsilon_i^j} \left\{ \sum_{j=1}^N \sum_{i=0}^n \xi^j \lambda_i^j \Psi_i^j(\epsilon_i^j) \mid \sum_{j=1}^N \sum_{i=0}^n \xi^j \lambda_i^j \epsilon_i^j = \epsilon \right\}. \quad (4.6)$$

Due to this simplest possible constraint the relaxation problem in Eq. (4.6) is called *convexification*. It is easy to imagine that the resulting energy hull gives the lower energy the less constraints have to be fulfilled. Hence, the convexification gives the minimum energy and serves as lower bound for the exact energy just like a REUSS energy. Details for that and other convexification possibilities as well as the complete derivation can be found in [19], [4] or [25]. General frameworks and other examples are found in [3], [8], [9] and [17]. Since it is beyond the scope of this work, here only the result for Eq. (4.6) is presented which is

$$\Psi^{\text{rel}} = \frac{1}{2} (\epsilon - \eta_{\text{eff}}) : \mathbb{C}_{\text{eff}} : (\epsilon - \eta_{\text{eff}}) + c_{\text{eff}}(\theta) \quad (4.7)$$

with

$$\eta_{\text{eff}} = \sum_{j=1}^N \sum_{i=0}^n \xi^j \lambda_i^j \eta_i^j, \quad \mathbb{C}_{\text{eff}} = \left[ \sum_{j=1}^N \sum_{i=0}^n \xi^j \lambda_i^j (\mathbb{C}_i^j)^{-1} \right]^{-1}, \quad c_{\text{eff}}(\theta) = \sum_{j=1}^N \sum_{i=0}^n \xi^j \lambda_i^j c_i(\theta). \quad (4.8)$$

An energy bound including lamination can be found additionally in [17] and [14].

## 4.2.2 A basic Model

Outgoing from the previously presented principle of maximum dissipation, in this section a basic model for poly-crystalline shape memory alloys is derived. The intention of the

following approach is the modeling of the main characteristics of shape memory alloys such as the dissipative (hysteresis) and anisotropic behavior in the stress-strain-diagram but neglecting any coupling between phase transitions and temperature which means

$$\theta = \text{const} \Leftrightarrow \dot{\theta} = 0 \quad (4.9)$$

and

$$\mathbf{q} = \mathbf{0} . \quad (4.10)$$

Therefore, the entropy production or dissipation  $\mathcal{D}$ , introduced in Sec. 2.1.7 is simplified to

$$\mathcal{D} \stackrel{(4.9), (4.10)}{=} \frac{1}{\theta} \left( \boldsymbol{\sigma} : \dot{\boldsymbol{\varepsilon}} - \dot{\Psi}^{\text{rel}} \right) . \quad (4.11)$$

Following the principle of maximum dissipation the entropy production is maximized with respect to its free variables which are, of course, problem dependent as the ansatz for  $\mathcal{D}$  itself. The maximization has to be executed under certain constraints. Naturally, the identity in Eq. (4.11) has to hold. Additionally the problem itself requires two constraints. First, mass conservation has to be fulfilled. The same parameters as in Sec. 4.2.1 are used to identify the specific volume fractions in grains with the same orientation. Thus, mass conservation, Eq. (2.48), has to hold for every direction of grains assumed and is expressed here by

$$\sum \dot{\lambda}_i^j = 0 \quad \forall j . \quad (4.12)$$

Furthermore, negative volume fractions do not yield any physical plausibility which yields the additional constraints

$$\lambda_i^j \geq 0 \quad \forall i, j . \quad (4.13)$$

For the constraints of mass conservation, Eq. (4.12), LAGRANGE parameters are introduced, denoted by  $\kappa^j$ , whereas for the non-negativity, Eq. (4.13) KUHN-TUCKER parameters come into play,  $\gamma_i^j$ ,

$$\gamma_i^j = \begin{cases} 0 & \text{for } \lambda_i^j > 0 \vee \left( \lambda_i^j = 0 \wedge \dot{\lambda}_i^j > 0 \right) \\ \bar{\gamma}_i^j > 0 & \text{else} \end{cases} . \quad (4.14)$$

Using the free energy's property  $\Psi^{\text{rel}} = \Psi^{\text{rel}}(\boldsymbol{\varepsilon}, \boldsymbol{\lambda})$  the energy's rate gives

$$\dot{\Psi}^{\text{rel}} = \frac{\partial \Psi^{\text{rel}}}{\partial \boldsymbol{\varepsilon}} : \dot{\boldsymbol{\varepsilon}} + \frac{\partial \Psi^{\text{rel}}}{\partial \boldsymbol{\lambda}} : \dot{\boldsymbol{\lambda}} . \quad (4.15)$$

Combination of the constraints for the volume fractions and the thermodynamical identity Eq. (4.11) (LAGRANGE parameter  $\beta$ ) in a maximum problem allows the introduction of a LAGRANGE functional

$$\begin{aligned} \mathcal{L} &= \mathcal{L}(\dot{\boldsymbol{\varepsilon}}, \dot{\boldsymbol{\lambda}}) \\ &= \mathcal{D} + \beta \left\{ \mathcal{D} - \frac{1}{\theta} \left( \boldsymbol{\sigma} : \dot{\boldsymbol{\varepsilon}} - \frac{\partial \Psi^{\text{rel}}}{\partial \boldsymbol{\varepsilon}} : \dot{\boldsymbol{\varepsilon}} - \frac{\partial \Psi^{\text{rel}}}{\partial \boldsymbol{\lambda}} : \dot{\boldsymbol{\lambda}} \right) \right\} + \\ &\quad \sum_{j=1}^N \kappa^j \sum_{i=0}^n \dot{\lambda}_i^j - \sum_{j=1}^N \sum_{i=0}^n \gamma_i^j \dot{\lambda}_i^j \rightarrow \max_{\dot{\boldsymbol{\varepsilon}}, \dot{\boldsymbol{\lambda}}} . \end{aligned} \quad (4.16)$$

The stationary conditions of the problem read

$$\frac{\partial \mathcal{L}}{\partial \dot{\boldsymbol{\varepsilon}}} = \mathbf{0} \quad \Leftrightarrow \quad \boldsymbol{\sigma} = \frac{\partial \Psi^{\text{rel}}}{\partial \boldsymbol{\varepsilon}} \quad (4.17)$$

$$\frac{\partial \mathcal{L}}{\partial \dot{\boldsymbol{\lambda}}} = \mathbf{0} \quad \Leftrightarrow \quad \frac{\partial \mathcal{D}}{\partial \dot{\boldsymbol{\lambda}}} (1 + \beta) + \frac{\beta}{\theta} \frac{\partial \Psi^{\text{rel}}}{\partial \boldsymbol{\lambda}} + \boldsymbol{\kappa} - \boldsymbol{\gamma} = \mathbf{0}, \quad (4.18)$$

with

$$\boldsymbol{\kappa} = \kappa^j \mathbf{e}_j \mathbf{e}_i, \quad \boldsymbol{\gamma} = \gamma_i^j \mathbf{e}_j \mathbf{e}_i, \quad \mathbf{e}_i, \mathbf{e}_j : \text{unit vectors}. \quad (4.19)$$

Regarding Eq. (4.17), it becomes obvious that the presented approach provides the constitutive equation for stress immediately, Eq. (2.70).

In order to circumvent the need of finding explicit expressions for the KUHN-TUCKER parameters  $\gamma_i^j$ , the *active set* strategy is applied. Two sets are used for each direction  $j$ , one passive set  $\mathcal{B}^j$  for all phases which have zero volume fraction, and one active set  $\mathcal{A}^j$  which collects on the one hand all the phases with zero volume fraction but fulfilling the constraint of positivity identically since they have a positive rate and on the other hand all the rest. Thus,

$$\mathcal{B}^j = \{i \mid \lambda_i^j = 0\} \quad (4.20)$$

$$\mathcal{A}^j = \{i \in \mathcal{B}^j \mid \dot{\lambda}_i^j > 0\} \cup \{i \notin \mathcal{B}^j\} \quad (4.21)$$

Applying this strategy to every component of Eq. (4.18) and summing over all phases  $i$  yields for every direction  $j$

$$\kappa^j = -\frac{\beta}{\theta} \frac{1}{n_{\mathcal{A}^j}} \sum_{k \in \mathcal{A}^j} \frac{\partial \Psi^{\text{rel}}}{\partial \lambda_k^j}, \quad (4.22)$$

where  $n_{\mathcal{A}^j}$  denotes the number of active phases according to Eq. (4.21) in each direction. Here, the property of  $\mathcal{D}$  being a homogeneous function of rank one has been used. This implies

$$\sum_{k \in \mathcal{A}^j} \frac{\partial \mathcal{D}}{\partial \dot{\lambda}_k^j} = 0. \quad (4.23)$$

Now, Eq. (4.18) can be transformed to

$$\frac{1}{\theta} \frac{\partial \Psi^{\text{rel}}}{\partial \boldsymbol{\lambda}} = -\frac{1+\beta}{\beta} \frac{\partial \mathcal{D}}{\partial \dot{\boldsymbol{\lambda}}} - \frac{1}{\beta} \boldsymbol{\kappa} + \frac{1}{\beta} \boldsymbol{\gamma} \quad (4.24)$$

and inserted in Eq. (4.11) which yields

$$\begin{aligned} \mathcal{D} - \frac{1+\beta}{\beta} \frac{\partial \mathcal{D}}{\partial \dot{\boldsymbol{\lambda}}} : \dot{\boldsymbol{\lambda}} + \frac{1}{\beta} \underbrace{\boldsymbol{\kappa} : \dot{\boldsymbol{\lambda}}}_{\equiv 0} - \frac{1}{\beta} \underbrace{\boldsymbol{\gamma} : \dot{\boldsymbol{\lambda}}}_{\equiv 0} &= 0 \\ \frac{1+\beta}{\beta} &= \frac{\mathcal{D}}{\frac{\partial \mathcal{D}}{\partial \dot{\boldsymbol{\lambda}}} : \dot{\boldsymbol{\lambda}}} =: \frac{1}{f}. \end{aligned} \quad (4.25)$$

The thermodynamical conjugated forces are denoted as

$$\mathbf{P} = -\frac{\partial \Psi^{\text{rel}}}{\partial \boldsymbol{\lambda}}. \quad (4.26)$$



Using Eqs. (4.25) and (4.26), Eq. (4.18) turns

$$\begin{aligned}
 & \underbrace{\frac{\beta}{1+\beta}}_{=f} \underbrace{\frac{1}{\theta} \left( -\frac{\partial \Psi^{\text{rel}}}{\partial \dot{\lambda}} \right)}_{=P} - \frac{1}{1+\beta} \kappa + \frac{1}{1+\beta} \gamma = \frac{\partial \mathcal{D}}{\partial \dot{\lambda}} \\
 \Rightarrow & \begin{cases} \frac{f}{\theta} P_i^j + \frac{\beta}{1+\beta} \frac{1}{\theta} \frac{1}{n_{\mathcal{A}^j}} \sum_{k \in \mathcal{A}^j} \frac{\partial \Psi^{\text{rel}}}{\partial \dot{\lambda}_k^j} = \frac{\partial \mathcal{D}}{\partial \dot{\lambda}_i^j} & , i \in \mathcal{A}^j \\ \frac{f}{\theta} P_i^j + \frac{\beta}{1+\beta} \frac{1}{\theta} \frac{1}{n_{\mathcal{A}^j}} \sum_{k \in \mathcal{A}^j} \frac{\partial \Psi^{\text{rel}}}{\partial \dot{\lambda}_k^j} = -\frac{1}{1+\beta} \gamma_i^j & , i \notin \mathcal{A}^j \end{cases} \\
 \Leftrightarrow & \begin{cases} \frac{f}{\theta} P_i^j + \frac{f}{\theta} \frac{1}{n_{\mathcal{A}^j}} \sum_{k \in \mathcal{A}^j} \frac{\partial \Psi^{\text{rel}}}{\partial \dot{\lambda}_k^j} = \frac{\partial \mathcal{D}}{\partial \dot{\lambda}_i^j} & , i \in \mathcal{A}^j \\ \frac{f}{\theta} P_i^j + \frac{f}{\theta} \frac{1}{n_{\mathcal{A}^j}} \sum_{k \in \mathcal{A}^j} \frac{\partial \Psi^{\text{rel}}}{\partial \dot{\lambda}_k^j} = -\frac{1}{1+\beta} \gamma_i^j < 0 & , i \notin \mathcal{A}^j \end{cases} \quad (4.27)
 \end{aligned}$$

The expression

$$P_i^j - \frac{1}{n_{\mathcal{A}^j}} \sum_{k \in \mathcal{A}^j} P_k^j = : \text{dev}_{\mathcal{A}^j} P_i^j \quad (4.28)$$

in Eq. (4.27) is termed *active deviator*.

The equations in Eq. (4.27) are sufficient to predict the evolution of phase fractions. However, they can be evaluated first when a specific ansatz for the free energy  $\Psi^{\text{rel}}$  and the entropy production  $\mathcal{D}$  has been chosen. For the free energy the approach of [19], mentioned in Sec. 4.2.1, is taken and for the dissipation the ansatz

$$\begin{aligned}
 \mathcal{D} &= \frac{r}{\theta} \sqrt{\sum_{j=1}^N \xi^j \sum_{i=0}^n \left( \dot{\lambda}_i^j \right)^2} \\
 &= \frac{r}{\theta} |\dot{\lambda}|. \quad (4.29)
 \end{aligned}$$

is chosen.  $\mathcal{D}$  is homogeneous in  $\dot{\lambda}$  of first order. Therefore, derivation of  $\mathcal{D}$  yields a subdifferential as

$$\frac{\partial \mathcal{D}}{\partial \dot{\lambda}_i^j} =: \partial \mathcal{D}_{ij} = \begin{cases} \frac{r \xi^j}{\theta} \frac{\dot{\lambda}_i^j}{|\dot{\lambda}|} & , \dot{\lambda} \neq 0 \\ \left\{ \dot{\lambda}_i^j \left| \sqrt{\sum_{j=1}^N \xi^j \sum_{i=0}^n \left( \dot{\lambda}_i^j \right)^2} \leq \frac{r}{\theta} \right. \right\} & , \dot{\lambda} = 0. \end{cases} \quad (4.30)$$

Now, the evolution equations can be analyzed since plugging  $\partial \mathcal{D} / \partial \dot{\lambda}$  from Eq. (4.30) into

the first part of Eq. (4.27) gives

$$\begin{aligned} \frac{f}{\theta} \operatorname{dev}_{\mathcal{A}^j} P_i^j &= \frac{\partial \mathcal{D}}{\partial \dot{\lambda}_i^j}, \quad i \in \mathcal{A}^j \\ \Rightarrow \begin{cases} \frac{f}{\theta} \operatorname{dev}_{\mathcal{A}^j} P_i^j = \frac{r \xi^j}{\theta} \frac{\dot{\lambda}_i^j}{|\dot{\lambda}|} & , \quad i \in \mathcal{A}^j, \dot{\lambda} \neq \mathbf{0} \\ \sqrt{\sum_{j=1}^N \frac{1}{\xi^j} \sum_{i=0}^n (\operatorname{dev}_{\mathcal{A}^j} P_i^j)^2} \leq \frac{r}{\theta} & , \quad i \in \mathcal{A}^j, \dot{\lambda} = \mathbf{0} \end{cases} \end{aligned} \quad (4.31)$$

where the first line of Eq. (4.31) gives

$$\dot{\lambda}_i^j = \frac{f |\dot{\lambda}|}{r \xi^j} \operatorname{dev}_{\mathcal{A}^j} P_i^j, \quad i \in \mathcal{A}^j, \dot{\lambda} \neq \mathbf{0}. \quad (4.32)$$

The remaining factor  $f$  is determined as, Eq. (4.25),

$$f = \frac{\frac{\partial \mathcal{D}}{\partial \dot{\lambda}} : \dot{\lambda}}{\mathcal{D}} = \frac{\mathcal{D}}{\mathcal{D}} = 1. \quad (4.33)$$

Analyzing Eq. (4.25) under consideration of Eq. (4.33) gives

$$\frac{1 + \beta}{\beta} \stackrel{!}{=} 1 \Rightarrow \beta \rightarrow \infty. \quad (4.34)$$

Thus, for quasi-static problems, which is the current one as well, the constraints 'definition of entropy production', Eq. (4.11), 'mass conservation', Eq. (4.12), and 'positivity', Eq. (4.13), play the important roles (the LAGRANGE and KUHN-TUCKER parameters may be redefined as  $\kappa^j \rightarrow \kappa^j/\beta$  and  $\gamma_i^j \rightarrow \gamma_i^j/\beta$ ). Hence, the LAGRANGE functional can be rewritten as

$$\mathcal{L} = \mathcal{D} - \frac{1}{\theta} \left( \boldsymbol{\sigma} : \dot{\boldsymbol{\varepsilon}} - \frac{\partial \Psi^{\text{rel}}}{\partial \boldsymbol{\varepsilon}} : \dot{\boldsymbol{\varepsilon}} - \frac{\partial \Psi^{\text{rel}}}{\partial \boldsymbol{\lambda}} : \dot{\boldsymbol{\lambda}} \right) + \boldsymbol{\kappa} : \dot{\boldsymbol{\lambda}} - \boldsymbol{\gamma} : \dot{\boldsymbol{\lambda}} \rightarrow \max_{\dot{\boldsymbol{\varepsilon}}, \dot{\boldsymbol{\lambda}}}. \quad (4.35)$$

An analogous derivation to the previously presented gives

$$\dot{\lambda}_i^j = \frac{|\dot{\lambda}|}{r \xi^j} \operatorname{dev}_{\mathcal{A}^j} P_i^j, \quad i \in \mathcal{A}^j \text{ and } \dot{\lambda} \neq \mathbf{0}. \quad (4.36)$$

In order to evaluate the evolution equation as well as the yield function, the driving forces remain to be calculated. Since they are well defined through

$$P_i^j = - \frac{\partial \Psi^{\text{rel}}(\boldsymbol{\varepsilon}, \boldsymbol{\lambda})}{\partial \lambda_i^j} \quad (4.37)$$

the thermodynamical driving forces can be found as

$$P_i^j = \xi^j \left[ \boldsymbol{\eta}_i^j : \mathbb{C}_{\text{eff}} : (\boldsymbol{\varepsilon} - \boldsymbol{\eta}_{\text{eff}}) + \frac{1}{2} (\boldsymbol{\varepsilon} - \boldsymbol{\eta}_{\text{eff}}) : \left( \mathbb{C}_{\text{eff}} : (\mathbb{C}_i^j)^{-1} : \mathbb{C}_{\text{eff}} \right) : (\boldsymbol{\varepsilon} - \boldsymbol{\eta}_{\text{eff}}) - c_i \right], \quad (4.38)$$

compare to [19]. Now, everything is derived which is needed to describe the evolution in poly-crystalline shape memory alloys. Furthermore the inclusion of hysteresis and tension-compression asymmetry was reported.

A model which provides completely same results was presented in [19], a continuation of the model in [20] and its analysis in [21]. In contrast to the approach based on the principle of maximum dissipation which was presented here, in [19] the principle of the minimum of the dissipation potential was used. As explained in [18] both principles yield the same result, under the consideration that the dissipation  $\mathcal{D}$  shows certain properties, see Sec. 3.3. The comparison between material point evaluation of the model with experimental observations showed good agreement, [24].

The presented equations completely describe the evolution of the internal variables. Thus, the model in its current state could be implemented into a proper solution scheme. However, for further mathematical simplification a LEGENDRE transformation of the variational problem in Eq. (4.16) is executed. This idea is straight forward due to the origin of the principle of the minimum of the dissipation potential which was derived through a LEGENDRE transformation of the original problem formulation as explained in Sec. 3.2.

The LEGENDRE transformation of Eq. (4.16) is

$$\begin{aligned} \mathcal{J}(\mathbf{P}) &= \sup_{\dot{\lambda}} \left\{ \frac{1}{\theta} \mathbf{P} : \dot{\lambda} - \mathcal{D}(\dot{\lambda}) \mid (4.11), (4.12), (4.13) \right\} \\ &= \sup_{\dot{\lambda}} \left\{ \frac{|\dot{\lambda}|}{\theta r} \underbrace{\left( \sum_{j=1}^N \frac{1}{\xi^j} \sum_{i=0}^n (\text{dev}_{\mathcal{A}^j} P_i^j)^2 - r^2 \right)}_{=: \Phi(\mathbf{P}) \leq 0} \mid \mathcal{A} \right\}. \end{aligned} \quad (4.39)$$

The function  $\Phi(\mathbf{P})$  fulfills a similar purpose as yield functions in classical plasticity. The rate of volume fractions may take every arbitrary value. Hence, in order to keep  $\mathcal{J}$  bounded,  $\Phi$  has to be less or equal zero. In combination with Eq. (4.31) where the active deviator plays the role of the stress deviator in plasticity showing the direction normal to the yield surface, the factor  $|\dot{\lambda}|/r =: \rho$  is interpreted as step size which is needed to reach again the yield surface characterized by  $\Phi(\mathbf{P})$ . Thus, the fraction is denoted from now as  $\rho$  which results in the entire set of equations

$$\dot{\lambda}_i^j = \frac{\rho}{\xi^j} [\text{dev}_{\mathcal{A}^j} P_i^j]_{\mathcal{A}^j} \quad (4.40)$$

with the KUHN-TUCKER conditions

$$\rho \geq 0, \quad \Phi \leq 0, \quad \rho \Phi = 0 \quad (4.41)$$

and the consistency condition

$$\text{dev}_{\mathcal{A}^j} P_i^j \leq 0 \quad \text{for } i \notin \mathcal{A}^j \quad (4.42)$$

from the second part in Eq. (4.27).

An evaluation of the model on the material point level may be found in [19] and [25] and a comparison to experiments in [24].

This work focuses on the simulation of entire specimens made of shape memory alloys. Therefore, the model is scaled on the finite element level, see Sec. 5, and numerical results are presented and discussed in Sec. 6. It turns out that the model, although providing good results on the material point level, is not able to display the material behavior on the

specimen level. For further details see Sec. 6.1. Hence, further extensions of the model are necessary. In Sec. 4.2.3 a modified model is presented taking into account different energy costs of phase *nucleation* and *evolution*. This model is still limited to the isothermal case. A fully thermo-mechanically coupled model is presented afterwards in Sec. 4.2.4.

### 4.2.3 An extended Model

Due to the insufficient results of the basic model in the simulation of entire specimens a modification of the model has to be carried out. As discussed in detail in Sec. 6.1, the basic model predicts a homogeneous phase transformation over the specimen. This does not coincide with experimental results, [48], and gives a hint that the entropy production for which always an ansatz has to be made is not taking into account sufficiently enough the physical behavior. Equivalently spoken, energy costs caused by phase transitions are not mapped correctly by the current approach for  $\mathcal{D}$  if the transformations are not only evolving over time or load – as it was the case for the material point analyses in [19] – but also evolving over *space*.

As it was stated in Sec. 4.1.2, the different crystallographic phases of shape memory alloys can be classified in austenite and martensite. They are coupled via a shear and shuffle relation. Obviously, there exists an energetic difference between two cases: case one is when a martensitic phase wants to *nucleate* in a purely austenitic lattice. Case two is when a certain amount of martensite has already nucleated and only wants to *grow*. Then, it is quite clear that the energy barriers which have to be overcome in order to transform the material from one phase to another have to be different. If there is already a certain amount of martensitic 'interface' from which a further phase transition can evolve the energetic cost and thus the dissipated energy is lower. Hence, the approach for the entropy production has to take that phenomenon into account by having a *state* or *phase* dependent dissipation coefficient. In order to do so, the average amount of austenite at one specific material point is denoted by  $|\lambda_0|$  and calculated by

$$|\lambda_0| := \sum_{j=1}^N \xi^j \lambda_0^j. \quad (4.43)$$

Then, the approach for the entropy production can be modified according to

$$\mathcal{D} = \frac{r(|\lambda_0|)}{\theta} \sqrt{\sum_{j=1}^N \xi^j \sum_{i=0}^n \left(\dot{\lambda}_i^j\right)^2} = \frac{r(|\lambda_0|)}{\theta} |\dot{\lambda}|. \quad (4.44)$$

Applying this ansatz for the entropy production to the principle of maximum dissipation, analogous equations to the basic model can be found. The main difference is the modified yield function. The set of equations is

$$\dot{\lambda}_i^j = \frac{\rho}{\xi^j} [\text{dev}_{\mathcal{A}^j} P_i^j]_{\mathcal{A}^j} \quad (4.45)$$

as evolution equations for the crystallographic phases and

$$\Phi = \sum_{j=1}^N \frac{1}{\xi^j} \sum_{i=0}^n (\text{dev}_{\mathcal{A}^j} P_i^j)^2 - r^2(|\lambda_0|) \quad (4.46)$$

as yield function with the state dependent 'yield limit'  $r(|\lambda_0|)$  for which an appropriate ansatz has to be made. Again, the KUHN-TUCKER conditions

$$\rho \geq 0, \quad \Phi \leq 0, \quad \rho \Phi = 0 \quad (4.47)$$

together with the consistency conditions

$$\text{dev}_{\mathcal{A}^j} P_i^j \leq 0 \quad \text{for } i \notin \mathcal{A}^j \quad (4.48)$$

have to hold. Numerical results for this model are given and discussed in detail in Sec. 6.2. It is obvious that the modification of the basic model yields the desired results as localized transformations. However, due to the softening character of the resulting yield function the results are mesh dependent. In order to circumvent that problem, a method presented in [10] and [11] is applied here.

In order to solve the problem of mesh dependent results a strategy presented in [11] for damage models with softening character is adapted for the case of simulations of shape memory alloys. The internal variable, damage variable in [11], volume fractions  $\lambda$  in this work, is boosted by the specific approaches to evolve where it has nucleated. Although the internal variables at different GAUSS points are coupled through the displacement field in a finite element implementation this evolution may proceed very localized. Due to the coupling between displacements and internal variables the effect of boosting *locally limited* is enhanced and since the displacements themselves are only an approximation and directly solved only at the nodes, the discretization over space, realized by the meshing, influences the phenomenon of localization ( $\rightarrow$  mesh dependence). This may occur since the formulation of the problem does not take into account any space related gradient of the internal variables. As presented in Sec. 5.1, a finite element calculation in mechanics is equivalent to the minimization of the free energy  $\Psi^{\text{rel}}$ . Hence, it seems very convenient to modify the potential provided to the calculation in a way that the gradient of the internal variables contributes to the free energy. This can be carried out by introducing an additional space dependent field variable termed as  $\varphi$  which is coupled with the locally defined volume fractions. Since an average information is sufficient and furthermore the average amount of austenite is the variable the softening dissipation coefficient  $r$  depends on,  $\varphi$  will be coupled with  $|\lambda_0|$ . Due to the associated shift of the information carried by the internal variables on the GAUSS point level to the space dependent level of  $\varphi$ , penalizing the gradient of the field function will indirectly penalize the gradient of the internal variables. Therefore, the localized transformation can be retained but detached from the discretizing finite element mesh. So, the total energy is introduced as

$$\Psi^{\text{tot}}(\epsilon, \lambda, |\lambda_0|, \varphi) := \Psi^{\text{rel}}(\epsilon, \lambda) + \underbrace{\frac{\beta_\varphi}{2} (\varphi + 1 - |\lambda_0|)^2}_{\text{coupling}} + \underbrace{\frac{c_\varphi}{2} |\nabla \varphi|^2}_{\text{penalization}} \quad (4.49)$$

with some at first glance numerical parameters  $\beta_\varphi$  and  $c_\varphi$ . As shown in [11] the parameter  $\beta_\varphi$  does not have any influence on the solution and just has to be positive. The second parameter  $c_\varphi$  in contrast has direct physical meaning: increasing the parameter, and thus penalizing the gradient more strongly, results in the limit in the homogeneous transformation as for the basic model. Decreasing the parameter on the other hand causes a more and more localized behavior and yields in the limit to the mesh dependent results ( $c_\varphi \rightarrow 0$ ). Thus, that parameter may be interpreted as 'averaged interface or surface energy'. The corresponding LAGRANGE functional in this case, analogous to Eq. (4.35), is

$$\mathcal{L} = \mathcal{D} - \frac{1}{\theta} \left( \sigma : \dot{\epsilon} - \frac{\partial \Psi^{\text{tot}}}{\partial \epsilon} : \dot{\epsilon} - \frac{\partial \Psi^{\text{tot}}}{\partial \lambda} : \dot{\lambda} \right) + \kappa : \dot{\lambda} - \gamma : \dot{\lambda} \rightarrow \max_{\dot{\epsilon}, \dot{\lambda}}, \quad (4.50)$$

where  $\kappa$  and  $\gamma$  are again LAGRANGE and KUHN-TUCKER parameters respectively to fulfill the constraints of mass conservation and positivity. The maximization conditions and a

subsequent LEGENDRE transformation of the dissipation  $\mathcal{D}$  yield same results as for the not-regularized extended model, namely

$$\dot{\lambda}_i^j = \rho [\text{dev}_{\mathcal{A}^j} P_i^j]_{\mathcal{A}^j} \quad (4.51)$$

and

$$\Phi = \sum_{j=1}^N \frac{1}{\xi^j} \sum_{i=0}^n (\text{dev}_{\mathcal{A}^j} P_i^j)^2 - r^2(|\lambda_0|) \quad (4.52)$$

with

$$\rho \geq 0, \quad \Phi \leq 0, \quad \rho \Phi = 0 \quad (4.53)$$

and

$$\text{dev}_{\mathcal{A}^j} P_i^j \leq 0 \quad \text{for } i \notin \mathcal{A}^j. \quad (4.54)$$

In contrast to the basic model, now the thermodynamic driving forces are

$$\begin{aligned} P_i^j &= - \frac{d\Psi^{\text{tot}}(\varepsilon, \lambda, |\lambda_0|, \varphi)}{d\lambda_i^j} \\ &= \xi^j \left[ \eta_i^j : \mathbb{C}_{\text{eff}} : (\varepsilon - \boldsymbol{\eta}_{\text{eff}}) + \frac{1}{2} (\varepsilon - \boldsymbol{\eta}_{\text{eff}}) : \left( \mathbb{C}_{\text{eff}} : (\mathbb{C}_i^j)^{-1} : \mathbb{C}_{\text{eff}} \right) : (\varepsilon - \boldsymbol{\eta}_{\text{eff}}) - c_i \right] \\ &\quad + \underbrace{\beta_\varphi \xi^j (\varphi + 1 - |\lambda_0|)}_{\star} \delta_{0i}. \end{aligned} \quad (4.55)$$

Thus, the value of the field function or better to say the deviation between  $\varphi$  and the average amount of austenite has a direct influence on the evolution of the volume fractions through the part  $(\star)$ . Via this approach, the volume fractions being internal or equivalently GAUSS point quantities are shifted from the GAUSS point level to a field level.

Missing is an approach for the dissipation coefficient  $r$ . To postulate an appropriate ansatz first imagine a crystal of pure austenite. Now, an applied load forces the atoms to leave the austenitic state and transform to martensite, Fig. 4.11. This process does not affect the entire crystal immediately but only a certain amount of mass will transform which is denoted by its volume fraction. Since the evolution of martensite will be easier to perform compared to the nucleation of martensite the energy costs vary between these states. The *nucleation* will cost more energy compared to the *evolution* of martensite. Thus, the entropy produced will be more during nucleation and less during evolution. Now, imagine a completely transformed crystal for which the applied load is reduced again. Obviously, similar effects are to be expected. The creation of the first austenite costs more energy and deductively produces more entropy compared to the austenite which is manifested later on. Therefore the argumentation remains the same but the energy costs depend on the *evolution direction* the material favors. This direction is naturally determined by the thermodynamical driving forces,  $\mathbf{P}$ . In order to take the constraints into account it is necessary to use the sign of the rate of volume fractions instead of the ones of the driving forces. If now an entropy production is a linear function of the average amount of austenite  $|\lambda_0|$ , it changes its slope depending on the sign of  $(|\lambda_0|)$ . Thus, an ansatz according to

$$r(|\lambda_0|, \text{sign}(|\lambda_0|)) = \begin{cases} r_{\text{As}} + (r_{\text{Af}} - r_{\text{As}})(1 - |\lambda_0|) & , \text{sign}(|\lambda_0|) < 0 \\ \min\{r_{\text{As}}, r_{\text{Mf}}\} & , \text{sign}(|\lambda_0|) = 0 \\ r_{\text{Ms}} + (r_{\text{Mf}} - r_{\text{Ms}})|\lambda_0| & , \text{sign}(|\lambda_0|) > 0 \end{cases} \quad (4.56)$$

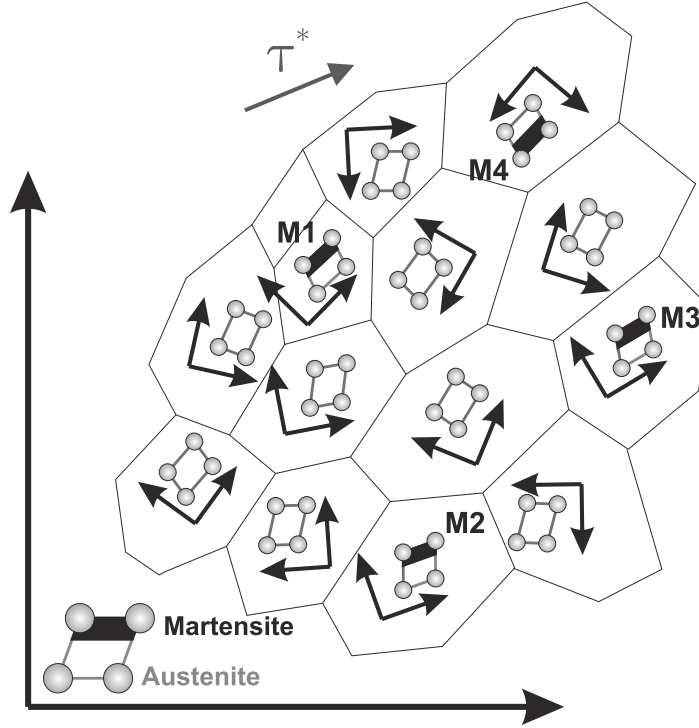


Figure 4.11: Idealization of a poly-crystal with individual grain orientations. Under load in different grains with preferred orientation a specific amount of martensite evolves. Black indicates martensite, gray is austenite. Filled volume in the schematic unit cell in the left corner shows the average amount of transformed austenite in the entire material point (= GAUSS point).

with  $r_{As}$ ,  $r_{Af}$ ,  $r_{Ms}$ ,  $r_{Mf}$  as dissipation parameters for start and finish of austenite and martensite, respectively, is chosen.  $\text{sign}(|\lambda_0|)$  terms the average sign of the driving force for austenite calculated by

$$\text{sign}(|\lambda_0|) = \frac{1}{n_A} \sum_{k \in \mathcal{A}} \text{sign} \dot{\lambda}_0^k, \quad (4.57)$$

where  $n_A$  is the total number of active austenitic phases in the entire material point. The finite element implementation scheme is given in Sec. 5.2 and numerical results as well as their discussion can be found in Sec. 6.2. This extended model provides far better results compared to the basic model since now the localized transformation behavior known from experiments is caught in a *mesh independent* manner. However, this model still only allows the simulation of pseudo-elastic shape memory alloys which additionally may only be loaded very slowly. This is not caused mainly by the neglect of inertial forces but due to the missing influence of *temperature*. As it will be pointed out in the upcoming Sec. 6.3, the temperature distribution is more than just an additional information. Indeed, due to the also temperature driven phase transformations in shape memory alloys, there exists an important coupling between mechanical loading and temperature which influences the phase transitions. The corresponding material model for the numerical results in Sec. 6.3 is presented in Sec. 4.2.4.

#### 4.2.4 A thermo-mechanically coupled Model

In order to take effects due to temperature and heat into account as well, the thermodynamical identity of Eq. (2.67) for the entropy production is now taken in its complete form

as

$$\mathcal{D} = \frac{1}{\theta} \left( \boldsymbol{\sigma} : \dot{\boldsymbol{\varepsilon}} - \dot{\Psi} - s \dot{\theta} \right) + \mathbf{q} \cdot \nabla \frac{1}{\theta}. \quad (4.58)$$

Again, the principle of maximum dissipation is applied for which a LAGRANGE functional  $\mathcal{L}$  is introduced. This functional takes into account the constraints of mass conservation and positivity as in the cases before. In contrast to those, the LAGRANGE functional now depends on more free variables which are rate of strain,  $\dot{\boldsymbol{\varepsilon}}$ , and volume fractions,  $\dot{\boldsymbol{\lambda}}$  as before and additionally rate of temperature,  $\dot{\theta}$ , and heat flux,  $\mathbf{q}$ . This leads to

$$\mathcal{L} = \mathcal{D} - \frac{1}{\theta} \left( \boldsymbol{\sigma} : \dot{\boldsymbol{\varepsilon}} - \dot{\Psi} - s \dot{\theta} \right) + \mathbf{q} \cdot \nabla \frac{1}{\theta} + \boldsymbol{\kappa} : \dot{\boldsymbol{\lambda}} - \boldsymbol{\gamma} : \dot{\boldsymbol{\lambda}} \rightarrow \max_{\dot{\boldsymbol{\varepsilon}}, \dot{\boldsymbol{\lambda}}, \dot{\theta}, \mathbf{q}}. \quad (4.59)$$

Modified to both models presented before, the free energy is now temperature dependent to leave the isothermal case. Thus, the time derivative of the free energy  $\Psi$  gives

$$\dot{\Psi} = \frac{\partial \Psi}{\partial \boldsymbol{\varepsilon}} : \dot{\boldsymbol{\varepsilon}} + \frac{\partial \Psi}{\partial \boldsymbol{\lambda}} : \dot{\boldsymbol{\lambda}} + \frac{\partial \Psi}{\partial \theta} \dot{\theta}. \quad (4.60)$$

Inserting the identity of Eq. (4.60) into the LAGRANGE function in Eq. (4.59) allows to find its stationary point by setting the derivatives of  $\mathcal{L}$  with respect to its free variables to zero. So,

$$\frac{\partial \mathcal{L}}{\partial \dot{\boldsymbol{\varepsilon}}} = \mathbf{0} \Leftrightarrow \boldsymbol{\sigma} = \frac{\partial \Psi}{\partial \boldsymbol{\varepsilon}}, \quad (4.61)$$

$$\frac{\partial \mathcal{L}}{\partial \dot{\boldsymbol{\lambda}}} = \mathbf{0} \Leftrightarrow \frac{\partial \mathcal{D}}{\partial \dot{\boldsymbol{\lambda}}} + \frac{1}{\theta} \frac{\partial \Psi}{\partial \boldsymbol{\lambda}} + \boldsymbol{\kappa} - \boldsymbol{\gamma} = \mathbf{0}, \quad (4.62)$$

$$\frac{\partial \mathcal{L}}{\partial \dot{\theta}} = 0 \Leftrightarrow s = -\frac{\partial \Psi}{\partial \theta}, \quad (4.63)$$

$$\frac{\partial \mathcal{L}}{\partial \mathbf{q}} = \mathbf{0} \Leftrightarrow \frac{\partial \mathcal{D}}{\partial \mathbf{q}} - \nabla \frac{1}{\theta} = \mathbf{0}. \quad (4.64)$$

Additionally to the constitutive equation for stress, Eq. (4.61), the principle of maximum dissipation provides the constitutive equation for entropy  $s$  as well, Eq. (4.63).

Analogously to the basic model, the evolution equations can be determined from Eq. (4.62) which gives again

$$\begin{cases} \text{dev}_{\mathcal{A}^j} P_i^j &= \frac{\partial \mathcal{D}}{\partial \dot{\lambda}_i^j}, & i \in \mathcal{A}^j \\ \text{dev}_{\mathcal{A}^j} P_i^j &= -\gamma_i^j \leq 0, & i \notin \mathcal{A}^j \end{cases} \quad (4.65)$$

with the *active deviator*

$$\text{dev}_{\mathcal{A}^j} P_i^j := P_i^j - \frac{1}{n_{\mathcal{A}^j}} \sum_{k \in \mathcal{A}^j} P_k^j. \quad (4.66)$$

The driving forces can be calculated as

$$\begin{aligned} P_i^j &= -\frac{d\Psi^{\text{tot}}(\boldsymbol{\varepsilon}, \boldsymbol{\lambda}, |\boldsymbol{\lambda}_0|, \varphi, \theta)}{d\lambda_i^j} \\ &= \xi^j \left[ \eta_i^j : \mathbb{C}_{\text{eff}} : (\boldsymbol{\varepsilon} - \boldsymbol{\eta}_{\text{eff}}) + \frac{1}{2} (\boldsymbol{\varepsilon} - \boldsymbol{\eta}_{\text{eff}}) : \left( \mathbb{C}_{\text{eff}} : (\mathbb{C}_i^j)^{-1} : \mathbb{C}_{\text{eff}} \right) : (\boldsymbol{\varepsilon} - \boldsymbol{\eta}_{\text{eff}}) - c_i(\theta) \right] \\ &\quad + \beta_\varphi \xi^j (\varphi + 1 - |\boldsymbol{\lambda}_0|) \delta_{0i}. \end{aligned} \quad (4.67)$$

where the same energy as for the extended model has been used ( $\Psi = \Psi^{\text{tot}}$ ), but now with temperature dependent chemical parts  $c_i = c_i(\theta)$ .



Until now, there is no difference between the previous models and the current, thermo-mechanically coupled one. Again, assumptions for the energy and the entropy production have to be made. For the energy, the relaxed energy  $\Psi^{\text{rel}}$  is used which now depends on the temperature as well. Thus,

$$\Psi^{\text{rel}} = \frac{1}{2}(\boldsymbol{\varepsilon} - \boldsymbol{\eta}_{\text{eff}}) : \mathbb{C}_{\text{eff}} : (\boldsymbol{\varepsilon} - \boldsymbol{\eta}_{\text{eff}}) + c_{\text{eff}}(\theta) \quad (4.68)$$

where for the chemical part the approach of [28] is followed. This is

$$c_i(\theta) = c_\theta (\theta - \theta_R) + c_\theta \theta \log \left( \frac{\theta}{\theta_R} \right) + a_i - b_i \theta \quad (4.69)$$

with phase dependent constants  $a_i$  and  $b_i$ , the heat capacity  $c_\theta$  and a reference temperature  $\theta_R$ .

Furthermore, the entropy production now does not only depend on the rate of the volume fractions but additionally on the heat flux  $\mathbf{q}$ . Hence, the ansatz

$$\begin{aligned} \mathcal{D} &= \frac{r(|\boldsymbol{\lambda}_0|, \text{sign}(|\boldsymbol{\lambda}_0|))}{\theta} \sqrt{\sum_{j=1}^N \xi^j \sum_{i=0}^n (\dot{\lambda}_i^j)^2} + \frac{\alpha_\theta}{2} |\mathbf{q}|^2 \\ &= \frac{r(|\boldsymbol{\lambda}_0|, \text{sign}(|\boldsymbol{\lambda}_0|))}{\theta} |\dot{\boldsymbol{\lambda}}| + \frac{\alpha_\theta}{2} |\mathbf{q}|^2 \end{aligned} \quad (4.70)$$

with some parameter  $\alpha_\theta$  is used.

Similar to previous calculations, again a LEGENDRE transformation of the LAGRANGE functional  $\mathcal{L}$  is executed. This yields

$$\begin{aligned} \mathcal{J}(\mathbf{P}, \mathbf{q}) &= \sup_{\dot{\boldsymbol{\lambda}}} \left\{ \frac{1}{\theta} \mathbf{P} : \dot{\boldsymbol{\lambda}} - \mathcal{D}(\boldsymbol{\lambda}, \mathbf{q}) \mid (4.12), (4.13), (4.58) \right\} \\ &= \sup_{\boldsymbol{\lambda}} \left\{ \frac{|\boldsymbol{\lambda}_0|}{\theta r} \underbrace{\left( \sum_{j=1}^N \frac{1}{\xi^j} \sum_{i=0}^n (\text{dev}_{\mathcal{A}^j} P_i^j)^2 - r^2 \right)}_{=: \Phi \leq 0} \mid \mathcal{A} \right\} - \frac{\alpha_\theta}{2} |\mathbf{q}|^2 - \mathbf{q} \cdot \nabla \frac{1}{\theta}. \end{aligned} \quad (4.71)$$

So, the yield function remains the same as before as well.

Temperature is now a variable. Therefore, an equation for the temperature is searched for. In order to do so, energy conservation is regarded once more, Eq. (2.62), which is

$$\begin{aligned} \dot{E} &= \dot{\Psi} + \dot{s} \theta + s \dot{\theta} = \boldsymbol{\sigma} : \dot{\boldsymbol{\varepsilon}} - \nabla \cdot \mathbf{q} \\ \Leftrightarrow \underbrace{\frac{\partial \Psi}{\partial \boldsymbol{\varepsilon}}}_{(4.61) \boldsymbol{\sigma}} : \dot{\boldsymbol{\varepsilon}} + \underbrace{\frac{\partial \Psi}{\partial \boldsymbol{\lambda}}}_{(4.37) -\mathbf{P}} : \dot{\boldsymbol{\lambda}} + \underbrace{\frac{\partial \Psi}{\partial \theta}}_{(4.63) -s} \dot{\theta} + \dot{s} \theta + s \dot{\theta} &= \boldsymbol{\sigma} : \dot{\boldsymbol{\varepsilon}} - \nabla \cdot \mathbf{q} \\ \Leftrightarrow -\mathbf{P} : \dot{\boldsymbol{\lambda}} + \dot{s} \theta &= -\nabla \cdot \mathbf{q}. \end{aligned} \quad (4.72)$$

In Eq. (4.72) all quantities are already determined except the rate of entropy  $\dot{s}$ . Hence, the constitutive equation for entropy, Eq. (4.63), is used together with the ansatz for energy, Eqs. (4.68) and (4.69). This allows to calculate

$$s = -\frac{\partial \Psi}{\partial \theta} = 2c_\theta + c_\theta \log \left( \frac{\theta}{\theta_R} \right) + \sum_{j=1}^N \sum_{i=0}^n \xi^j \lambda_i^j b_i \quad (4.73)$$

and following

$$\dot{s} = c_\theta \frac{\dot{\theta}}{\theta} + \sum_{j=1}^N \sum_{i=0}^n \xi^j \dot{\lambda}_i^j b_i . \quad (4.74)$$

Inserting Eq. (4.74) into Eq. (4.72) yields

$$\begin{aligned} -\mathbf{P} : \dot{\boldsymbol{\lambda}} + c_\theta \dot{\theta} + \theta \sum_{j=1}^N \sum_{i=0}^n \xi^j \dot{\lambda}_i^j b_i &= -\nabla \cdot \mathbf{q} \\ \Leftrightarrow c_\theta \dot{\theta} &= \mathbf{P} : \dot{\boldsymbol{\lambda}} - \theta \sum_{j=1}^N \sum_{i=0}^n \xi^j \dot{\lambda}_i^j b_i - \nabla \cdot \mathbf{q} \\ \stackrel{(4.64)}{\Leftrightarrow} c_\theta \dot{\theta} &= \mathbf{P} : \dot{\boldsymbol{\lambda}} - \theta \sum_{j=1}^N \sum_{i=0}^n \xi^j \dot{\lambda}_i^j b_i - \nabla \cdot \left( \frac{1}{\alpha_\theta} \nabla \frac{1}{\theta} \right) . \end{aligned} \quad (4.75)$$

Finally, together with the approach for the entropy production in Eq. (4.70) the evolution equations can be derived from Eq. (4.65) which provides in combination with Eqs. (4.71) and (4.75) the entire set of governing equations as

$$\dot{\lambda}_i^j = \frac{\rho}{\xi^j} [\text{dev}_{\mathcal{A}^j} P_i^j]_{\mathcal{A}^j} \quad (4.76)$$

$$c_\theta \dot{\theta} = \mathbf{P} : \dot{\boldsymbol{\lambda}} - \theta \sum_{j=1}^N \sum_{i=0}^n \xi^j \dot{\lambda}_i^j b_i - \nabla \cdot \left( \frac{1}{\alpha_\theta} \nabla \frac{1}{\theta} \right) \quad (4.77)$$

with the KUHN-TUCKER conditions

$$\rho \geq 0 , \quad \Phi \leq 0 , \quad \rho \Phi = 0 \quad (4.78)$$

and the consistency condition

$$\text{dev}_{\mathcal{A}^j} P_i^j \leq 0 \quad , i \notin \mathcal{A}^j . \quad (4.79)$$

Eq. (4.77) is the heat conduction equation for this problem. It can be seen that it has quite a standard form – except that not the gradient of the temperature itself occurs but the gradient of the temperature's inverse. This different 'scaling' of the differences in temperature over space is accompanied with a negative sign compared to more regular heat conduction equations. However, without any assumptions for the coupling between phase transformations and heat production the coupling comes out automatically. This emphasizes the great advantage of the principle of maximum dissipation compared to the approach of defining a yield function. In that case, not only the yield function has to be assumed but also the terms for internal heat sources due to phase transformation. To find a stringent relation between both is a much more difficult task than just assuming the entropy production which has been carried out without any coupling.

The temperature is driven by the phase transformations while the evolution of the crystallographic phases is influenced by the temperature since the driving forces are now directly depending on the temperature through the chemical part in it.

The governing equations are implemented in a finite element scheme, Sec. 5.2, and numerical results are discussed in Sec. 6.3.

### 4.3 Phenomenological Modeling of Shape Memory Alloys

The derived models are not only compared to each other in Sec. 6 but furthermore the models' results are supposed to be evaluated in a broader framework. Therefore, a comparison to the phenomenological material model for shape memory alloys of Auricchio and Taylor, [2], is carried out. Since the results are obtained using the program ABAQUS, a very brief review of the model is given in its ABAQUS version [1].

In this model, there is no explicit distinction between the different martensitic variants nor grains. Rather there is a parameter for the volume fraction of austenite, indicated by  $\gamma_A$ , and for martensite it is  $\gamma_M$ . In order to maintain mass conservation,

$$\gamma_A + \gamma_M = 1 \quad (4.80)$$

has to hold. To distinguish between elastic behavior and phase transformation a yield function is introduced as

$$\tilde{\Phi} := \tilde{q} + \vartheta \operatorname{tr} \sigma \quad (4.81)$$

with

$$\tilde{q} := \sqrt{\sum_{i,j}^3 \sigma_{ij}^2}. \quad (4.82)$$

The parameter  $\vartheta$  is used to include tension-compression asymmetry. It is calculated according to

$$\vartheta := \frac{\sigma_c^{\text{AS}} - \sigma_t^{\text{AS}}}{\sigma_c^{\text{AS}} + \sigma_t^{\text{AS}}} \quad (4.83)$$

where  $\sigma_c^{\text{AS}}$  and  $\sigma_t^{\text{AS}}$  are the plateau stresses at the beginning of a pseudo-elastic phase transformation. The index 'c' is used for compression, 't' for tension. Both stresses have to be found from experimental data of an appropriate test.

The evolution law for the martensitic volume fraction is assumed to be

$$\dot{\gamma}_M := \begin{cases} -H^{\text{AS}}(1 - \gamma_M) \frac{\dot{\tilde{\Phi}}}{\tilde{\Phi} - R_f^{\text{AS}}} & \text{austenite to martensite} \\ H^{\text{SA}} \gamma_M \frac{\dot{\tilde{\Phi}}}{\tilde{\Phi} - R_f^{\text{SA}}} & \text{martensite to austenite} \end{cases} \quad (4.84)$$

where the factors  $R_f^{\text{AS}}$  and  $R_f^{\text{SA}}$  are found from

$$R_f^{\text{AS}} := \sigma_f^{\text{AS}}(1 + \vartheta) \quad \text{and} \quad R_f^{\text{SA}} := \sigma_f^{\text{SA}}(1 + \vartheta) \quad (4.85)$$

and analogously

$$R_s^{\text{AS}} := \sigma_s^{\text{AS}}(1 + \vartheta) \quad \text{and} \quad R_s^{\text{SA}} := \sigma_s^{\text{SA}}(1 + \vartheta). \quad (4.86)$$

The factors  $H^{\text{AS}}$  and  $H^{\text{SA}}$  take the values

$$H^{\text{AS}} = \begin{cases} 1 & \text{if } R_s^{\text{AS}} < \tilde{\Phi} < R_f^{\text{AS}} \wedge \dot{\tilde{\Phi}} > 0 \\ 0 & \text{else} \end{cases} \quad (4.87)$$

and

$$H^{\text{SA}} = \begin{cases} 1 & \text{if } R_f^{\text{SA}} < \tilde{\Phi} < R_s^{\text{SA}} \wedge \dot{\tilde{\Phi}} < 0 \\ 0 & \text{else} \end{cases}. \quad (4.88)$$

Finally the stress as well as the evolution of the transformation strains are formulated in an incremental way to

$$\dot{\boldsymbol{\sigma}} := \mathbb{C} : (\dot{\boldsymbol{\varepsilon}} - \dot{\boldsymbol{\varepsilon}}^{\text{tr}}) \quad (4.89)$$

and

$$\dot{\boldsymbol{\varepsilon}}^{\text{tr}} := \dot{\gamma}_{\text{M}} \varepsilon_{\text{L}} \frac{\partial \tilde{\Phi}}{\partial \boldsymbol{\sigma}}. \quad (4.90)$$

In Eq. (4.90),  $\varepsilon_{\text{L}}$  is the (scalar) maximum transformation strain observed in a tension test. Taking only the maximum transformation strain measured in a tension test, gives a hint that for a general loading case this assumption might not provide best results. However, for tension test simulations this model will be taken as a reference to compare the models presented in this work.



# Chapter 5

## The Finite Element Method

In this section the essential motivation and the working principles of the finite element method are laid down. More detailed derivations can be found - for instance - in [5], [63] or [61].

Generally spoken, the finite element method is nothing else but a mathematical tool for the numerical solution of partial differential equations (PDE) of certain classes. The equilibrium equation for solids as well as the heat conduction equation or the equations from electrodynamics belong to these classes. Although in mechanical and civil engineering the term 'finite elements' is directly linked in mind to the calculation of solids, the concept of finite elements goes much further. Since the material models derived in Secs. 4.2.2, 4.2.3 and 4.2.4 are supposed to be evaluated on the macroscopic space level, thus for entire specimens, the method of finite elements is introduced through linear elastic solids in this section. Furthermore, deductions are discussed and a general procedure for the application of finite elements is presented.

### 5.1 Fundamentals of the Finite Element Method

In Sec. 2.1.11 the potential of a material is introduced as sum of internal and external parts contributing to the potential. A minimization of the potential results in the equilibrium condition

$$\nabla \cdot \boldsymbol{\sigma} + \boldsymbol{f} = \mathbf{0} \quad (5.1)$$

From the mathematical point of view Eq. (5.1) is a system of PDEs. Since there exists by the HOOKE's law

$$\boldsymbol{\sigma} = \mathbb{C} : \boldsymbol{\varepsilon} \quad (5.2)$$

and the relation between strain and displacements

$$\boldsymbol{\varepsilon} = \frac{1}{2} (\nabla \boldsymbol{u} + \boldsymbol{u} \nabla) \quad (5.3)$$

a relation between stress and displacements as well, the system of PDEs in Eq. (5.1) has to be solved for the unknown (function)  $\boldsymbol{u}(\boldsymbol{x})$ . Of course, for every physical body displacements are known at some surfaces, for example through supports or other prescribed non-zero displacements termed  $\boldsymbol{u}^*$ . The boundary where the displacements are known is indicated as  $\partial\Omega_{\boldsymbol{u}}$ . Consequently,

$$\boldsymbol{u} \stackrel{!}{=} \boldsymbol{u}^* \quad \text{on } \partial\Omega_{\boldsymbol{u}} . \quad (5.4)$$

Additionally, the condition

$$\boldsymbol{\sigma} \cdot \mathbf{n} \stackrel{!}{=} \mathbf{t}^* \quad (5.5)$$

has to be fulfilled, see Eq. (2.43). Therefore, Eq. (5.1) with Eqs. (5.4) and (5.5) constitute as a boundary value problem. For an arbitrary body in three dimensions it is not possible to find the solution for the problem analytically, consequently a numerical approach has to be followed. This can be carried out by going back to minimizing the potential which gives due to the symmetry of  $\boldsymbol{\sigma}$ , Eq. (2.94),

$$\int_{\Omega} \boldsymbol{\sigma} : \nabla \delta \mathbf{u} \, dV = \int_{\Omega} \mathbf{f} \cdot \delta \mathbf{u} \, dV + \int_{\partial\Omega} \mathbf{t} \cdot \delta \mathbf{u} \, dA \quad \forall \delta \mathbf{u} . \quad (5.6)$$

The comparison between Eqs. (5.1) and (5.6) shows that two properties differ: first, in Eq. (5.6) a formulation in *integral* form is given. This allows all functions to be defined just piecewise which is a great advantage from the point of solving the equations. Secondly, only  $\boldsymbol{\sigma}$  occurs in Eq. (5.6) in contrast to its divergence  $\nabla \cdot \boldsymbol{\sigma}$  in Eq. (5.1). This implies that the order of the PDE system has been reduced from second to first, thus only first derivatives of  $\mathbf{u}$  occur. Hence, since both equations are equivalent a focus on Eq. (5.6) is of huge advantage.

As it has already been mentioned, an analytical solution of Eq. (5.6) is in general not possible to find. Therefore, an approximation of the solution is the aim left. Due to the integral form of the problem a piecewise or *elementwise* approximation is applicable. This allows to formulate

$$\mathbf{u}(\mathbf{x}) \approx \mathbf{N}_u(\mathbf{x}) \cdot \hat{\mathbf{u}} = \mathbf{N}_u \cdot \hat{\mathbf{u}} \quad (5.7)$$

and similarly

$$\delta \mathbf{u}(\mathbf{x}) \approx \mathbf{N}_u(\mathbf{x}) \cdot \delta \hat{\mathbf{u}} = \mathbf{N}_u \cdot \delta \hat{\mathbf{u}} \quad (5.8)$$

with so-called *shape functions*  $\mathbf{N}_u$  and *nodal values*  $\hat{\mathbf{u}}$  and  $\delta \hat{\mathbf{u}}$ , respectively. By this, the entire body of volume  $\Omega$  has been divided into a certain number of sub-volumes, indicated by  $z$ , which are called *elements*, see Fig. 5.1. The elements are defined through their surfaces which themselves have so-called *nodes* as construction parts. Then, the differential equations are to be solved exactly only at the nodes. The purpose of the shape functions is an interpolation between the nodal values in order to find an approximation for  $\mathbf{u}(\mathbf{x})$  and  $\delta \mathbf{u}(\mathbf{x})$ . Thus, for given nodal values the functions can be constructed under the limitation the shape functions imply: depending on the class of function the shape functions are chosen from, the approximation will have different accuracy. However, if the shape functions are chosen the gradient of the solution function can be found according to

$$\nabla \mathbf{u} = \nabla \mathbf{N}_u \cdot \hat{\mathbf{u}} \quad (5.9)$$

from which immediately with Eq. (5.8)

$$\nabla \delta \mathbf{u} = \nabla \mathbf{N}_u \cdot \delta \hat{\mathbf{u}} \quad (5.10)$$

follows.

For further simplification MEHRABADI-COWIN introduced in [37] a special notation for strain, stress and the elastic modulus  $\mathbb{C}$  outgoing from the VOIGT notation. The key idea is a shift from the three dimensional space in which the variables are originally defined to a six dimensional space. Due to the symmetry properties of the variables it is possible to

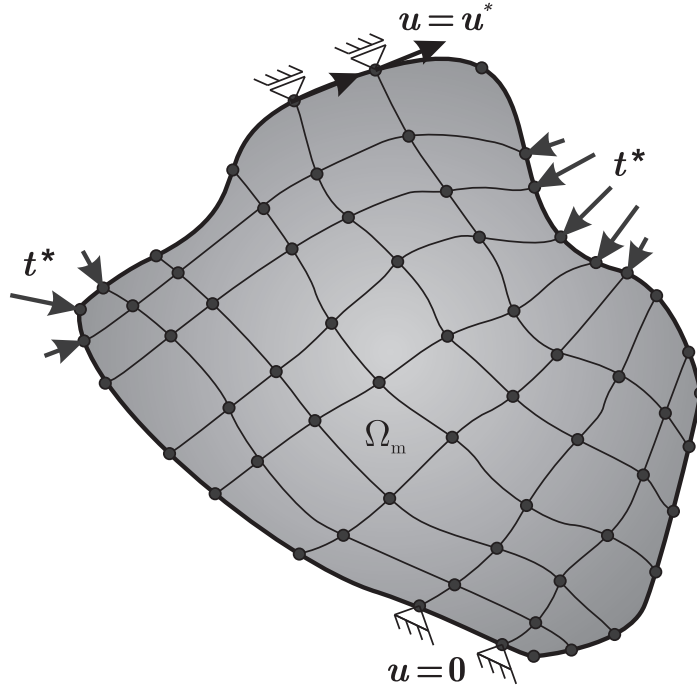


Figure 5.1: Discretized body. Volume of a single element,  $\Omega_m$ , prescribed zero and non-zero displacements  $u^*$  and nodal forces  $t^*$ .

neglect multiple 'transportation', for instance  $\sigma^T = \sigma$ . In order to maintain Eigenvalue characteristics the HOOKE's law can be expressed as

$$\begin{pmatrix} \sigma_{11} \\ \sigma_{22} \\ \sigma_{33} \\ \sqrt{2} \sigma_{23} \\ \sqrt{2} \sigma_{13} \\ \sqrt{2} \sigma_{12} \end{pmatrix} = \begin{pmatrix} C_{11} & C_{12} & C_{13} & \sqrt{2} C_{14} & \sqrt{2} C_{15} & \sqrt{2} C_{16} \\ C_{21} & C_{22} & C_{23} & \sqrt{2} C_{24} & \sqrt{2} C_{25} & \sqrt{2} C_{26} \\ C_{31} & C_{32} & C_{33} & \sqrt{2} C_{34} & \sqrt{2} C_{35} & \sqrt{2} C_{36} \\ \sqrt{2} C_{41} & \sqrt{2} C_{42} & \sqrt{2} C_{43} & 2 C_{44} & 2 C_{45} & 2 C_{46} \\ \sqrt{2} C_{51} & \sqrt{2} C_{52} & \sqrt{2} C_{53} & 2 C_{54} & 2 C_{55} & 2 C_{56} \\ \sqrt{2} C_{61} & \sqrt{2} C_{62} & \sqrt{2} C_{63} & 2 C_{64} & 2 C_{65} & 2 C_{66} \end{pmatrix} \cdot \begin{pmatrix} \varepsilon_{11} \\ \varepsilon_{22} \\ \varepsilon_{33} \\ \sqrt{2} \varepsilon_{23} \\ \sqrt{2} \varepsilon_{13} \\ \sqrt{2} \varepsilon_{12} \end{pmatrix} \quad (5.11)$$

where the matrix valued quantities stress and strain have been transformed to vectors and the elasticity tensor of fourth order to a matrix (elastic constants  $C_{ij}$  are from the VOIGT notation). Furthermore, the inner product reduces from a double scalar product to a regular single dot scalar product. Quantities denoted in the MEHRABADI-COWIN notation are from now on indicated by a tilde, thus  $\sigma \rightarrow \tilde{\sigma}$ ,  $\varepsilon \rightarrow \tilde{\varepsilon}$  and  $\mathbb{C} \rightarrow \tilde{\mathbb{C}}$ .

The modification of notation allows furthermore the introduction of an operator matrix denoted as  $\tilde{B}$  which allows a linear mapping between strains and displacements. The operator matrix is defined in the three dimensional space according to

$$\tilde{B} := \begin{bmatrix} \frac{\partial}{\partial x} & 0 & 0 \\ 0 & \frac{\partial}{\partial y} & 0 \\ 0 & 0 & \frac{\partial}{\partial z} \\ 0 & \frac{1}{2} \frac{\partial}{\partial z} & \frac{1}{2} \frac{\partial}{\partial y} \\ \frac{1}{2} \frac{\partial}{\partial z} & 0 & \frac{1}{2} \frac{\partial}{\partial x} \\ \frac{1}{2} \frac{\partial}{\partial y} & \frac{1}{2} \frac{\partial}{\partial x} & 0 \end{bmatrix} \quad (5.12)$$



from which results

$$\begin{aligned}\tilde{\boldsymbol{\varepsilon}} &= \tilde{\mathbf{B}} \cdot \mathbf{u} \\ \Leftrightarrow \quad \tilde{\boldsymbol{\varepsilon}} &= \tilde{\mathbf{B}} \cdot \mathbf{N}_u \cdot \hat{\mathbf{u}}.\end{aligned}\quad (5.13)$$

The product between operator matrix and shape function in Eq. (5.13) is synthesized to  $\mathbf{B}$ , so

$$\mathbf{B} := \tilde{\mathbf{B}} \cdot \mathbf{N}_u. \quad (5.14)$$

Application of the MEHRABADI-COWIN notation to Eq. (5.6) gives then

$$\int_{\Omega} \mathbf{B}^T \cdot \tilde{\boldsymbol{\sigma}} \, dV - \int_{\Omega} \mathbf{N}_u \cdot \mathbf{f} \, dV - \int_{\partial\Omega} \mathbf{N}_u \cdot \mathbf{t} \, dA = \mathbf{0} \quad (5.15)$$

where the (constant) variation of the displacements,  $\delta\mathbf{u}$ , can be taken out of the integral and canceled out.

Eq. (5.15) is supposed to be solved with respect to the unknown displacements from which the stress depends on through

$$\begin{aligned}\tilde{\boldsymbol{\sigma}} &= \tilde{\mathbb{C}} \cdot \tilde{\boldsymbol{\varepsilon}} \\ \Leftrightarrow \quad \tilde{\boldsymbol{\sigma}} &= \tilde{\mathbb{C}} \cdot \mathbf{B} \cdot \hat{\mathbf{u}}.\end{aligned}\quad (5.16)$$

Hence, Eq. (5.15) can be brought into its final form

$$\begin{aligned}\sum_m^z \int_{\Omega_m} \mathbf{B}^T \cdot \tilde{\boldsymbol{\sigma}} \, dV &= \sum_m^z \int_{\Omega_m} \mathbf{N}_u \cdot \mathbf{f} \, dV + \sum_m^z \int_{\partial\Omega_m} \mathbf{N}_u \cdot \mathbf{t} \, dA \\ \Leftrightarrow \quad \sum_m^z \underbrace{\int_{\Omega_m} \mathbf{B}^T \cdot \tilde{\mathbb{C}} \cdot \mathbf{B} \, dV}_{=: \mathbf{K}_m} \cdot \hat{\mathbf{u}} &= \sum_m^z \underbrace{\int_{\Omega_m} \mathbf{N}_u \cdot \mathbf{f} \, dV}_{=: \mathbf{f}_{f\,m}} + \sum_m^z \underbrace{\int_{\partial\Omega_m} \mathbf{N}_u \cdot \mathbf{t} \, dA}_{=: \mathbf{f}_{t\,m}} \\ \Leftrightarrow \quad \mathbf{K} \cdot \hat{\mathbf{u}} &= \mathbf{f}_f + \mathbf{f}_t\end{aligned}\quad (5.17)$$

with the so-called (assembled) stiffness matrix  $\mathbf{K}$  and the (assembled) internal and external forces  $\mathbf{f}_f$  and  $\mathbf{f}_t$ , respectively.  $\Omega_m$  is the volume of every element  $m$  and  $\partial\Omega_m$  its surface. The only remaining unknowns in Eq. (5.17) are the displacements at the nodes. Thus, the PDE system of Eq. (5.1) of second order could be transformed to a system of algebraic equations which is obviously much easier to solve. For elastic materials this system of equations is indeed a linear one which reduces the problem to the calculation of the inverse of  $\mathbf{K}$ .

It remains to calculate the integrals in (5.17) until a solution for  $\mathbf{u}$  can be found. In a general application of the finite element method on a specific boundary value problem, the integration has to be performed in a numerical way due to time expenses. For this the common GAUSS integration can be used. This is based on

$$\int_a^b g(x) \, dx \approx \sum_i w_i g(x_i) \quad (5.18)$$

where the specific integral of a polynomial  $g(x)$  can be approximated best by the sum of the function, evaluated at certain so-called *integration* or GAUSS *points*  $x_i$ , multiplied with some weighting factors  $w_i$ . The GAUSS points are the zero points of the corresponding LEGENDRE polynomial, depending on  $g(x)$ 's order, and the weighting factors can be found from a coefficient comparison of the integral of the LAGRANGE polynomial. Thus, if the

order of  $g(x)$  is fixed, the GAUSS points as well as the weighting factors are constant. Furthermore, the discretization of the body's volume is carried out by elements of different shape. Thus, it is convenient to introduce a special space where each element can be described by means of a so-called *isoparametric element*. The isoparametric element serves as template both defining the shape functions and finding the integrals. Figure 5.2 shows the isoparametric element for the three dimensional case. In the three dimensional case the

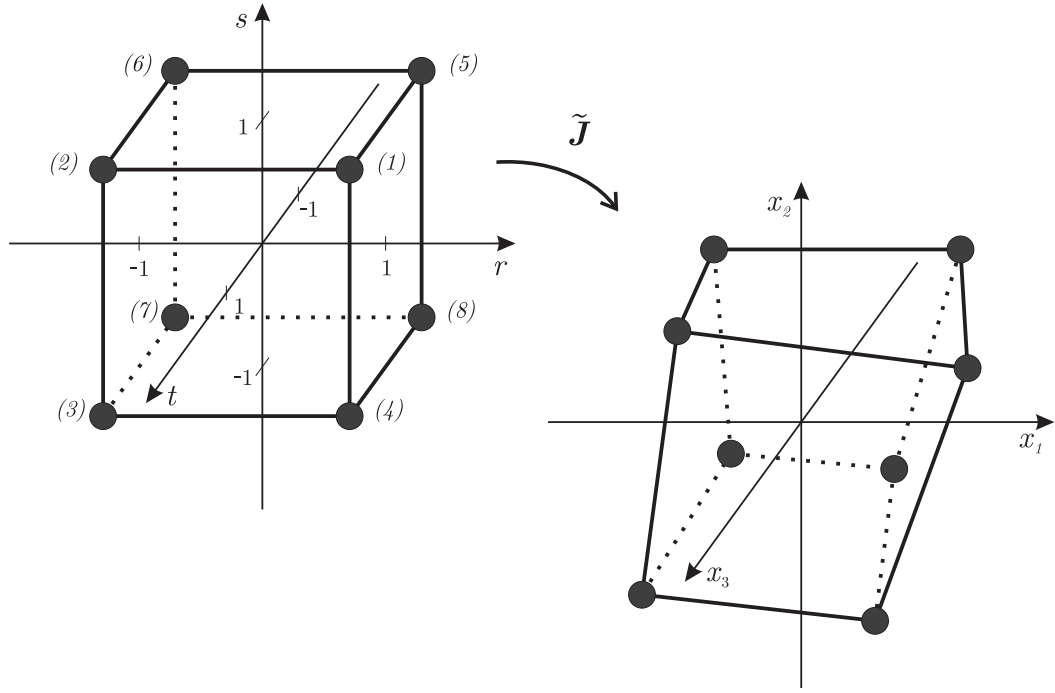


Figure 5.2: Isoparametric element with length 2 in each direction and nodes (1) to (8). JACOBIAN  $\tilde{\mathbf{J}}$  maps on the element in the physical space.

tri-linear shape functions (eight nodes) can be found as

$$\begin{aligned}
 N^1(r, s, t) &= \frac{1}{8} (r + 1) (s + 1) (t + 1) \\
 N^2(r, s, t) &= \frac{1}{8} (r - 1) (s + 1) (t + 1) \\
 N^3(r, s, t) &= \frac{1}{8} (r - 1) (s - 1) (t + 1) \\
 N^4(r, s, t) &= \frac{1}{8} (r + 1) (s - 1) (t + 1) \\
 N^5(r, s, t) &= \frac{1}{8} (r + 1) (s + 1) (t - 1) \\
 N^6(r, s, t) &= \frac{1}{8} (r - 1) (s + 1) (t - 1) \\
 N^7(r, s, t) &= \frac{1}{8} (r - 1) (s - 1) (t - 1) \\
 N^8(r, s, t) &= \frac{1}{8} (r + 1) (s - 1) (t - 1)
 \end{aligned} \tag{5.19}$$

with the GAUSS points

$$\tilde{\mathbf{x}}^i \in \left\{ \begin{pmatrix} \pm \frac{1}{\sqrt{3}} \\ \pm \frac{1}{\sqrt{3}} \\ \pm \frac{1}{\sqrt{3}} \end{pmatrix} \right\} \quad i \in \{1, \dots, 8\} \quad (5.20)$$

The shape functions are defined in the space of the isoparametric element. In contrast, for the calculation of the operator matrix  $\mathbf{B}$ , Eq. (5.14), it is necessary to find the derivatives of the shape functions with respect to the spacial coordinates  $\mathbf{x} = \{x_1, x_2, x_3\}$  instead of  $\tilde{\mathbf{x}} = \{r, s, t\}$ . By use of the chain rule the demanded coordinate transformation can be executed, so

$$\begin{bmatrix} \frac{\partial}{\partial r} \\ \frac{\partial}{\partial s} \\ \frac{\partial}{\partial t} \end{bmatrix} = \underbrace{\begin{bmatrix} \frac{\partial x_1}{\partial r} & \frac{\partial x_2}{\partial r} & \frac{\partial x_3}{\partial r} \\ \frac{\partial x_1}{\partial s} & \frac{\partial x_2}{\partial s} & \frac{\partial x_3}{\partial s} \\ \frac{\partial x_1}{\partial t} & \frac{\partial x_2}{\partial t} & \frac{\partial x_3}{\partial t} \end{bmatrix}}_{=: \tilde{\mathbf{J}}} \cdot \begin{bmatrix} \frac{\partial}{\partial x_1} \\ \frac{\partial}{\partial x_2} \\ \frac{\partial}{\partial x_3} \end{bmatrix} \quad (5.21)$$

where  $\tilde{\mathbf{J}}$  is called JACOBIAN. Then, the derivatives with respect to the coordinates  $\mathbf{x}$  can be found according to

$$\frac{\partial}{\partial \mathbf{x}} = \tilde{\mathbf{J}}^{-1} \cdot \frac{\partial}{\partial \tilde{\mathbf{x}}} \quad (5.22)$$

from which  $\mathbf{B}$  can be constructed. The entries of the JACOBIAN can be calculated by means of the shape functions and the coordinates of the nodes  $i$  which are denoted by  $\hat{\mathbf{x}}^i$ . This yields

$$\tilde{\mathbf{J}} = \begin{bmatrix} \frac{\partial N^1}{\partial r} & \dots & \frac{\partial N^8}{\partial r} \\ \frac{\partial N^1}{\partial s} & \dots & \frac{\partial N^8}{\partial s} \\ \frac{\partial N^1}{\partial t} & \dots & \frac{\partial N^8}{\partial t} \end{bmatrix} \cdot \begin{bmatrix} \hat{x}_1^1 & \hat{x}_2^1 & \hat{x}_3^1 \\ \vdots & \vdots & \vdots \\ \hat{x}_1^8 & \hat{x}_2^8 & \hat{x}_3^8 \end{bmatrix}. \quad (5.23)$$

Furthermore, the integration over the material body has to be transformed. The determinant of the JACOBIAN serves per its definition as measure for the coordination transformation  $\tilde{\mathbf{x}} \mapsto \mathbf{x}$  for the integrals. Thus,

$$\int_{\Omega} g(\tilde{\mathbf{x}}) \underbrace{dx_1 dx_2 dx_3}_{=dV} \approx \det \tilde{\mathbf{J}} \sum_i w_i g(\tilde{\mathbf{x}}^i) \quad (5.24)$$

with  $\tilde{\mathbf{x}}^i$  again as GAUSS points.

With these tools at hands the equilibrium conditions for solid materials can be solved. However, the scheme of finite elements can be applied to many partial differential equations (a counter-example are equations where jumps occur and hence non-smooth functions have to be found as solution - in this case an extended finite element method can be used). A general framework to convert a differential equation into a finite element based formulation is to multiply both sides with a so-called *testing function* which is denoted as  $\delta \mathbf{u}$ , if the equation

is expressed in terms of  $\mathbf{u}$ , and called *variation*. This is done since the equation itself can be interpreted as extremal condition for an associated variational problem in which the variation would have come out as result of an 'inner derivation'. Then, the original differential equation is called EULER equation which is always a result of minimizing or maximizing a corresponding functional. The generality of the equation multiplied with its variation is still maintained when the equation is integrated over the space the function is defined in. After that, an integration by parts is applied with the motivation to reduce the order of the differential equation by shifting this order of derivative from the original function to its variation. When the minimum order of derivative is reached, the integration by parts is stopped. Then, the function as well as its variation and all derivatives are approximated by means of shape functions where the entire space is divided in a certain number of  $z$  elements. The remaining integrals can be solved and leave an algebraic system of equations for the nodal values of the function. Concluding,

$$\begin{aligned}
& \mathbf{g}(\mathbf{u}) = \mathbf{0} \\
\Leftrightarrow & \mathbf{g}(\mathbf{u}) \delta \mathbf{u} = \mathbf{0} \quad \forall \delta \mathbf{u} \\
\Leftrightarrow & \int_{\Omega} \mathbf{g}(\mathbf{u}) \delta \mathbf{u} \, dV = \mathbf{0} \quad \forall \delta \mathbf{u} \\
\stackrel{\text{i.B.}}{\Leftrightarrow} & \int_{\Omega} \mathbf{g}_{\Omega}^f(\mathbf{u}) \delta \mathbf{u}' \, dV + \int_{\partial\Omega} \mathbf{g}_{\partial\Omega}^f(\mathbf{u}) \delta \mathbf{u} \, dA = \mathbf{0} \quad \forall \delta \mathbf{u} \\
\Leftrightarrow & \sum_z \int_{\Omega^z} \mathbf{g}_{\Omega}^f(\mathbf{u}) \delta \mathbf{u}' \, dV + \sum_z \int_{\partial\Omega^z} \mathbf{g}_{\partial\Omega}^f(\mathbf{u}) \delta \mathbf{u} \, dA = \mathbf{0} \quad \forall \delta \mathbf{u} \\
\Rightarrow & \mathbf{K} \cdot \hat{\mathbf{u}} + \mathbf{f} = \mathbf{0} \tag{5.25}
\end{aligned}$$

Trivially,  $\delta \mathbf{u} \neq \mathbf{0}$  has to hold. In Eq. (5.25),  $\mathbf{g}(\mathbf{u})$  synthesizes the entire specific differential equation whereas  $\mathbf{g}_{\Omega}^f(\mathbf{u})$  and  $\mathbf{g}_{\partial\Omega}^f(\mathbf{u})$  indicate the parts of  $\mathbf{g}(\mathbf{u})$  integrated over the volume,  $dV$ , or an area,  $dA$ , respectively. Of course, space and area are not necessarily their physical compliances. It indicates solely that  $dA$  has a reduced number of integrands compared to  $dV$ . The index  $\delta \mathbf{u}'$  refers to a corresponding derivative of  $\delta \mathbf{u}$  which is accompanied by the associated part of  $\mathbf{g}_{\Omega}(\mathbf{u})$  with reduced order of derivatives, termed  $\mathbf{g}_{\Omega}^f(\mathbf{u})$ , due to integration by parts.

Since the functions  $\mathbf{u}$  are approximated by means of shape functions and for which the values at the nodal points are the only unknowns, the derivatives  $\delta \mathbf{u}'$  can be calculated - except for the interpolation values, of course.

## 5.2 The Finite Element Method for non-linear Materials

In Sec. 5.1 the fundamentals for linear elastic materials have been recalled. However the strategy is quite similar when dealing with non-linear materials, in this section an introduction to the application of the finite element method to non-linear materials is given. It is emphasized that 'non-linear' means in this context a non-linear relation between stress and strain, thus non-linear constitutive equations for example in the form

$$\boldsymbol{\sigma} = \mathbb{C}(\boldsymbol{\varepsilon}) : \boldsymbol{\varepsilon} . \tag{5.26}$$

Non-linearity due to a non-linear relation between displacements and strains, following Eq. (2.35) for instance, is not treated in this work and so it is not considered in this section.

The example of the application of the finite element method to linear elastic materials is based on minimizing a potential of the form

$$\Pi = \int_{\Omega} \Psi \, dV - \int_{\Omega} \mathbf{f} \cdot \mathbf{u} \, dV - \int_{\partial\Omega} \mathbf{t} \cdot \mathbf{u} \, dA \rightarrow \min_{\mathbf{u}} . \quad (5.27)$$

In Eq. (5.27) no assumptions for the material have been made. The only assumption is the most general that this potential tends to a minimum for every physical material. The dependence on the specific material comes into play when the free energy  $\Psi$  has to be defined which can obviously only be a material dependent procedure. That means, plugging the 'correct' energy into Eq. (5.27) allows to solve the equilibrium equations for every arbitrary material.

In general the minimizing condition of Eq. (5.27) reads

$$\int_{\Omega} \frac{\partial \Psi}{\partial \boldsymbol{\varepsilon}} : \delta \boldsymbol{\varepsilon} \, dV - \int_{\Omega} \mathbf{f} \cdot \delta \mathbf{u} \, dV - \int_{\partial\Omega} \mathbf{t} \cdot \delta \mathbf{u} \, dA \stackrel{!}{=} 0 \quad (5.28)$$

for which the previously presented discretization method by means of shape functions and operator matrix  $\mathbf{B}$  can be applied. Furthermore, the constitutive equation for stress, as Eq. (2.70),

$$\boldsymbol{\sigma} = \frac{\partial \Psi}{\partial \boldsymbol{\varepsilon}} \quad (5.29)$$

has to hold even for non-linear materials. This yields as well as for the linear case

$$\mathbf{R}_u := \int_{\Omega} \mathbf{B}^T \cdot \tilde{\boldsymbol{\sigma}} \, dV - \int_{\Omega} \mathbf{N}_u \cdot \mathbf{f} \, dV - \int_{\partial\Omega} \mathbf{N}_u \cdot \mathbf{t} \, dA \stackrel{!}{=} \mathbf{0} . \quad (5.30)$$

$\mathbf{R}_u$  is called *residual* since its norm serves as criteria to stop an iterative solution process. In contrast to the linear case, now a direct separation of  $\boldsymbol{\sigma}$  in the (constant) elasticity tensor and operator matrix times displacements is not possible due to the non-linear relation of Eq. (5.26). This yields a non-linear algebraic system of equations for the displacements. Thus, the well known NEWTON scheme can be applied to seek for the zero point of  $\mathbf{R}_u$  in an iterative way. Therefore

$$\mathbf{R}_u^{i+1} = \mathbf{R}_u^i + \frac{\partial \mathbf{R}_u^i}{\partial \mathbf{u}} \cdot \Delta \mathbf{u}^{i+1} \stackrel{!}{=} \mathbf{0} \quad (5.31)$$

with  $i$  as iteration number. From Eq. (5.31) the displacement increment  $\Delta \mathbf{u}^{i+1}$  can be found according to

$$\Delta \mathbf{u}^{i+1} = - \left[ \frac{\partial \mathbf{R}_u^i}{\partial \mathbf{u}} \right]^{-1} \cdot \mathbf{R}_u^i . \quad (5.32)$$

Then, the displacements are updated as

$$\mathbf{u}^{i+1} = \mathbf{u}^i + \Delta \mathbf{u}^{i+1} . \quad (5.33)$$

Of course, this iterative scheme can be applied to the linear case as well, where the so-called tangent matrix can be calculated analytically to

$$\frac{\partial \mathbf{R}_u^i}{\partial \mathbf{u}} = \int_{\Omega} \mathbf{B}^T \cdot \tilde{\mathbb{C}} \cdot \mathbf{B} \, dV \quad (5.34)$$

since

$$\tilde{\boldsymbol{\varepsilon}} = \mathbf{B} \cdot \mathbf{u} \quad (5.35)$$

holds, Eq. (5.13). Hence, in the linear elastic case the derivative of the residual equals the stiffness matrix  $\mathbf{K}$  as introduced in Eq. (5.17).

### 5.2.1 Implementation of the basic Model

As pointed out in Sec. 5.2, the application of the finite element method is carried out in order to solve the EULER equations, resulting from the minimization of the functional  $\Pi$ . The functional is the so-called total potential of the body and based on fundamental physical axioms. Consequently, this scheme is valid for all mechanical bodies. The only aspect which has to be adopted is the elastic energy  $\Psi$  which is - of course - material dependent. For purely linear elastically behaving material this scheme has been used in Sec. 5.2.

Now, this method is applied to the basic model for shape memory alloys derived in Sec. 4.2.2. The corresponding energy is the relaxed energy  $\Psi^{\text{rel}}$ . Using this energy in the potential yields

$$\Pi_{\text{basic}} = \int_{\Omega} \Psi^{\text{rel}} dV - \int_{\Omega} \mathbf{f} \cdot \mathbf{u} dV - \int_{\partial\Omega} \mathbf{t} \cdot \mathbf{u} dA \rightarrow \min_{\mathbf{u}} \quad (5.36)$$

which - again - is supposed to be minimized with respect to the unknown displacement field  $\mathbf{u}$  for fixed time. The minimization condition of Eq. (5.36) constitutes as variational equation and reads

$$\delta \Pi_{\text{basic}} = \int_{\Omega} \frac{\partial \Psi^{\text{rel}}}{\partial \boldsymbol{\varepsilon}} : \delta \boldsymbol{\varepsilon} dV - \int_{\Omega} \mathbf{f} \cdot \delta \mathbf{u} dV - \int_{\partial\Omega} \mathbf{t} \cdot \delta \mathbf{u} dA \stackrel{!}{=} 0. \quad (5.37)$$

According to the relaxed energy  $\Psi^{\text{rel}}$ , Eq. (4.7), its derivative with respect to the strains can be calculated to ( $\boldsymbol{\lambda}$  is fixed)

$$\frac{\partial \Psi^{\text{rel}}}{\partial \boldsymbol{\varepsilon}} \stackrel{(2.70)}{=} \boldsymbol{\sigma} = \mathbb{C}_{\text{eff}} : (\boldsymbol{\varepsilon} - \boldsymbol{\eta}_{\text{eff}}). \quad (5.38)$$

This allows to apply the scheme of finite elements to Eq. (5.37). The residual which has to become zero is then

$$\mathbf{R}_{\mathbf{u}} = \int_{\Omega} \mathbf{B}^T \cdot \tilde{\boldsymbol{\sigma}} dV - \int_{\Omega} \mathbf{N}_{\mathbf{u}} \cdot \mathbf{f} dV - \int_{\partial\Omega} \mathbf{N}_{\mathbf{u}} \cdot \mathbf{t} dA \stackrel{!}{=} 0 \quad (5.39)$$

with  $\tilde{\boldsymbol{\sigma}}$  the stress from Eq. (5.38) in the notation of MEHRABADI-COWIN. Due to the non-linearity of  $\mathbf{R}_{\mathbf{u}}$  the iterative solution scheme presented in Sec. 5.2 is used. Thus, the derivative of  $\mathbf{R}_{\mathbf{u}}$  has to be found which gives

$$\frac{\partial \mathbf{R}_{\mathbf{u}}}{\partial \mathbf{u}} = \int_{\Omega} \mathbf{B}^T \cdot \frac{\partial \tilde{\boldsymbol{\sigma}}}{\partial \tilde{\boldsymbol{\varepsilon}}} \cdot \mathbf{B} dV. \quad (5.40)$$

Obviously, for the evaluation of the integrals in Eqs. (5.39) and (5.40) the stress as well as its derivative with respect to strains have to be found. Although the stress can be calculated analytically if the internal variables, the volume fractions  $\boldsymbol{\lambda}$ , are known, its derivative can only be found numerically when having a reasonable computation time in mind. Since the integrals are computed numerically using the GAUSS quadrature, both the stresses and their derivative have to be evaluated for every integration or GAUSS point. Thus, from the current approximative solution of the displacement field,  $\mathbf{u}^{i+1}$ , the strains at each GAUSS point can be derived. These serve as input parameter for the basic model derived in Sec. 4.2.2. Depending on the results of the previous time (and thus load) step,  $\boldsymbol{\lambda}^n$  and  $\mathcal{A}^n$ , the volume fractions and the active set are updated.  $(\cdot)^n$  counts the time step. Then, the evolution equations can be discretized as presented in Sec. 3.2 as

$$\boldsymbol{\lambda}^{n+1} = \boldsymbol{\lambda}^n + \tilde{\rho} \dot{\boldsymbol{\lambda}} \quad (5.41)$$

with the KUHN-TUCKER conditions

$$\tilde{\rho} \geq 0 \quad \Phi \leq 0 \quad \tilde{\rho} \Phi = 0 . \quad (5.42)$$

The active set is updated according to Eq. (4.42).

With the updated internal quantities the norm of the residual in Eq. (5.39) is tested whether it gives approximately zero. If the residual is sufficiently small the updated volume fractions as well as the active set is taken as input for the next time step. Another convergence criteria is the so-called *energy norm* instead of the simple norm of  $\mathbf{R}_u$ . The energy norm is defined as  $\mathbf{R}_u^{i+1} \cdot \mathbf{u}^{i+1}$ . Thus,

$$\mathbf{R}_u^{i+1} \cdot \mathbf{u}^{i+1} \leq \text{tol} : \quad \boldsymbol{\lambda}^{i+1} \rightarrow \boldsymbol{\lambda}^{n+1} , \quad \mathcal{A}^{i+1} \rightarrow \mathcal{A}^{n+1} , \quad (5.43)$$

where tol is a numerical tolerance. Hence, in order to solve the governing equations for entire specimens in a finite element algorithm two NEWTON schemes have to be executed: one on the material (or equivalently GAUSS ) point level and one for the non-linear algebraic system of equations resulting from the approximation of the equilibrium condition which yields the unknown displacements at the nodes.

## 5.2.2 Implementation of the extended Model

Although the changes for the material model in the extended version are relatively small, the treatment of its finite element implementation is a remarkably higher effort. This influences the calculation time in a negative way. As pointed out in Secs. 2.1.11 and 5.2, for the finite element implementation of different materials only their corresponding free energies have to be put into the total potential. This yields in the case of the extended model

$$\Pi_{\text{ext}} = \int_{\Omega} \Psi^{\text{tot}} dV - \int_{\Omega} \mathbf{f} \cdot \mathbf{u} dV - \int_{\partial\Omega} \mathbf{t} \cdot \mathbf{u} dA \rightarrow \min_{\mathbf{u}, \varphi} . \quad (5.44)$$

In contrast to the basic model, now the total potential is a functional of two functions: similarly it depends on the displacement field  $\mathbf{u}$  but furthermore on the field function  $\varphi$ , too. Thus, the variation of  $\Pi_{\text{ext}}$  gives

$$\delta \Pi_{\text{ext}} = \int_{\Omega} \left( \frac{\partial \Psi^{\text{tot}}}{\partial \boldsymbol{\varepsilon}} : \delta \boldsymbol{\varepsilon} + \frac{\partial \Psi^{\text{tot}}}{\partial \varphi} \delta \varphi \right) dV - \int_{\Omega} \mathbf{f} \cdot \delta \mathbf{u} dV - \int_{\partial\Omega} \mathbf{t} \cdot \delta \mathbf{u} dA \stackrel{!}{=} 0 . \quad (5.45)$$

In the variation of  $\Pi_{\text{ext}}$  parts occur which depend on the variation of the displacements (or their derivative which is strain). Additionally, parts depending on the variation of  $\varphi$ ,  $\delta \varphi$ , come into play. Since the field functions  $\mathbf{u}$  and  $\varphi$  may be treated independently at first glance, a separation of Eq. (5.45) into two individual equations is possible. This yields

$$\int_{\Omega} \boldsymbol{\sigma} : \nabla \delta \mathbf{u} dV - \int_{\Omega} \mathbf{f} \cdot \delta \mathbf{u} dV - \int_{\partial\Omega} \mathbf{t} \cdot \delta \mathbf{u} dA \stackrel{!}{=} 0 \quad \forall \delta \mathbf{u} \quad (5.46)$$

$$\int_{\Omega} \beta_{\varphi} (\varphi + 1 - |\boldsymbol{\lambda}_0|) \delta \varphi dV + \int_{\Omega} c_{\varphi} (\nabla \varphi \cdot \nabla \delta \varphi) dV \stackrel{!}{=} 0 \quad \forall \delta \varphi \quad (5.47)$$

where the derivatives of  $\Psi^{\text{rel}}$  with respect to strain and field function have been directly plugged in.

For the Eqs. (5.46) and (5.47) the finite element approximations are applied. In the case of the displacements, Eq. (5.46), the results are the same as for the basic model. It remains to approximate the equation for the field function. In order to do so, the field function and its variation are replaced by

$$\varphi = \mathbf{N}_{\varphi} \cdot \hat{\varphi} , \quad \delta \varphi = \mathbf{N}_{\varphi} \cdot \delta \hat{\varphi} . \quad (5.48)$$

The gradient of  $\varphi$  as well as the gradient of the variation are approximated by

$$\nabla \varphi = \nabla \mathbf{N}_\varphi \cdot \hat{\boldsymbol{\varphi}}, \quad \nabla \delta \varphi = \nabla \mathbf{N}_\varphi \cdot \delta \hat{\boldsymbol{\varphi}}. \quad (5.49)$$

Of course, similarly to the displacements the exact values of the field functions are approximated by an interpolation of values known at the nodes. These nodal values are, again, collected in a vectorial quantity  $\hat{\boldsymbol{\varphi}}$ . The interpolating functions are shape functions which may be chosen differently from those for the displacements in general. They are denoted by  $\mathbf{N}_\varphi$ .

Now, for the two variational equation, Eqs. (5.46) and (5.47), the finite element formulation is

$$\mathbf{R}_u = \int_{\Omega} \mathbf{B}^T \cdot \boldsymbol{\sigma} \, dV - \int_{\Omega} \mathbf{N}_u \cdot \mathbf{f} \, dV - \int_{\partial\Omega} \mathbf{N}_u \cdot \mathbf{t} \, dA \stackrel{!}{=} \mathbf{0} \quad (5.50)$$

$$\mathbf{R}_\varphi = \int_{\Omega} \beta_\varphi (\mathbf{N}_\varphi \cdot \hat{\boldsymbol{\varphi}} + 1 - |\boldsymbol{\lambda}_0|) \mathbf{N}_\varphi \, dV + \int_{\Omega} c_\varphi (\nabla \mathbf{N}_\varphi \cdot \nabla \mathbf{N}_\varphi \cdot \hat{\boldsymbol{\varphi}}) \, dV \stackrel{!}{=} \mathbf{0} \quad (5.51)$$

It is convenient to introduce a new vector, denoted by  $\mathbf{R}$ , which collects both individual residual vectors. Then, the NEWTON scheme gives

$$\begin{bmatrix} \mathbf{R}_u \\ \mathbf{R}_\varphi \end{bmatrix}^{i+1} = \mathbf{R}^{i+1} = \mathbf{R}^i + \mathbf{J} \cdot \begin{bmatrix} \Delta \hat{\mathbf{u}} \\ \Delta \hat{\boldsymbol{\varphi}} \end{bmatrix} \stackrel{!}{=} \mathbf{0}, \quad (5.52)$$

again with  $i$  as iteration number for fixed load step  $n$ . In Eq. (5.52),  $\mathbf{J}$  indicates the JACOBIAN, thus the partial derivatives of the entries of  $\mathbf{R}$  with respect to the displacements and the field function, so

$$\mathbf{J} = \begin{bmatrix} \frac{\partial \mathbf{R}_u}{\partial \hat{\mathbf{u}}} & \frac{\partial \mathbf{R}_u}{\partial \hat{\boldsymbol{\varphi}}} \\ \frac{\partial \mathbf{R}_\varphi}{\partial \hat{\mathbf{u}}} & \frac{\partial \mathbf{R}_\varphi}{\partial \hat{\boldsymbol{\varphi}}} \end{bmatrix}. \quad (5.53)$$

The derivatives are

$$\frac{\partial \mathbf{R}_u}{\partial \mathbf{u}} = \int_{\Omega} \mathbf{B}^T \cdot \frac{\partial \tilde{\boldsymbol{\sigma}}}{\partial \tilde{\boldsymbol{\varepsilon}}} \cdot \mathbf{B} \, dV \quad (5.54)$$

$$\frac{\partial \mathbf{R}_u}{\partial \hat{\boldsymbol{\varphi}}} = \int_{\Omega} \mathbf{B}^T \cdot \frac{\partial \tilde{\boldsymbol{\sigma}}}{\partial \varphi} \otimes \mathbf{N}_\varphi \, dV \quad (5.55)$$

$$\frac{\partial \mathbf{R}_\varphi}{\partial \hat{\mathbf{u}}} = \int_{\Omega} \beta_\varphi \mathbf{N}_\varphi \otimes \left( -\frac{\partial |\boldsymbol{\lambda}_0|}{\partial \tilde{\boldsymbol{\varepsilon}}} \right) \cdot \mathbf{B} \, dV \quad (5.56)$$

$$\frac{\partial \mathbf{R}_\varphi}{\partial \hat{\boldsymbol{\varphi}}} = \int_{\Omega} \beta_\varphi \left( 1 - \frac{\partial |\boldsymbol{\lambda}_0|}{\partial \varphi} \right) \mathbf{N}_\varphi \otimes \mathbf{N}_\varphi \, dV + \int_{\Omega} c_\varphi (\nabla \mathbf{N}_\varphi)^T \cdot \nabla \mathbf{N}_\varphi \, dV \quad (5.57)$$

The remaining derivatives in the Eqs. (5.54) until (5.57) have to be calculated numerically. Of course, the derivative of  $\mathbf{R}_u$  with respect to  $\mathbf{u}$  is identical to that in the basic model. Then, this derivative can be interpreted as the entire JACOBIAN for the basic model. From the JACOBIAN  $\mathbf{J}$  for the extended model, which is equivalent to the stiffness matrix  $\mathbf{K}$  when applied to the entire set of nodes, it can be seen that in the case of the extended model the material model has to be executed eight times (including six times for the derivatives with respect to all components of strain; both derivatives with respect to  $\varphi$  are evaluated with one single call of the material model - one additional call for the residuals). In contrast, for the basic model seven single executions of the material model per GAUSS point were necessary (six for the JACOBIAN - one additional call for the calculation of the residuals again). Additionally, for tri-linear shape functions with eight nodes per element the stiffness matrix increases from a  $24 \times 24$ -matrix to a  $32 \times 32$ -matrix. Thus, the mentioned increased time consumption becomes evident.



### 5.2.3 Implementation of the thermo-mechanically coupled Model

The thermo-mechanically coupled model is a continuation of the extended model with the difference that now the temperature may change and have an influence on the phase transitions. This means that for the finite element implementation of the thermodynamically coupled model the total potential remains the same as for the extended model. Additionally to the resulting variational equations for displacements and field function the heat conduction equation has to be solved. The character of the heat conduction equation allows a finite element based solution. Therefore,

$$c_\theta \dot{\theta} = \mathbf{P} : \dot{\boldsymbol{\lambda}} - \theta \sum_{j=1}^N \sum_{i=0}^n \xi^j \dot{\lambda}_i^j b_i - \nabla \cdot \left( \frac{1}{\alpha_\theta} \nabla \frac{1}{\theta} \right) \quad (5.58)$$

can be interpreted as EULER equation of an associated variational problem for which Eq. (5.58) is reformulated by following the method in Sec. 5.1 to

$$\begin{aligned} \int_{\Omega} c_\theta \dot{\theta} \delta \theta \, dV &= \int_{\Omega} \mathbf{P} : \dot{\boldsymbol{\lambda}} \delta \theta \, dV - \int_{\Omega} \theta \sum_{j=1}^N \sum_{i=0}^n \xi^j \dot{\lambda}_i^j b_i \delta \theta \, dV \\ &\quad - \int_{\partial\Omega} \underbrace{\frac{1}{\alpha_\theta} \nabla \frac{1}{\theta} \cdot \mathbf{n}}_{=\mathbf{q}} \delta \theta \, dA + \frac{1}{\alpha_\theta} \int_{\Omega} \nabla \frac{1}{\theta} \cdot \nabla \delta \theta \, dV \quad \forall \delta \theta. \end{aligned} \quad (5.59)$$

with a normal vector  $\mathbf{n}$  pointing outside of the body. Similarly to the displacements as well as the field function, the temperature and its gradients are approximated by means of shape functions. Thus,

$$\theta = \mathbf{N}_\theta \cdot \hat{\boldsymbol{\theta}}, \quad \nabla \frac{1}{\theta} = \nabla \left( \mathbf{N}_\theta \cdot \hat{\boldsymbol{\theta}} \right)^{-1}, \quad \delta \theta = \mathbf{N}_\theta \cdot \delta \hat{\boldsymbol{\theta}}, \quad \nabla \delta \theta = \nabla \mathbf{N}_\theta \cdot \delta \hat{\boldsymbol{\theta}}. \quad (5.60)$$

Inserting this into Eq. (5.59) results in the residual for temperature

$$\begin{aligned} \mathbf{R}_\theta &:= \int_{\Omega} c_\theta \mathbf{N}_\theta \cdot \dot{\hat{\boldsymbol{\theta}}} \mathbf{N}_\theta \, dV - \int_{\Omega} \mathbf{P} : \dot{\boldsymbol{\lambda}} \mathbf{N}_\theta \, dV + \int_{\Omega} \mathbf{N}_\theta \cdot \hat{\boldsymbol{\theta}} |\dot{\boldsymbol{\lambda}} : \mathbf{b}_\theta| \mathbf{N}_\theta \, dV \\ &\quad - \int_{\partial\Omega} \mathbf{q} \cdot \mathbf{n} \mathbf{N}_\theta \, dA + \frac{1}{\alpha_\theta} \int_{\Omega} \frac{\nabla \mathbf{N}_\theta \cdot \hat{\boldsymbol{\theta}}}{(\mathbf{N}_\theta \cdot \hat{\boldsymbol{\theta}})^2} \cdot \nabla \mathbf{N}_\theta \, dV \stackrel{!}{=} \mathbf{0} \end{aligned} \quad (5.61)$$

with

$$|\dot{\boldsymbol{\lambda}} : \mathbf{b}_\theta| := \sum_{j=1}^N \sum_{i=0}^n \xi^j \dot{\lambda}_i^j b_i. \quad (5.62)$$

In contrast to the previously presented residuals for displacements and field function respectively, in  $\mathbf{R}_\theta$  a time dependent derivative occurs for which it is a *transient* equation. For the time derivative a direct discretization is chosen to be

$$\dot{\hat{\boldsymbol{\theta}}} = \left( \hat{\boldsymbol{\theta}}^{n+1} - \hat{\boldsymbol{\theta}}^n \right) \frac{1}{\Delta t} \quad (5.63)$$

where  $n$  is, again, the number of previous load step. By choosing a specific value for the time increment  $\Delta t$  implicitly the loading *velocity*  $\mathbf{v}$  can be taken into account by

$$\mathbf{v} \approx \frac{\Delta \mathbf{u}}{\Delta t}. \quad (5.64)$$

Since the increment of displacements  $\Delta \mathbf{u}$  has to be chosen, the known testing velocity can be displayed by an appropriate time increment.

Again, a residual vector is defined, collecting all single residual vectors

$$\begin{bmatrix} \mathbf{R}_u \\ \mathbf{R}_\varphi \\ \mathbf{R}_\theta \end{bmatrix}^{i+1} = \mathbf{R}^{i+1} = \mathbf{R}^i + \mathbf{J} \cdot \begin{bmatrix} \Delta \hat{\mathbf{u}} \\ \Delta \hat{\varphi} \\ \Delta \hat{\theta} \end{bmatrix} \stackrel{!}{=} \mathbf{0}. \quad (5.65)$$

In this case the JACOBIAN reads

$$\mathbf{J} = \begin{bmatrix} \frac{\partial \mathbf{R}_u}{\partial \hat{\mathbf{u}}} & \frac{\partial \mathbf{R}_u}{\partial \hat{\varphi}} & \frac{\partial \mathbf{R}_u}{\partial \hat{\theta}} \\ \frac{\partial \mathbf{R}_\varphi}{\partial \hat{\mathbf{u}}} & \frac{\partial \mathbf{R}_\varphi}{\partial \hat{\varphi}} & \frac{\partial \mathbf{R}_\varphi}{\partial \hat{\theta}} \\ \frac{\partial \mathbf{R}_\theta}{\partial \hat{\mathbf{u}}} & \frac{\partial \mathbf{R}_\theta}{\partial \hat{\varphi}} & \frac{\partial \mathbf{R}_\theta}{\partial \hat{\theta}} \end{bmatrix}. \quad (5.66)$$

The derivatives in the upper left  $2 \times 2$  sub-matrices are the same as in the extended model. The missing derivatives are calculated to

$$\frac{\partial \mathbf{R}_u}{\partial \hat{\theta}} = \int_{\Omega} \mathbf{B}^T \cdot \frac{\partial \tilde{\boldsymbol{\sigma}}}{\partial \theta} \otimes \mathbf{N}_\theta \, dV \quad (5.67)$$

$$\frac{\partial \mathbf{R}_\varphi}{\partial \hat{\theta}} = \int_{\Omega} \beta_\varphi \mathbf{N}_\varphi \otimes \left( \frac{\partial |\boldsymbol{\lambda}_0|}{\partial \theta} \right) \mathbf{N}_\theta \, dV \quad (5.68)$$

$$\begin{aligned} \frac{\partial \mathbf{R}_\theta}{\partial \hat{\mathbf{u}}} &= - \int_{\Omega} \mathbf{N}_\theta \otimes \left( \frac{\partial (\mathbf{P} : \dot{\boldsymbol{\lambda}})}{\partial \tilde{\boldsymbol{\varepsilon}}} \cdot \mathbf{B} \right) \, dV \\ &+ \int_{\Omega} (\mathbf{N}_\theta \cdot \hat{\boldsymbol{\theta}}) \mathbf{N}_\theta \otimes \left( \frac{\partial |\dot{\boldsymbol{\lambda}} : \mathbf{b}_\theta|}{\partial \tilde{\boldsymbol{\varepsilon}}} \cdot \mathbf{B} \right) \, dV \end{aligned} \quad (5.69)$$

$$\frac{\partial \mathbf{R}_\theta}{\partial \hat{\varphi}} = - \int_{\Omega} \frac{\partial (\mathbf{P} : \dot{\boldsymbol{\lambda}})}{\partial \varphi} \mathbf{N}_\varphi \otimes \mathbf{N}_\theta \, dV + \int_{\Omega} \mathbf{N}_\theta \cdot \hat{\boldsymbol{\theta}} \frac{\partial |\dot{\boldsymbol{\lambda}} : \mathbf{b}_\theta|}{\partial \varphi} \mathbf{N}_\varphi \otimes \mathbf{N}_\theta \, dV \quad (5.70)$$

$$\begin{aligned} \frac{\partial \mathbf{R}_\theta}{\partial \hat{\theta}} &= \int_{\Omega} \frac{c_\theta}{\Delta t} \mathbf{N}_\theta \otimes \mathbf{N}_\theta \, dV - \int_{\Omega} \frac{\partial (\mathbf{P} : \dot{\boldsymbol{\lambda}})}{\partial \theta} \mathbf{N}_\theta \otimes \mathbf{N}_\theta \, dV \\ &+ \int_{\Omega} |\dot{\boldsymbol{\lambda}} : \mathbf{b}_\theta| \mathbf{N}_\theta \otimes \mathbf{N}_\theta \, dV + \int_{\Omega} \mathbf{N}_\theta \cdot \hat{\boldsymbol{\theta}} \frac{\partial |\dot{\boldsymbol{\lambda}} : \mathbf{b}_\theta|}{\partial \theta} \mathbf{N}_\theta \otimes \mathbf{N}_\theta \, dV \\ &+ \frac{1}{\alpha_\theta} \int_{\Omega} \left( \frac{(\nabla \mathbf{N}_\theta)^T \cdot \mathbf{N}_\theta}{(\mathbf{N}_\theta \cdot \hat{\boldsymbol{\theta}})^2} - 2 \frac{((\nabla \mathbf{N}_\theta \cdot \hat{\boldsymbol{\theta}}) \otimes \mathbf{N}_\theta)^T}{(\mathbf{N}_\theta \cdot \hat{\boldsymbol{\theta}})^3} \cdot \nabla \mathbf{N}_\theta \right) \, dV \end{aligned} \quad (5.71)$$

The derivative of the residual for the temperature,  $\mathbf{R}_\theta$ , with respect to the temperature is executed for the *discretized* rate of temperature. Then, there exists the possibility to find the derivative with respect to the current time step,  $\hat{\boldsymbol{\theta}}^{n+1}$ , or with respect to the previous time step,  $\hat{\boldsymbol{\theta}}^n$ . Here, the derivative is found with respect to the current time step. In this case the resulting JACOBIAN is called *consistent tangent operator*.

In the thermo-mechanically coupled model only one additional call of the material model has to be executed compared to the eight calls of the material model in the extended model. This is an increase as from the basic to the extended model. Consequently, the calculations are once again remarkably slower than the extended model due to the much more complicated and larger stiffness matrix. In this case the element-stiffness matrix contains  $40 \times 40$  entries because each of the eight nodes has five unknowns.



# Chapter 6

## Numerical Results

In this section numerical results for all three material models are presented and discussed. First, simple geometries are regarded in order to validate the results with experimental observations in [48]. In the experiment, a stripe of pseudo-elastic NiTi has been clamped in a tension machine and the resulting displacement field was measured by a method called Digital-Image-Correlation. From the displacement field the strain field could be derived which itself serves as indicator for the different crystallographic phases (small strains: austenite; large strains: martensite). The results are recalled in Fig. 6.1. There, it can be seen that the phase

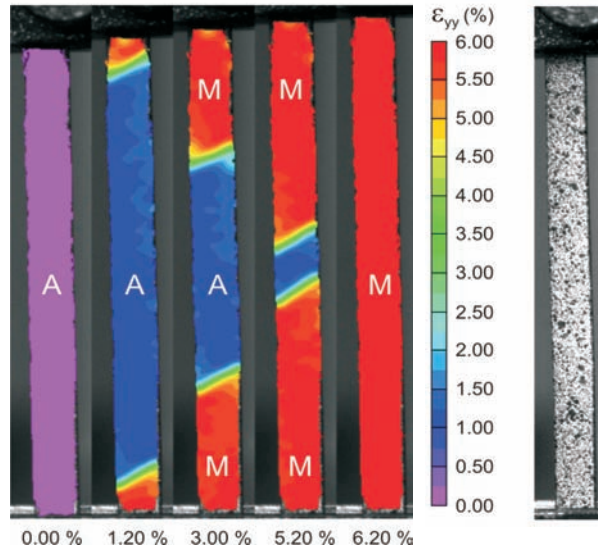


Figure 6.1: Experimentally observed distribution of austenite and martensite at various time steps, [48].

transformation from austenite to a specific martensitic combination initiates at the supports due to resulting stress peaks. Outgoing from these nucleation zones at both ends, the transformation evolves in a front like behavior, similar to LÜDERS bands known from plasticity. Due to stochastic imperfections, the inclination of the front may change.

The experiment is discretized by a rectangular body with free length of 35 mm, width of 3.3 mm and thickness of 0.68 mm. In order to capture the experimental conditions best, for the numerical investigations of the models' qualities the displacements for the very first rows of nodes *within* the discretized body are prescribed. The nodes at the lower side are fixed whereas for the nodes at the upper side the displacements in longitudinal direction (corresponds to the  $x_1$ -direction) are prescribed. The displacements in  $x_2$ - and  $x_3$ - direction

are set to zero at these nodes.

To compare the models with the experiments two different results are presented. First, corresponding stress-strain diagrams are presented which provide information of the entire material reaction. The occurring residual forces at the nodes with prescribed non-zero displacements are summed up and divided by the original cross section. This is interpreted as stress. The prescribed displacements are referred to the original free length which is used as average strain. The stress is plotted over strain. For the experimental data similar treatment was performed. Measured forces as well as prescribed displacements were divided by original cross section and free length, respectively. Thereby, the material reaction and the influence of geometry are visualized and the models' capacities on a *global* scale are investigated.

Secondly, the distribution of austenite over the geometry is discussed which can be compared to the experimentally estimated one in [48], Fig. 6.1. This gives a hint about the models' capacities to display a realistic material behavior on a *local* scale.

At lower temperatures, the evolution of the so-called R-phase takes place as interstate of the austenite-martensite phase transformation, [46]. This effect is not included in the model. Hence some characteristics cannot be displayed. Due to this and furthermore in order to have experimental basis for the dependence of the material reaction on room temperature, experimental results with wires of NiTi at different temperatures are taken into consideration, too. These experiments can be found in [59].

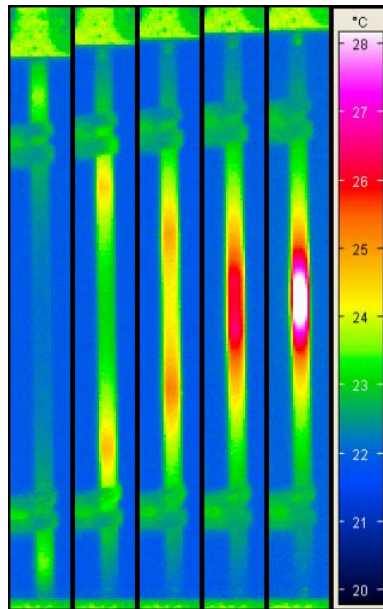


Figure 6.2: Experimentally observed distribution of temperature at various time steps. Courtesy of A. Schäfer & M.F.-X. Wagner. The background is colored in blue. Zones of increased temperature move analogously to the transformation zones. If these zones collide a remarkable peak in temperature is observed.

After these analyses, a more complex geometry is considered which is a spring. In this case the predominant loading state is torsion. So the models are tested to their applicability to this loading state as well. All models are executed for all geometries.

Furthermore, the field model is tested with focus on the influence of different parameters for the interface energy  $c_\varphi$ . In this way, the parameter can be found such that the experiments are displayed best and furthermore the desired state of mesh independence is achieved.

The distribution of temperature calculated with the thermo-mechanical model is brought into comparison with experimental results again from [48] which is recast in Fig. 6.2.

A heating–cooling process on material point level is discussed from which a new understanding of the dissipation coefficient  $r$  is derived which allows the calculation of  $r$  just by means of the chemical energy and experimentally observable transformation temperatures for austenite and martensite. Then, the thermo-mechanical model is used to simulate various examples of pseudo-elasticity to prove its capability of displaying realistic results.

## 6.1 Numerical Results for the basic Model

The model is based on a subset of all possible grain orientations which may be found in a real poly-crystal. This subset is included in the model in order to display the material behavior of poly-crystalline shape memory alloys. Thus, first investigations using the basic model are focused on the influence of the specific number  $N$  of assumed grain orientations. Since the orientations are chosen randomly, a lower bound for the minimum number of  $N$  has to be found in order to receive reproducible results. Hence, the first results presented here show the material reaction of a stripe of NiTi which is fixed in a way that catches the experimental conditions best, see Sec. 6. In Fig. 6.3 the resulting force displacement diagrams for a wire at 50° C are presented. So, the geometry as well as loading conditions were exactly the same but the randomly chosen specific set of angles forming the grain orientation differs for every single curve.

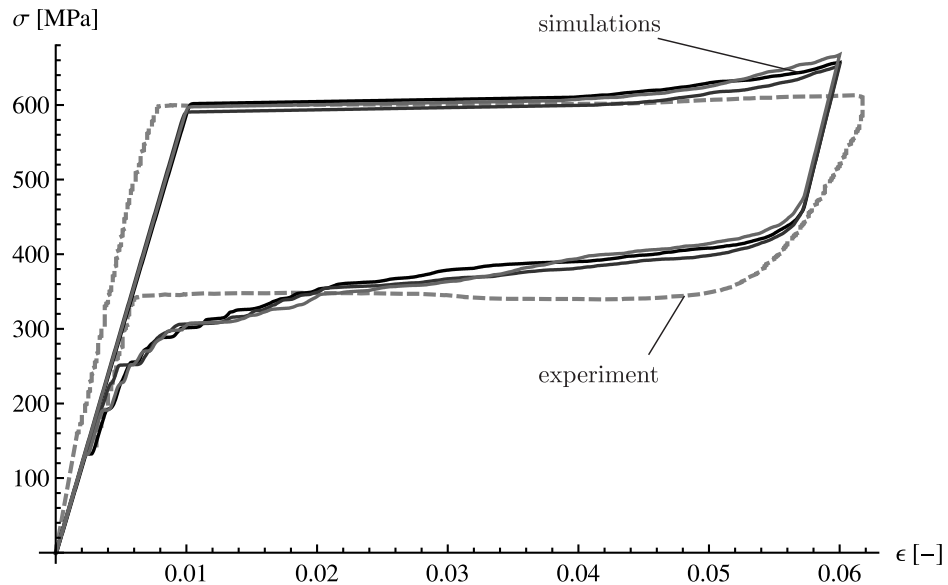


Figure 6.3: Basic model. Stress-strain diagram for a wire made of NiTi at 50° C. Dashed line reflects experimental results by [59], the solid lines are observed from numerical simulations. Only difference was the specific set of  $N = 30$  randomly chosen orientations.

The material parameters were set to  $r = 0.0084$  [GPa] and  $c_0 = -0.065$  [GPa] (all other  $c_{i>0} = 0$ ). The volume fraction of grains is taken as  $\xi^j = 1/N$  for all calculations. The diagrams prove in an empirical way that the number of  $N = 30$  orientations is sufficient to receive reproducible results, of course with a small stochastic fluctuation. Consequently,

in all subsequent calculation this number of grain orientations is used. Although in general an even higher number would be possible to calculate, the benefit in the simulation's quality would not justify the remarkably higher numerical effort.

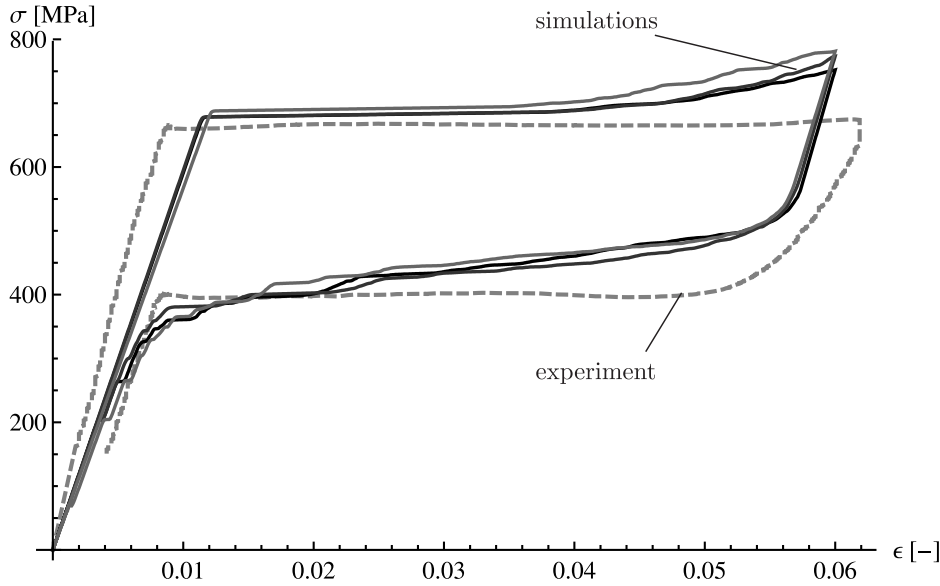


Figure 6.4: Basic model. Stress-strain diagram for a wire made of NiTi at 60° C. Dashed line reflects experimental results by [59], the solid lines are observed from numerical simulations. Only difference was the set of  $N = 30$  randomly chosen orientations.

Fig. 6.4 shows the numerical results for the same experiment now at 60° C room temperature. Here  $r$  has been hold constant and  $c_0 = -0.075$  [GPa] (all other  $c_{i>0} = 0$ ). For both temperatures same observations can be made. After a purely linear reaction when no transformation takes place (app. 600 MPa at 50° C or 700 MPa at 60° C), a plateau-like branch follows which accompanies the phase transition from austenite to martensite. At a strain of 0.05 at 50° C or 0.045 at 60° C, in the simulations the stress increases slightly which is in contrast to the experimental results. In this part the plateau is left and a non-linear part indicates that less transformation occurs compared to the transformation which would be needed to keep on track to the plateau. In other words, the rate of phase transformation is higher in the experiments. This is due to the remaining austenite which could transform but which is found in grains orientated in a less favorable direction which inhibits further transformation.

During unloading the stress decreases first linearly while the material contains both rest-austenite and martensite. So, it has the elastic properties of a mixture of austenite and martensite. After reaching a certain threshold, which is lower than the one for the transformation during loading, the material transforms back. This can be seen in first plateau like and then non-linear curve in the stress-strain diagram. The entire process of transformation during loading and unloading with the plateau like and non-plateau like parts and the hysteretic character is well known from experiments, [46]. Although the calculations were performed with the elastic constants from [60] the slope in the first linear part does not match the experimental results. Even more interestingly the slope of the simulated stress-strain diagram coincides very well after back transformation. Despite this artifact, the basic model gives a quite nice material answer.

Beside the *global* material reaction, reflected in stress-strain diagrams, the accuracy of the basic model for the *local* behavior is of interest. Therefore, the distribution of austenite



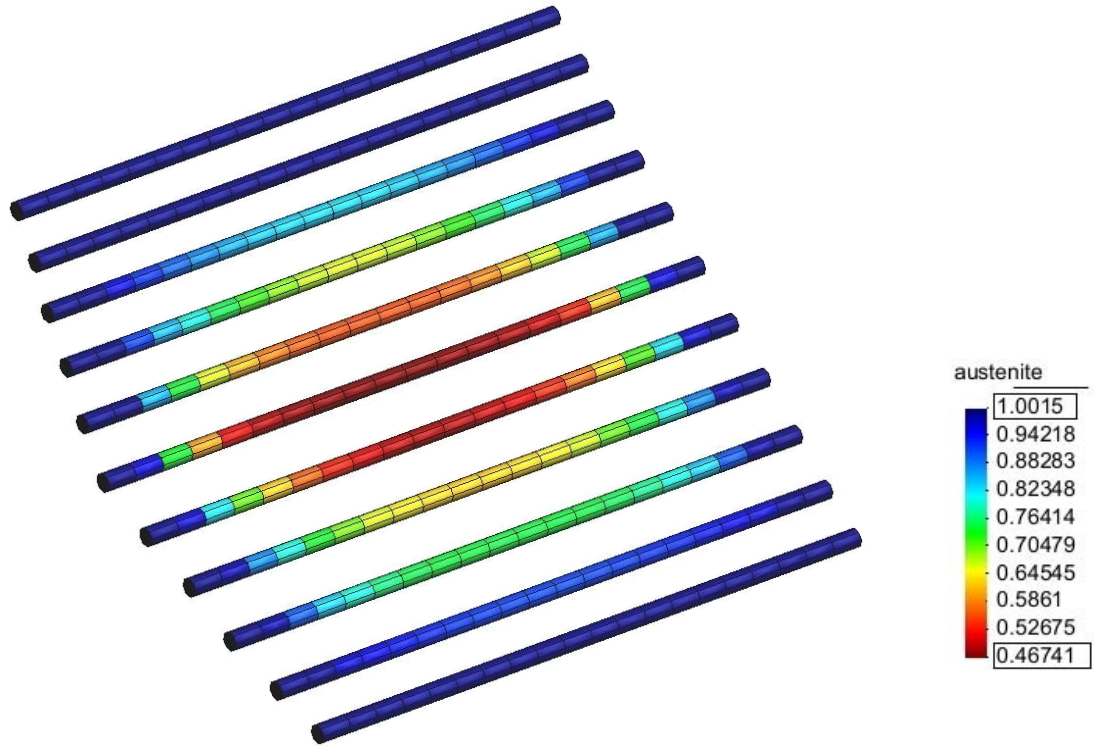


Figure 6.5: Basic model. Distribution of austenite over time for a wire made of NiTi at 50° C. Geometry as well as free length are based on the experimental conditions in [59].

over the wire is displayed in Fig. 6.5. It can be seen that the transformation starts quite in the center of the wire and proceeds in a rather homogeneous way. The dissipative character of the material, which can also be seen from the hysteresis in the stress-strain diagrams, may be observed in the finite element results, too. While the transformation starts at higher strains the end of transformation during unloading takes place at lower strains.

To focus more on the local behavior of the material model, the geometry of the stripe mentioned above is used in additional simulations, see Figs. 6.6 and 6.7. Again, NiTi at 50° C and at 60° C is simulated and the distribution of austenite presented.

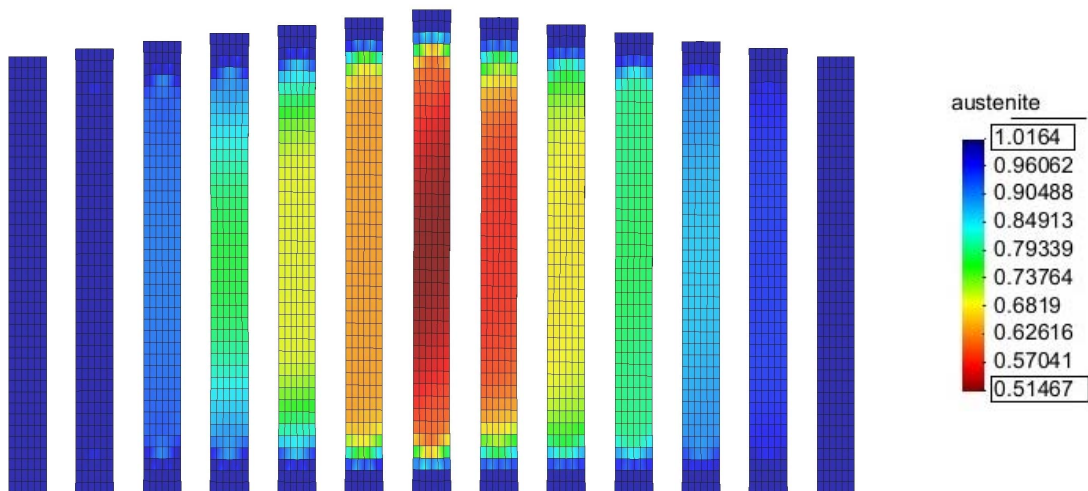


Figure 6.6: Basic model. Distribution of austenite over time for a stripe of NiTi at 50°C.

The differences in the distributions at the two different temperatures are very low: the transformation initiates at the nodes with fixed or prescribed non-zero displacements which



is in accordance to the experiment. In contrast to the material behavior in reality, the austenite does not drop until a very low value in a localized way before transformation zones run through the specimen: after the initial transformation at the nodes with prescribed displacements all further transformations take place very homogeneously distributed over the entire volume between the supports. In order to improve the coincidence between the local material reaction in the simulations and experimental observations, the extended material model is used for same boundary value problems in Sec. 6.2.

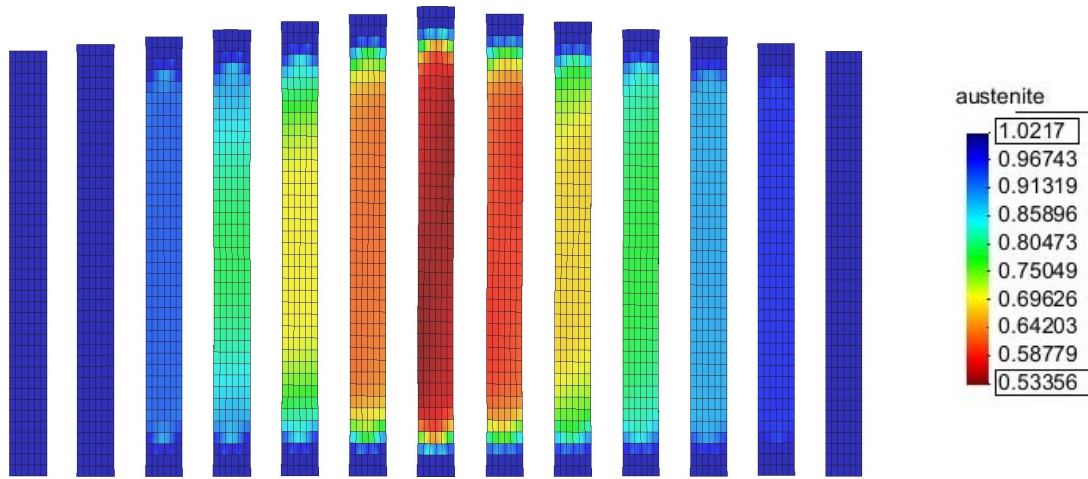


Figure 6.7: Basic model. Distribution of austenite over time for a stripe of NiTi at 60° C.

To prove the independence of the material model from the finite element mesh, a rather fine mesh is used for the simulation of the same boundary value problem. The results for this fine mesh are presented in Fig. 6.8 for 50° C and in Fig. 6.9 for 60° C room temperature. The results differ very slightly compared to those obtained from the coarse mesh.

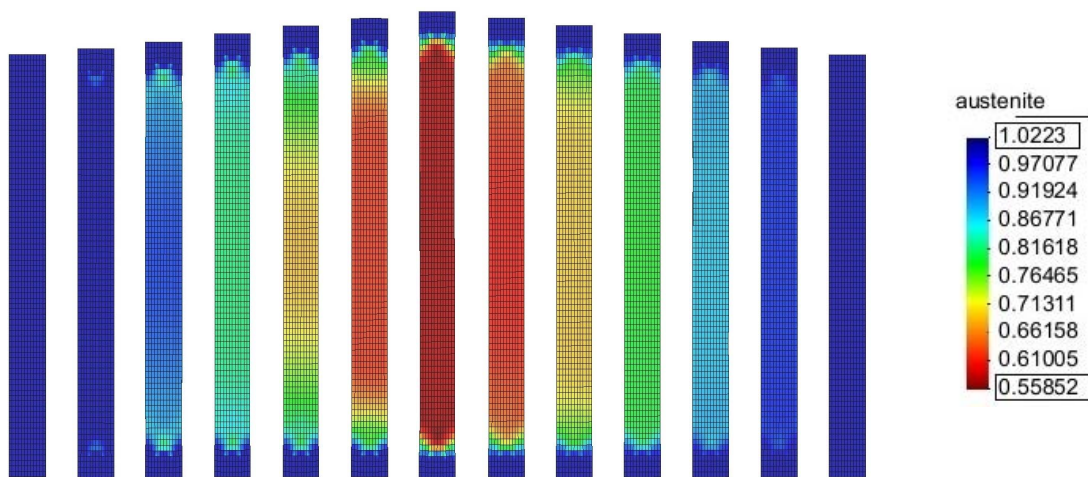


Figure 6.8: Basic model. Distribution of the austenite for a stripe of NiTi at 50° C, refined mesh (by factor two compared to the other results).

In Figs. 6.10 and 6.11 the material answer in the stress-strain space at 50° C and 60° C respectively is shown, each time for the coarse and the fine mesh. The differences which occur here are due to stochastic fluctuations since different subsets of  $N = 30$  orientations

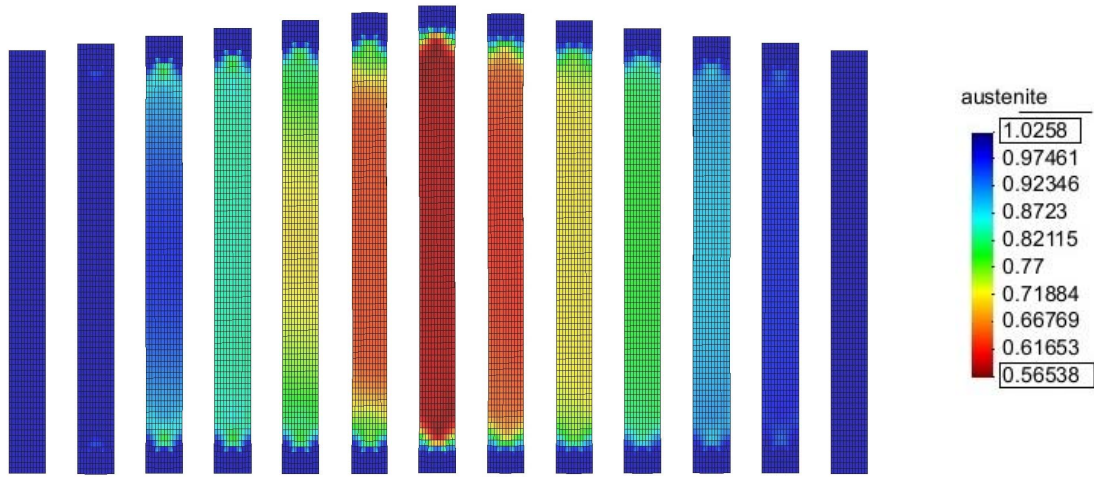


Figure 6.9: Basic model. Distribution of the austenite for a stripe of NiTi at 60° C, refined mesh (by factor two compared to the other results).

are used. In conclusion, there is no indicator that the results are mesh depended and particularly from the curve in the stress-strain diagram - which gives a hint to a (globally) convex energy which has been minimized during calculation - the results for the basic model are in fact mesh *independent*.

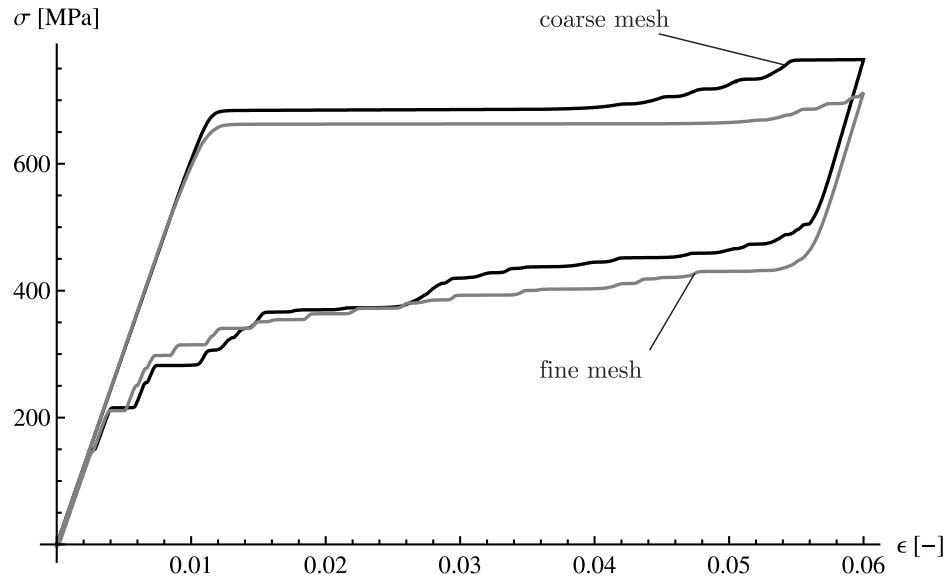


Figure 6.10: Basic model. Stress-strain diagram for stripe of NiTi at 50° C. Different meshing: coarse (black), fine (gray).

The influence of the free length of the specimen is investigated in the next simulations. Here, a free length of 70 mm has been chosen. All input parameters were kept constant for the respective temperatures of 50° C and 60° C (of course, the chemical energy is set to  $c_0 = -0.065$  [GPa] and  $c_0 = -0.075$  [GPa]). The global material reaction is presented in the associated stress-strain diagrams in Figs. 6.12 and 6.13.

At 50° C, Fig. 6.12, for the specimen with a free length of 70 mm the plateau is kept until maximum load. Due to the increased amount of mass between the supports there exist more possibilities that grains with appropriate orientations are loaded and the rate of phase transformation increases. So, the plateau during loading evolves in a more pronounced way.

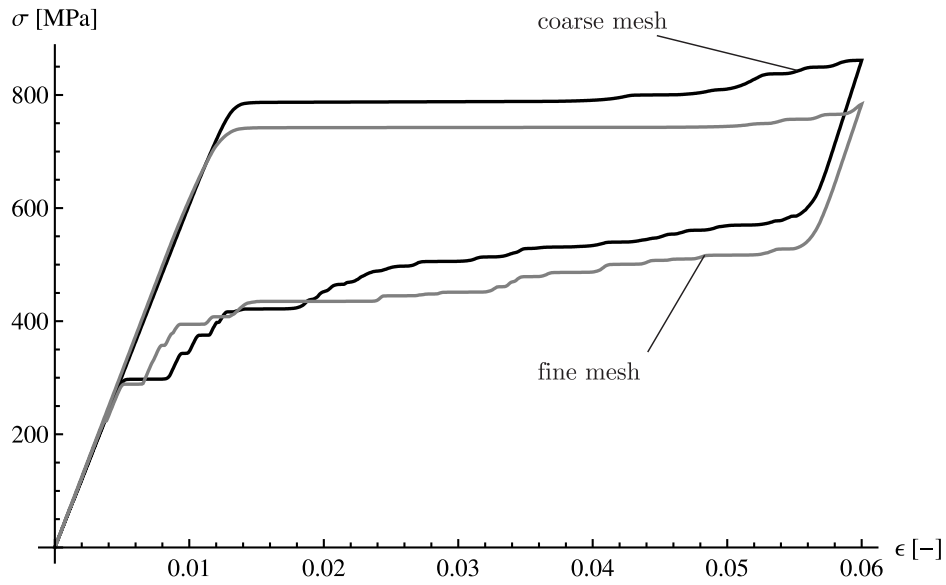


Figure 6.11: Basic model. Stress-strain diagram for stripe of NiTi at 60° C. Different meshing: coarse (black), fine (gray).

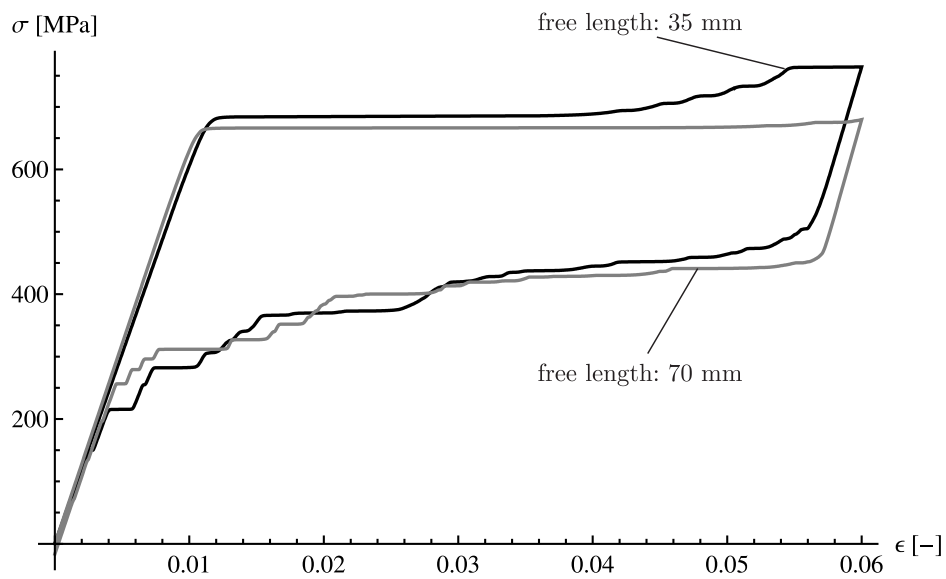


Figure 6.12: Basic model. Stress-strain diagram for stripe of NiTi at 50° C. Free length: 35 mm (black), 70 mm (gray).

During unloading first a quite perfect plateau is established. If the load is decreased further this parallel line to the  $x$ -axis is left although the behavior in total has a better coincidence to the real plateau.

This effect is lost when temperature increases, Fig. 6.13. At this higher temperature austenite is more stable for which the rate of phase transformation is - again - not sufficiently high to show a perfect plateau. This is valid for loading and unloading, and the results are quite the same as for the specimen with a free length of 35 mm.

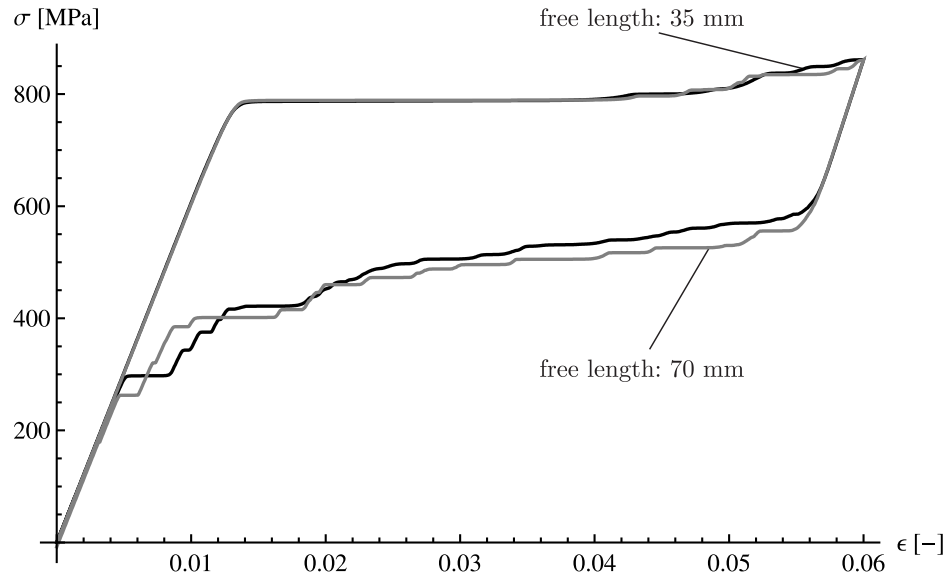


Figure 6.13: Basic model. Stress-strain diagram for stripe of NiTi at 60° C. Free length: 35 mm (black), 70 mm (gray).

The distribution of austenite is displayed in Fig. 6.14 for 50° C and in Fig. 6.15 for 60° C. Similar to the simulations for a free length of 35 mm the martensite evolution starts at the supports. However, this stress peaks do not trigger the material to continue transforming at these localized zones. In contrast, the evolution proceeds very homogeneously in the entire material between the supports. This allows the conclusion that the occurring driving forces are only slightly increased due to the supports' influences. Since this impact is very slow on the one hand but on the other hand the global stress state is quite constant, the material reacts very homogeneously.

Same observations can be made during unloading. In the entire process the material transforms back from some mixture state of austenite and martensite to a purely austenitic state. The remaining amount of austenite is slightly increased in the specimens with free length of 70 mm compared to those with 35 mm. Similar to the reaction in the stress-strain diagrams there are more possibilities for the material to transform so that an individual zone has to transform slightly less than in the shorter specimen. However, stochastic fluctuations are playing some role, too.

Additionally, results are presented for a more interesting geometry than in the previous examples. The last example for the basic model investigated here is a spring with fixed displacements at the lower front surface and prescribed displacements in longitudinal axes at the upper front surface. In this geometry mainly shear loads occur. The resulting entire material answer is presented in a force-displacement diagram, Fig. 6.16, where the resulting

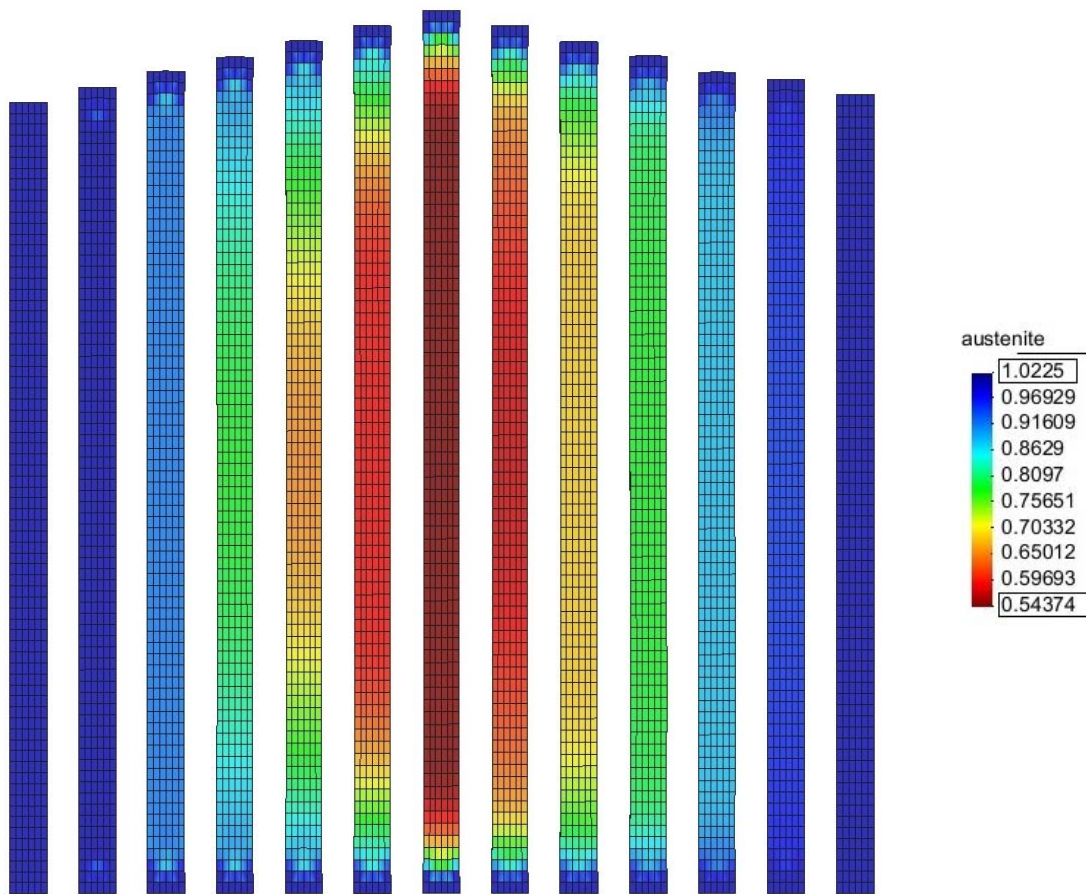


Figure 6.14: Basic model. Distribution of austenite in stripe of NiTi at 50° C. Free length is 70 mm.



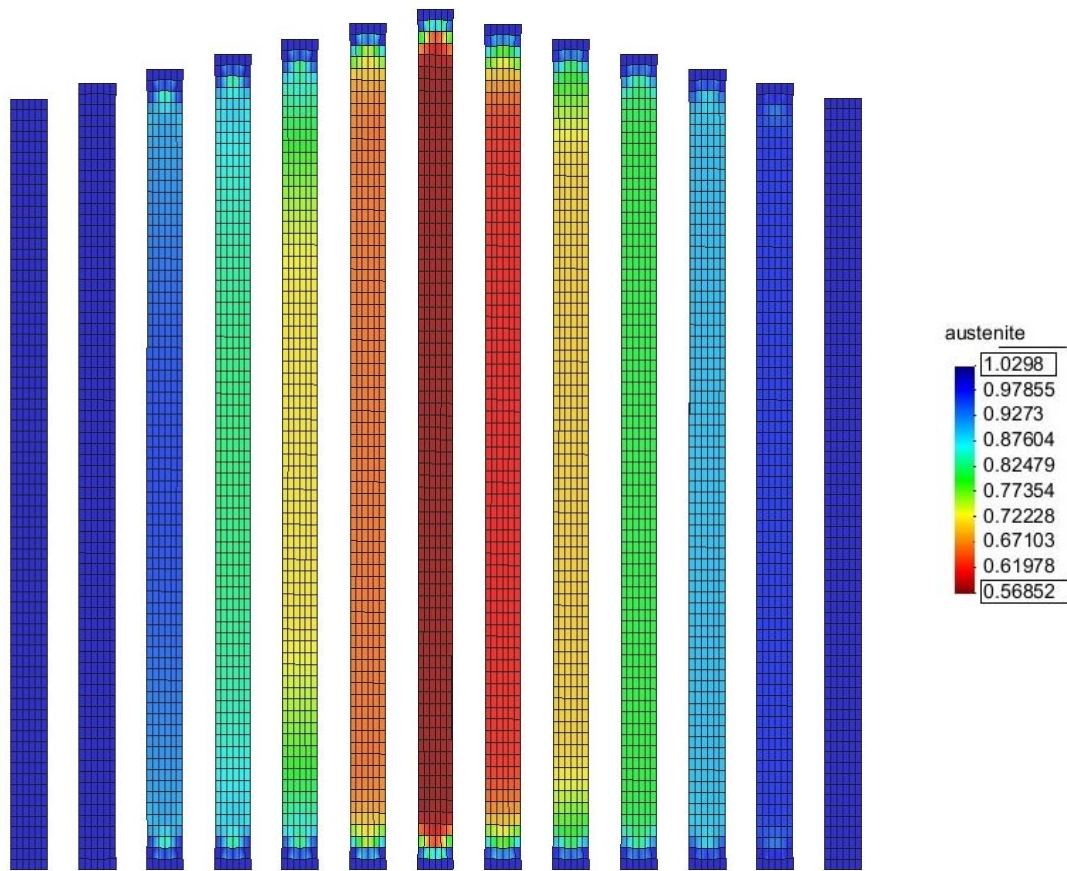


Figure 6.15: Basic model. Distribution of austenite in stripe of NiTi at 60° C. Free length is 70 mm.

forces in longitudinal direction are averaged and plotted over the displacement in longitudinal direction. In this case, a non-linear material response is observed which is neither a plateau. The non-linearity is rather smooth compared to the quite distinct kink which occurs in the tension tests when transformation starts. Same is valid when back transformation from austenite to martensite takes place. The transition from the linear part to the non-linear one during unloading cannot be identified by a specific point. However, a hysteresis and deductively dissipative material behavior occur as expected.

The local material behavior can be seen in Fig. 6.17 where the distribution of austenite is shown during loading as well as during unloading. Time starts in the first row at the left side, then middle row at left and so on. In the inner part of the spring most phase transformation happens. The amount of transformed material is higher in the centered region of the spring in its longitudinal length (spring interpret as coiled wire). The total amount of austenite left is similar to all other simulations (app. 50%). Due to transformation no particular deformations are observed such as in the tension tests.

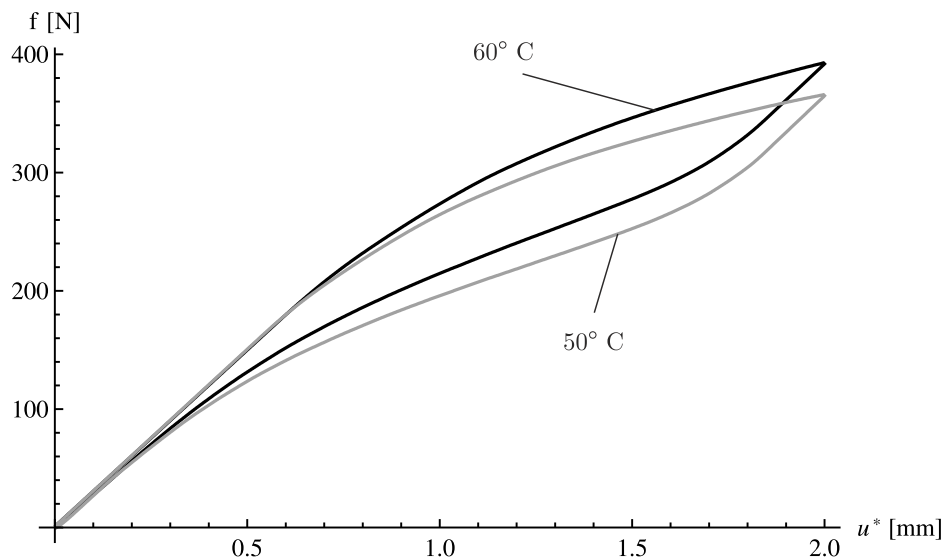


Figure 6.16: Basic model. Force-displacement diagram for a spring of NiTi at 50° C (gray curve) and 60° C (black curve).

Concluding, although the results from the basic model are not as good as demanded on the *local* layer, the *global* material reaction is displayed with a satisfying accuracy since it shows good agreement to the characteristic and therefore expected properties of shape memory alloys. Despite the missing localized transformations this model may be used for a rather rough investigation of industrial pieces since the global response in stress-strain or force-displacement diagrams is in good agreement to the desired characteristics. The energetic formulation of the entire model is the reason why the results are of same quality for the wires, at which the model was calibrated, and for the stripe which exhibits a different geometry and additionally was tested at a different temperature, see Fig. 6.18. Therefore, the model is able not only to calculate problems for which the material reaction can be measured but for even more complex geometries and loadings. However, in Sec. 6.2 results are presented where much better coincidence can be achieved by means of the extended model.

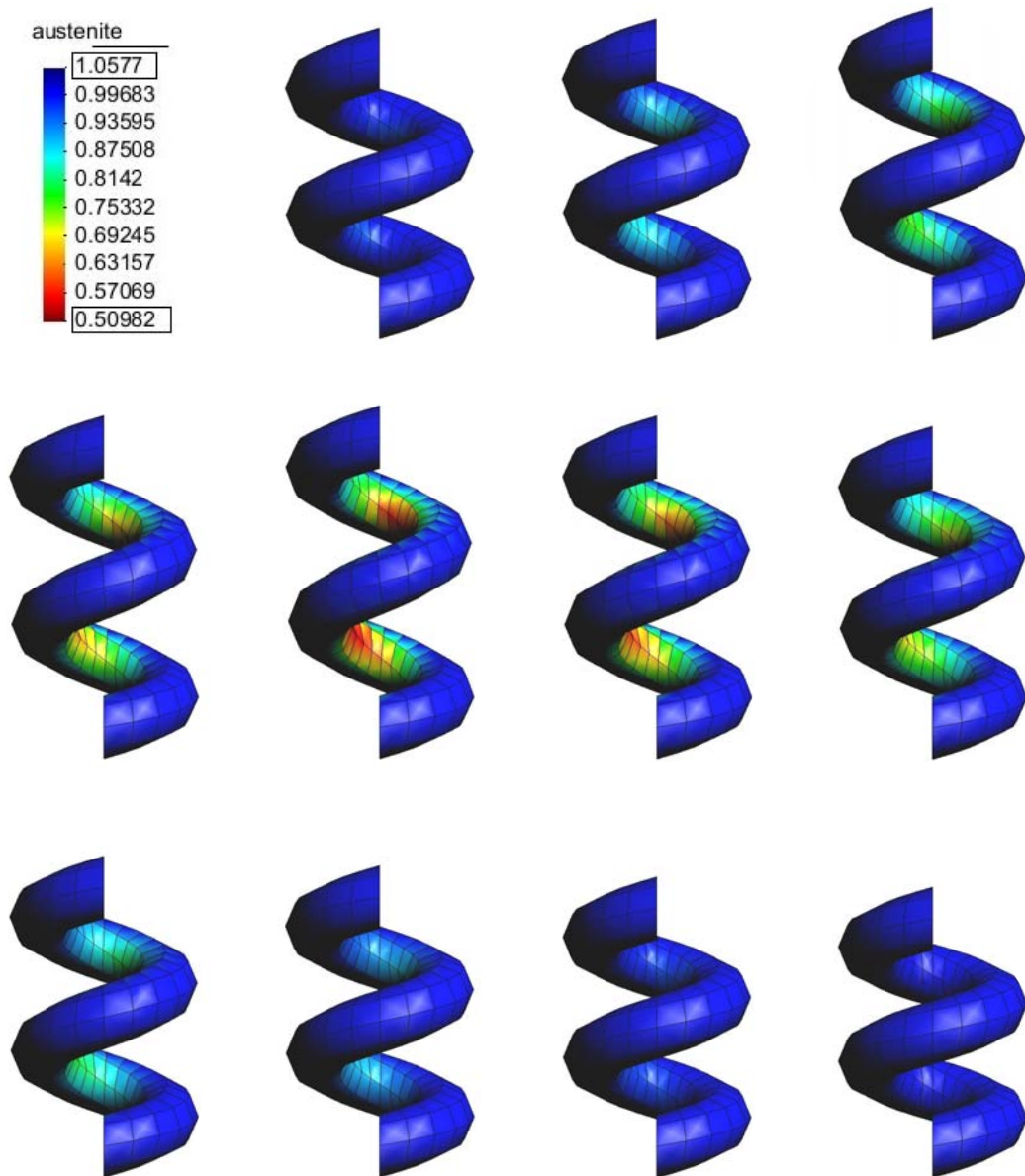


Figure 6.17: Basic model. Distribution of austenite in a spring of NiTi at 50° C. Time runs row wise.



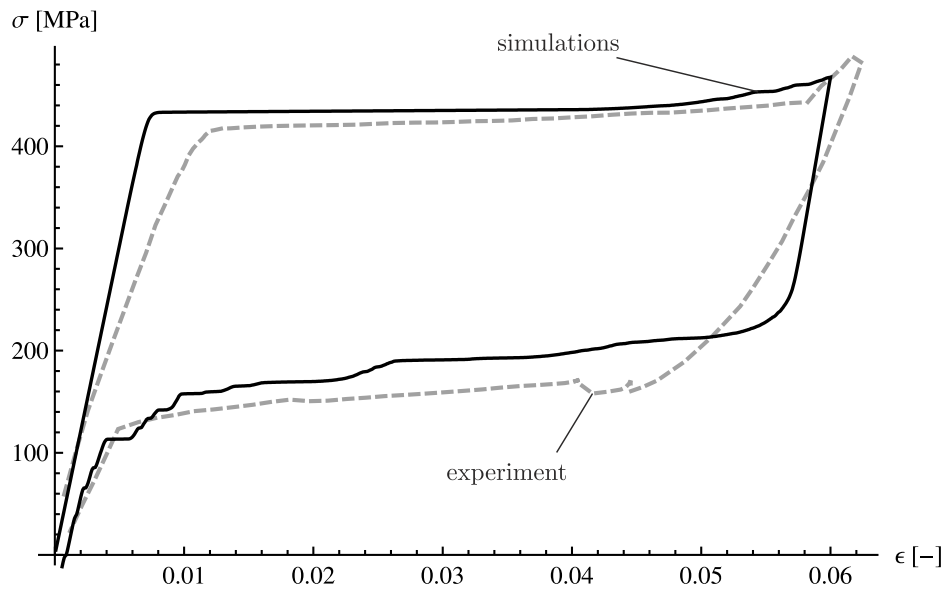


Figure 6.18: Basic model. Resulting stress-strain diagram of a stripe of NiTi at 22° C. Solid line: simulation. Dashed line: experiment.  $r = \text{const} = 0.0084$  [GPa],  $c_0 = -0.037$  [GPa].

## 6.2 Numerical Results for the extended Model

As it was mentioned in Sec. 4.2.2 and presented in Sec. 6.1, the basic model is not able to display the localized transformations which evolve in shape memory alloys. Since the exact distribution of crystallographic phases has a high influence on the resulting stresses, it is necessary to expand the model in a way that exactly these localized transformations can be displayed. In order to do so, the basic model was modified in a way that the dissipation coefficient was assumed to be a function of average austenite, Sec. 4.2.3. Figure 6.20 presents stress-strain diagrams for the completely same initial boundary value problem of a stripe of NiTi as used before but now with  $r = r(|\lambda_0|, \text{sign}(|\lambda_0|))$  according to Fig. 6.19.

$r_{A_f} = 0.017 \text{ [GPa]}$	$r_{A_s} = 0.0004 \text{ [GPa]}$
$r_{M_f} = 0.018 \text{ [GPa]}$	$r_{M_s} = 0.006 \text{ [GPa]}$

Table 6.1: Material parameters for the extended model.

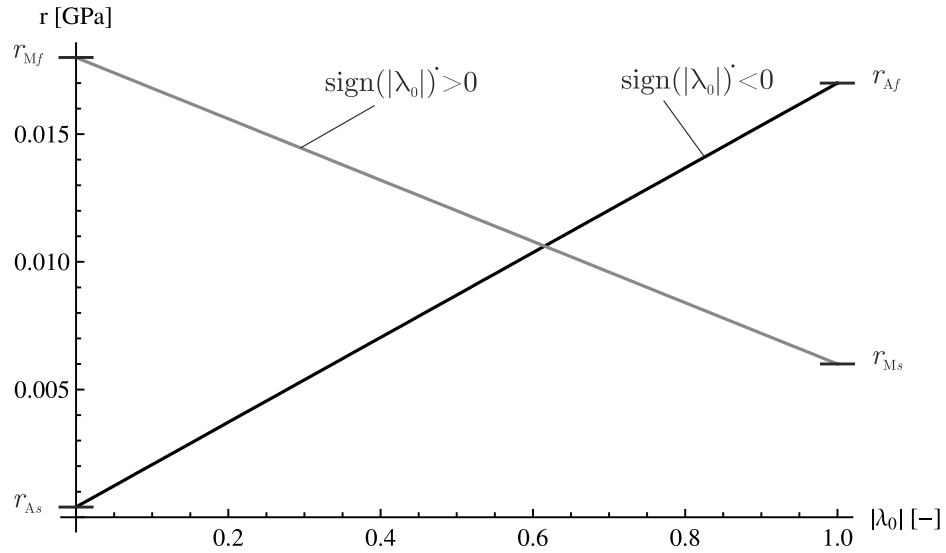


Figure 6.19: Dissipation parameter in dependence of the average volume fraction of austenite,  $|\lambda_0|$ , and the sign of its rate,  $\text{sign}(|\lambda_0|)$ .

The specific values for  $r_{A_s}$ ,  $r_{A_f}$ ,  $r_{M_s}$  and  $r_{M_f}$  can be taken from Tab. 6.1. The chemical energy for austenite was set to  $c_0 = -0.030 \text{ [GPa]}$  and for martensite  $c_{i>0} = 0.0 \text{ [GPa]}$ .

In Fig. 6.20  $c_\varphi$  has been varied, so the penalization of the spatial gradient of the volume fractions. The values are  $a : c_\varphi = 0.0 \text{ [GPa]}$ ,  $b : c_\varphi = 0.001 \text{ [GPa]}$ ,  $c : c_\varphi = 0.01 \text{ [GPa]}$ ,  $d : c_\varphi = 0.03 \text{ [GPa]}$ . Due to the missing penalization in  $a$  there are oscillations during the plateau. This results from single rows in the finite element discretization which soften one after the other, see Fig. 6.21. Since the gradient is penalized more with increasing value for  $c_\varphi$ , the effect of oscillations is reduced from  $b$  to  $d$ . The softening can be clearly identified in all stress-strain diagrams: After reaching a certain threshold all stresses reduce in a remarkably way before the curves turn into the plateau. During unloading the stress decreases - again - first linearly. Then, back transformation starts and a non-linear behavior is observed. Now, using the extended model the stress has the plateau like character in a much more pronounced way compared to the basic model, see Fig. 6.18. Although the stresses remain not completely constant during unloading, a much better agreement to experimental

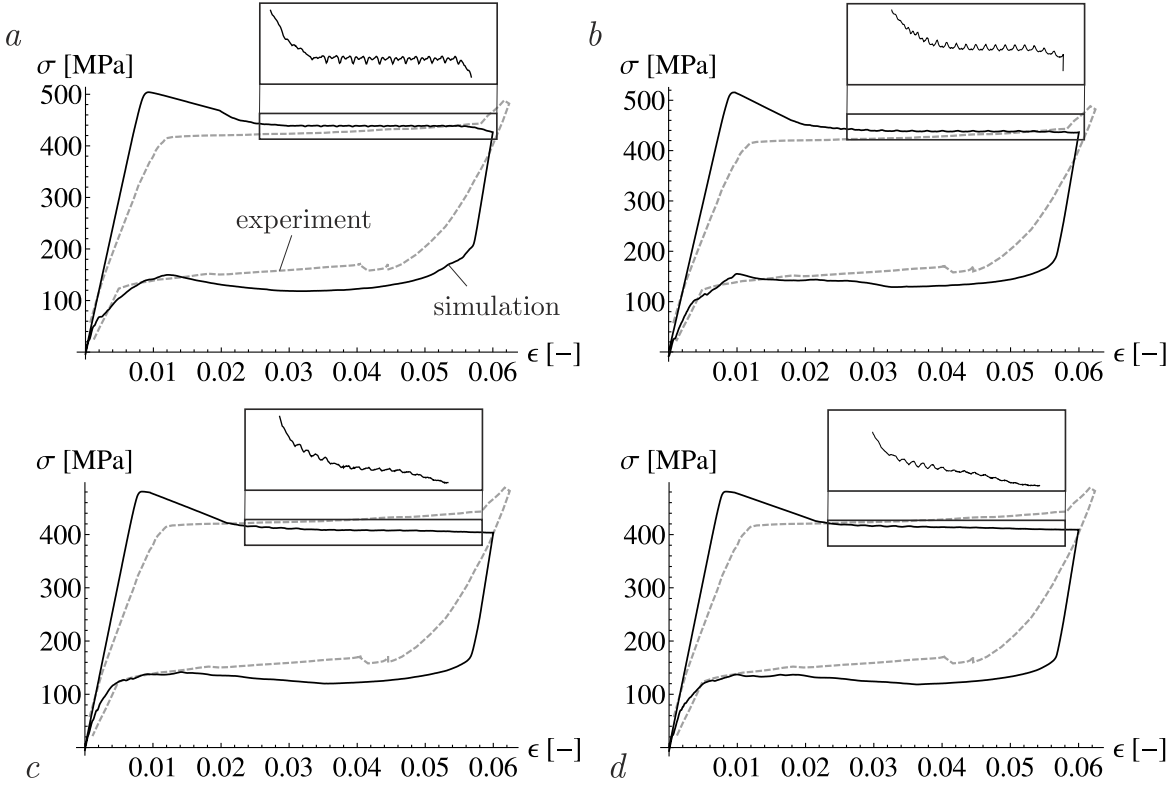


Figure 6.20: Extended model. Stress-strain diagrams for a stripe of NiTi at 22° C. *a*:  $c_\varphi = 0.0$  [GPa], *b*:  $c_\varphi = 0.001$  [GPa], *c*:  $c_\varphi = 0.01$  [GPa], *d*:  $c_\varphi = 0.03$  [GPa]. Dashed line: experimental result after [48].

results is achieved. In the experiments a non-constant plateau stress is observed as well. The deviations during loading in the elastic region, hence before any austenite–martensite transformation has started, are due to the R-phase which is not included in the model. This phase is an interstate phase between austenite and martensite and causes the small changes from a purely elastic behaving material.

The distribution of austenite for a coarse mesh with no regularization is presented in Fig. 6.21. Here, it can be seen that exactly the desired effect evolves: the transformation starts at the supports and the amount of average austenite drops until only austenite has left in orientations which are unfavorable for transformation. Then, starting from both sides the transformation takes place in a very localized way. In contrast to experiments, only at one side the transformation proceeds until a distinct front has evolved. This front is moving subsequently through the specimen. During unloading phase transformation takes place at both fronts which are moving back to the center of the transformed zone in the stripe. In the simulations a set of  $N = 30$  orientations was used. In the elastic region before any phase transformation a mixture of all rotated elastic constants of austenite has been used (the elastic constants for austenite are anisotropic). Of course, due to the mixture of rotated elastic constants an isotropic behavior is reached in the limit  $N \rightarrow \infty$ . Unfortunately, the convergence rate is quite slow. Hence, there is still a very slight anisotropic behavior included in the elastic region. In combination with quite small dissipation parameters this is why the transformation fronts start to evolve at both sides but establish completely only at one side.

The resulting amount of austenite which is left is much smaller compared to the results

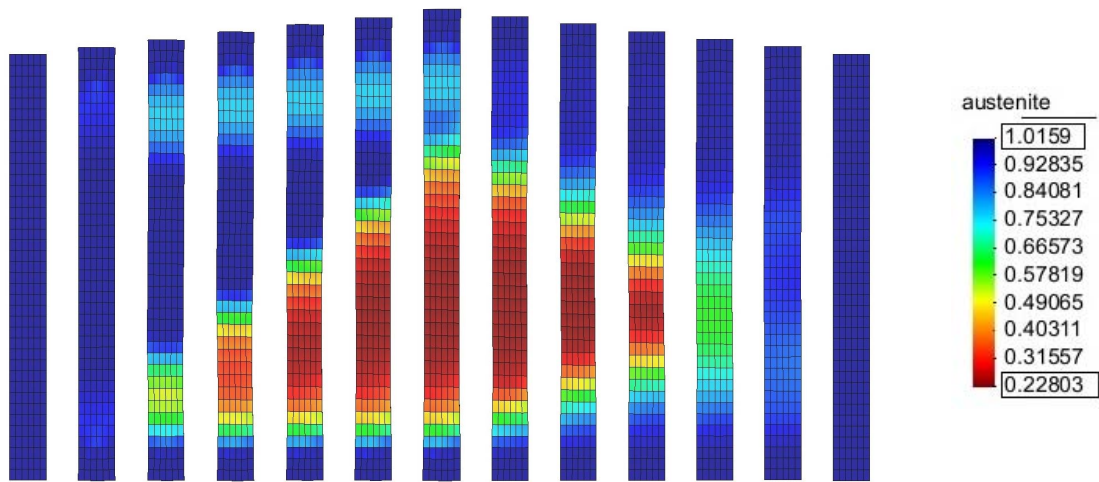


Figure 6.21: Extended model. Distribution of austenite in a stripe of NiTi at 22° C. Coarse meshing. No regularization.

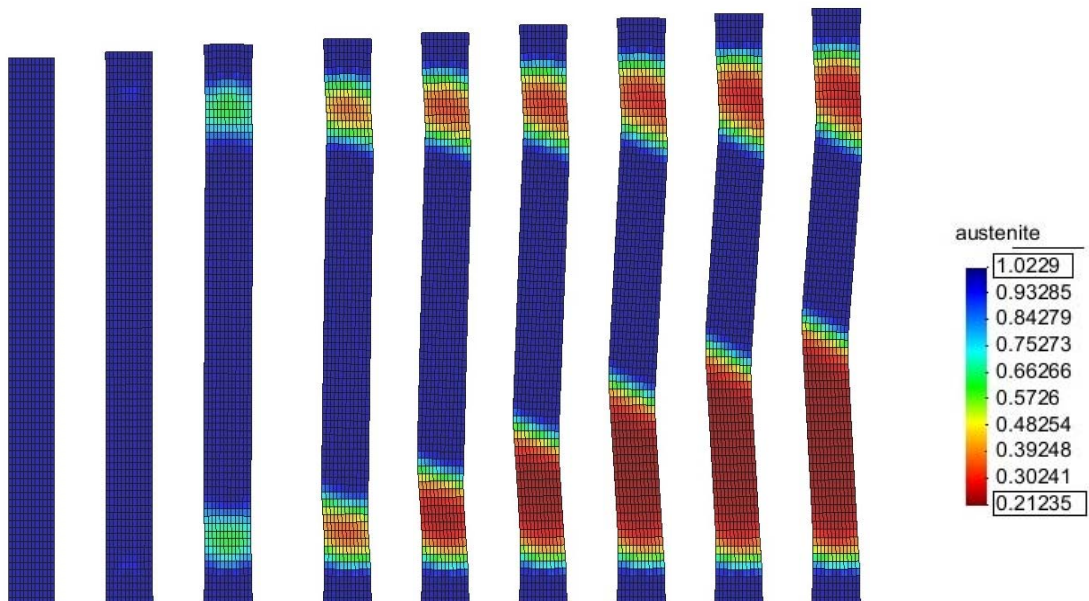


Figure 6.22: Extended model. Distribution of austenite in a stripe of NiTi at 22° C. Fine meshing. No regularization.

of the basic model (now app. 22%, previously app. 50%). This is obvious because now in the extended model a comparable amount of material transforms but distributed on a smaller volume. Consequently more austenite has to transform locally to martensite. In the stress-strain diagram the evolution of the front is accompanied by the softening character. While the front is moving the plateau like behavior takes place. During this, in the distribution of austenite the transformation starts in one row of elements in the discretization and only there all transformation evolves before the next row of elements transforms. Since only one row transforms, and all the neighboring rows do not, the spatial gradient of the volume fractions for the phases tends to infinity. This behavior has influence on the stress-strain diagram as explained: here the sawtooth-like, oscillating behavior occurs during transformation. Final prove is made by applying all the same parameters and approaches to the finer mesh used in Sec. 6.1 as well. The result for this mesh is presented in Figs. 6.22. Now, when the mesh size is smaller the transformation front is smaller, too. It has exactly the width of the mesh width. The inclination of the front is just due to the different set of orientations represented by the randomly chosen orientation matrices. Concluding, the results for the material model only using the non-constant approach for the dissipation (which is equivalent to  $c_\varphi = 0.0$  [GPa]) yields mesh *dependent* results which have to be avoided in any case. Although it would be possible to set the mesh discretization in a way that the mesh size coincides with the width of the transformation front in a tension test, application of this - if any possible - to other problems and geometries would only yield doubtful results. Hence, the extended material model using the additional field function  $\varphi$  by choosing  $c_\varphi \neq 0$  [GPa] is applied from now on.

The distribution of austenite for different values for the penalization parameter  $c_\varphi$  are presented in the upcoming. For all calculations the coupling parameter was set to  $\beta_\varphi = 1$  [GPa]. Other values yield only to a different valuation between the coupling and the gradient term which has the same influence like fixing  $\beta_\varphi$  and changing only  $c_\varphi$ .

Two remarkable aspects can be seen immediately: first, and most important, the results are not mesh dependent anymore which is proven by the transformation zones moving smoothly spread over several rows of elements, see Figs. 6.23, 6.24 and 6.25, and secondly, the width of the transformation front depends directly on the value of  $c_\varphi$ , compare Figs. 6.23 and 6.25. Thus, there exists now an additional parameter which can be brought to the physical level -  $c_\varphi$  is a measure for the surface energy - and the mesh size is no simulation parameter which would have to be determined very hard. The shift of information mentioned in Sec. 4.2.3 which was carried formerly only by the volume fractions from a GAUSS point level to a field level by means of  $\varphi$  results in a smooth distribution of the volume fractions.

The characteristic small jumps of GAUSS point quantities such as stress or internal variables at the element bounds do not occur any longer but the appearance is similar to one of the nodal variables such as displacements.

The resulting amount of austenite is nearly the same and all differences come from stochastic fluctuations due to the different set of orientation matrices.

Numerical results for a stripe with a free length of 70 mm with different penalization parameter  $c_\varphi$  are presented in Fig. 6.26. It can be seen that the oscillations are smeared out with higher  $c_\varphi$ . However, the results are very similar. The zone of material softening is much smaller compared to those obtained for stripe with free length of 35 mm. Due to localized character of the phase transformations the discretization is finer in comparison to strain. Despite the regularization approach the results still exhibit some mesh dependence: the width of the softening region is dependent on the mesh discretization. This effect will be removed by the incorporation of temperature which is carried out in the next section.



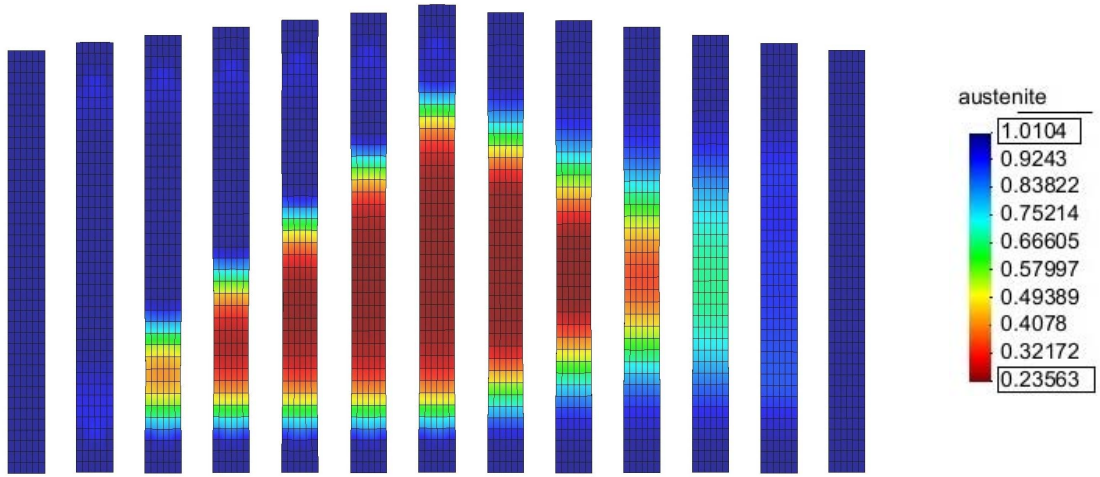


Figure 6.23: Extended model. Distribution of austenite in a stripe of NiTi at 22° C. Coarse meshing. Regularized with  $c_\varphi = 0.001$  [GPa].

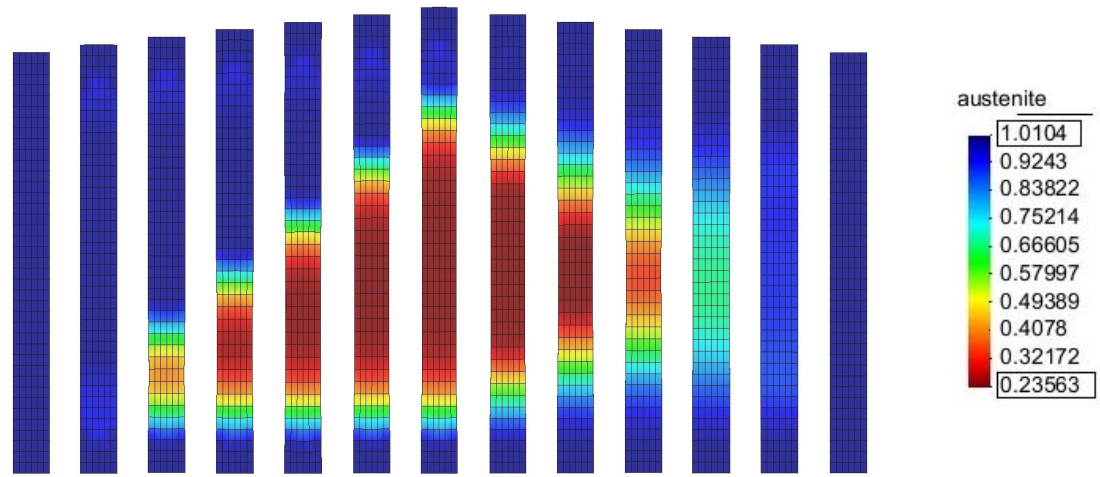


Figure 6.24: Extended model. Distribution of austenite in a stripe of NiTi at 22° C. Coarse meshing. Regularized with  $c_\varphi = 0.01$  [GPa].

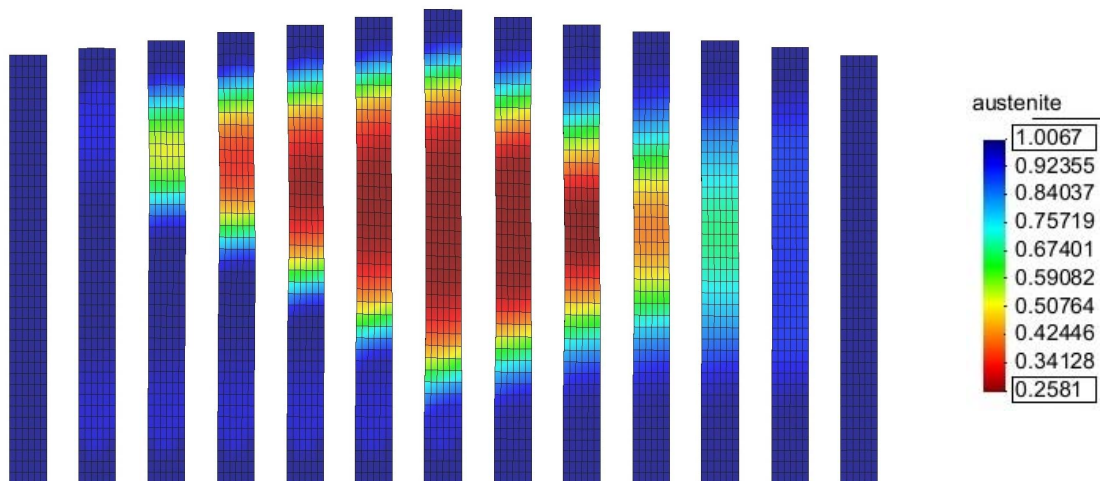


Figure 6.25: Extended model. Distribution of austenite in a stripe of NiTi at 22° C. Coarse meshing. Regularized with  $c_\varphi = 0.03$  [GPa].

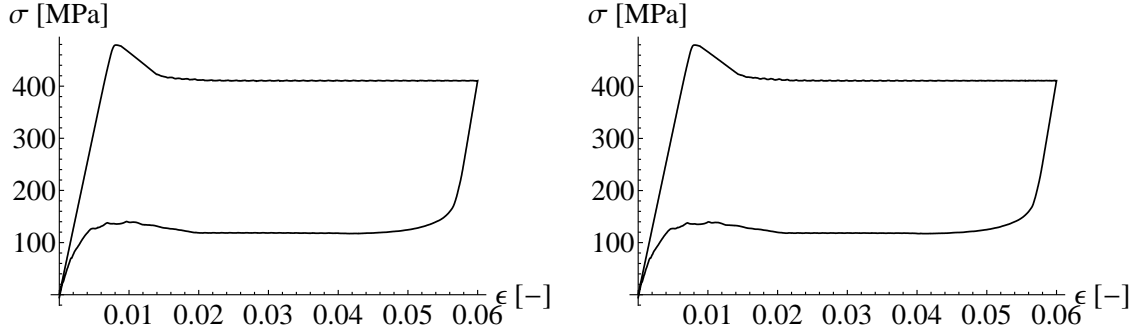


Figure 6.26: Extended model. Stress-strain diagram for a stripe with free length of 70 mm at 22° C. Regularization parameter was  $c_\varphi = 0.01$  [GPa] (left) and  $c_\varphi = 0.03$  [GPa] (right). Oscillations were smeared out with higher  $c_\varphi$ .

The distribution of austenite is presented in Figs. 6.27 and 6.28 for  $c_\varphi = 0.01$  [GPa] and  $c_\varphi = 0.03$  [GPa], respectively. Similar to the shorter specimen the evolution of austenite starts at the supports. Again, due to effects of anisotropy the complete front establishes only at one side before it begins to move from its origin into the direction of the specimen's center. During unloading from both sides of the transformed region transformation fronts run to the center of the transformed material and finally collide. This restores the original configuration. The entire material behavior is quite the same as for the short specimen.

The extended model is applied to the spring, too. The resulting distribution can be found in Fig. 6.29. Similarly to the basic model austenite evolves at the inner parts of the spring.

Again, the zone with maximum transformation is located in the center of the unwound wire. This result is reasonable since there are no stress peaks due to supports which influence the phase transition. Main loading is due to shear which is of quite constant intensity in the entire spring. Thus, the transformation is rather smooth such as in the basic model. However, the effect of the field function is evident. The entire distribution of austenite is spread in a smooth way. Although the underlying material model works on the GAUSS point level the results are now - due to the field coupling - similar as it would have been using a phase field model. Of course, since only the average amount of austenite is coupled to the field function  $\varphi$  which is used here, only this single 'phase' has to be solved on the nodal level. In contrast to a real phase field model where all the phases would have been discretized individually by means of individual field functions, in this model only the single field function is sufficient to create a phase field character for the entire model. All further field functions are of no need due to the coupling of the volume fractions at the GAUSS point level.

The resulting global material reaction is displayed in a stress-strain diagram, see Fig. 6.30. Similar to the results for the basic model in Fig. 6.16 a very smooth transition occurs without any distinct kink. A detailed comparison with the result for the basic model yields the inside that the values are quite comparable to the results at 60° C in the basic model. This is surprising at first glance since same values as for the tension test at for 22° C room temperature have been used. The effect can be explained by the specific values used in the basic and the extended model: the starting value in the extended model,  $r_{Af}$ , has app. double the value as the dissipation parameter  $r$  in the basic model. On the other hand, the chemical energy was chosen to be app. half the value as in the basic model to display the experimental observations for tension tests. Due to the used values and the structure of the model (see the yield condition), it is reasonable that similar results appear although this is not very physical. Hence, the reason for this quite strange behavior does not lie solely in the chosen parameters for the model. Rather the *manner* how the phase transformation takes place is

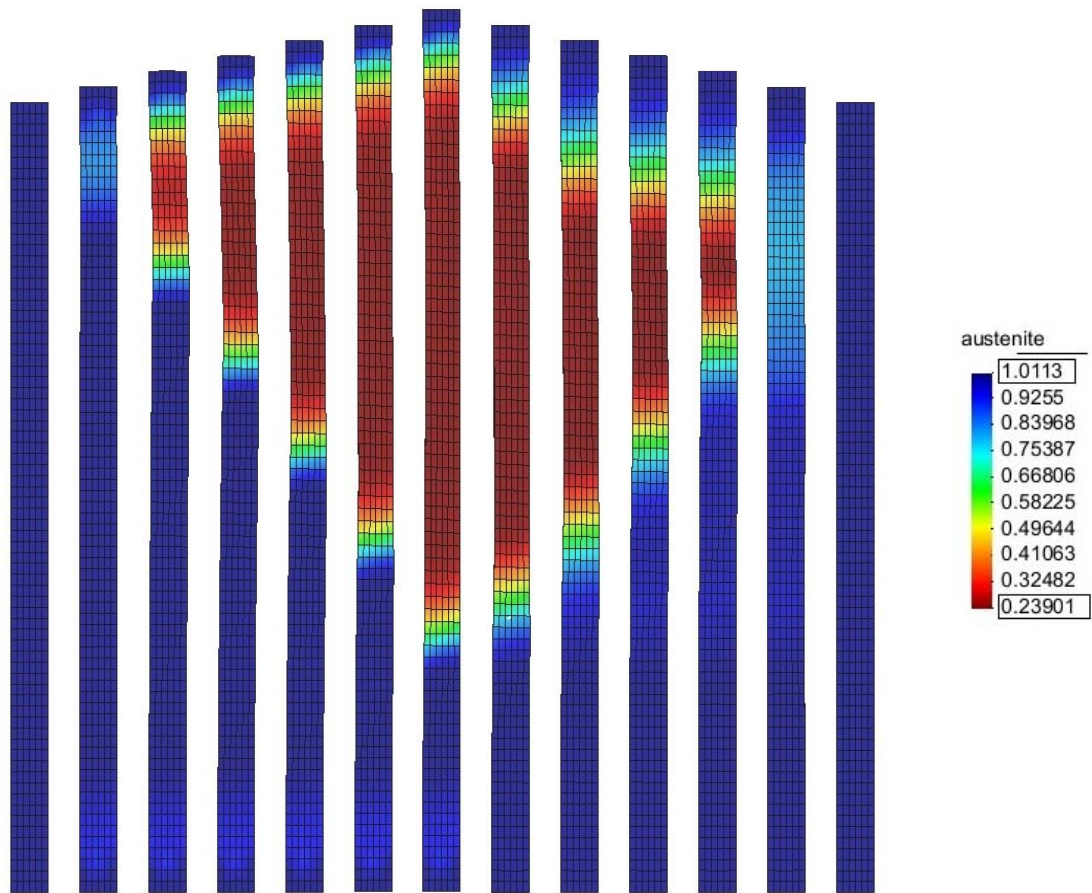


Figure 6.27: Extended model. Distribution of austenite in a stripe of NiTi at 22° C. Free length is 70 mm, regularization with  $c_\varphi = 0.01$  [GPa].



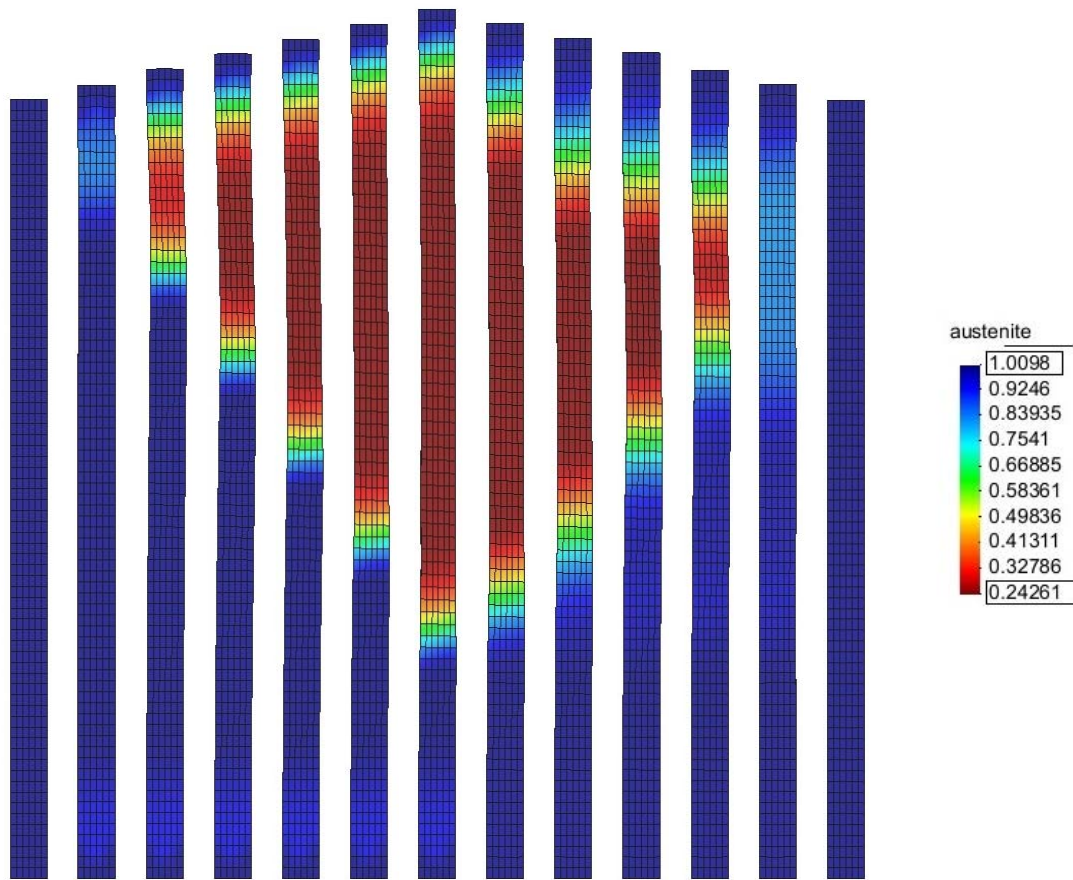


Figure 6.28: Extended model. Distribution of austenite in a stripe of NiTi at 22° C. Free length is 70 mm, regularization with  $c_\varphi = 0.03$  [GPa].

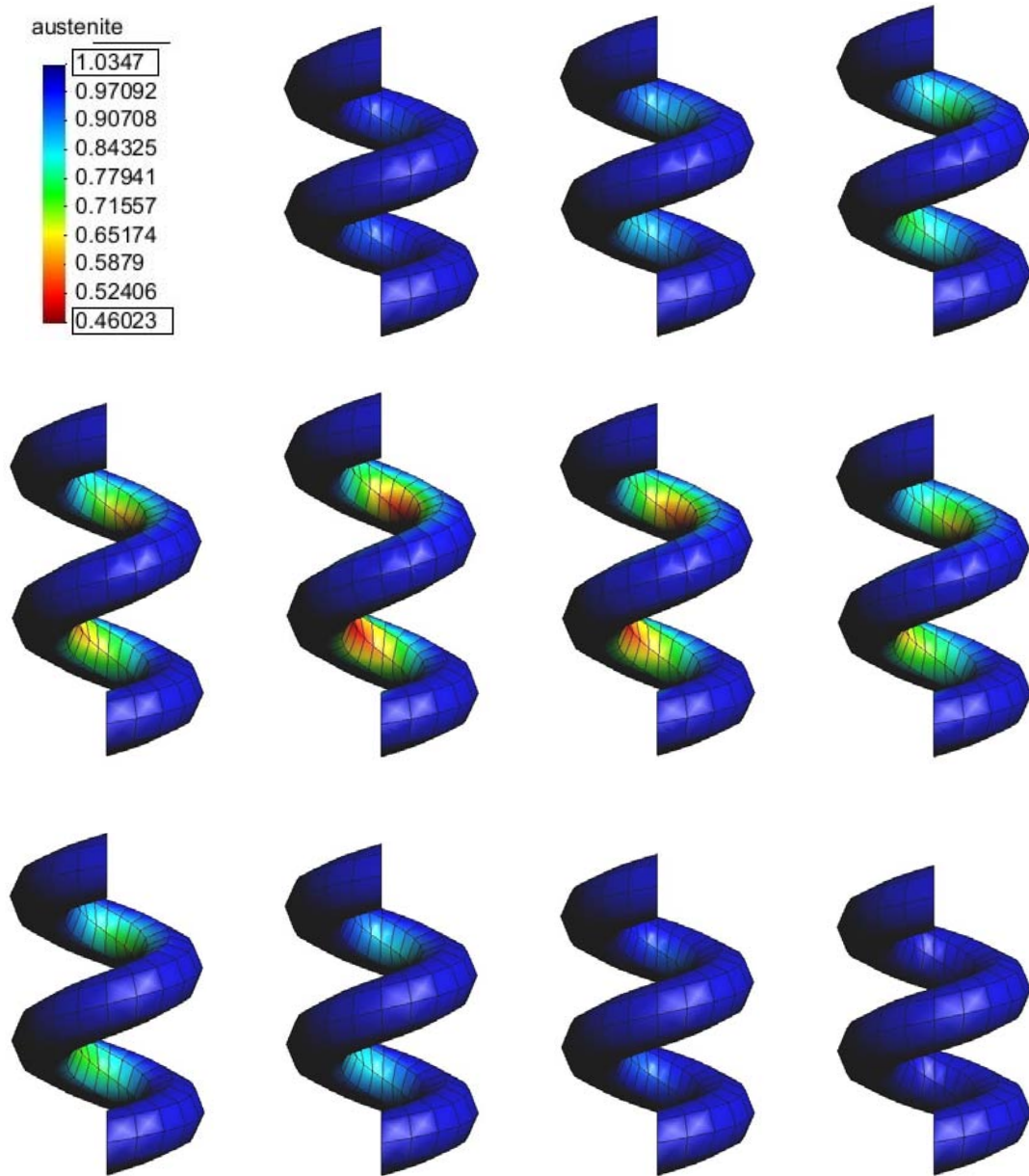


Figure 6.29: Extended model. Distribution of austenite in a spring of NiTi at 22° C. Regularized with  $c_\varphi = 0.01$  [GPa]. Time runs row wise.

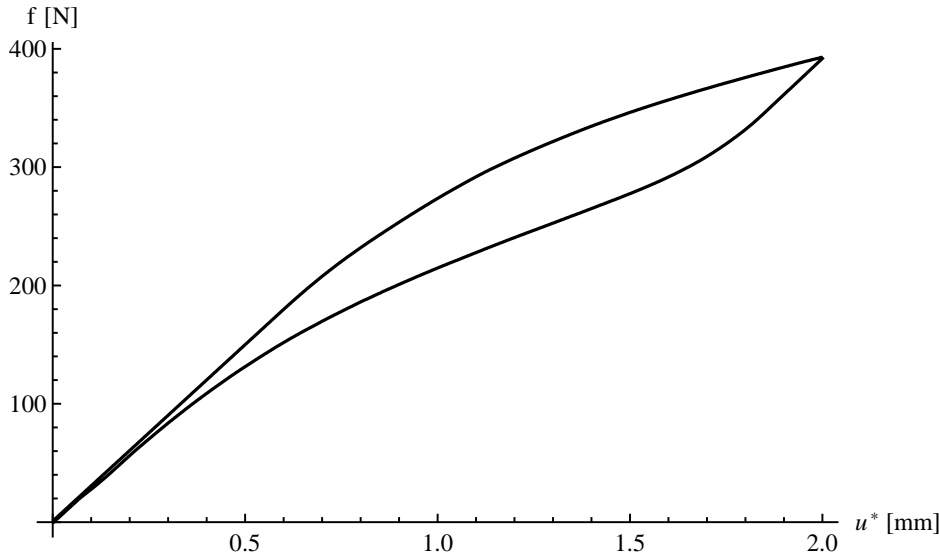


Figure 6.30: Extended model. Force-displacement diagram for a spring of NiTi at 22° C. Regularized with  $c_\varphi = 0.01$  [GPa].

important. In both cases, for the basic as well as for the extended model, a very homogeneous phase transformation takes place in the case of the spring. In contrast, in the tension test a localization occurs in the extended model. This is accompanied by a remarkable softening in the stress-strain diagrams for the tension test for which the parameter  $r_{A_f}$  has to be set quite high so that the final plateau coincides with the experimental observation. Since there is no localized but homogeneous phase transition in the spring there is no remarkable drop of stresses in the force-displacement diagram. In combination with the explained set of model parameters the resulting curve for the spring in the force-displacement diagram for the extended model has to be quite the same as for the basic model at higher temperatures.

Concluding, the extended model is able to display the localized transformation fronts moving forward during loading and backward during unloading which are well known from experiments. This effect was achieved by non-constant parameters for the dissipation which yield a softening character and deductively mesh dependent results. The applied method of regularization was successful to yield results which are independent of the finite element discretization. After a remarkable drop of stresses, the resulting material behavior on the global level, investigated in the space of stresses and strains, is in good agreement to experimental data. However, if no localized phase transformation occurs due to boundary and geometry reasons the extended model yields remarkable too high forces, see the example of a spring. Hence, if no investigations about the local material reaction are made the basic model should be used since here the dissipation is not as much spatial dependent as in the extended model. On the other hand, to be sure that no localized phase transformations occur in a specific specimen first calculations with the extended model are recommended. The effect of the dependence of the extended model on localized phase transformations is extinct by the thermo-mechanically coupled model for which numerical results are presented in the upcoming section.

## 6.3 Numerical Results for the thermo-mechanically coupled Model

For the case of including the non-isothermal character of phase transformations in shape memory alloys, the thermo-mechanically coupled model is applied - like the previous models - first to basic problems which serve as validation to experiments. As initial problem a heating-cooling experiment is simulated which gives rise of an approach how to interpret and - even more interesting - how to *estimate* the dissipation coefficient which has been assumed quite arbitrarily before. After the prove of the model's quality, the example of the spring is presented for the thermo-mechanically coupled model.

### 6.3.1 Evaluation on the GAUSS point level

As short preface, the material model is evaluated on the material point level for a purely thermal load and with a *constant* dissipation parameter  $r = 0.01137$  [GPa]. Hence, temperature is changed over time and serves as given input for the model for which an evaluation of the heat conduction equation according to Eq. (4.76) is not necessary. In Fig. 6.31

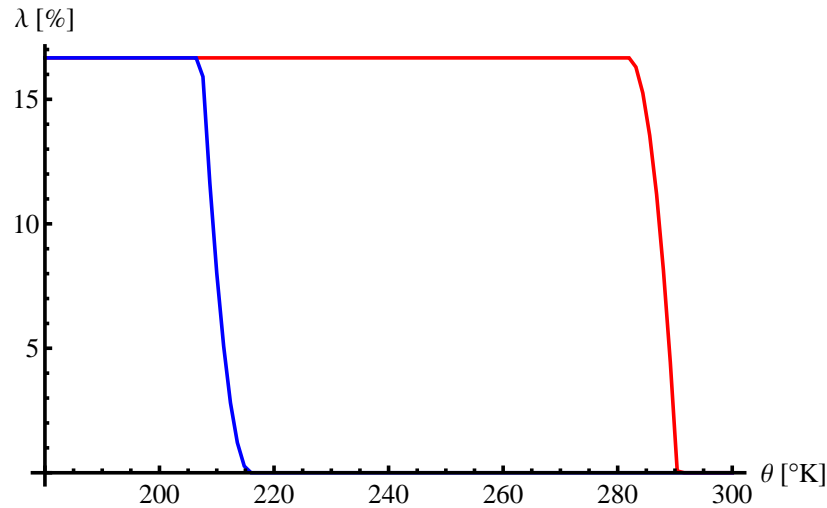


Figure 6.31: Phase fraction of one martensitic variant over time. Red curve is during heating, blue curve during cooling.

the resulting distribution of one martensite phase in CuAlNi is shown. This alloy shows a cubic-orthorhombic phase transformation. In this case there exist six different martensitic variants ( $n = 6$ ). From energetic considerations it is obvious that the volume fraction of that particular martensitic phase equals  $1/n$ , again with  $n$  as number of martensitic variants, see Sec. 4.2.1 and Fig. 4.10. Differently to the schematic plot in Fig. 4.10, the transformation between austenite and martensite does not take place immediately but quite smoothly over a small temperature interval. This fact comes from the inclusion of dissipation in the model - dissipation has been neglected in the schematic plots due to simplicity.

Without any further modifications, the model provides the attribute of showing a hysteresis which is well known from experiments, Fig. 6.33.

From this result the value for the quite arbitrary introduced dissipation coefficient  $r$  can be derived in terms of entropy and enthalpy differences analytically which is presented in the next section.

### 6.3.2 Estimation of the dissipation coefficient $r$ from experiments

The observation of hysteresis in the diagram volume fraction over temperature yields the idea to calculate the dissipation parameter from experimentally determined quantities. In order to do so, the condition that the yield function  $\Phi$  equals zero when phase transformation takes place is recalled. For the special case of thermal loading this means that the active deviator has the form

$$\text{dev}_{\mathcal{A}^j} P_i^j = \begin{cases} P_0^j - \frac{1}{n+1} \sum_{i=0}^n P_i^j & \forall j, i = 0 \quad (\text{austenite}) \\ P_{i>0}^j - \frac{1}{n+1} \sum_{i=0}^n P_i^j & \forall j, i > 0 \quad (\text{martensite}) \end{cases} \quad (6.1)$$

Here, the driving forces are only the chemical energies (no mechanical loading) which are the same for all martensitic variants and do not depend on the orientation  $j$ . Same is valid for the active phase. All the phases become active in this case. Then, the driving forces are renamed to  $P_A$  for austenite and for martensite  $P_M$ . Hence, the deviator reads

$$\begin{aligned} \text{dev}_{\mathcal{A}^j} P_i^j &= \begin{cases} P_A \left(1 - \frac{1}{n+1}\right) - \frac{n}{n+1} P_M & \forall j, i = 0 \\ P_M \left(1 - \frac{n}{n+1}\right) - \frac{1}{n+1} P_A & \forall j, i > 0 \end{cases} \\ \Leftrightarrow \text{dev}_{\mathcal{A}^j} P_i^j &= \begin{cases} \frac{n}{n+1} (P_A - P_M) & \forall j, i = 0 \quad (\text{austenite}) \\ \frac{1}{n+1} (P_M - P_A) & \forall j, i > 0 \quad (\text{martensite}) \end{cases} \end{aligned} \quad (6.2)$$

Inserting this result in the condition for transformation gives

$$\begin{aligned} \Phi &\stackrel{!}{=} 0 \\ \Leftrightarrow \left[ \sum_{j=1}^N \frac{1}{\xi^j} \sum_{i=0}^n (\text{dev}_{\mathcal{A}^j} P_i^j)^2 \right] &= r^2 \\ \Leftrightarrow \left( \frac{n}{n+1} \right)^2 (-c_A + c_M)^2 + \frac{n}{(n+1)^2} (-c_M + c_A)^2 &= r^2 \\ \Rightarrow r &= \sqrt{\frac{n}{n+1}} |\Delta c| \end{aligned} \quad (6.3)$$

with  $|\Delta c| = |c_A - c_M|$  and the chemical energies at transformation temperature for austenite  $c_A$  and martensite  $c_M$ , respectively.

In Fig. 6.32 the chemical energies for both austenite and martensite are presented.

From the approach of [28], see Eq. (4.69), it is clear that the difference in the chemical energies for austenite and martensite is a linear function with temperature as argument, namely

$$\Delta c(\theta) := \Delta a - \Delta b \theta \quad (6.4)$$

where  $\Delta a = a_0 - a_{k>0}$ ,  $\Delta b = b_0 - b_{k>0}$  and some arbitrary martensitic phase  $k$  (all the martensitic phases have the same values for  $a_{i>0}$  and  $b_{i>0}$ ). According to Eq. (6.3), the dissipation coefficient equals the absolute differences of the chemical energies, despite the factor  $(n/n+1)^{1/2}$ . Since the chemical energies and their difference are functions of temperature, the dissipation coefficient cannot be a constant value. This fact coincides with the experimental observation in Fig. 6.33, [12].

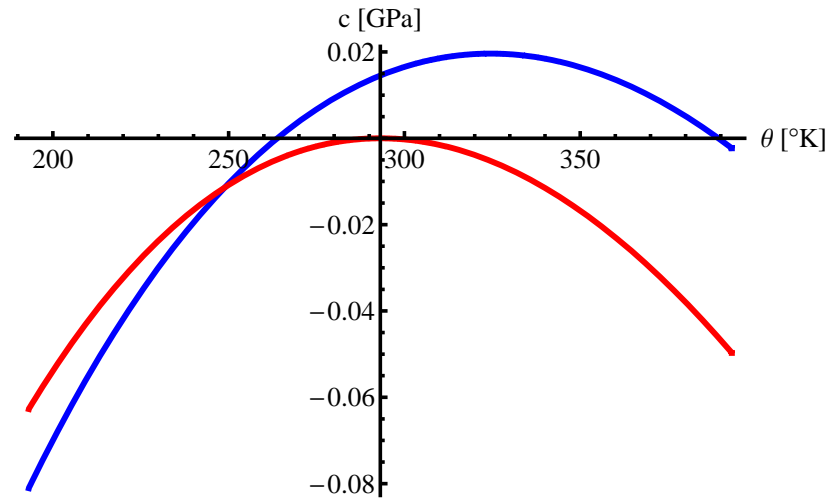


Figure 6.32: Chemical energies in dependence of temperature. Energy for austenite is plotted in red, blue indicates the martensitic energy.

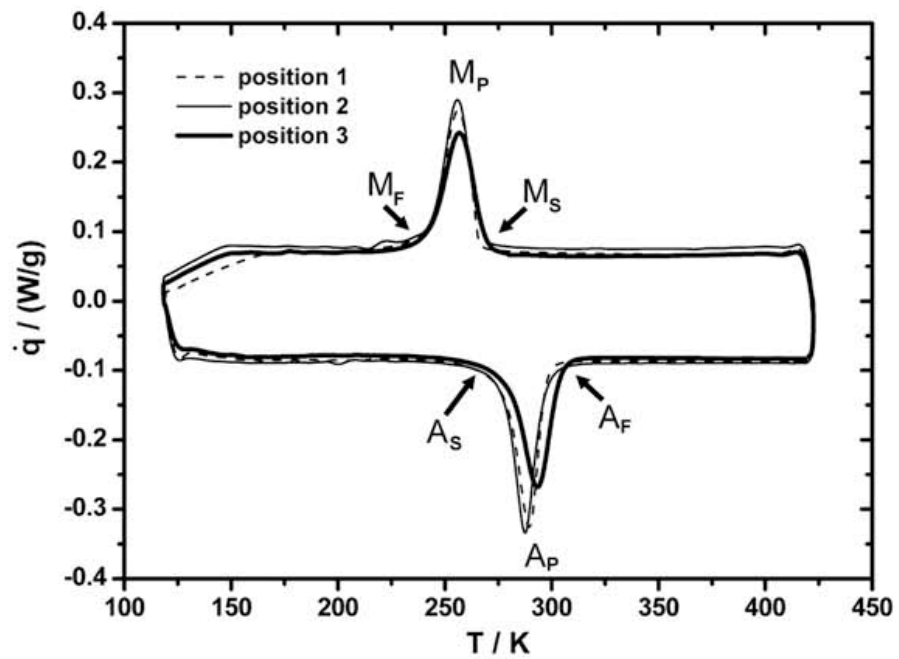


Figure 6.33: DSC curve for NiTi with marked phase transformations, [12].

There, a result of a DSC measurement is plotted from which the transformation over temperature can be derived: When the peaks in the heat flux occur, phase transformation takes place. Thus, it is obvious that the *temperature interval* in which transformation happens is of unequal length: the bounds are  $\theta_{A_s}$  for the beginning and  $\theta_{A_f}$  for the end of a martensite  $\rightarrow$  austenite transformation, and  $\theta_{M_s}$  for the beginning and  $\theta_{M_f}$  for the end of an austenite  $\rightarrow$  martensite transformation. This fact gives an additional hint that  $r$  cannot be constant.

Unfortunately, no satisfactory scheme for the calculation of the chemical energies nor their differences could be found in the literature. However, if they would be known the dissipation parameters were known immediately, too. Then, the transformation temperatures can be taken from experiments to calculate

$$\begin{aligned} r_{A_s} &= |\Delta c(\theta_{A_s})|, & r_{A_f} &= |\Delta c(\theta_{A_f})| \\ r_{M_s} &= |\Delta c(\theta_{M_s})|, & r_{M_f} &= |\Delta c(\theta_{M_f})|. \end{aligned} \quad (6.5)$$

Due to the different temperature intervals for thermally driven phase transformation, temperature cannot be the variable describing the dependence of  $r$ . In fact, the parameter chosen best is the average amount of austenite, like in the approach for the extended model. This average amount of austenite will change its value during phase transformation from 0 to 1 or the other way round, without any direct dependence on the temperature interval. Hence,  $|\lambda_0|$  may be interpreted as mathematical parameter describing both temperature intervals. Furthermore, there exists obviously the possibility to transform from martensite to austenite (during heating) and backwards from austenite to martensite (during cooling). In both cases, the volume fraction of average austenite changes between the same boundaries. However, the differences in the chemical energies are not equal as pointed out before. So, an additional parameter is needed in order to distinguish between these two cases. Obviously, the *direction* of  $(|\lambda_0|)$ , precisely  $\text{sign}(|\lambda_0|)$ , changes. Hence, this parameter is taken into account by formulating the dissipation coefficient as

$$r(|\lambda_0|, \text{sign}(|\lambda_0|)) = \sqrt{\frac{n}{n+1}} \begin{cases} r_{A_s} + (r_{A_f} - r_{A_s})|\lambda_0| & , \text{sign}(|\lambda_0|) > 0 \\ \min\{r_{A_s}, r_{M_s}\} & , \text{sign}(|\lambda_0|) = 0 \\ r_{M_f} + (r_{M_s} - r_{M_f})|\lambda_0| & , \text{sign}(|\lambda_0|) < 0 \end{cases} \quad (6.6)$$

Using this non constant dissipation coefficient and performing the same calculation as for the example according to Fig. 6.31 the result is in very nice agreement to the experimental data, see Fig. 6.34, where the starting and finishing temperatures for austenite and martensite were chosen to be  $\theta_{A_s} = 265.0$  [K],  $\theta_{A_f} = 280.0$  [K],  $\theta_{M_s} = 230.0$  [K] and  $\theta_{M_f} = 210.0$  [K].

Summarizing, until here the presented approach for the dissipation coefficient is capable to describe in a thermodynamically convincing way and furthermore based only on experimental data the transformation between the crystallographic phases austenite and martensite in both directions. Additionally, the exact values for both  $\Delta a$  and  $\Delta b$  are not important – same results will occur for different values. This is obvious since not only the dissipation parameter depends on it but also the chemical energies which are used in the material model.

On the other hand, the formulation of  $r$  is not completed yet. The argumentation executed for the extended model in Sec. 4.2.3 that nucleation of martensite costs more than its evolution in the case of pseudo-elasticity is not incorporated yet. The current approach

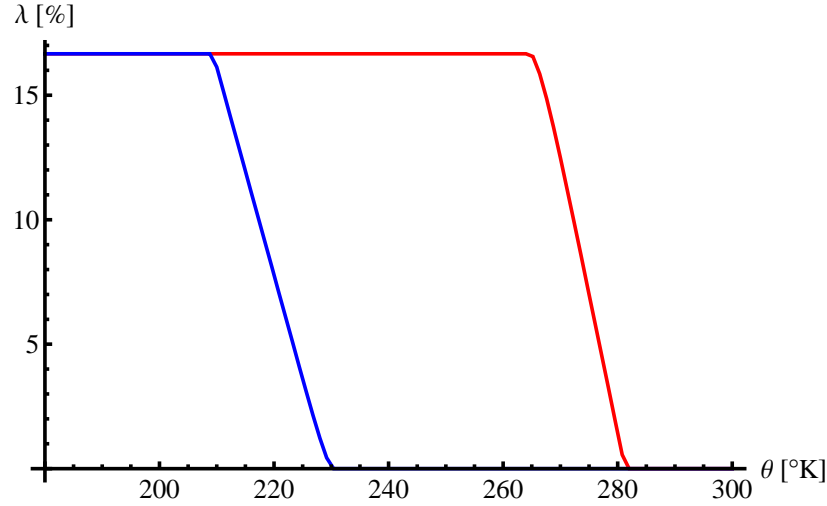


Figure 6.34: Phase fraction of one martensitic variant over time. Red curve is during heating, blue curve during cooling.

would yield a constant dissipation parameter, again. This is clear since 'pure' pseudo-elasticity - so starting from a purely austenitic crystal lattice - can only be performed when the surrounding temperature is above the finish temperature for austenite,  $\theta_{A_f}$ . So, the difference between the chemical energies has a constant value - if the heat production due to phase transformation is neglected for the moment.

In the case of pseudo-elasticity martensite evolves due to mechanical loading although austenite is the stable phase at that temperature. Hence, the approach for  $r$  - which was based only on thermal loadings - has to be modified. This is done in the way, that if the current temperature lies above  $\theta_{A_f}$  and *despite that fact*  $\text{sign}(|\lambda_0|) < 0$ , the dissipation has to be the curve chosen during heating which is now gone *backwards*. Same is valid during transformation from martensite back to austenite: then the curve from  $\theta_{M_s}$  to  $\theta_{M_f}$  has to be gone *backwards*, as well. This yields for the total dissipation parameter in dependence of  $|\lambda_0|$  and  $\text{sign}(|\lambda_0|)$  and accounting for  $\theta$

$$r(|\lambda_0|, \text{sign}(|\lambda_0|), \theta) = \sqrt{\frac{n}{n+1}} \begin{cases} r_{M_f} + (r_{M_s} - r_{M_f})|\lambda_0| & , \theta < \theta_{A_f} \wedge \text{sign}(|\lambda_0|) \leq 0 \\ r_{A_s} + (r_{A_f} - r_{A_s})|\lambda_0| & , \theta < \theta_{A_f} \wedge \text{sign}(|\lambda_0|) > 0 \\ r_{A_s} + (r_{A_f} - r_{A_s})|\lambda_0| & , \theta \geq \theta_{A_f} \wedge \text{sign}(|\lambda_0|) < 0 \\ r_{M_f} + (r_{M_s} - r_{M_f})|\lambda_0| & , \theta \geq \theta_{A_f} \wedge \text{sign}(|\lambda_0|) \geq 0 \end{cases} \quad (6.7)$$

The first two conditions of Eq. (6.7) are valid for room temperatures below the austenite finish temperature. The sign of the rate distinguishes - again - between austenite  $\rightarrow$  martensite and martensite  $\rightarrow$  austenite transformations. If the amount of austenite is zero and additionally its rate then the very first condition has to be taken which yields  $r = r_{M_f}$ , so the value for  $r$  for pseudo-plasticity.

The last two conditions account for pseudo-elasticity since here the approaches for  $r$  are exchanged according to the explanation above.

In combination, this formulation accounts for both pseudo-elastic and pseudo-plastic processes as well as heating and cooling.



### 6.3.3 Finite Element Results for the thermo-mechanically coupled Model

The intention is to have a model where the number of parameters is as small as possible. In other words, if there exists a relation between some parameters as derived in the previous section this relation should be used. Hence, due to the missing calculation of the differences in entropy and enthalpy between the different crystallographic phases they are simply chosen. It is possible to calculate the intersection point of the chemical energies just from

$$\Delta a - \Delta b \theta^* \stackrel{!}{=} 0 \quad (6.8)$$

which obviously yields

$$\theta^* = \frac{\Delta a}{\Delta b}. \quad (6.9)$$

It is clear that the start and finish temperature for martensite have to be smaller than  $\theta^*$  whereas those for austenite have to be greater. Hence, there exist the possible interval in which  $\theta^*$  may lie in. This is

$$\theta_{M_s} < \theta^* < \theta_{A_s}. \quad (6.10)$$

So, for the upcoming calculations  $\Delta a$  and  $\Delta b$  are chosen in a way that Eq. (6.10) is not violated. The parameters are collected in Tab. 6.2.

$\Delta a = -0.208199$ [GPa]	$\Delta b = -0.000775501$ [GPa]
$\theta^* = 268.47$ [K]	$\theta_R = 295.15$ [K]
$\theta_{A_f} = 291.79$ [K]	$\theta_{A_s} = 268.64$ [K]
$\theta_{M_f} = 233.47$ [K]	$\theta_{M_s} = 260.31$ [K]
$r_{A_f} = 0.0174$ [GPa]	$r_{A_s} = 0.0002$ [GPa]
$r_{M_f} = 0.026$ [GPa]	$r_{M_s} = 0.006$ [GPa]
$\beta_\varphi = 1.0$ [GPa]	$c_\varphi = 0.001$ [GPa]
$c_\theta = 0.0105$ [GPa/K]	$\alpha_\theta = 0.0075$ [mmK/W]

Table 6.2: Material parameters for the thermo-mechanically coupled model.

The transformation temperatures are taken from [12] and linearly interpolated to get values for a NiTi alloy with 50.9% Ni. No convincing measured values for the heat capacity nor the heat conductivity ( $\approx 1/\alpha_\theta$ ) could be found in the literature. Hence, they were chosen such that the experimental data was reached best. Due to the stabilizing influence of temperature the parameter for penalizing the gradient, which is  $c_\varphi$ , could be set relatively small. As mentioned before, the dissipation coefficients are calculated from the differences in entropy and enthalpy, the number of possible variants is  $n = 12$  for this alloy.

For the numerical simulations first investigations for the wire used already for the basic and the extended model are carried out. The result in the stress-strain diagram is presented in Fig. 6.35. Here, the dashed lines represent the experiments at different temperatures and the solid lines the associated simulations. It can be seen that there still exists some deviation between the individual plateau stresses. However, the principle character of the material behavior is displayed quite well. Although the model works with non-constant dissipation parameters there is no drop in the stresses at all. This is a great advantage compared to the extended model where this effect had some influence on the simulation of specimens which

do not show localized transformation zones due to their geometry and loading. Here, a very distinct kink occurs in the stresses when phase transformation initializes. The subsequent plateau is in rather perfect agreement despite the specific value. Only very slight slopes occur in the simulations which can be seen in a comparable way in the experiments as well.

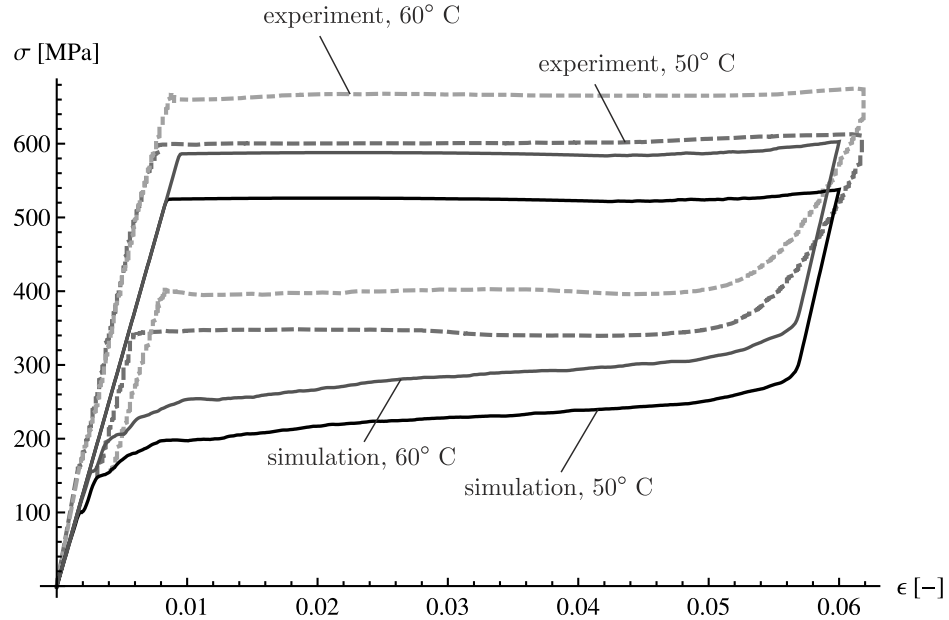


Figure 6.35: Thermo-mechanically coupled model. Stress-strain curves for a wire of NiTi at 50° C and 60° C. Dashed lines are experiments, solid lines are simulations.

During unloading the plateau is rather smooth. This is another improvement compared to the previous models since it coincides better to the experimental observations. Interestingly, the entire character of the material reaction which is in very nice agreement to experiments is incorporated in the model. Only difference between the two simulations was the respective starting temperature. Hence, a further investigation and even better estimation of the only two parameters  $\Delta a$  and  $\Delta b$  could improve the quantitative coincidence even more.

Next example is again the stripe of NiTi. The resultant material answer is depicted in Fig. 6.36. Only change between this simulation and the previous form Fig. 6.35 - despite the geometry - was the starting temperature. It can be seen that the general character of the material is simulated quite well. Similarly as in the previous result for the basic model there exists only a very slight softening in the stress-strain response. Temperature which is now an evolving variable stabilizes the austenite. Hence, the strong influence of the decreasing dissipation parameter and deductively the threshold for the yield function is damped. Again the experimental data is reached quantitatively not perfectly. Improvements in the values for the chemical energies could correct this. However, just by changing temperature and geometry the material model is able to predict the real behavior in a comparable manner as it could simulate the wires from Fig. 6.35.

The influence of different loading velocities can be observed in Fig. 6.36 as well. When a higher loading velocity is applied more heat is generated. This results in a smoother curve since all phase transformations are influenced by temperature. Particularly in the beginning of the plateau the stress is slightly higher because the rate of transformation is reduced due to the stabilizing effect of temperature to austenite. During unloading a line rather parallel to the abscissa shows up in the plateau.

Although only a very slight softening was observed in the stress-strain diagram the localizing phase transformations are desired as outcome since they are an experimental evi-

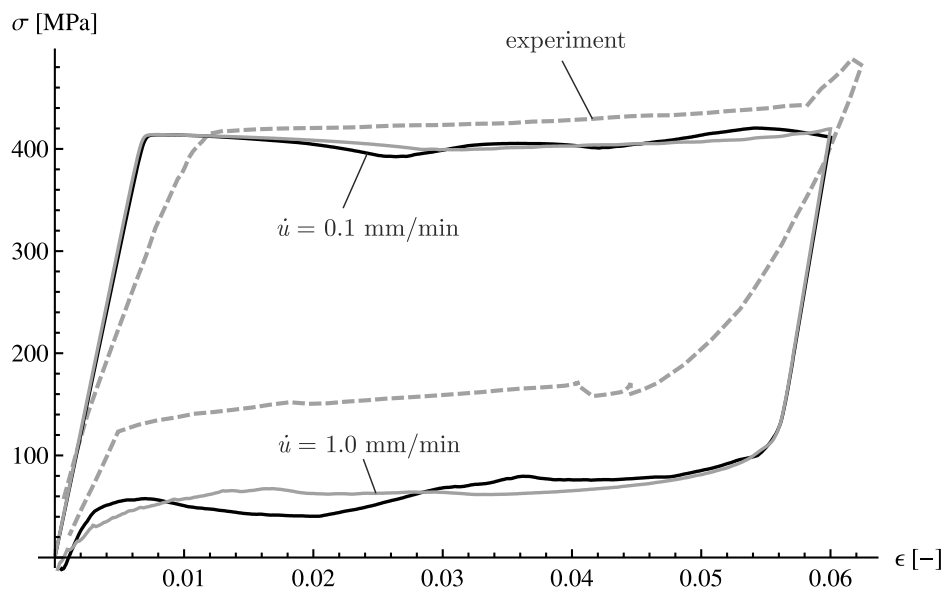


Figure 6.36: Thermo-mechanically coupled model. Stress-strain diagram for a stripe of NiTi at 22° C. Loading velocities are  $\dot{u}_{x_1} = 0.1$  [mm/min] (black curve) and  $\dot{u}_{x_1} = 1.0$  [mm/min] (gray curve).

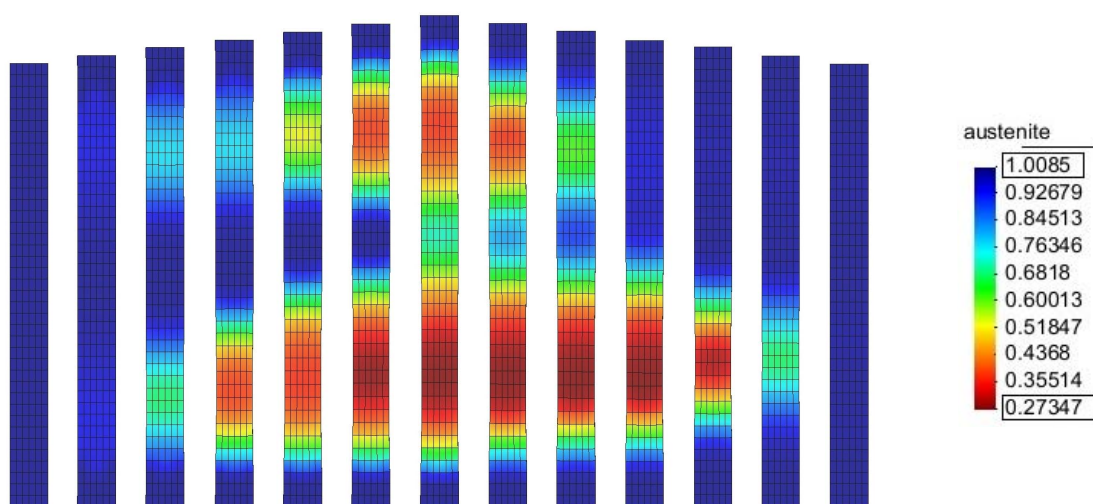


Figure 6.37: Thermo-mechanically coupled model. Distribution of austenite in a stripe of NiTi at 22° C. Loading velocity  $\dot{u} = 0.1$  [mm/min].

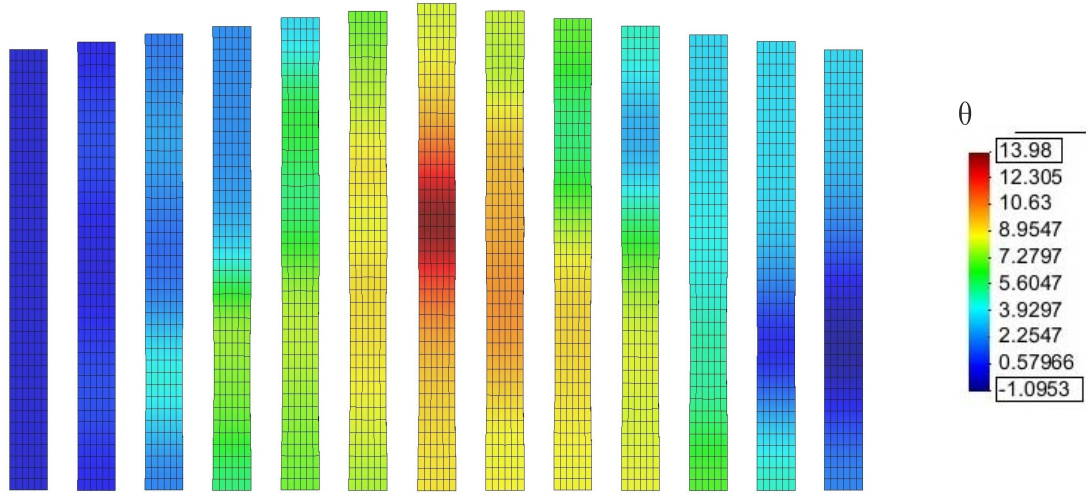


Figure 6.38: Thermo-mechanically coupled model. Distribution of temperature in a stripe of NiTi at 22° C. Loading velocity  $\dot{u} = 0.1$  [mm/min].

dence. In Fig. 6.37 the distribution of austenite over time in the specimen corresponding to the results of Fig. 6.36 can be seen. Here, the loading velocity was relatively small with  $\dot{u} = 0.1$  [mm/min]. The phase transformation starts - as well as in all previous tension examples - at the supports. In contrast to the basic model and the extended model, at both sides distinct localized transformation zones evolve. Due to the damping effect of temperature the small deviations in the elastic constants from a purely isotropic material in the beginning are smeared out. Consequently, at both sides fronts evolve. Still, the transformation zones do not move with the same velocity which is - again - due to the set of  $N = 30$  orientations.

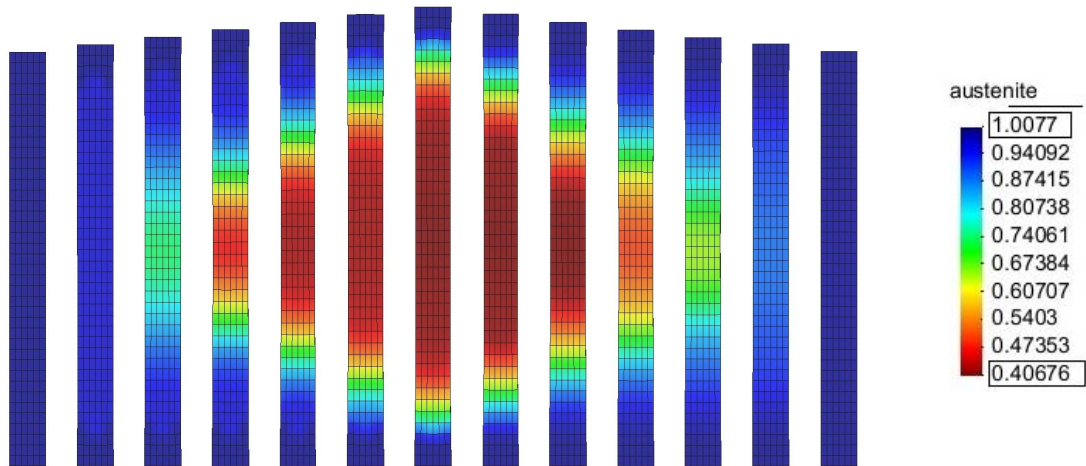


Figure 6.39: Thermo-mechanically coupled model. Distribution of austenite in a stripe of NiTi at 22° C. Loading velocity  $\dot{u} = 1.0$  [mm/min].

During unloading first the upper fronts vanish and afterwards the fronts in the lower parts collide. The amount of transformed material is of same order as in the extended model and much higher compared to the basic model.

In Fig. 6.38 the corresponding distribution of temperature is presented. Here, only the deviation from the start temperature is shown. Due to phase transformation heat is produced. Therefore, analogously to the evolution of martensite the temperature first increases quite localized. While the transformation zones are moving which serve as internal heat wells the

distribution of temperature is moving, too. Of course, due to its transient character the distribution of temperature is much more smeared out compared to the one of austenite. There occurs a peak in the distribution of temperature when the two heat fronts meet, compare to Fig. 6.2.

When the specimen is unloaded a phase transformation from martensite back to austenite takes place. According to this, the temperature is decreasing again. Since the entire process is dissipative there is a lower temperature in the specimen after complete unloading than in the original state. In reality this gap of heat would be compensated by a heat flux from the surrounding inside the specimen for which the model does not account for.

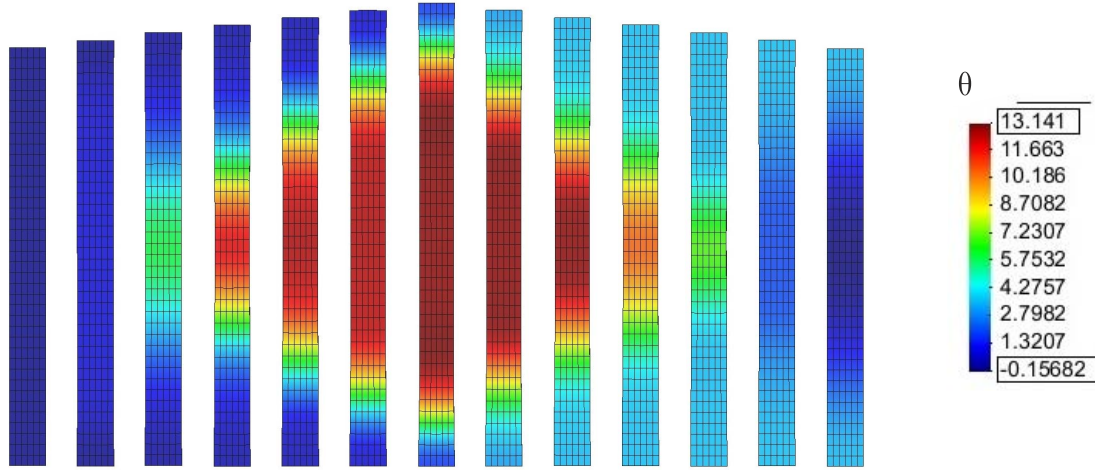


Figure 6.40: Thermo-mechanically coupled model. Distribution of temperature in a stripe of NiTi at 22° C. Loading velocity  $\dot{u} = 1.0$  [mm/min].

At higher loading velocities ( $\dot{u} = 1$  [mm/min]) the distribution of austenite is different, Fig. 6.39. Here, transformation initializes again at the supports but due to the high evolution of temperature its stopped quite immediately. In contrast, in the center of the specimen all further phase transition proceeds which comes from the fact that the temperature is minimal there. Two distinct transformation fronts evolve which move through the specimen in the direction of the supports. The influence of the relatively high temperature can be seen in the remaining amount of austenite. With a number of app. 40% it is quite high compared to the slow loading velocity. This is reasonable since temperature stabilizes the austenite and serves as driving force directed in the contrary direction than the mechanical ones. Thus, less material transforms.

During unloading both fronts move back in the center of the specimen and meet again there.

Figure 6.40 shows the evolution of temperature at high loading velocities. Again, temperature evolves strongly connected to the phase transformations. The maximum value for temperature is slightly lower than in the example of slow loading. The absolute value of its minimum is even remarkably smaller. However, the amount of produced heat is higher. This can be seen from the temperature which has the maximum and minimum value for a much broader expansion.

For a stripe with a free length of 70 mm the distribution of austenite is presented in Fig. 6.42. In all subsequent calculations the strain velocity was set to same values as for the short specimens so that the velocities vary between  $\dot{u} = 0.2$  [mm/min] and  $\dot{u} = 2.0$  [mm/min]. Here, the phase transformation starts at the lower end. Due to the stabilizing effect of temperature a second transformation zone in the upper part of the specimen evolves. Both zones



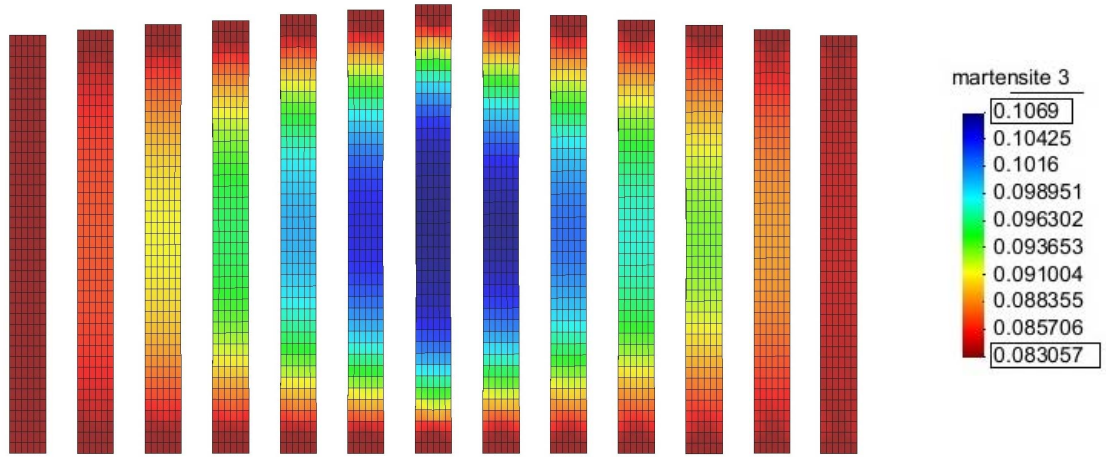


Figure 6.41: Thermo-mechanically coupled model. Distribution of averaged of all martensite three variants ( $\sum_{j=1}^N \xi^j \lambda_3^j$ ) in a stripe of NiTi at  $-40^\circ \text{C}$ . Loading velocity  $\dot{u} = 0.28 \text{ [mm/min]}$ .

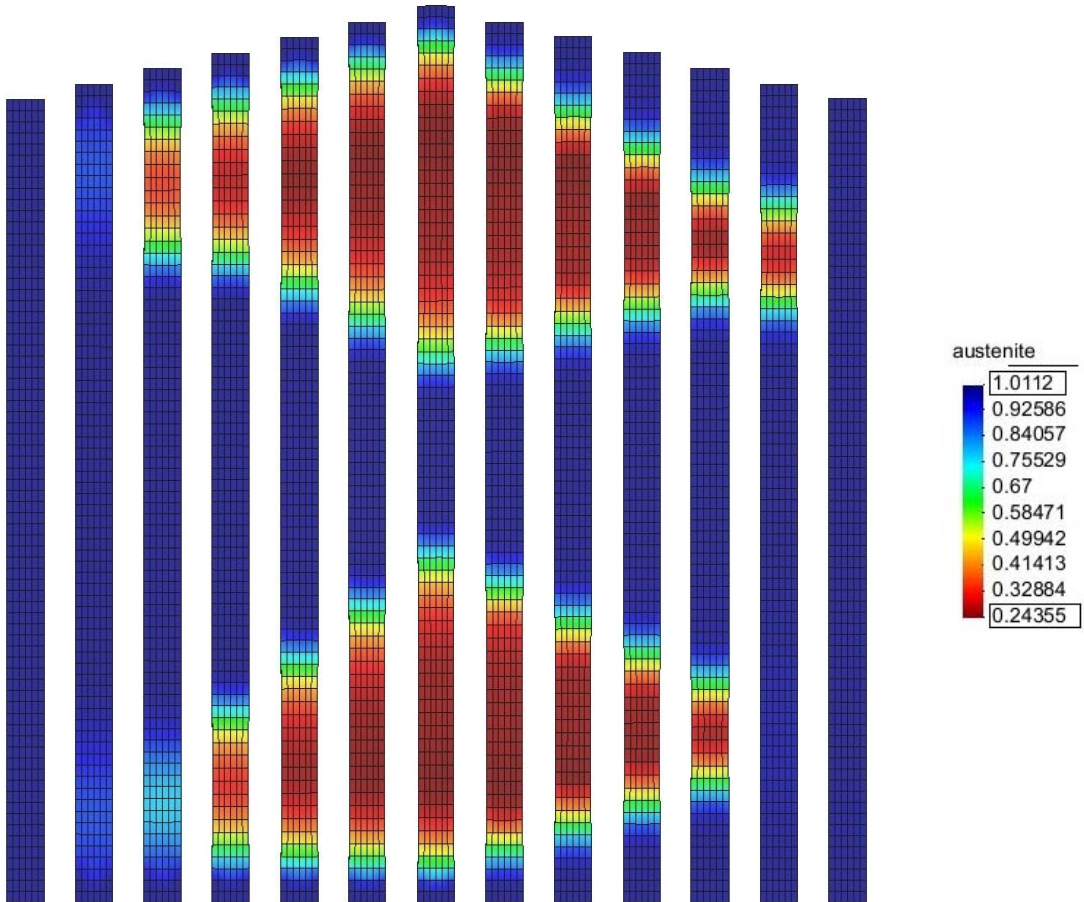


Figure 6.42: Thermo-mechanically coupled model. Distribution of austenite in a stripe of NiTi at  $22^\circ \text{C}$  with free length of 70 mm. Loading velocity  $\dot{u} = 0.2 \text{ [mm/min]}$ .

have a distinct transformation front. These fronts are moving from both ends to the center of the specimen. During unloading exactly these fronts move back to the supports where the transformation had initialized. The associated distribution of temperature in the stripe with free length of 70 mm is shown in Fig. 6.43. According to phase transformation temperature evolves first at the lower part. Then, it is increased in the upper part, too. While the transformation fronts are moving temperature is moving as well, exhibiting a distinct zone which separates the warm from the cool part. This is in good agreement to experimental observations, see Fig. 6.2. During unloading the edges of the hot part of the specimen which are located next to the center are cooled down. This is since the transformation zones are moving back to the supports.

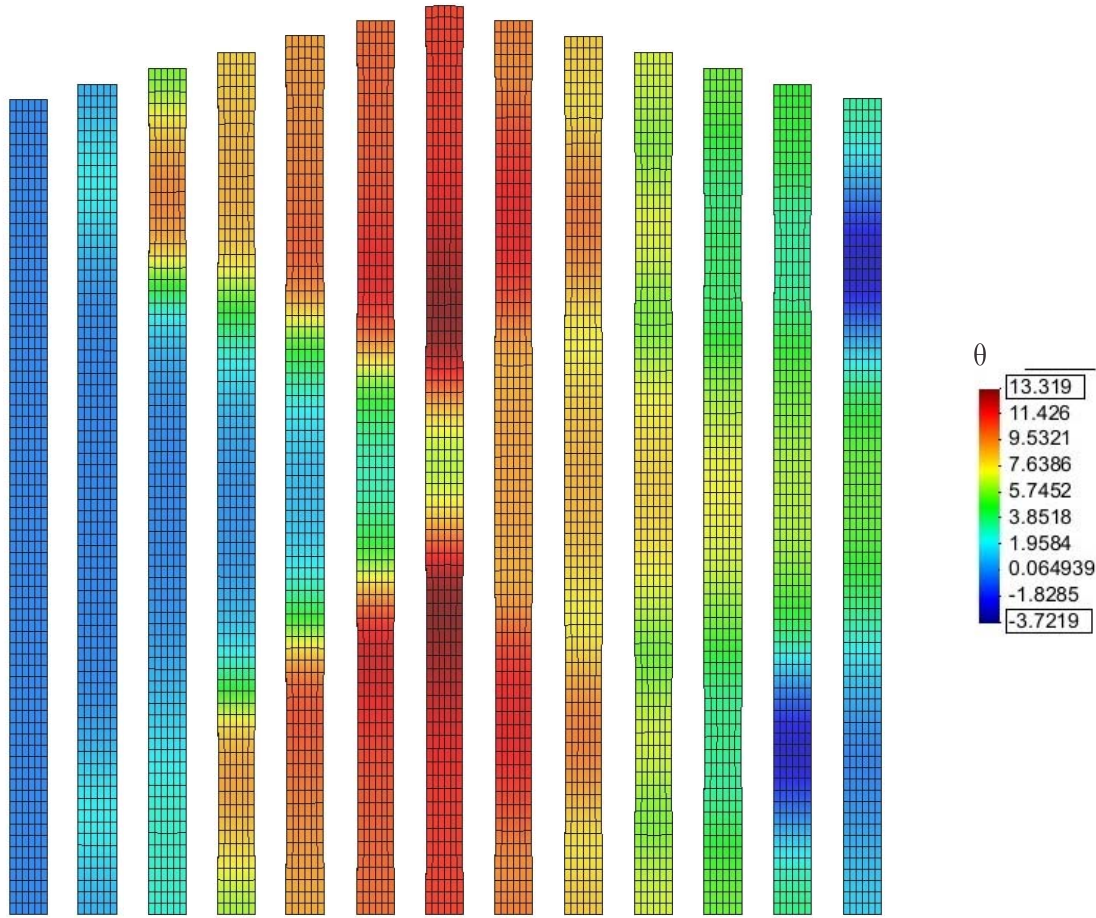


Figure 6.43: Thermo-mechanically coupled model. Distribution of temperature in a stripe of NiTi at 22° C with free length of 70 mm. Loading velocity  $\dot{u} = 0.2$  [mm/min].

Results for the same specimen but now with an increased loading velocity are presented in Fig. 6.44, distribution of austenite, and in Fig. 6.46, distribution of temperature. In contrast to the previous result at high loading velocity only one transformation zone evolves. Although temperature stabilizes again the austenite, due to the set of orientations it is still more favorable for the material to maintain only one transformation zone. Differently to the slow loading velocity the remaining amount of austenite is remarkably higher here. During unloading the same transformation front which has moved during loading is going backwards into the direction of the support.

The distribution of temperature shows a similar behavior like in the previous example. It is strongly in accordance with the phase transformations. During loading the material is heated up while unloading and the associated phase transformations cool the specimen

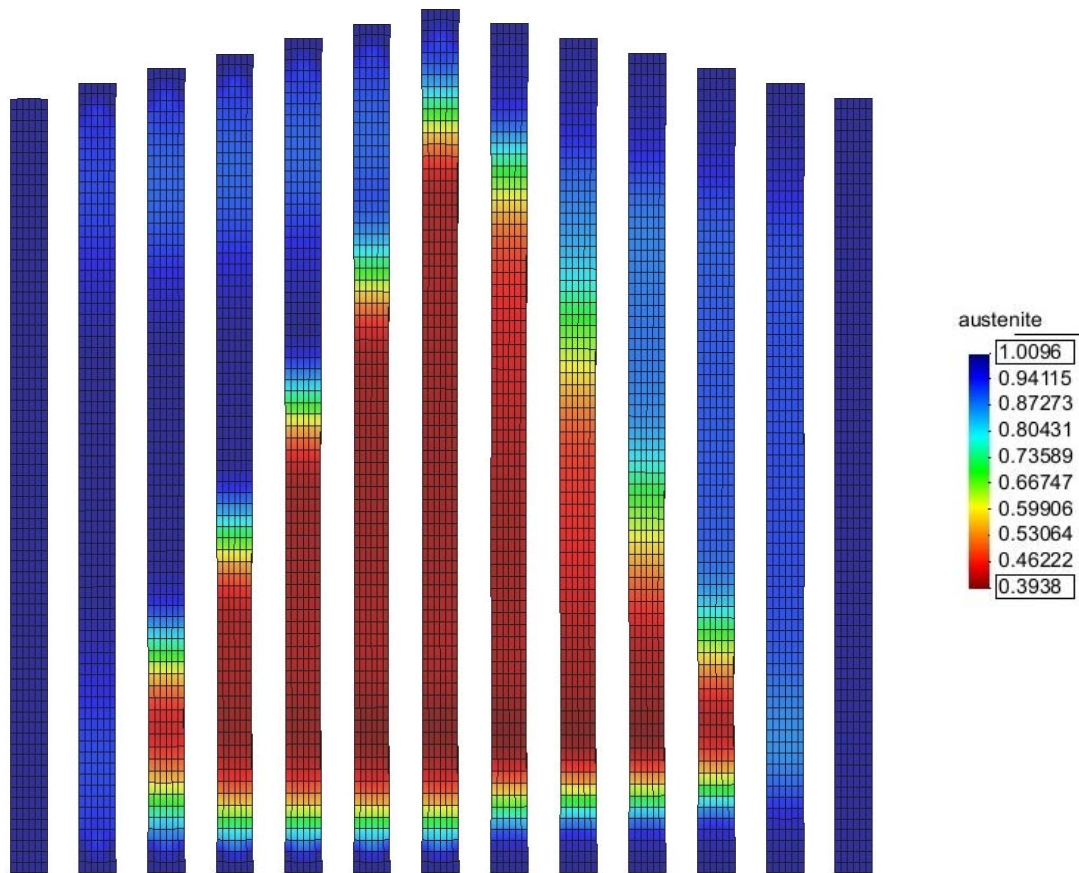


Figure 6.44: Thermo-mechanically coupled model. Distribution of austenite in a stripe of NiTi at 22° C with free length of 70 mm. Loading velocity  $\dot{u} = 2.0$  [mm/min].



again. The maximum heat produced in the material is quite the same as in the specimen with slow loading velocity. However, compared to the amount of transformed material the heat production is much higher. Although less martensite evolves in the specimen under fast loading the maximum enhancement of temperature is as high as in the case of slow loading.

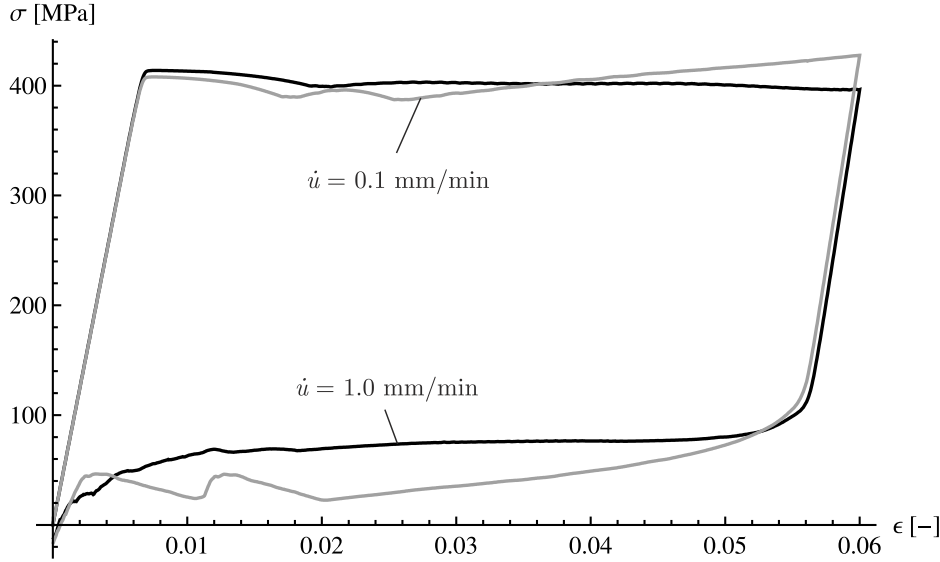


Figure 6.45: Thermo-mechanically coupled model. Stress-strain diagram for stripes of NiTi at 22° C with free length 70 mm. Loading velocities are  $\dot{u}_{x_1} = 2.0$  [mm/min] (black curve) and  $\dot{u}_{x_1} = 0.2$  [mm/min] (gray curve).

The entire material reaction is - again - represented in a stress-strain diagram, Fig. 6.45. In the case of slow loading there occur two regions of material softening in the stress-strain diagram. This coincides with the observation that two transformation zones are evolving. This happens in a row. Hence, the two small hills show up. After that, the material hardens which is slightly higher than expected. This results from the complex between stabilizing temperature and softening in the dissipation parameters. Due to the high temperature within the transformation zone the rate of phase transformation is reduced. On the other hand, a third transformation zone in the center does not evolve since temperature enhancement has spread to this region already. Therefore, a conflict between a simplified further transformation in the transformation zones where the temperature is quite high and an initializing transformation in the center where only austenite exists and temperature is relatively low. Since in both cases a transformation is impeded somehow the entire material reacts stiffer than expected. This effect is slightly neglected since in the case of fast loading some transformation at the upper part is able to compensate the 'missing' transformation in the main transformation zone.

In Fig. 6.47 the stress-strain diagram for the pseudo-plastic stripe is plotted. The elastic region is quite small. The transition from that region into the plateau is very sharp. The entire plateau has a very small slope and shows no softening due to the constant dissipation parameter.

Figures 6.41 and 6.48 show the evolution of martensite variant 3 and temperature, respectively. The room temperature was set to -40° C. Hence, pseudo-plastic material behavior occurred. The amount of martensite is just an averaging of all martensite 3 variants in all grains at each GAUSS point. Of course, martensite 3 is not a unique definition - still it gives

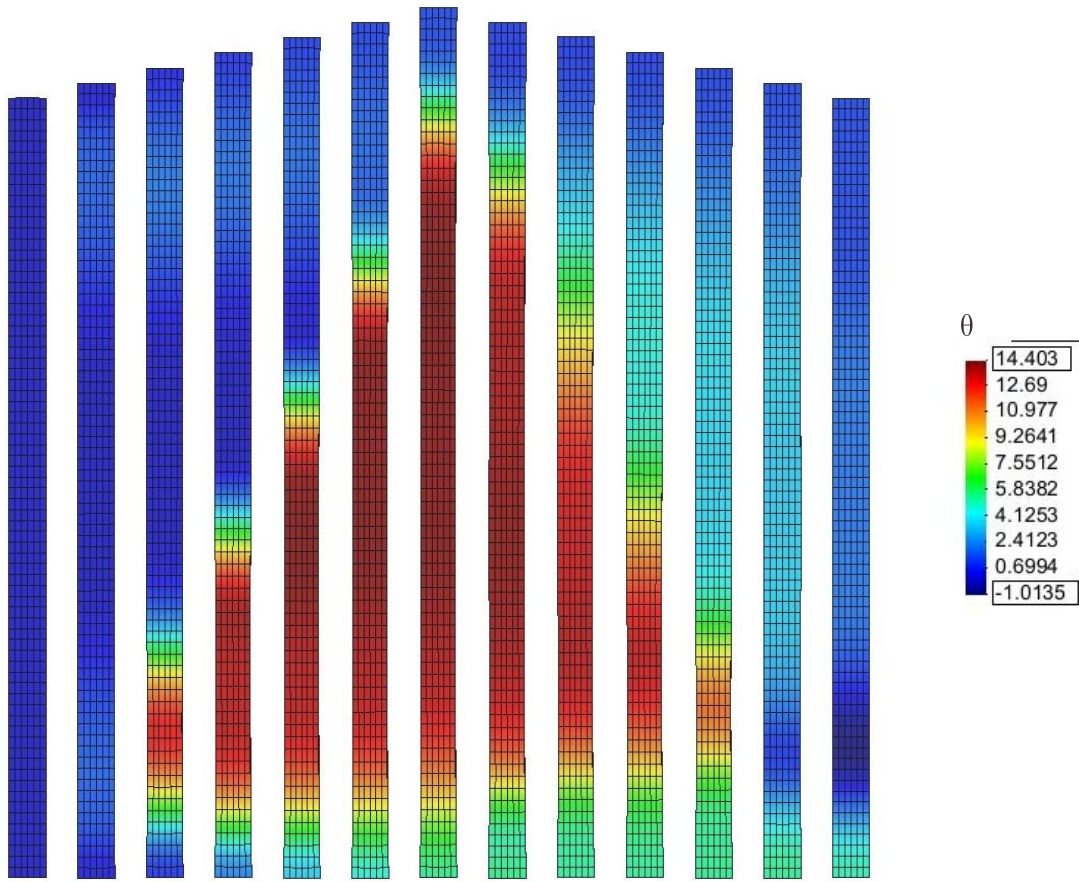


Figure 6.46: Thermo-mechanically coupled model. Distribution of temperature in a stripe of NiTi at 22° C with free length of 70 mm. Loading velocity  $\dot{u} = 2.0$  [mm/min].

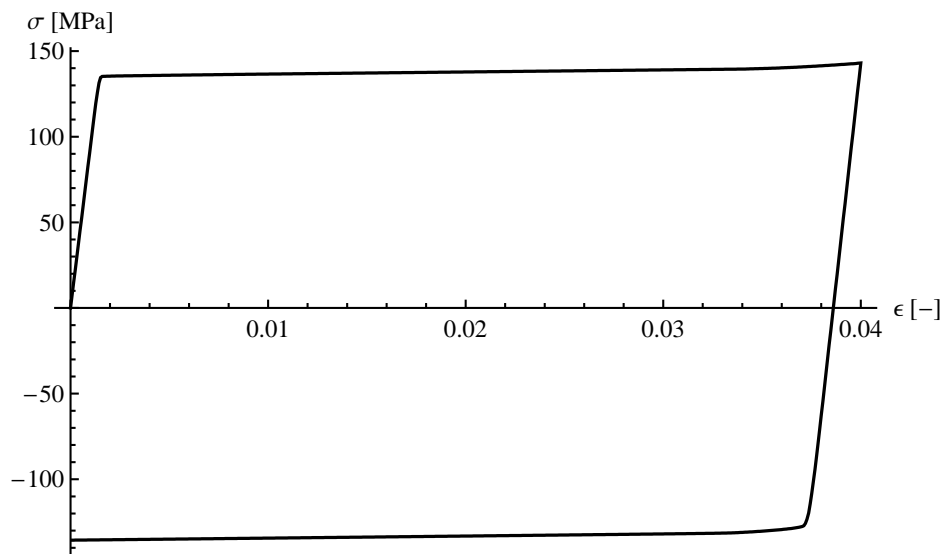


Figure 6.47: Thermo-mechanically coupled model. Stress-strain diagram for a stripe of NiTi at -40° C. Loading velocity is  $\dot{u} = 0.28$  [mm/min].

a hint how phase transformations evolve. The dissipation parameter is constant in this case, namely  $r = r_{M_f}$ . Consequently, the distribution of martensite reminds to the one received for the pseudo-elastic case with the basic model. Phase transformation starts at the supports and spreads rather homogeneously over the entire specimen.

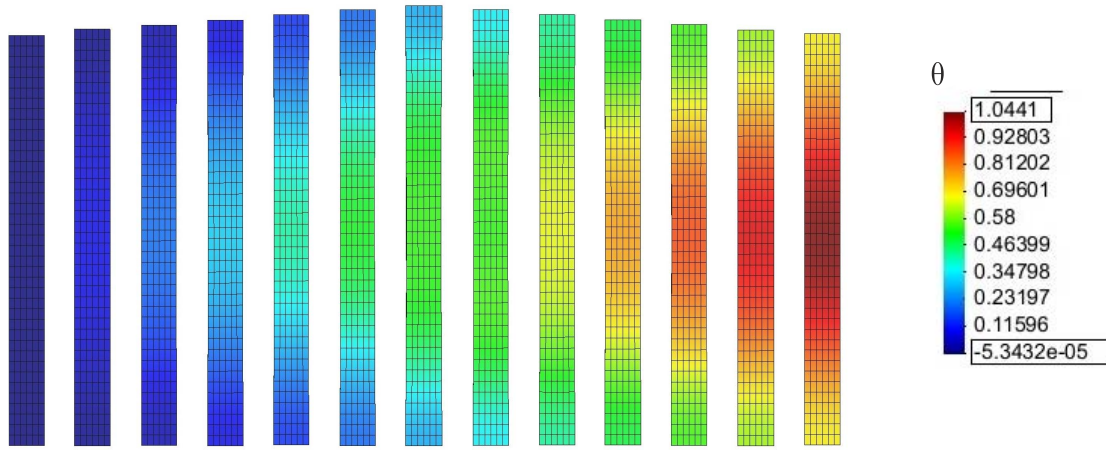


Figure 6.48: Thermo-mechanically coupled model. Distribution of temperature in a stripe of NiTi at  $-40^\circ \text{C}$ . Loading velocity  $\dot{u} = 0.28 \text{ [mm/min]}$ .

In the distribution of temperature a different effect than for the case of pseudo-elasticity can be observed. While in pseudo-elasticity a back transformation from martensite to austenite causes a decrease of temperature, the temperature in the case of pseudo-plasticity is just increasing, no matter whether the specimen is loaded or unloaded. This is in accordance to the fact that the original state is not restored during unloading but a certain combination of unevenly distributed martensitic variants. The absolute value for temperature is much smaller than in the case of pseudo-elasticity.

As the last geometric example simulations for the spring are executed. The numerical results for the case of pseudo-elasticity are presented in Fig. 6.49. Room temperature was set to  $22^\circ \text{C}$ . Similar to all previous examples including the spring most phase transformation takes place in the inner part of the spring, Fig. 6.50. Additionally, in the center of the unwound wire the maximum transformation is observed. Now, which is in strong contrast to the basic and the extended model, the remaining amount of austenite is only at app. 9%. This is app. only one fifth of the amount calculated by one of the other models. Although again a rather homogeneous load state is established due to the boundary conditions the transformation takes place quite distinct at the inner circle of the spring. The evolution of temperature is relatively small, Fig. 6.50. However, it is sufficient to force the material to transform at the inner circle in a more or less pronounced way. This happens on such a small volume that the heat produced here does not inhibit the transformation too much. In contrast, at different locations in the spring the mechanical driving forces are smaller and the temperature evolution too high that in these volumes phase transformation could occur in such a homogeneous way as in the other models. Hence, a more localized phase transformation takes place.

The temperature is the highest in the center of longitudinal axes of the spring. This causes the austenite to be more stable locally. Since the mechanical driving forces are the highest in the inner circle of the spring, here the localized phase transformations are ob-

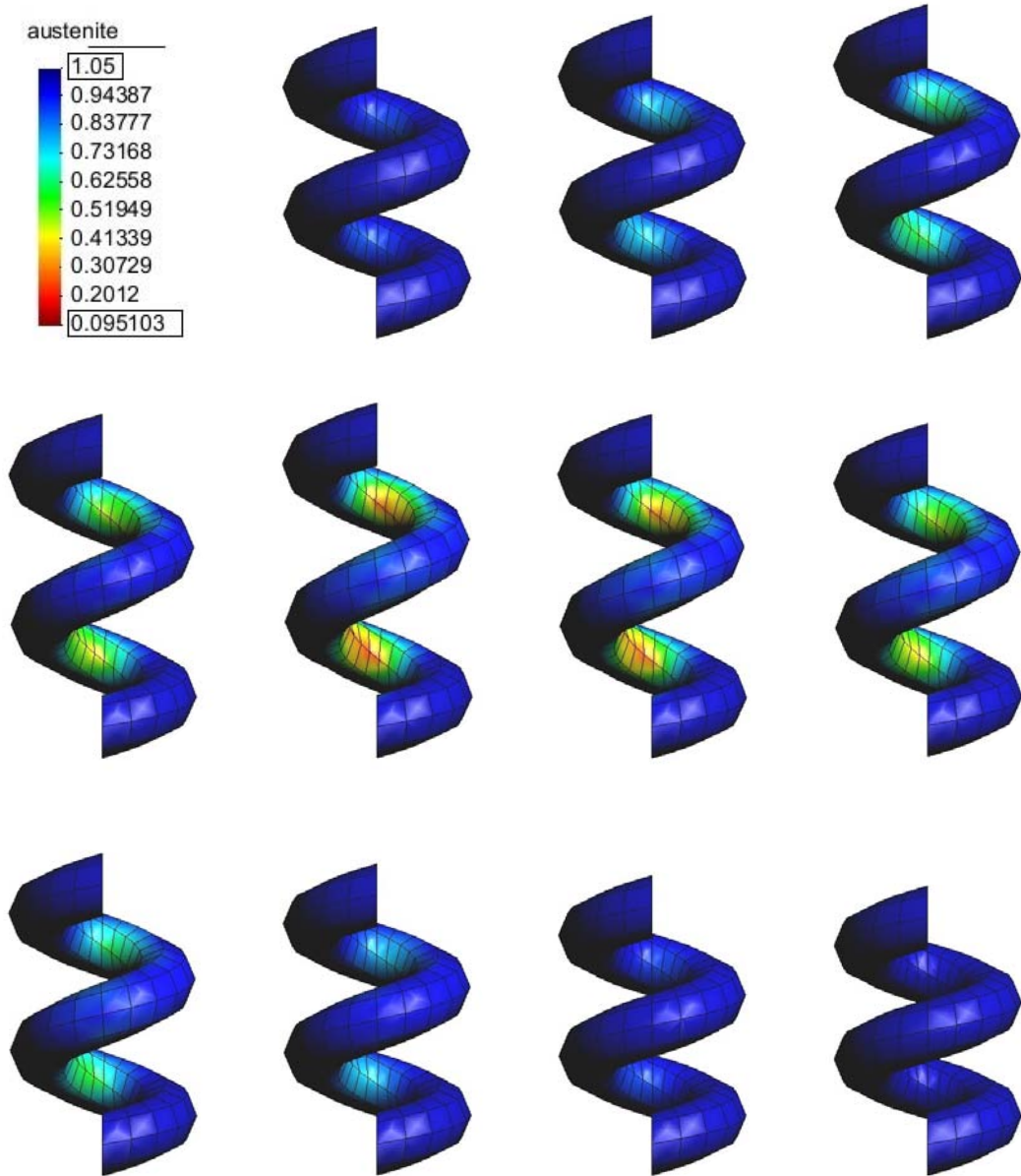


Figure 6.49: Thermo-mechanically coupled model. Distribution of austenite in a spring of NiTi at 22° C. Loading velocity  $\dot{u} = 0.4$  [mm/min].



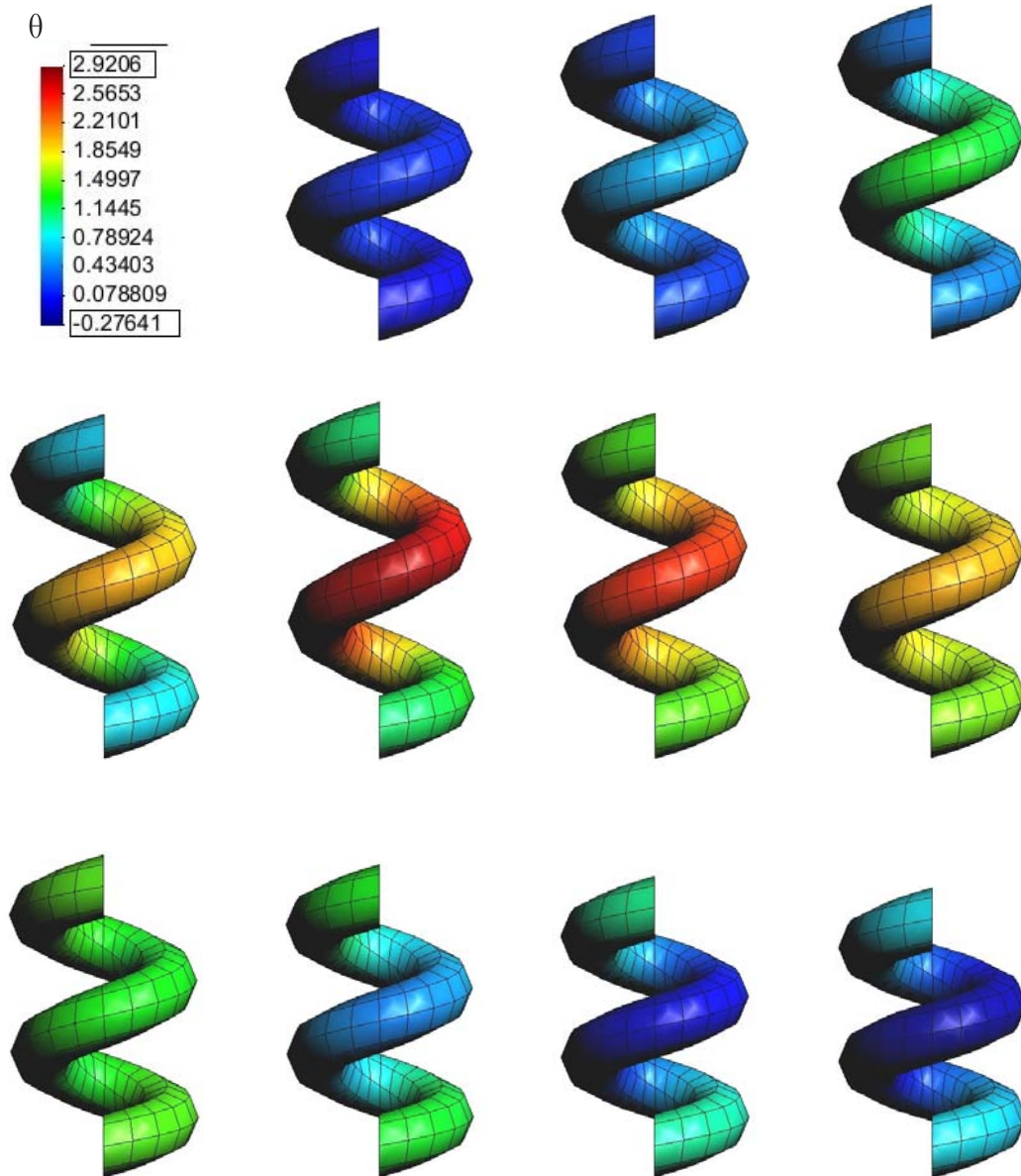


Figure 6.50: Thermo-mechanically coupled model. Distribution of temperature in a spring of NiTi at 22° C. Loading velocity  $\dot{u} = 0.4$  [mm/min].

served. During unloading temperature decreases again to a smaller value than in the initial state.

Figs. 6.51 and 6.52 show the result for a spring at  $-40^\circ\text{C}$  which behaves pseudo-plastically. In this case no austenite comes into play for which the average over the martensite six variant is plotted in Fig. 6.51. Again, this gives rather a hint where phase transitions take place not which variant exactly may be found. Similar to the previous results phase transformations occur mainly in the inner circle of the spring. Due to twisting in the spring the distribution of the average value for martensite is not even (more transition in the lower part, less transition in the upper part), see above.

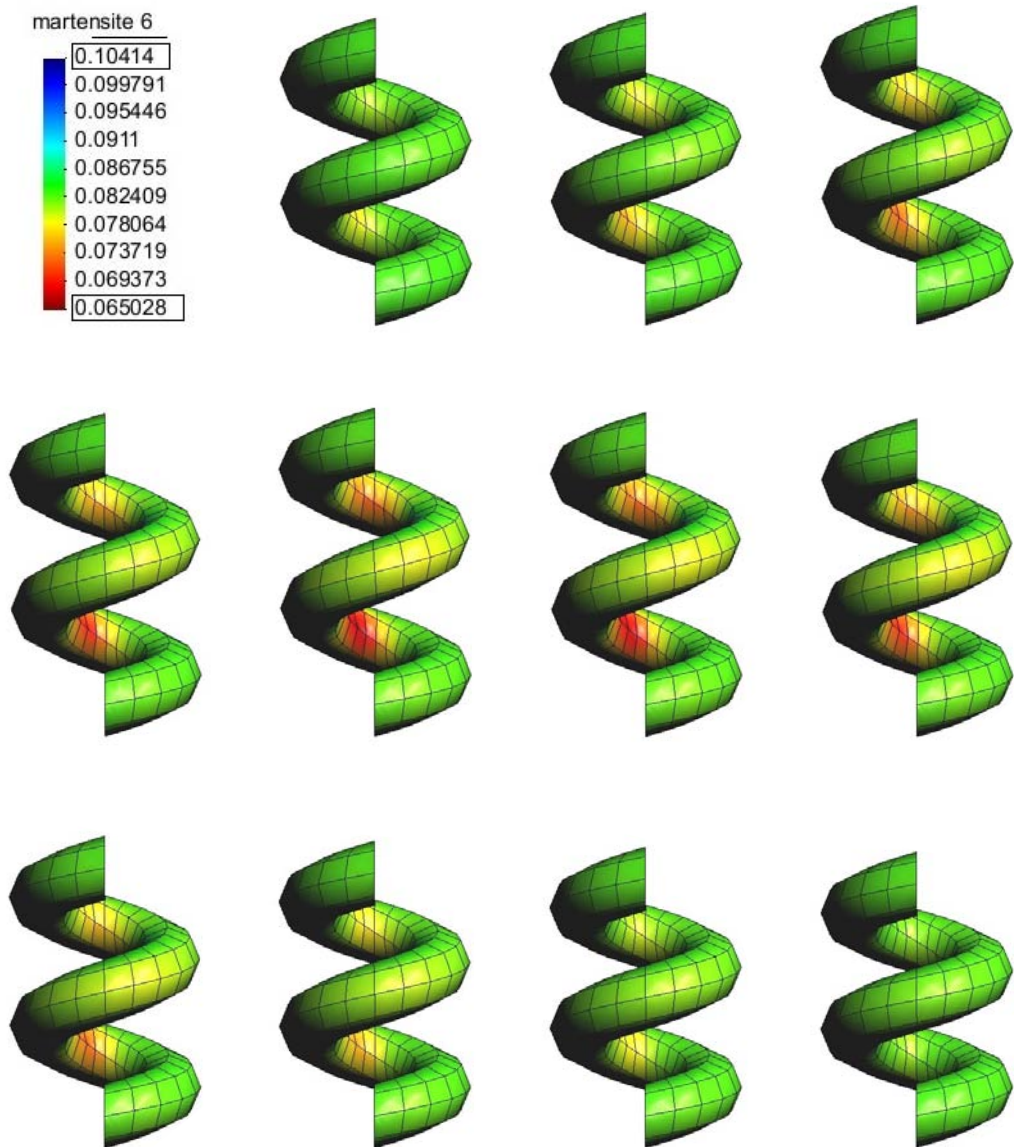


Figure 6.51: Thermo-mechanically coupled model. Distribution of averaged of all martensite six variants  $(\sum_{j=1}^N \xi^j \lambda_6^j)$  in a stripe of NiTi at  $-40^\circ\text{C}$ . Loading velocity  $\dot{u} = 0.4 [\text{mm/min}]$ .

The distribution of temperature, presented in Fig. 6.52, shows that main heat is produced in the center of the spring. This is in accordance to the phase transformation evolving.

Similar to the previous example of pseudo-plasticity, the produced heat in the specimen is higher at the end of the entire loading and unloading process. However, the entire amount of produced heat is much smaller than in the case of pseudo-elasticity for which only the starting temperature was changed. This effect holds true although the spring at  $-40^{\circ}\text{C}$  was only loaded half the way as the spring at  $22^{\circ}\text{C}$ .

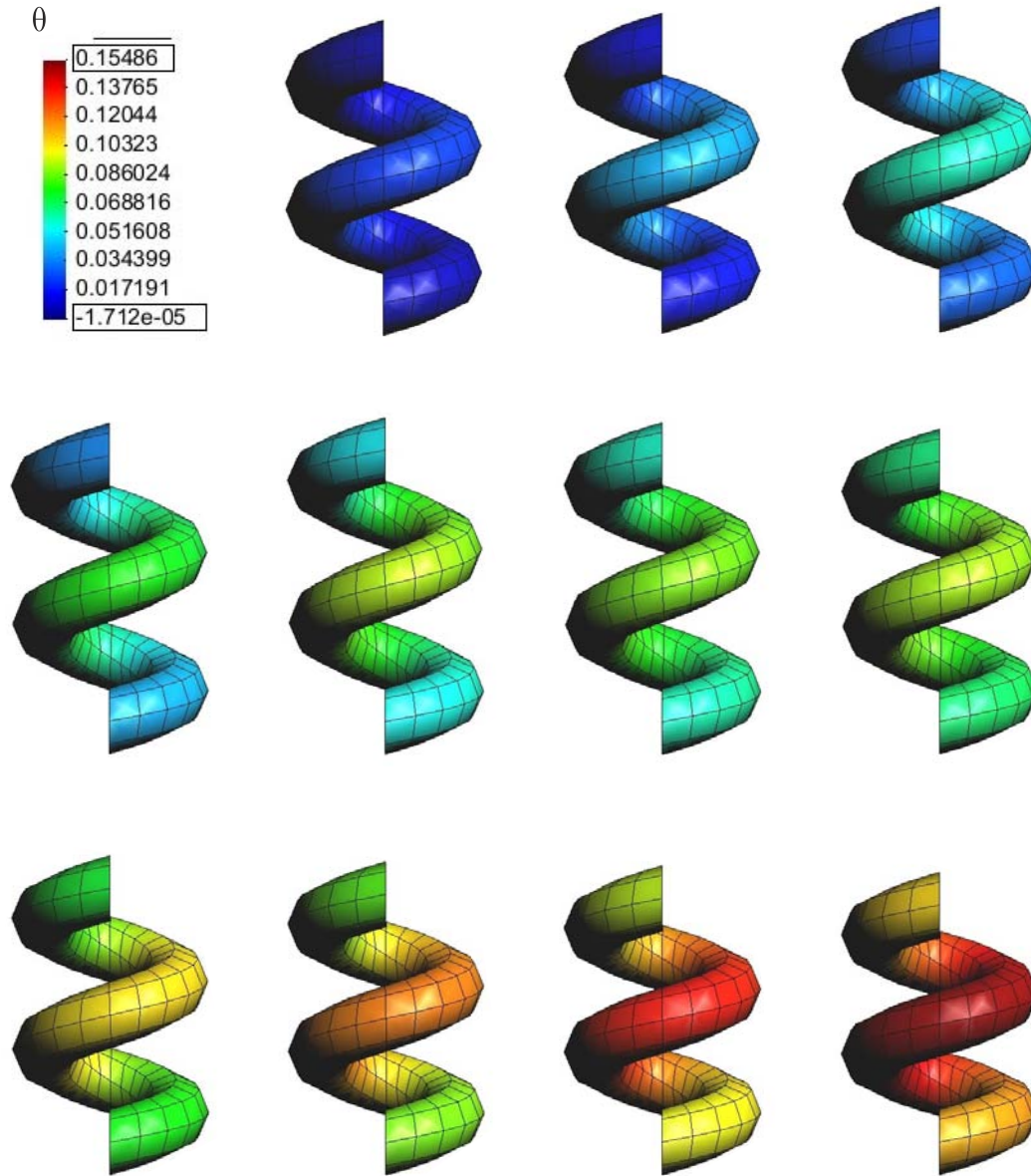


Figure 6.52: Thermo-mechanically coupled model. Distribution of temperature in a stripe of NiTi at  $-40^{\circ}\text{C}$ . Loading velocity  $\dot{u} = 0.4 [\text{mm/min}]$ .

The global material reaction is displayed in a force-displacement diagram, see Fig. 6.53. The result is in this case similar to the ones of the other models. However, there exists a remarkable difference. Although the total character is quite comparable for the case of pseudo-elasticity,  $22^{\circ}\text{C}$  room temperature, the resulting force is remarkably smaller than in the other results. Of course, higher forces for the basic model were expected since the input parameters for  $50^{\circ}\text{C}$  and  $60^{\circ}\text{C}$  were used. Still there was the first surprising result for the extended model which yield due to homogeneous phase transformation similar results as the basic model although the room temperatures differed much ( $50^{\circ}\text{C}$ ,  $60^{\circ}\text{C}$  for the basic model,  $22^{\circ}\text{C}$  for the extended model). Using the thermo-mechanically coupled

model gives for only changed input room temperature a resulting force which is of reasonable magnitude. This shows that the effect of temperature should be taken into account if a non-constant dissipation parameter is used.

Furthermore, the material reaction of the pseudo-plastically behaving spring at  $-40^\circ\text{C}$  is caught in the force-displacement diagram (gray curve). Due to the martensitic elastic constant the spring behaves much stiffer in the elastic region. When phase transformation takes place the force is quite constant. Despite the rather smooth transition from the elastic region into the plateau the resultant curve for the spring is of quite similar character like the curve for the pseudo-plastic stripe, Fig. 6.47. Of course, the forces have different values.

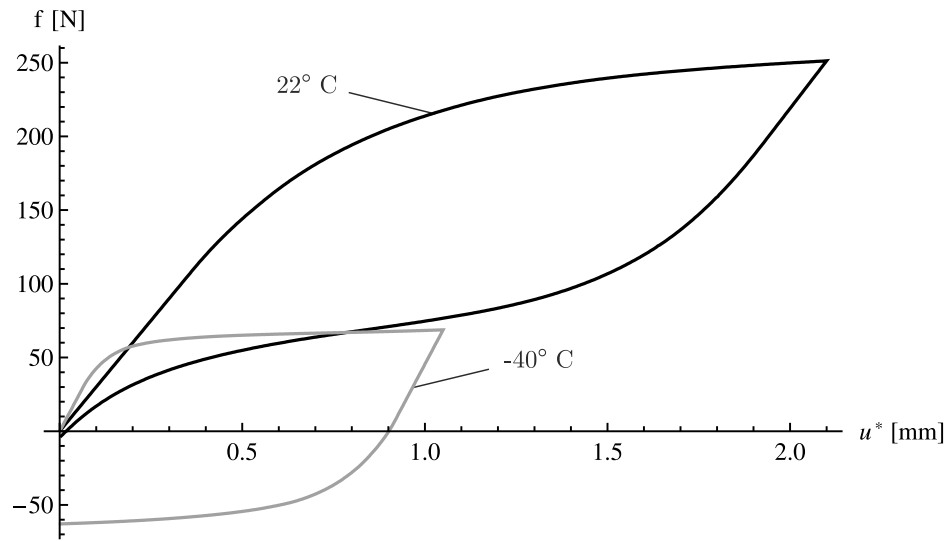


Figure 6.53: Thermo-mechanically coupled model. Force-displacement diagram of a spring of NiTi at  $22^\circ\text{C}$  (black curve) and  $-40^\circ\text{C}$  (gray curve). Loading velocity in both cases  $\dot{u} = 0.4 [\text{mm}/\text{min}]$ .

Concluding, the thermo-mechanically coupled model shows reasonable results. Evolution of temperature fulfills the physically motivated expectations. Additionally, the temperature has a remarkable influence on the results. Both for the case of pseudo-elastic material and pseudo-plastic material, temperature forces the material to react in a different way. Softening effects are damped but the localized character of phase transitions in pseudo-elasticity are maintained. Furthermore, the establishment of several transformation zones is supported. At higher loading velocities the material reaction is of quite different character which has been reported e.g. in [49]. Influence of temperature improves the applicability of the model since the resulting force-displacement curves are in much better coincidence as the results for the extended model applied on a spring. Pseudo-plastic problems could be simulated just by changing the room temperature as input.

The approach of calculating the dissipation parameter straight from the chemical constants is very promising. With a rather rough estimate of the chemical distances already quite good results could be obtained. As long as there exists no approach to calculate  $\Delta a$  and  $\Delta b$  analytically a continued parameter identification can be used to improve the results further.

There exists quite a bunch of different models for shape memory alloys. Hence, in the next section results for the famous model of Taylor and Auricchio are presented. These are used as benchmark for the quality of the models presented in this work.



### 6.3.4 Comparison between the basic model and the phenomenological model of Auricchio and Taylor

As reference model for the material models derived in this work, the model of Auricchio and Taylor is used in its ANSYS implementation. The distributions of the internal phases, on the one hand volume fraction of martensite,  $\gamma_M$ , for the Auricchio and Taylor model and on the other hand the average amount of austenite in the basic model,  $|\lambda_0|$ , are compared. The parameter for the model of Auricchio and Taylor introduced in Sec. 4.3 are fitted to the resulting stress-strain curve of the calculation obtained by the basic model. Hence, they are not displayed here.

The spatial phase distributions provide information about the models' qualities to display the materials reaction on a local level, as already mentioned before. The main characterization for the local material behavior are the localized phase transitions which are supposed to be displayed by the material models.

The regarded geometry is quite similar to the stripe treated before. The displacements are fixed at the left hand side and vary in time at the right hand side. The model of Auricchio and Taylor does not include temperature effects nor thermal coupling. Therefore, the basic model from this work is taken for comparison, Sec. 4.2.2.

Fig. 6.54 displays the distribution of austenite at various time steps calculated with the

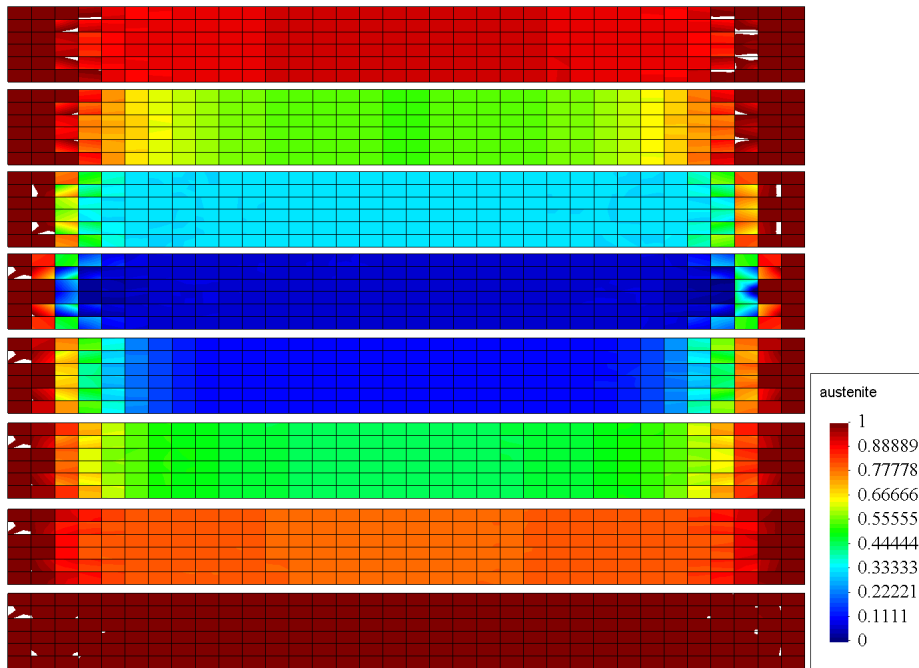


Figure 6.54: Distribution of austenite in a stripe of CuAlNi calculated with the basic model.

basic model of this work. Due to the similarity of the geometries in this section and in Sec. 6.1, the results are quite the same. The phase transformation initializes at the supports (first rows of nodes within the discretization at both ends) while afterwards a homogeneous transformation follows. As pointed out, this is in contrast to the experiments in [48], Fig. 6.1.

The numerical results for the material model of Auricchio and Taylor is presented in Fig. 6.55. The boundary conditions as well as the geometry and loading are completely the same as in the previous calculation with the basic model. Here, the phase transformations start at both ends due to stress peaks. After that a very homogeneous transformation takes place

where there is no spatial localization as observed in experiments. However, the results are

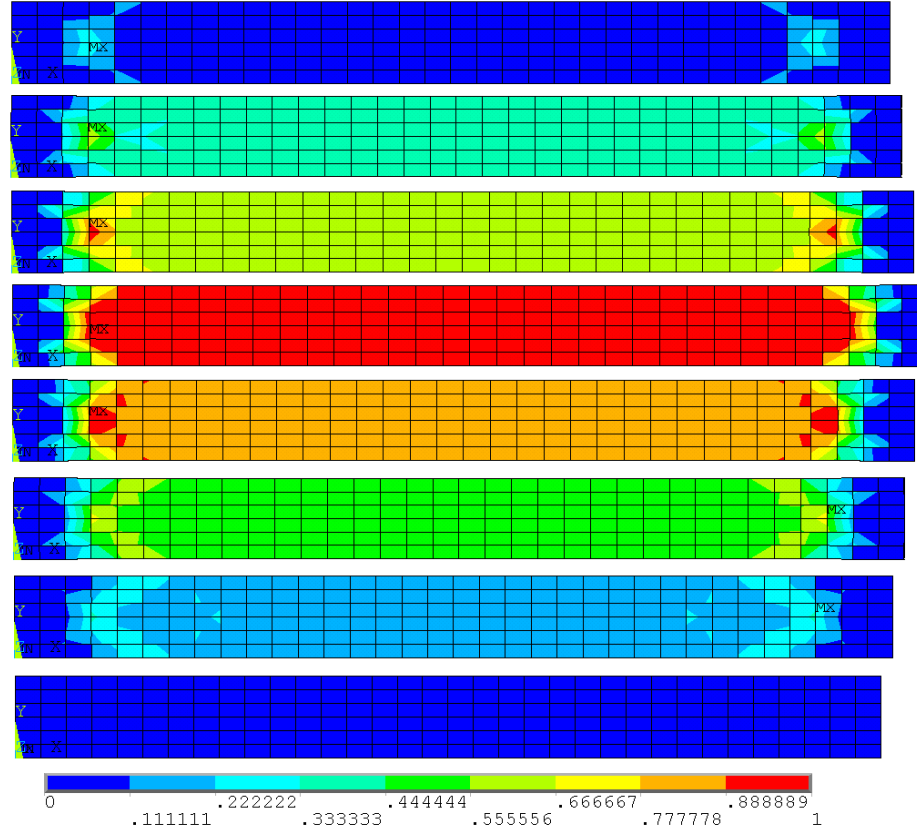


Figure 6.55: Distribution of martensite in a stripe of CuAlNi, calculated with the model of Auricchio and Taylor in its ANSYS implementation.

very similar to the results obtained by the basic model. This proves empirically that for a simple geometry and simple loading both models yield similar results.

The model of Auricchio and Taylor is quite comparable to a material model for plasticity. It does not account for different martensitic phases nor for different grain orientations. This makes the model very fast.

The basic model here resolves for the volume fractions of all the martensitic variants in all the different grain orientations. This makes the model quite slow. Still, the model is more robust from a numerical point of view. The calculations with the model of Auricchio and Taylor tend to fail if the values characterizing the hysteresis,  $\sigma_s^{AS}$  and  $\sigma_f^{As}$  as well as  $\sigma_s^{SA}$  and  $\sigma_f^{SA}$ , are set in a way that the hysteresis reveals a plateau. The basic micromechanical model is quite robust in that regard.

Due to the more detailed resolution more information is provided by the basic model which can be interesting from the material science's or material theory's point of view. However, both models are not able to display the localizing character of the phase transformations evolving in reality. Furthermore, the thermal character is neglected in both models.

The micromechanically motivated model, even in its basic version, does not need problem dependent parameters like stress values nor transformation strains as scalar quantity from a tension test. The parameters here, chemical energy and dissipation parameter, are both only global, problem and loading *independent* quantities. These quantities have to be set only once. After that they are fixed and can be transferred for any other problem due to

their universality. This testifies a broader applicability to micromechanical models like the basic one here, see the examples given above.

The extended as well as the thermo-mechanically coupled model yield results which are in remarkably better coincidence with experimental observations than the results for the basic model. Therefore, a substantial improvement has been performed during the further development of the basic model. Now, localized transformation fronts, well known from experiments, can be displayed and the thermal coupling is included which has a strong impact on the material reaction even in the case of pseudo-elasticity: the loading velocity changes the material behavior significantly which can be observed both in stress-strain diagrams and the amount of transformation fronts.

# Chapter 7

## Conclusions and Outlook

### 7.1 Conclusions

Main focus of this work laid on the discussion of the principle of maximum dissipation and its application to the simulation of shape memory alloys. First, different schemes for evolution equations were compared: the introduction of yield functions for elasto-plastically behaving materials, the principle of the minimum of the dissipation potential and the principle of maximum dissipation. All three methods are in general possible to use for mechanical material modeling. Since modeling is always based on some assumptions the different methods provide different advantages or disadvantages. Depending on the desired model's capability of reflecting different material properties, different concepts can be applied. The interrelation between the models and the respective interpretation in a thermodynamical context were highlighted.

It was pointed out that the desired governing equation which describe inelastic material reactions can be derived from yield functions. The derivative of the yield function with respect to the driving forces, in which the yield function is stated, gives the normal to the yield surface and thus the (relative) change of internal variables. Seeking for the root of the yield function gives then the 'length of the rate vector'. In combination with the general equations in continuum mechanics, the system of equations is closed and can be solved for the entire set of variables describing the current physical state of the treated mechanical body. It was explained that the difficulty of this method lies in the formulation of the yield function: in order to take constraints into account the yield function has to be found in a way that these constraints are fulfilled. While dealing with materials for which modeling is complex, it is complicated to find the correct yield function.

Based on the example of perfect plasticity, the principle of the minimum of the dissipation potential was derived. Starting from a yield function and deductively evolution equations, a LEGENDRE transformation of the problem was carried out. The result of this effort was that the problem could be reformulated by means of a (mathematical) potential which was called dissipation potential. Minimization of this potential resulted in the same evolution equations like in the case of introducing yield functions. The difference between the two concepts was that the mathematically different treatment of the same physical problem by using the dissipation principles allowed to introduce constraints very easily. A back LEGENDRE transformation of this potential gave then the corresponding yield function which already accounts for constraints.

The last principle of material modeling was the principle of maximum dissipation. This

concept used a thermodynamical identity which combined the first and second law of thermodynamics. Then, the principle of maximum dissipation is used to introduce a LAGRANGEan consisting of the dissipation itself, the mentioned thermodynamical identity and further, problem dependent constraints. This LAGRANGEan was then maximized with respect to all free variables. Resulting from the maximization conditions, the constitutive equations for stress and entropy respectively could be derived and additionally the heat conduction equation and evolution equations for the internal variables. A final LEGENDRE transformation of the problem gave then the yield function for the problem.

This concept combined the advantage of an easy introduction of constraints with the inclusion of thermal effects.

After a detailed discussion and general methods to deal with the different principles, the principle of maximum dissipation was applied to the modeling of shape memory alloys. Giving an introduction to the topic both on the material science as well as on the mathematical level, a basic model was derived. Starting from this basic model, two new models were presented whose abilities to predict the material reaction of shape memory alloys on a macroscopic level are much better. All three models were evaluated on a macroscopic level by means of the finite element method for the first time.

Although the basic model yields good results on the GAUSS point level, the material modeling for entire specimens was not satisfactory. This fact motivated the derivation of the two new models. The first one of the new models is able to display the localized transformation fronts which occur during pseudo-elasticity - this stands in contrast to the basic model. The extended model, including softening behavior, was regularized in order to yield still results independent of the finite element discretization of the boundary value problem. The last model takes the influence of temperature into account. This allows that the loading velocity is represented which has a direct influence on the number of transformation fronts evolving due to the stabilizing effect of temperature to austenite. Concluding, this model is able to simulate cooling and heating of shape memory alloys.

The heating-cooling simulations gave raise to a new interpretation of the dissipation parameter. This parameter was formerly a model parameter which was hard to derive from experimental data. Due to its new interpretation, it could be shown that the dissipation parameter is - just like elastic constants and transformation strains - a material parameter which can be examined from the chemical energies of austenite and martensite. This fact broads the even wide basis of the models more and increases the applicability of the models.

The numerical results for the three models proved the progress in modeling and simulating shape memory alloys which was shown by a comparison to the model of Auricchio and Taylor. Starting with the basic model, different boundary value problems were simulated and brought into comparison with experiments. Due to the gap between simulation and experiment, the extended model was derived taking into account different energetic thresholds for nucleation and evolution of crystallographic phases. This model delivered the desired result of localized transformations but in order to receive results independent of the finite element mesh, a regularization method had to be applied. The final, thermo-mechanically coupled model was used to simulate different problems which served as basis for discussion.

Concluding, particularly the extended and the thermo-mechanically coupled model show very good agreement to experimental observations both on local as on global scale. The simulation of pseudo-elasticity and pseudo-plasticity are possible, all based on the basic physical laws and on parameters which can completely be found from experiments, except for one phenomenological parameter (penalty parameter for the gradient of the field func-

tion: global surface energy). Since the parameters seem to have an universal character and even completely different material behavior is possible to be simulated the model presented here belongs to the class of *energetic* models described in Sec. 1.

## 7.2 Outlook

Although the results are now quite good, the models could be improved further. Particularly the exact values for the differences in the chemical energies have to be investigated in further parameter studies. A topic of recent origin is the interplay between phase transformations and plasticity. This effect is discussed right now in science. In order to understand the processes which evolve in real materials, the tool of simulation can be helpful. Hence, the inclusion of plasticity in the models is a point which is left to be done. Then, it might be easier to understand the underlying reasons and processes how and under which conditions material reactions occur which are observed in experiments. An example can be the functional fatigue which appears with increasing number of load cycles.

Furthermore, the extension of the model by means of damage is a very interesting goal for future activities. Then, the processes of structural as well as functional fatigue - maybe in combination with the inclusion of plasticity - can be eventually understood better, too. Although this topic shows a certain potential, its realization is a quite hard task as usual when dealing with damage: the estimation of material parameters which are valid for all loading cases in an optimal solution, is very complicated. However, as executed for the dissipation parameter simulations itself may show a better understanding of the underlying model and hence there may exist a way to estimate this parameters, as well.

Based on the new interpretation of the dissipation coefficient a database seems to be useful. Relying on experimental data, the chemical constants depending on the specific alloy composition and maybe temperature have to be found. Then, finally a universal model for shape memory alloys is available where the only input parameters are the current material and the current room temperature. If there are ways to accelerate the models calculation speed, the model derived in this work may be used even in industrial applications.

Finally, from the programmer's point of view a parallelization seems to be convenient to accelerate the model in order to simulate specimens with an even higher resolution. This would make the simulation for bending processes of shape memory alloys in an acceptable amount of time possible where a very high number of elements for the numerical treatment is necessary.



# Appendix A

## Material Data

### A.1 Nickel Titanium

The material data for Nickel Titanium (NiTi) are taken from [60] and collected in Tab. A.1, transformation strains, and Tab. A.2, elastic constants.

$\boldsymbol{\eta}_1 = \begin{pmatrix} \alpha & \delta & \epsilon \\ \delta & \alpha & \epsilon \\ \epsilon & \epsilon & \beta \end{pmatrix}$	$\boldsymbol{\eta}_2 = \begin{pmatrix} \alpha & \delta & -\epsilon \\ \delta & \alpha & -\epsilon \\ -\epsilon & -\epsilon & \beta \end{pmatrix}$	$\boldsymbol{\eta}_3 = \begin{pmatrix} \alpha & -\delta & -\epsilon \\ -\delta & \alpha & \epsilon \\ -\epsilon & \epsilon & \beta \end{pmatrix}$
$\boldsymbol{\eta}_4 = \begin{pmatrix} \alpha & -\delta & \epsilon \\ -\delta & \alpha & -\epsilon \\ \epsilon & -\epsilon & \beta \end{pmatrix}$	$\boldsymbol{\eta}_5 = \begin{pmatrix} \alpha & \epsilon & \delta \\ \epsilon & \beta & \epsilon \\ \delta & \epsilon & \alpha \end{pmatrix}$	$\boldsymbol{\eta}_6 = \begin{pmatrix} \alpha & -\epsilon & \delta \\ -\epsilon & \beta & -\epsilon \\ \delta & -\epsilon & \alpha \end{pmatrix}$
$\boldsymbol{\eta}_7 = \begin{pmatrix} \alpha & -\epsilon & -\delta \\ -\epsilon & \beta & \epsilon \\ -\delta & \epsilon & \alpha \end{pmatrix}$	$\boldsymbol{\eta}_8 = \begin{pmatrix} \alpha & \epsilon & -\delta \\ \epsilon & \beta & -\epsilon \\ -\delta & -\epsilon & \alpha \end{pmatrix}$	$\boldsymbol{\eta}_9 = \begin{pmatrix} \beta & \epsilon & \epsilon \\ \epsilon & \alpha & \delta \\ \epsilon & \delta & \alpha \end{pmatrix}$
$\boldsymbol{\eta}_{10} = \begin{pmatrix} \beta & -\epsilon & -\epsilon \\ -\epsilon & \alpha & \delta \\ -\epsilon & \delta & \alpha \end{pmatrix}$	$\boldsymbol{\eta}_{11} = \begin{pmatrix} \beta & -\epsilon & \epsilon \\ -\epsilon & \alpha & -\delta \\ \epsilon & -\delta & \alpha \end{pmatrix}$	$\boldsymbol{\eta}_{12} = \begin{pmatrix} \beta & \epsilon & -\epsilon \\ \epsilon & \alpha & -\delta \\ -\epsilon & -\delta & \alpha \end{pmatrix}$

Table A.1: Material data for NiTi: transformation strains.  $\alpha = 0.02381$ ,  $\beta = -0.02480$ ,  $\delta = 0.07528$ ,  $\epsilon = 0.04969$

The elastic constants for martensite have to be rotated and / or mirrored into the direction of every variant. This is carried out by means of the operation matrices in Tab. A.3 which serve as input for special rotation matrices in the six-dimensional space according to MEHRABADI-COWIN . The general six-dimensional rotation matrix  $\tilde{\mathbf{Q}}$  is given, according



$\tilde{\mathbb{C}}_0 = \begin{pmatrix} 140 & 110 & 110 & 0 & 0 & 0 \\ 110 & 140 & 110 & 0 & 0 & 0 \\ 110 & 110 & 110 & 0 & 0 & 0 \\ 0 & 0 & 0 & 32 & 0 & 0 \\ 0 & 0 & 0 & 0 & 32 & 0 \\ 0 & 0 & 0 & 0 & 0 & 32 \end{pmatrix} \text{ GPa}$
$\hat{\mathbb{C}}_{i>0} = \begin{pmatrix} 223 & 129 & 99 & 0 & 7 & 0 \\ 129 & 241 & 125 & 0 & -9 & 0 \\ 99 & 125 & 200 & 0 & 4 & 0 \\ 0 & 0 & 0 & 76 & 0 & -8 \\ 7 & -9 & 4 & 0 & 21 & 0 \\ 0 & 0 & 0 & -8 & 0 & 77 \end{pmatrix} \text{ GPa}$

Table A.2: Material data for NiTi: elastic constants for austenite and martensite (in notation of MEHRABADI-COWIN ).

to [37], as

$$\tilde{\mathbf{Q}}(\mathbf{Q}) = \begin{pmatrix} Q_{1,1}^2 & Q_{1,2}^2 & Q_{1,3}^2 \\ Q_{2,1}^2 & Q_{2,2}^2 & Q_{2,3}^2 \\ Q_{3,1}^2 & Q_{3,2}^2 & Q_{3,3}^2 \\ \sqrt{2}Q_{2,1}Q_{3,1} & \sqrt{2}Q_{2,2}Q_{3,2} & \sqrt{2}Q_{2,3}Q_{3,3} \\ \sqrt{2}Q_{1,1}Q_{3,1} & \sqrt{2}Q_{1,2}Q_{3,2} & \sqrt{2}Q_{1,3}Q_{3,3} \\ \sqrt{2}Q_{1,1}Q_{2,1} & \sqrt{2}Q_{1,2}Q_{2,2} & \sqrt{2}Q_{1,3}Q_{2,3} \\ \sqrt{2}Q_{1,2}Q_{1,3} & \sqrt{2}Q_{1,1}Q_{1,3} & \sqrt{2}Q_{1,1}Q_{1,2} \\ \sqrt{2}Q_{2,2}Q_{2,3} & \sqrt{2}Q_{2,1}Q_{2,3} & \sqrt{2}Q_{2,1}Q_{2,2} \\ \sqrt{2}Q_{3,2}Q_{3,3} & \sqrt{2}Q_{3,1}Q_{3,3} & \sqrt{2}Q_{3,1}Q_{3,2} \\ Q_{2,3}Q_{3,2} + Q_{2,2}Q_{3,3} & Q_{2,3}Q_{3,1} + Q_{2,1}Q_{3,3} & Q_{2,2}Q_{3,1} + Q_{2,1}Q_{3,2} \\ Q_{1,3}Q_{3,2} + Q_{1,2}Q_{3,3} & Q_{1,3}Q_{3,1} + Q_{1,1}Q_{3,3} & Q_{1,2}Q_{3,1} + Q_{1,1}Q_{3,2} \\ Q_{1,3}Q_{2,2} + Q_{1,2}Q_{2,3} & Q_{1,3}Q_{2,1} + Q_{1,1}Q_{2,3} & Q_{1,2}Q_{2,1} + Q_{1,1}Q_{2,2} \end{pmatrix} \quad (\text{A.1})$$

with the components  $Q_{i,j}$  of the three-dimensional rotation matrix  $\mathbf{Q}$ . In that way, every rotation matrix in the three-dimensional space can be transferred to the corresponding rotation matrix in the six-dimensional space. For example,

$$\mathbf{Q}^T \cdot \boldsymbol{\eta} \cdot \mathbf{Q} \xleftrightarrow{3 \leftrightarrow 6} \tilde{\boldsymbol{\eta}} \cdot \tilde{\mathbf{Q}}(\mathbf{Q}) \quad (\text{A.2})$$

for the rotated transformation strains and

$$Q_{so}Q_{tp}Q_{uq}Q_{vr} \mathbb{C}_{stuv} \xleftrightarrow{3 \leftrightarrow 6} \tilde{\mathbf{Q}}(\mathbf{Q})_{so} \tilde{\mathbb{C}}_{sv} \tilde{\mathbf{Q}}(\mathbf{Q})_{vr} \quad (\text{A.3})$$

for the rotated elastic constants, both in the MEHRABADI-COWIN notation.

$\hat{\mathbf{M}}_1 = \begin{pmatrix} 1 & 0 & 0 \\ 0 & 1 & 0 \\ 0 & 0 & 1 \end{pmatrix}$	$\hat{\mathbf{M}}_2 = \begin{pmatrix} 1 & 0 & 0 \\ 0 & 1 & 0 \\ 0 & 0 & -1 \end{pmatrix}$	$\hat{\mathbf{M}}_3 = \begin{pmatrix} -1 & 0 & 0 \\ 0 & 1 & 0 \\ 0 & 0 & 1 \end{pmatrix}$
$\hat{\mathbf{M}}_4 = \begin{pmatrix} 1 & 0 & 0 \\ 0 & -1 & 0 \\ 0 & 0 & 1 \end{pmatrix}$	$\hat{\mathbf{M}}_5 = \begin{pmatrix} 1 & 0 & 0 \\ 0 & 0 & 1 \\ 0 & 1 & 0 \end{pmatrix}$	$\hat{\mathbf{M}}_6 = \begin{pmatrix} 1 & 0 & 0 \\ 0 & 0 & 1 \\ 0 & -1 & 0 \end{pmatrix}$
$\hat{\mathbf{M}}_7 = \begin{pmatrix} -1 & 0 & 0 \\ 0 & 0 & 1 \\ 0 & 1 & 0 \end{pmatrix}$	$\hat{\mathbf{M}}_8 = \begin{pmatrix} 1 & 0 & 0 \\ 0 & 0 & -1 \\ 0 & 1 & 0 \end{pmatrix}$	$\hat{\mathbf{M}}_9 = \begin{pmatrix} 0 & 0 & 1 \\ 0 & 1 & 0 \\ 1 & 0 & 0 \end{pmatrix}$
$\hat{\mathbf{M}}_{10} = \begin{pmatrix} 0 & 0 & 1 \\ 0 & 1 & 0 \\ -1 & 0 & 0 \end{pmatrix}$	$\hat{\mathbf{M}}_{11} = \begin{pmatrix} 0 & 0 & 1 \\ 0 & -1 & 0 \\ 1 & 0 & 0 \end{pmatrix}$	$\hat{\mathbf{M}}_{12} = \begin{pmatrix} 0 & 0 & -1 \\ 0 & 1 & 0 \\ 1 & 0 & 0 \end{pmatrix}$

Table A.3: Material data for NiTi: operation matrices to calculate the elastic constants for the specific martensitic variants according to  $\tilde{\mathbf{Q}}(\hat{\mathbf{M}}_i^T) \cdot \hat{\mathbb{C}}_{i>0} \cdot \tilde{\mathbf{Q}}(\hat{\mathbf{M}}_i) = \tilde{\mathbb{C}}_{i>0}$ .



# Bibliography

- [1] ANSYS. Ansys. release 11.0 documentation for ansys.
- [2] Ferdinando Auricchio and Robert L. Taylor. Shape-memory alloys: modelling and numerical simulations of the finite-strain superelastic behavior. *Computer Methods in Applied Mechanics and Engineering*, 143(1-2):175 – 194, 1997.
- [3] J. M. Ball and R. D. James. Fine phase mixtures as minimizers of energy. *Arch. Rat. Mech. Anal.*, 100:13–52, 1987.
- [4] Th. Bartel and K. Hackl. A micromechanical model for single-crystal shape-memory alloys. *Proc. Appl. Math. Mech.*, 4:298–299, 2004.
- [5] K.J. Bathe. *Finite-Elemente-Methoden*. 1990.
- [6] K. Bhattacharya. *Microstructure of Martensite. Why it forms and how it gives rise to the shape-memory effect*. Oxford University Press, 2003.
- [7] C. Bouvet, S. Calloch, and C. Lexcellent. A phenomenological model for pseudoe-lasticity of shape memory alloys under multiaxial proportional and nonproportional loadings. *Eur. J. Mech. A-Solids*, 23:37–61, 1987.
- [8] C. Carstensen, K. Hackl, and A. Mielke. Non-convex potentials and microstructures in finite-strain plasticity. *Proceedings of the Royal Society A: Mathematical, Physical & Engineering Sciences*, 458(2018):299–317, 2002.
- [9] B. Dacorogna. Quasiconvexity and relaxation of nonconvex problems in the calculus of variations. *J. Funct. Anal.*, 46:102–118, 1982.
- [10] B. J. Dimitrijevic and K. Hackl. A method for gradient enhancement of continuum damage models. *Technische Mechanik*, 28(1):43–52, 2008.
- [11] B. J. Dimitrijevic and K. Hackl. A variational coupled damage-plasticity model via gradient enhancement of the free energy function. *Proc. Appl. Math. Mech.*, 9(1):199–200, 2009.
- [12] J. Frenzel, E.P. George, A. Dlouhy, Ch. Somsen, M.F.-X. Wagner, and Eggeler G. Influence of ni on martensitic phase transformations in niti shape memory alloys. *Acta Materialia*, 58(9):3444 – 3458, 2010.
- [13] G. Gottstein. *Physical Foundations of Materials Science*. Springer, 2004.
- [14] S. Govindjee, K. Hackl, and R. Heinen. An upper bound to the free energy of mixing by twin-compatible lamination for n-variant martensitic phase transformations. *Continuum Mech. Therm.*, 18(7-8):443–453, 2007.

- [15] S. Govindjee and G. Hall. A computational model for shape memory alloys. *Int. J. Sol. Struct.*, 37:735–760, 2000.
- [16] S. Govindjee and C. Miehe. A multi-variant martensitic phase transformation model: formulation and numerical implementation. *Comput. Methods Appl. Mech. Engrg.*, 191:215–238, 2001.
- [17] S. Govindjee, A. Mielke, and G. J. Hall. The free energy of mixing for n-variant martensitic phase transformations using quasi-convex analysis. *J. Mech. Phys. Solids*, 51:763+, 2003.
- [18] K. Hackl and F.D. Fischer. On the relation between the principle of maximum dissipation and inelastic evolution given by dissipation potentials. *Proc. R. Soc. A*, 464(2089):117–132, 2008.
- [19] K. Hackl and R. Heinen. A micromechanical model for pre textured polycrystalline shape-memory alloys including elastic anisotropy. *Continuum Mech. Therm.*, 19:8, 2008.
- [20] K. Hackl, M. Schmidt-Baldassari, and W. Zhang. A micromechanical model for polycrystalline shape-memory alloys. *Materials Science and Engineering A*, 378(1-2):503–506, 2004.
- [21] K. Hackl, W. Zhang, M. Schmidt-Baldassari, and U. Hoppe. Micromechanics of tension-compression asymmetry of polycrystalline shape-memory-alloys. *Mat.-wiss. u. Werkstofftech.*, 35(5):284–288, 2004.
- [22] H. G. Hahn. *Elastizitätstheorie*. B. G. Teubner Stuttgart, 1985.
- [23] B. Halphen and Q. S. Nguyen. Sur les matériaux standard généralisés. *J. Méch.*, 14:39–63, 1975.
- [24] M. Hasan, W. W. Schmahl, K. Hackl, R. Heinen, J. Frenzel, S. Gollerthan, G. Eggeler, J. Khalil-Allafi, and A. Baruj. Hard x-ray studies of stress-induced phase transformations of superelastic niti shape memory alloys under uniaxial load. *Mat. Sci. Eng. A-Struct.*, 481(Sp. Iss. SI):414–419, 2008.
- [25] R. Heinen and K. Hackl. A micromechanical model for polycrystalline shape memory alloys – formulation and numerical validation. In K. Hackl, editor, *IUTAM Symposium on Variational Concepts with Applications to the Mechanics of Materials*, volume 21 of *IUTAM Bookseries*, pages 91–103. Springer Netherlands, 2010.
- [26] D. Helm and P. Haupt. Shape memory behaviour: modelling within continuum mechanics. *Int. J. Sol. Struct.*, 40:827–849, 2003.
- [27] G. A. Holzapfel. *Nonlinear Solid Mechanics: A Continuum Approach for Engineering*. John Wiley & Sons Ltd., Baffins Lane, Chichester, West Sussex PO19 1UD, England, 2000.
- [28] Y. Huo and I. Mueller. Nonequilibrium thermodynamics of pseudoelasticity. *Continuum Mech. Thermodyn.*, 5:163–204, 1993.
- [29] E. Klingbeil. *Tensorrechnung für Ingenieure*. BI-Wiss.-Verl., 1989.

- [30] Vivet A. et al. L'excellent, C. Experimental and numerical determination of the initial surface of phase transformation under biaxial loading in some polycrystalline shape-memory alloys. *J. Mech. Phys. Sol.*, 50:2717–2735, 2001.
- [31] J. Lubliner. A maximum-dissipation principle in generalized plasticity. *Acta Mechanica*, 52:225–237, 1984. 10.1007/BF01179618.
- [32] P. Luig and O.T. Bruhns. On the modeling of shape memory alloys using tensorial internal variables. *Materials Science and Engineering: A*, 481-482:379 – 383, 2008. Proceedings of the 7th European Symposium on Martensitic Transformations, ESO-MAT 2006.
- [33] E. Fried M. Gurtin and L. Anand. *The Mechanics and Thermodynamics of Continua*. Cambridge University Press, 2009.
- [34] K. Melton S. Miyazaki I. Ohkata K. Otsuka T. Saburi R. Stalmans Y. Suzuki T. Tadaki K. Uchino J. van Humbeeck C.M. Wayman M. Irie, T. Maki. *Shape Memory Materials*. Cambridge University Press, 1998.
- [35] J. B. Martin and A. S. Ponter. A note on a work inequality in linear viscoelasticity. *Q. Appl. Math.*, 24:161–165, 1966.
- [36] G. A. Maugin. *The thermomechanics of plasticity and fracture*. Cambridge University Press, 1992.
- [37] M. Mehrabadi and S. Cowin. Eigentensors of linear anisotropic elastic materials. *The Quarterly Journal of Mechanics and Applied Mathematics*, 43(1):15–41, 1990.
- [38] C. Miehe, Gürses, and M. Birkle. A computational framework of configurational-force-driven brittle fracture based on incremental energy minimization. *Int. J. Frac.*, 145:245 – 259, 2007.
- [39] Ch. Miehe and M. Lambrecht. Analysis of microstructure development in shearbands by energy relaxation of incremental stress potentials: Large-strain theory for standard dissipative solids. *International Journal for Numerical Methods in Engineering*, 58(1):1–41, 2003.
- [40] A. Mielke. Energetic formulation of multiplicative elasto-plasticity using dissipation distances. *Cont. Mech. Thermodyn.*, 15:351–382, 2003.
- [41] Ch. Müller and O.T. Bruhns. A thermodynamic finite-strain model for pseudoelastic shape memory alloys. *International Journal of Plasticity*, 22(9):1658 – 1682, 2006.
- [42] N. Nabiran, H. Berns, and S. Riedner. High interstitial stainless austenitic steel: As-cast vs. esr and hot worked. In *Super-High Strength Steels, Oct. 17.-20. 2010, Italy*, 2010.
- [43] L. Onsager. Reciprocal relations in irreversible processes. i. *Phys. Rev.*, 37(4):405–426, Feb 1931.
- [44] L. Onsager. Theories and problems of liquid diffusion. *Ann. NY Acad. Sci.*, 46:241–265, 1945.
- [45] K. Otsuka and X. Ren. Physical metallurgy of ti-ni-based shape memory alloys. *Progress in Materials Science*, 50(5):511 – 678, 2005.

- [46] K. Otsuka and C.M. Wayman. *Shape Memory Materials*. Cambridge University Press, 1999.
- [47] S. Reese, M. Böl, and D. Christ. Finite element-based multi-phase modelling of shape memory polymer stents. *Computer Methods in Applied Mechanics and Engineering*, 199(21-22):1276 – 1286, 2010. Multiscale Models and Mathematical Aspects in Solid and Fluid Mechanics.
- [48] A. Schaefer and M.F.-X. Wagner. Strain mapping at propagating interfaces in pseudoelastic niti. *ESOMAT*, page 06031, 2009.
- [49] J.A. Shaw. Simulations of localized thermo-mechanical behavior in a niti shape memory alloy. *International Journal of Plasticity*, 16(5):541 – 562, 2000.
- [50] M. Silhavý. *The Mechanics and Thermodynamics of Continuous Media*. Springer, 1997.
- [51] J. C. Simo and T. J. R. Hughes. *Computational Inelasticity*. Springer, 1998.
- [52] E. Stein and G. Sagar. Theory and finite element computation of cyclic martensitic phase transformation at finite strain. *Int. J. Numer. Meth. Engng*, 2008:1–31, 74.
- [53] S. Stupkiewicz and H. Petryk. Modelling of laminated micro-structures in stress-induced martensitic transformation. *J. Mech. Phys. Sol.*, 2002:2303–2331, 50.
- [54] J. Svoboda, F. D. Fischer, P. Fratzl, and A. Kroupa. Diffusion in multi-component systems with no or dense sources and sinks for vacancies. *Acta Mater.*, 50:1369–1381, 2002.
- [55] J. Svoboda and I. Turek. On diffusion-controlled evolution of closed solid-state thermodynamic systems at constant temperature and pressure. *Philosophical Magazine Part B*, 64(6):749–759, 1991.
- [56] J. Svoboda, I. Turek, and F. D. Fischer. Application of the thermodynamic extremal principle to modeling of thermodynamic processes in material sciences. *Philosophical Magazine*, 85(31):3699–3707, 2005.
- [57] V. Triani, C. Papenfuss, V. Cimmelli, and W. Muschik. Exploitation of the second law: Coleman–noll and liu procedure in comparison. *J. of Non-Equ. Thermodyn.*, 33:47–60, 2008.
- [58] C. Truesdell and W. Noll. *The Non-Linear Field Theories of Mechanics*. Springer, 1965.
- [59] M.F.-X. Wagner. *Ein Beitrag zur strukturellen und funktionalen Ermüdung von Drähten und Federn aus NiTi-Formgedächtnislegierungen*. PhD thesis, Ruhr-University of Bochum, 2005.
- [60] M.F.-X. Wagner and W. Windl. Lattice stability, elastic constants and macroscopic moduli of niti martensites from first principles. *Acta Materialia*, 56(20):6232 – 6245, 2008.
- [61] P. Wriggers. *Nichtlineare Finite-Elemente-Methoden*. Springer, 2001.
- [62] W. Zhang, K. Hackl, and U. Hoppe. Micromechanical modelling of the constitutive behaviour of niti shape memory alloys. *Proc. Appl. Math. Mech.*, 4(1):272–273, 2004.

- [63] O. C. Zienkiewicz and R. L. Taylor. *The Finite Element Method (6 ed.)*. Butterworth - Heinemann, 2005.



## Pre-Publications

In accordance with §7(1) parts of this dissertation have been published in international scientific journals and conference proceedings in consultation with the supervisors, Professors Klaus Hackl and Alexander Hartmaier. These pre-publications are listed below.

- Junker, P., Hackl, K., (2009). Numerical simulations of poly-crystalline shape-memory-alloys based on a micromechanical model. PAMM, 9: 339–340.  
doi: 10.1002/pamm.200910143
- Junker, P., Hackl, K., (2009). On the numerical simulation of material inhomogeneities due to martensitic phase-transformations in poly-crystals. ESOMAT, 2009.  
doi: 10.1051/esomat/200903007
- Junker, P., Hackl, K., (2010). On the thermo-mechanically coupled simulation of poly-crystalline Shape Memory Alloys. PAMM, 10: 295–296.  
doi: 10.1002/pamm.201010140
- Junker, P., Hackl, K., (2011). Finite element simulations of poly-crystalline shape memory alloys based on a micromechanical model. Comput. Mech., 47, 5: 505–517.  
doi: 10.1007/s00466-010-0555-4
- Junker, P., Hackl, K., (2011). About the influence of heat conductivity on the mechanical behavior of poly-crystalline shape memory alloys. Int. J. Struct. Chang., 3, 1: 49–62.
- Hackl, K., Junker, P., Heinen, R., (2011). Variational modeling of shape memory alloys – an overview. Int. J. Mat. Res., 2011/06: 643–651.  
doi: 10.3139/146.110527
- Junker, P., Hackl, K., (2011). Simulation of pseudo-plasticity in shape-memory-alloys. PAMM, 11: to appear.

## Curriculum Vitae

### Personal Data

Name	Philipp Junker
Date of Birth	May 31, 1983
Place of Birth	Bochum, NRW, Germany
Nationality	German
Marital Status	Single

### School Education

08/1989 – 03/1992	Grundschule, Gärtringen, BW, Germany
03/1992 – 08/1993	Brantropschule, Bochum, NRW, Germany
08/1993 – 06/2002	Graf-Engelbert-Gymnasium, Bochum, NRW, Germany

### Military Service

10/2002 – 06/2003	3./WachBtl., BMVg, Siegburg, NRW, Germany
-------------------	---

### University Education

10/2003 – 02/2008	Mechanical Engineering Ruhr-University of Bochum, Germany, field of special interest: structural mechanics Diploma (Dipl.-Ing.)
-------------------	--

### Professional Occupation

10/2006 – 02/2008	student assistant, Lehrstuhl für Allgemeine Mechanik, Ruhr-University of Bochum, Germany
03/2008 – present	research assistant, Lehrstuhl für Allgemeine Mechanik, Ruhr-University of Bochum, Germany

**Mitteilungen aus dem Institut für Mechanik  
RUHR-UNIVERSITÄT BOCHUM  
Nr. 155**

**ISBN 978-3-935892-33-9**